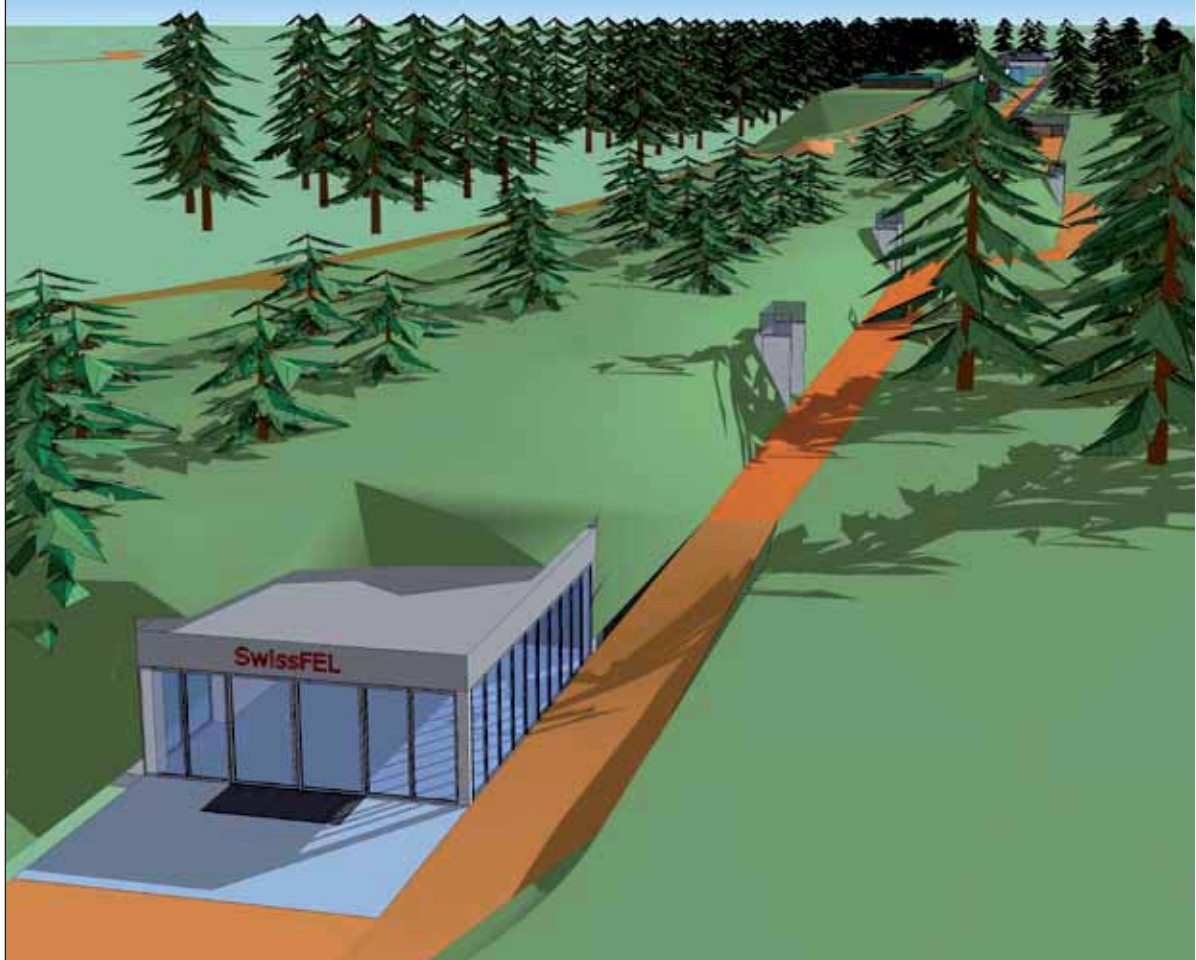


PAUL SCHERRER INSTITUT



Update SwissFEL CDR
Version 03.03.2011 – V19
PSI Bericht 10 -04

SwissFEL Conceptual Design Report



Cover figure description

SwissFEL building layout: With a total length of 713 m, the accelerator and undulator are located in the lower floor of a two-storey building. Most of the building will be underground, but the upper floor (technical buildings) will only be semi-covered with soil, to ensure good maintainance access. The experimental area building is a single-storey building which is naturally covered by the surrounding land, and the main entrance to this area is clearly visible (Front View).

Editor

Romain Ganter

Editorial Board

Rafael Abela
Hans Heinrich Braun
Terry Garvey
Bruce Patterson
Marco Pedrozzi
Sven Reiche

With contributions
from:

Executive Summary

Braun H.H.
Ganter R.
Patterson B.

Design Strategy and Parameters Choice

Abela R.
Adelmann A.
Beutner B.
Falone A.
Flehsig U.
Kim Y.
Milas N.
Oppelt A.
Reiche S.

Electron Components

Alex J.
Aiba M.
Arsov V.
Calvi M.
Egli S.
Gough C.
Hauri C.
Hunziker S.
Ischebeck R.
Joehri H.
Keil B.
Kuenzi R.
Pedrozzi M.
Raguin J.-Y.
Sanfilippo S.
Schilcher T.
Schlott V.
Schmidt T.
Schulz L.
Trisorio A.
Vermeulen D.
Wiegand P.
Zennaro R.

Photon Components

Patterson B.
Pedrini B.

Machine Assembly

Aiba M.
Dreyer K.
Keil B.
Kuenzi R.
Luethy M.
Wickstroem J.

Building and Infrastructure

Baechli A.
Fuchs A.
Ganter R.
Janzi G.
Kiselev D.
Loertscher Y.
Luescher R.
Ming P.
Roser W.
Teichmann S.

Acknowledgements

The author list of this report is limited to the people who have actually written text or supplied figures or tables appearing in the CDR. Many more people from PSI and abroad have contributed to SwissFEL and indirectly to the content of the CDR. The authors of this CDR recognize in particular that the concept for SwissFEL emerged from the “LEG/FEL” R&D activity which was launched at PSI under the leadership of Prof. Albin Wrulich in 2003 [1,2]. Many contributions to the concept as well as to technical solutions which appear in this conceptual design report can be traced back to the work of this R&D activity, although it was not always possible to put references to this work.

Furthermore we profited from the advice and collaboration with many experts from other laboratories. In particular we would like to thank our colleagues from CANDLE, CERN, DESY, ELETTRA, EMPA, HZB, INFN-LNF, SINAP, SLAC and SPRING8.

Last, not least we acknowledge the enormous help and constructive critics we got from the SwissFEL machine advisory committee FLAC chaired by Prof. Jörg Rossbach.

Version Modifications SwissFEL CDR:

| Version Number | Date | Description of modifications since last version |
|----------------|----------------------|--|
| V1 | 10.04.16 | First Version of CDR for the FLAC Meeting of 19th – 20th April 2010 |
| V2 | 10.04.19 | With summary tables on Experiments with Athos and Aramis |
| V3 | 10.04.20 | Cosmetic Changes |
| V4 | 10.05.19 | |
| V5 | 10.05.20 | Cosmetic Changes |
| V6 | 10.05.27 | Version sent to Joel Mesot for ETH Rat Meeting With section on RF modulator concept With RF phase stability measurement from solid state modulator |
| V7 | 10.06.15 | With the new RF frequencies 2.9988, 5.712, 11.9952 GHz. |
| V8 | 10.06.17 | Cosmetic changes |
| V9 | 10.06.18 | Cosmetic changes |
| V10 | 10.06.22 | With Building Half covered with earth. With improved section 3.3 on synchronization First Version sent to Irma Herzog for Layout preparation |
| V11 | 10.07.04 | With new Kicker Magnet design With new Undulator Girder Design (undulator quads on stand alone posts) undulator tolerance. With latest RF gun drawing With new inside dimension of Technical Buildings (4 m). |
| V13 | 10.07.08 | Corrections from Trevor Dury (English Corrections) Removal of Appendix on Radiation Protection |
| V14 | 10.07.12 | With new Tolerances from Bolko Beutner in Chapter 2 With new Mechanical Support concept from Peter Wiegand With English Corrections of those new sections |
| V15 | 10.07.12 | Same as V14 but the Word file is splitted in 4 chapters to handle it more easily (large memory size due to the numerous Track changes) |
| V16 | 10.07.19 | With new Switchyard and Collimator Design from Natalia Milas Removal of Fig 1.2.3 (SwissFEL layout too many times in manuscript). |
| V17 | 10.07.22 | With Versioning Tables With RF structures key parameters table (filling time, ...) Minor format corrections; Numerous Typos This is the version used by Irma Herzog for Layout Preparation |
| V18 | 10.08.19 | Version in pdf only and which has the nice Layout prepared by Irma Herzog for the Inauguration Day of WLHA |
| V19 | Dec2010- Jan 2011 | Chapter1: Update figs, numbers, add correction Pedrozzi: 31.01.11 New SwissFEL overall schedule + Text: 03.03.11 Chapter 2: New Fig 2.1.1 with new BC scheme from Bolko presented at FLAC april 2010 (no more the BC |

| | | |
|--|--|--|
| | | <p>scheme from Yujong) New Tolerances according to new BC scheme (from FLAC Nov. 2010). New Astra Simulation Results from A. Fallone (17.12.10) Some RF precisions (dual coupler) from J-Y. Raguin (18.12.10). Chapter 3: 3.2: RF: modifications from Jean-Yves, X band power consumption, r/Q for C band structure (18.12.10); C band power paragraph from Juergen Alex (01.02.11) . Update on magnets, (Sanfilippo 22.11.10) +drawings (Romain Jan 11) and PS parameters (Kuenzi – 20.12.10) Undulator: new parameter table (Romain) Diagnostics: New Layouts from Rasmus (Jan. 2011) Vac: new figs and summary table vac level Chapter 4 : New Sketch up images from 13.01.11 New summary of the FLUTE THz source (Romain); One example of Athos experiment; With slides from Bill Pedrini on CuO exp. Chapter 5: Reference Coordinate system description (K. Dreyer 20.12.10); New transport concept (Johann Wickstrom 31.01.11) Magnet PS commissioning steps (R. Kuenzi) 20.12.10 Chapter 6: Exchange of all building figures with New Sketch up V29 images from 07.01.11 Links and summary to Fuchs's latest SU documents; New Zonung Table (01.02.11) 20.01.11: Add corrections from P. Ming With new Electrical Consumption Table – Romain (19.01.11) With W. Roser Corrections (20.01.11) 16.02.11: Implementation of various feedback from Authors. Opal simulations, distance aramis-athos,.</p> |
|--|--|--|

Table of Contents

| | | |
|----------|---|-----------|
| 1 | EXECUTIVE SUMMARY..... | 10 |
| 1.1 | SwissFEL project goals and CDR objectives..... | 10 |
| 1.2 | SwissFEL design rational..... | 10 |
| 1.2.1 | Introduction..... | 10 |
| 1.2.2 | Technical highlights of SwissFEL..... | 13 |
| 1.2.3 | The injector..... | 13 |
| 1.2.4 | The accelerator..... | 14 |
| 1.2.5 | The FELs..... | 14 |
| 1.3 | SwissFEL building..... | 15 |
| 1.3.1 | Building overview..... | 15 |
| 1.3.2 | SwissFEL facility site..... | 18 |
| 1.4 | Key parameters and operational modes..... | 19 |
| 1.5 | SwissFEL project schedule..... | 21 |
| 1.5.1 | Overview of SwissFEL construction phases..... | 21 |
| 1.5.2 | Future extensions..... | 23 |
| 1.6 | Overview of SwissFEL Science Case..... | 23 |
| 1.6.1 | Nanoscale magnetization dynamics..... | 24 |
| 1.6.2 | Solution chemistry and surface catalysis..... | 24 |
| 1.6.3 | Coherent diffraction by nanostructures..... | 24 |
| 1.6.4 | Ultrafast biochemistry..... | 25 |
| 1.6.5 | Time-resolved spectroscopy of correlated electron materials..... | 25 |
| 2 | DESIGN STRATEGY AND PARAMETER CHOICE..... | 28 |
| 2.1 | Overview and design parameters..... | 28 |
| 2.2 | Simulation tools..... | 32 |
| 2.3 | Accelerator simulation..... | 32 |
| 2.3.1 | Gun and booster section..... | 32 |
| 2.3.2 | Bunch compression scheme (Booster 2, BC1, Linac 1 and BC2)..... | 38 |
| 2.3.3 | Linac layout (Linac 2 and Linac 3)..... | 43 |
| 2.3.4 | Switchyard and collimators..... | 45 |
| 2.4 | Undulator line parameters and simulations..... | 51 |
| 2.4.1 | Aramis..... | 52 |
| 2.4.2 | Athos..... | 53 |
| 2.4.3 | D'Artagnan and Seeding..... | 55 |
| 2.4.4 | Sensitivity and tolerance study for the bunch compression layout..... | 59 |

| | | |
|------------|---|------------|
| 2.4.5 | Sensitivity of FEL performance | 63 |
| 2.5 | Photon beamline layout..... | 64 |
| 2.5.1 | Introduction..... | 64 |
| 2.5.2 | Ablation and single-shot damage | 64 |
| 2.5.3 | Conceptual beamline layout | 65 |
| 2.6 | THz pump source at the SwissFEL | 68 |
| 2.6.1 | Motivation..... | 68 |
| 2.6.2 | Basic considerations | 69 |
| 2.6.3 | Design parameters..... | 69 |
| 2.6.4 | THz radiated energy per pulse..... | 75 |
| 3 | ELECTRON BEAM COMPONENTS | 77 |
| 3.1 | Laser system | 77 |
| 3.1.1 | Gun laser system | 77 |
| 3.1.2 | General layout..... | 78 |
| 3.1.3 | UV temporal and spatial pulse shaping..... | 78 |
| 3.1.4 | Laser room for the SwissFEL injector | 81 |
| 3.1.5 | HHG-based seeding laser system | 81 |
| 3.1.6 | Laser system for laser heater | 82 |
| 3.2 | RF systems | 83 |
| 3.2.1 | Main parameters of different SwissFEL RF Structures..... | 83 |
| 3.2.2 | RF photogun design..... | 83 |
| 3.2.3 | RF systems of the SwissFEL injector..... | 85 |
| 3.2.4 | RF systems of the SwissFEL Linacs 1, 2 and 3 | 90 |
| 3.2.5 | Power systems for SwissFEL Injector..... | 95 |
| 3.2.6 | Power systems for the C Band SwissFEL linac | 101 |
| 3.2.7 | Low-Level RF | 103 |
| 3.3 | Timing and synchronization..... | 106 |
| 3.3.1 | Reference distribution system | 106 |
| 3.3.2 | Optical synchronization system..... | 109 |
| 3.3.3 | Stabilization of lasers..... | 114 |
| 3.3.4 | RF generation..... | 115 |
| 3.3.5 | Synchronization system for mixed European/US RF frequencies | 116 |
| 3.4 | Magnets..... | 118 |
| 3.4.1 | Solenoid magnets | 118 |
| 3.4.2 | Quadrupole Magnets..... | 121 |
| 3.4.3 | Dipole magnets | 126 |
| 3.4.4 | Corrector magnets..... | 129 |
| 3.4.5 | DC magnet power supplies | 129 |
| 3.4.6 | Kicker systems | 131 |
| 3.5 | Undulators | 133 |
| 3.5.1 | Aramis undulator | 134 |
| 3.5.2 | Athos undulator..... | 137 |
| 3.5.3 | Undulator module | 138 |
| 3.5.4 | Mechanics | 140 |
| 3.5.5 | Phase matching unit (phase shifters) design | 142 |
| | FIGURE 3.5.5.1 CONCEPTUAL PHASE SHIFTER MAGNETIC STRUCTURE CHOSEN FOR BOTH THE HARD AND SOFT X-RAY BEAM LINES..... | 142 |
| | ARAMIS PHASE SHIFTER DESIGN | 143 |

| | |
|---|------------|
| ATHOS PHASE SHIFTER DESIGN..... | 144 |
| 3.5.6 Undulator tolerances:..... | 146 |
| 3.6 Electron beam diagnostics concept (Rasmus, Volker) | 146 |
| 3.6.1 Dedicated electron beam diagnostics sections | 146 |
| 3.6.2 Transverse beam profile measurements | 149 |
| 3.6.3 Bunch compressor and longitudinal diagnostics..... | 152 |
| 3.6.4 SwissFEL beam position monitor system | 155 |
| 3.7 Vacuum concept (Lothar)..... | 161 |
| 3.7.1 Main accelerator..... | 161 |
| 3.7.2 Undulator vacuum system (Aramis)..... | 165 |
| 3.7.3 Undulator vacuum system (Athos)..... | 166 |
| 3.8 Mechanical support systems..... | 168 |
| 3.8.1 Girder Concept..... | 168 |
| 3.8.2 Simulation and Tests..... | 170 |
| 3.8.3 Girder feet adjustment system | 172 |
| 3.8.4 Local support system | 173 |
| 3.9 Control system..... | 174 |
| 3.9.1 Network infrastructure | 174 |
| 3.9.2 EPICS environment | 175 |
| 3.9.3 Software maintenance and distribution | 176 |
| 3.9.4 Control hardware | 176 |
| 3.9.5 Machine interlock concept..... | 177 |
| 4 PHOTON BEAM COMPONENTS..... | 179 |
| 4.1 Front End Enclosure Layout (Athos and Aramis) | 179 |
| 4.1.1 Gas Attenuator | 180 |
| 4.1.2 Beam Shutter..... | 180 |
| 4.1.3 Other Front End Components..... | 180 |
| 4.2 Photon Beam Diagnostics..... | 180 |
| 4.3 X ray Switchyard (Athos, Aramis) | 180 |
| 4.3.1 X ray Optics Layout..... | 180 |
| 4.3.2 X ray Optics Components..... | 181 |
| 4.3.3 X ray Optics Mechanical Support and Alignment | 181 |
| 4.4 Experiment Hall Layout | 181 |
| 4.4.1 Experimental Hall general layout | 181 |
| 4.4.2 Aramis Experimental Stations | 182 |
| 4.4.3 Athos Experimental Stations | 182 |
| 4.4.4 Safety..... | 186 |
| 4.5 Experiment Hall Components | 186 |
| 4.5.1 Pump Lasers | 186 |
| 4.5.2 THz Pump Source | 187 |
| 5 MACHINE ASSEMBLY AND COMMISSIONING..... | 192 |
| 5.1 Machine installation | 192 |
| 5.1.1 Assembly Plan | 192 |
| 5.1.2 Components Assembly Concept..... | 194 |
| 5.1.3 Components Transport..... | 195 |
| 5.1.4 Assembly Alignment Concept..... | 197 |
| 5.2 Components to Infrastructure Interface..... | 200 |

| | | |
|------------|---|------------|
| 5.3 | Machine Commissioning Plan | 200 |
| 5.3.1 | Hardware commissioning without beam | 200 |
| 5.3.2 | Beam Commissioning Plan | 200 |
| 5.4 | Feedback systems and electron beam-based alignment | 201 |
| 5.4.1 | Beam-based magnet and trajectory alignment | 201 |
| 5.4.2 | Transverse trajectory feedback | 204 |
| 6 | BUILDING AND INFRASTRUCTURE | 207 |
| 6.1 | Building layout | 207 |
| 6.2 | Safety issues | 221 |
| 6.2.1 | Radiation protection | 221 |
| 6.2.2 | Activation | 230 |
| 6.2.3 | Personal Security System (PSYS: PSA; LAC) | 233 |
| 6.2.4 | General safety | 233 |
| 6.2.5 | Fire safety | 234 |
| 6.3 | Supply installations (status as of January 2011) | 234 |
| 6.3.1 | Electrical supply and consumption | 234 |
| 6.3.2 | Heating, cooling, air conditioning and water supplies | 239 |
| 6.4 | Appendix 6.1: Functional layout of SwissFEL infrastructure | 242 |
| 6.5 | Appendix 6.2: Drawing SwissFEL Building (Jan 2011) | 243 |
| 7 | REFERENCES | 244 |

1 EXECUTIVE SUMMARY

1.1 *SwissFEL project goals and CDR objectives*

The goal of SwissFEL is to provide a source of extremely bright and short X-ray pulses enabling scientific discoveries in a wide range of disciplines, from fundamental research to applied science. The eminent scientific need for such a source is well documented in the SwissFEL Science Case Report [3].

The technical design of SwissFEL has to keep a delicate balance between the demand from experimentalists for breathtaking performance in terms of photon beam properties, on the one hand, and essential requirements for a user facility, such as confidence in technical feasibility, reliable and stable functioning, and economy of installation and operation, on the other hand. A baseline design has therefore been defined which relies entirely on state-of-the-art technologies without fundamental feasibility issues. This SwissFEL Conceptual Design Report (CDR) describes the technical concepts and parameters used for this baseline design, as of the end of 2009. The objective of the CDR is to provide a reference for the machine design, thus ensuring that the various teams working on SwissFEL use consistent planning assumptions. A positive side-effect of the considerable work which went into this CDR is the identification and correction of several design inconsistencies. Given that the design is still evolving, all relevant modifications relative to the CDR have to be documented in an unambiguous manner accessible to all personnel involved in SwissFEL. Right before construction of SwissFEL starts, the design with all accumulated modifications and more detailed technical component descriptions and specifications will have to be compiled again in the technical design report (TDR), which will then be the technical reference for project execution.

R&D on various advanced options beyond the baseline design choices is being pursued at PSI, namely on field-emitter arrays, pulsed-diode electron guns and advanced FEL seeding schemes. Although these options are not included in the CDR, they can still be integrated into SwissFEL, either during the project preparation phase or as a later upgrade if technical maturity and superior performance compared to the baseline design are demonstrated. The same is of course true for relevant advancements on FEL technology elsewhere.

1.2 *SwissFEL design rational*

1.2.1 Introduction

In a free-electron laser, the active medium is a beam of relativistic electrons. This beam moves in vacuum through a periodic magnet array, called an undulator, forcing the electrons to follow a wiggling orbit. The wiggling orbit introduces a transverse velocity component, which allows the electrons to exchange energy with a light wave which is co-linear with the electron beam. The electrons become accelerated or decelerated, depending on the phase of the transverse electric field of the light wave. For a particular wavelength of the light beam, this

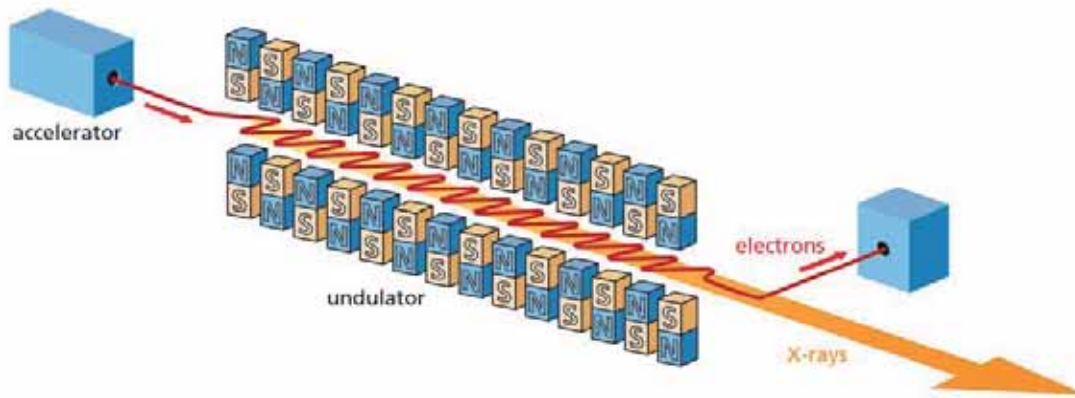


Fig.1.2.1: e^- beam in undulator with lightwave

exchange becomes resonant for a single electron, leading to a continuous transfer of energy from the electron to the light wave. The resonant wavelength is given by

$$\lambda = \frac{\lambda_U}{2\gamma^2} \left(1 + \frac{K^2}{2} \right)$$

where λ_U is the period length of a planar undulator and K is the undulator parameter, defined by

$$K = \frac{1}{2\pi} \frac{e}{mc} B_U \lambda_U$$

with B_U the peak magnetic field of the undulator on the axis. Since the path length of the electrons depends on the electron energy, the energy modulation induced by the radiation field is converted to a bunching of the electrons with the periodicity of the light wave. Thus the electrons are concentrated at the phase of the light wave where efficient energy transfer occurs and the light wave becomes coherently amplified. As a result, the entire system acts analogously to a light amplifier in the well-known optical quantum laser. However, the FEL has the fundamental advantage that its operation does not depend on quantum transitions in a specific laser medium. Therefore, the FEL scheme can be applied over a much wider photon wavelength range than the quantum laser principle, as shown in Figure 1.2.2.

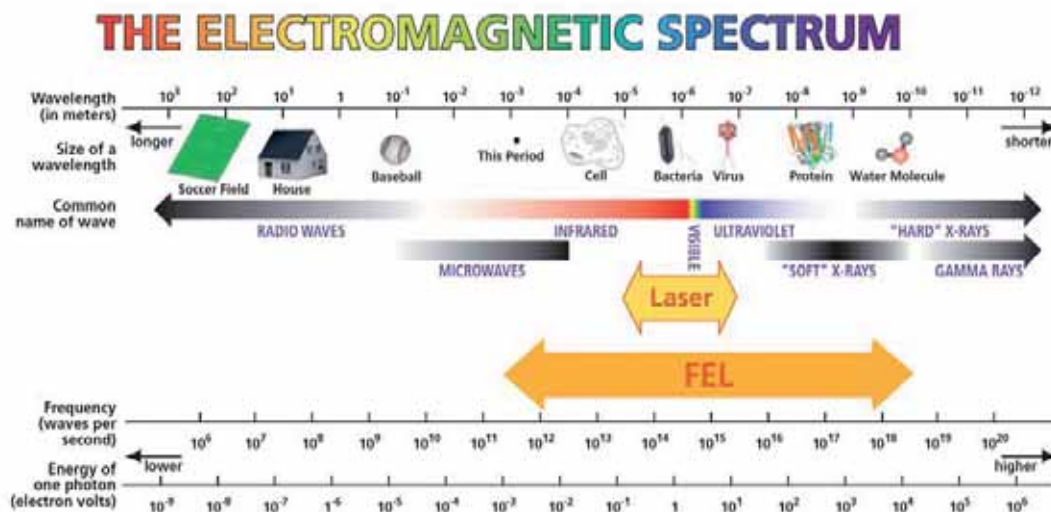


Fig. 1.2.2: Wavelength range of the FEL vs. a quantum laser

The FEL principle is the only proven method for providing coherent light pulses reaching the hard X-ray wavelength regime. However, the FEL scheme is also faced with severe difficulties at these wavelengths. No mirrors with sufficient reflectivity and bandwidth exist; therefore, the FEL cannot be built in an oscillator configuration but has rather to operate in a single-pass mode, lining up a large number of undulator magnets to drive the lasing process into saturation. Furthermore, no seeding source is readily available for these wavelengths. This latter problem is overcome by using the broadband signal from the shot noise spectrum of the electron beam and using it to start the amplification process. This type of FEL operation is called self-amplified spontaneous emission (SASE) and has recently been demonstrated to work for wavelengths as short as 1.5 Å [4]. There is worldwide research on alternative seeding methods at X-ray wavelengths, with the hope of obtaining even better X-ray FEL performance. PSI is participating in this research, but SASE is presently the only proven method, and other approaches become increasingly difficult as the wavelength is made shorter.

Another challenge comes from the requirement to maintain a good overlap between the electron beam and the light beam. Since the divergence of the light beam decreases proportional to λ , the demands on electron beam quality become more stringent at shorter wavelengths. The figure of merit for electron beam quality is the normalized emittance, which is given by the “surface” occupied by the beam particles in a plane spanned by the deviation in the transverse position from the nominal orbit. The normalized emittance is conserved under beam acceleration and therefore depends mainly on the performance of the electron injector. This makes the design of the injector a particular challenging task for X-ray FELs. Optimum matching of the electron beam to the light beam can be achieved if the condition

$$\varepsilon_N \leq \gamma \frac{\lambda}{4\pi}$$

is met, where ε_N is the normalized emittance, γ is the relativistic factor, proportional to the electron’s energy, and λ is the lasing wavelength. Present injector technology requires acceleration of electrons to very high energy in order to operate a FEL in the X-ray regime. However, it has been demonstrated that FELs can operate with reduced efficiency even if the normalized emittance exceeds this optimum condition by a factor four to five. Despite this, progress in injector performance is very desirable until the emittance condition is met. An introduction to the theory of FELs can be found in [5].

The SwissFEL baseline design aims to produce FEL pulses covering the wavelength range 1 Å to 70 Å, with a compact and economic design which is affordable on the scale of a national laboratory. The overall cost of a linear accelerator is almost proportional to the final beam energy. Therefore, a key design goal is to minimise the required electron beam energy for a given radiation wavelength. The dependence of photon beam wavelength on electron beam energy and undulator wavelength, as discussed in the last Section, implies the use of undulators with short period length and rather low K -value. The emittance achievable with the injector puts another lower limit on the beam energy. Both constraints are most stringent for the shortest lasing wavelength.

Table 1.2.1:

| Parameters for lasing at 1 Å | |
|------------------------------|---------|
| Beam energy | 5.8 GeV |
| λ_U | 15 mm |
| K | 1.2 |

Based on these factors, and considering the best performance achievable with leading edge undulator and electron injector technology, the parameters of table 1.2.1 were chosen to achieve lasing with the SwissFEL at 1 Å wavelength.

1.2.2 Technical highlights of SwissFEL

In order to meet both the performance requirements and the cost constraints, substantial technical developments for some key components are underway to push their performance beyond the present state of the art. For these developments, SwissFEL profits not only from the excellent R&D performed at PSI since 2004, but also from the vast experience and progress achieved at other laboratories active in electron linac and FEL design. In particular, active collaboration and information exchange with SLAC, DESY, SPRING8, KEK, BESSY, CERN, LNF, ELETTRA and LAL has inspired the design concepts described here. Introduction of key technologies makes the SwissFEL accelerator unique. These innovations can be listed as follows:

- A newly developed 2.6 cell RF gun which combines the advantages of two existing electron guns, namely the PHIN gun from LAL and the LCLS gun at SLAC.
- A wavelength-tunable gun laser system, in order to minimize the intrinsic emittance (the ultimate theoretical limit to high beam brightness). This laser has already been used and its beneficial effects on intrinsic emittance have been experimentally demonstrated at PSI.
- SwissFEL will utilise solid-state power modulators on a large scale for the linac RF sources. PSI is pioneering, with this technology, an approach which promises superior RF stability and a more compact construction compared to existing linear accelerators.
- The main linac uses C-band RF technology, which has been developed in Japan during recent years. SwissFEL will use this technology for the first time for a large-scale accelerator project outside Japan. The RF parameters chosen for SwissFEL are the result of new overall system optimization performed at PSI to minimize electricity consumption and overall system cost.
- The hard X-ray line (the first of the two SwissFEL FEL lines to be built) is based on in-vacuum undulator technology with an unprecedented short magnet period for this kind of applications. This requires pushing the limits of undulator technology in terms of magnetic materials and mechanical precision. Here, the extensive experience of PSI with a similar state-of-the-art undulator built at the SLS, as well as collaboration with SPRING8, is a major advantage.
- The soft X-ray line (the second of the two SwissFEL FEL lines to be built) is based on APPLE II undulator technology, with the capability of full polarization control. These objects are very demanding in terms of magnetic and mechanical engineering. SwissFEL profits from the experience gathered with the APPLE II undulators built by PSI in collaboration with BESSY for SLS.

1.2.3 The injector

The baseline technology for the SwissFEL electron injector relies on the RF gun photo-injector concept. A photocathode placed in a high-field RF cavity is illuminated with a short-pulse laser. The timing of the laser pulses is synchronized to the RF, so that electrons are emitted when the accelerating RF field on the cathode reaches an optimum value. For the past two decades, RF gun technology has been the subject of intense R&D activities at various leading accelerator laboratories worldwide, and remarkable progress has been achieved. The present state of the art allows the production of electron pulses of 200 pC with normalized emittances below 0.4 μm . This is sufficient to operate the SwissFEL at nominal wavelength and beam energy. However, to reach these parameters, the pulses produced from the gun have to be much longer (typically several ps) than the final pulse of a few fs required in the FEL. Therefore, the pulse has to be longitudinally compressed in the linear accelerator, downstream from the injector.

Demonstration of intrinsic emittance reduction by tuning the gun laser wavelength has been performed at the LEG test-facility [6]. The SwissFEL photo-injector laser system was developed with the novel feature of a large tunable wavelength capability, to allow thermal emittance reduction.

1.2.4 The accelerator

The SwissFEL linear accelerator (linac) must fulfil two functions:

- acceleration of the electron pulse from the injector to the nominal energy of the FEL
- time compression of the electron pulse from 5 ps rms to 25 fs rms

The demands for compactness and economy suggest the use of a normal-conducting, pulsed RF system for acceleration, with rather high accelerating fields. A key design parameter for such a linac is the total RF energy supplied per pulse by the RF transmitters to the accelerating cavities. This parameter strongly influences the investment cost and electric power consumption of the overall facility, and can be minimized either by reducing the local accelerating field or by increasing the RF frequency. Since reducing the field increases the overall facility length, an increase of the RF frequency is the more promising approach. However, such an increase goes together with a decrease of the size of the accelerator components, thus leading to even tighter mechanical and electrical tolerances. While most normal-conducting electron linear accelerators nowadays operate at an RF frequency of 3 GHz, the SwissFEL foresees the use of a 5.7 GHz C-band RF system, and will be the first large-scale linac of this type in Europe.

For temporal pulse compression, two magnetic chicanes are placed in the linac at 410 MeV and 2.1 GeV. The electron pulse is accelerated in the linac slightly off the crest of the RF wave. This introduces a time/energy chirp along the electron pulse. The energy dependence of the electron path length in the magnetic chicane leads to a time compression, as depicted in Figure 1.2.3. Two 12 GHz RF structures are used to linearize this dependence before entering in the magnetic chicane.

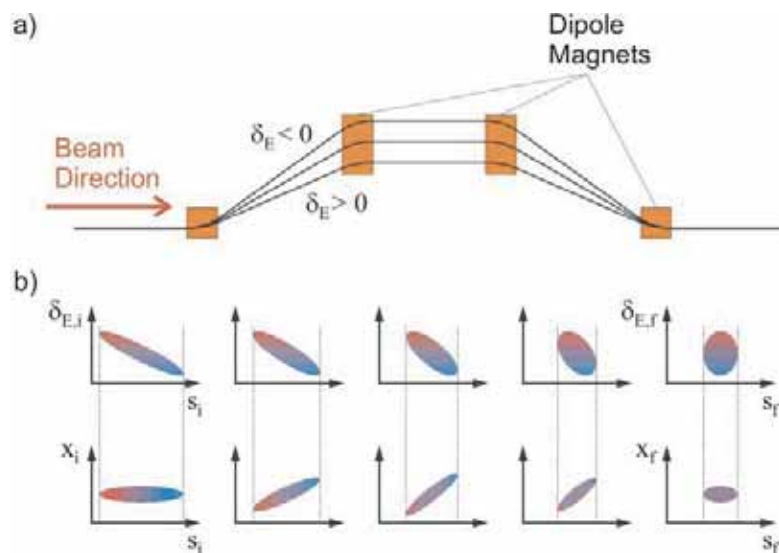


Fig. 1.2.3: The rotation of electrons in the energy–time plane by a magnetic chicane. $\delta_{E,i}$ represents the relative energy spread over the bunch, s_i is the longitudinal coordinate along the bunch and X_i is the transverse beam size (Figure Courtesy of A. Bolzmann [7]).

1.2.5 The FELs

Two SASE FEL lines will be driven by the linac – a hard X-ray FEL named Aramis and a soft X-ray line named Athos. Aramis covers the wavelength range 1-7 Å, and Athos the wavelength range 7-70 Å.

For Aramis, a planar undulator with a novel type of permanent magnet (dysprosium-enriched NdFeB) is planned. The magnet array is mounted inside the vacuum tank. To reach the required parameters, the inter-magnet gap which is available for the beam is as small as 4.5 mm. The use of dysprosium-enriched NdFeB magnets allows these undulators to be operated at room temperature, thus avoiding a costly liquid nitrogen cooling system, as is normally required for undulators with comparable parameters. A total of 12 undulators of this type, each 4 m long, have to be aligned in a row within tight tolerances to ensure that the Aramis FEL can reach the SASE saturation regime.

For the Athos FEL, the undulator period length is more relaxed, and the permanent magnet arrays can therefore be situated outside the vacuum chamber. These undulators are built in the so-called APPLE II configuration, which allows full control of the FEL polarization and wavelength by adjusting the mechanical position of the magnet arrays with high precision. Movements of the magnet arrays with submicron accuracy have to be performed in the presence of very strong magnetic forces, making the mechanical design of the mover systems particularly challenging. The feature of polarization control will be particularly advantageous for magnetization dynamics experiments.

Furthermore, it is foreseen that the Athos FEL be operated with seeding by an optical laser system. Such a seeding scheme allows the spectral width of the FEL radiation to be narrowed by an order of magnitude, providing full longitudinal coherence. However, despite its obvious attractiveness, FEL seeding at these short wavelengths is an as-yet unproven technology, and considerable R&D, with uncertain outcome, is required in order to apply it for the SwissFEL. The subject of FEL seeding is a strong focus of R&D worldwide, with PSI playing a strong role in the theoretical modelling of the process and in technical developments. Nevertheless, without experimental proof of feasibility, the SwissFEL baseline design has to rely on SASE operation for both FEL lines.

1.3 SwissFEL building

1.3.1 Building overview

As well as for the machine design, the building concept should meet both the cost constraints and the safety requirements. The overall length of the facility is about 700 m, with a width varying between 10 and 20 m. The building will be located in the direct vicinity of PSI and a drawing of the facility is shown in Figure 1.3.1.1.

The electron accelerator (gun to Linac 3) is built on two levels (see Figure 1.3.1.2), with the electron beam tunnel below ground, to minimize the radiation protection requirements (concrete wall thickness). This also has the advantages of better temperature and mechanical stability, and the overall visual impact on the landscape is minimized. On the top floor of the electron accelerator section, a series of infrastructure buildings will host all the necessary RF power stations, control units, water cooling system, electrical power supply and air conditioning system. These infrastructure buildings are separated from the electron beam tunnel by a thick concrete floor, for radiation shielding. This allows easy access for maintenance to all infrastructure devices.

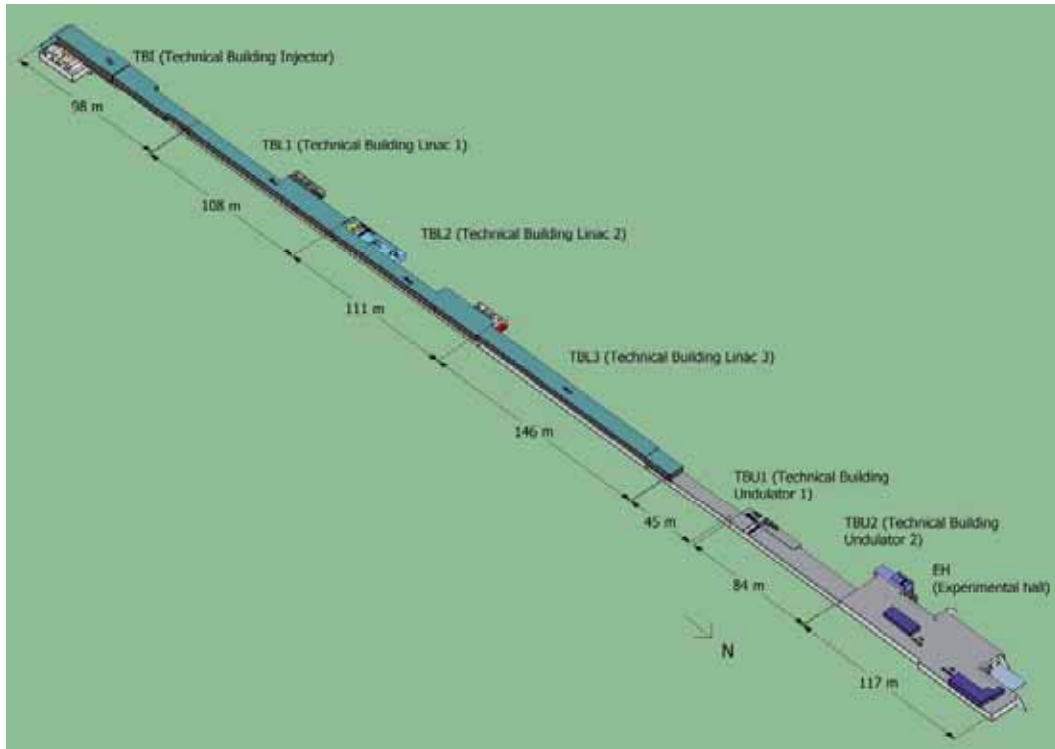


Fig. 1.3.1.1: SwissFEL Facility overview from the electron gun (at the left end) to the Aramis experimental hall (on the right). Surrounding ground is not represented.

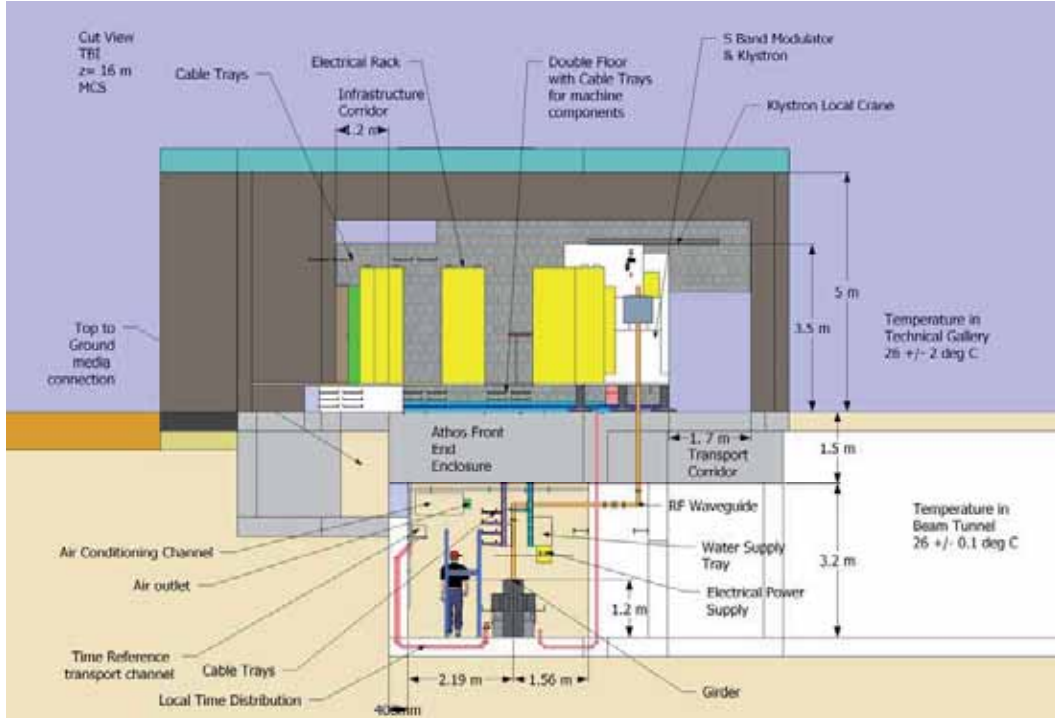


Fig. 1.3.1.2: Sectional view of the SwissFEL Electron Accelerator Facility, showing the electron beam axis in the underground tunnel and the technical building on the upper level.

The undulator hall (100 m long) is mainly underground, and a dedicated area near the experimental hall is foreseen for the preparation and measurements of the undulator modules. The undulator hall is then followed by a drift section of ~ 120 m, dedicated to X ray diagnostics, before it enters the experimental stations. The Aramis experimental hall is divided into 3 separated experimental ‘hutches’ to ensure full-time use of the FEL light: one experimental station is in operation, while the other two are preparing their experiments.

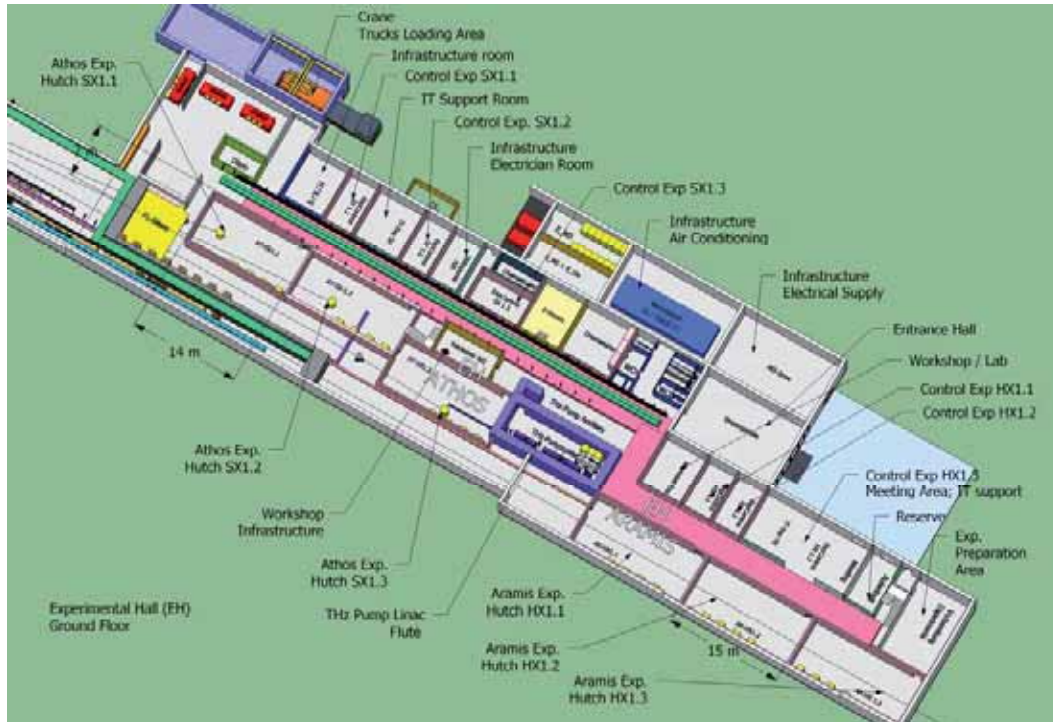


Fig. 1.3.1.3: Inside view of the experimental halls (underground). There are three experimental hutches for Aramis and three for Athos.

1.3.2 SwissFEL facility site



Fig. 1.3.2.1: The locations of the SwissFEL facility and auxiliary buildings.

The location of the 700m-long SwissFEL facility and the auxiliary buildings for the SwissFEL project is shown on Figure 1.3.2.1. The site has been chosen because of almost ideal conditions for stability and the availability of ground water for an efficient cooling-water supply at low and constant incoming temperature.

All the activities related to the preparation of SwissFEL are located within one kilometre of the installation site. Of particular importance is the assembly hall, where all undulator modules should be aligned before careful transportation to their final destination. The C-band RF test stand will enter into operation in 2011 and will be able to test a full RF module with 4 C-band structures of 2 m in length. The SwissFEL Injector Test Facility is currently being commissioned (2010) and should be moved to the SwissFEL site in 2015.

1.4 Key parameters and operational modes

Some key parameters and features of SwissFEL are summarized in Table 1.4.1 below.

Table 1.4.1

| Key parameters and features of SwissFEL | |
|--|---|
| Overall length (incl. experimental hall) | 713 m |
| Total electrical power consumption | 5 MW |
| Maximum electron beam energy | 5.8 GeV |
| Height of beamline above tunnel floor | 1.2 m |
| Electron gun | 3 GHz RF gun with 2.5 cells |
| Cathode type | Cu photocathode driven by a frequency-tripled TiSa laser |
| Injector booster | Normal-conducting travelling wave structures (copper) with $\nu=3$ GHz |
| RF source main linac | Klystron with solid-state modulator and RF pulse compression |
| Accelerating structures, main linac | Normal conducting travelling wave structures (copper) with $\nu=5.7$ GHz and $G=26$ MV/m |
| Linac repetition rate | 100 Hz |
| Bunch compression | Two 4-magnet chicane bunch compressors at 0.41 GeV and 2.1 GeV, With X-band harmonic cavity at 1 st bunch compressor |
| Number of FEL lines | 2 (Aramis and Athos) |
| Undulator type, Aramis | In-vacuum permanent magnet with $\lambda_U=15$ mm |
| Wavelength range, Aramis FEL | 1Å-7Å |
| Polarization, Aramis | Linear |
| Undulator type, Athos | Apple II permanent magnet with $\lambda_U=40$ mm |
| Wavelength range, Athos FEL | 7Å-70Å |
| Polarization, Athos | Variable (circular, elliptical and linear) |

The SwissFEL injector and accelerator permit a wide range of electron beam parameters. When setting the ranges of these parameters, two modes – “long pulse” and “short pulse” – are defined. The beam parameters for these modes, and the corresponding performance of the Aramis FEL, are summarized in Table 1.4.2.

Table 1.4.2: Expected Performance of Linac, Aramis and Athos lines. Performances for different operation regimes are detailed in Chapter 2.

| Design parameters for the electron beam | Operation Mode | |
|---|----------------|---------------|
| | Long Pulses | Short Pulses |
| Charge per bunch (pC) | 200 | 10 |
| Core slice emittance (mm.mrad) | 0.43 | 0.18 |
| Projected emittance (mm.mrad) | 0.65 | 0.25 |
| Slice energy spread (keV, rms) | 350 | 250 |
| Relative energy spread (%) | 0.006 | 0.004 |
| Peak current at undulator (kA) | 2.7 | 0.7 |
| Bunch length (fs, rms) | 30 | 6 |
| Bunch compression factor | 125 | 240 |
| Performance of Aramis for 5.8 GeV electron energy and 1 Å lasing wavelength | | |
| Maximum saturation length (m) | 50 | 50 |
| Saturation pulse energy (μJ) | 60 | 3 |
| Effective saturation power (GW) | 2 | 0.6 |
| Photon pulse length at 1 Å (fs, rms) | 13 | 2.1 |
| Number of photons at 1 Å ($\times 10^9$) | 31 | 1.7 |
| Bandwidth, rms (%) | 0.03 | 0.04 |
| Peak brightness (# photons. $\text{mm}^{-2}.\text{mrad}^{-2}.\text{s}^{-1}/0.1\%$ bandwidth) | 3.10^{32} | 1.10^{32} |
| Average Brightness (# photons. $\text{mm}^{-2}.\text{mrad}^{-2}.\text{s}^{-1}/0.1\%$ bandwidth) | 1.10^{21} | $5.7.10^{18}$ |
| Performance of Athos (SASE) For example at 3.4 GeV electron energy and 2.8 nm lasing wavelength | | |
| Maximum saturation length (m) | 22 m | |
| Saturation pulse energy (μJ) | 360 | |
| Effective saturation power (GW) | 11.2 | |
| Photon pulse length at 1 Å (fs, rms) | 13 | |
| Number of photons at 1 Å ($\times 10^9$) | 5000 | |
| Bandwidth (%) | 0.19 | |
| Peak brightness (# photons. $\text{mm}^{-2}.\text{mrad}^{-2}.\text{s}^{-1}/0.1\%$ bandwidth) | 6.10^{35} | |
| Average Brightness (# photons. $\text{mm}^{-2}.\text{mrad}^{-2}.\text{s}^{-1}/0.1\%$ bandwidth) | 8.10^{23} | |

The SwissFEL linac operates with a repetition rate of 100 Hz. At each linac pulse, two microbunches are accelerated with a spacing of 28 ns. While the first pulse goes straight to the Aramis FEL line, the second is deviated to the Athos FEL by a fast kicker in the switchyard between Linac 2 and Linac 3. This timing scheme allows both FEL lines to be operated simultaneously at 100 Hz, thus doubling the number of photon pulses sent to the experiments. This scheme, however, cannot be used for all variants of Aramis and Athos operation parameters. In

particular, the operational mode of Athos with 2.1 GeV is not compatible with running Aramis at maximum electron energy, i.e. shortest wavelength. For details of these operational modes, see Chapter 2 of this report. For these modes, one bunch is accelerated and sent alternately to Aramis or Athos. The main characteristic of Athos is that it will be a seeded FEL light, giving the possibility of better synchronized pump - probe experiments (better than with SASE light).

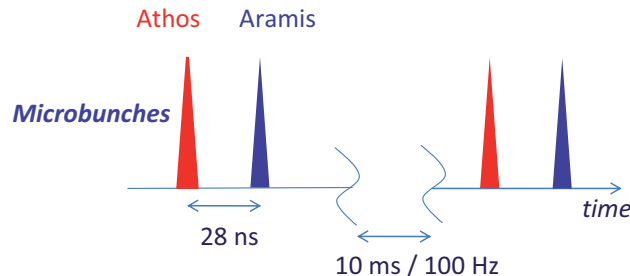


Fig: 1.4.1 Time structure of linac beam

1.5 SwissFEL project schedule

1.5.1 Overview of SwissFEL construction phases

The present planning for SwissFEL is summarized in Figure 1.5.1. Presently, the R&D for key components, such as linac RF systems and undulators, is already in progress, together with the definition of the buildings and the procedures for building permits. Thus, civil construction and component procurement can start in end 2012, if a positive funding decision is taken in 2012. The construction of the SwissFEL tunnel and buildings, including experimental halls and the technical infrastructure, will be in 2013 and 2014, while the installation of the accelerator in the tunnel will start at the end of 2014, after civil engineering and technical infrastructure installation has been completed. The preparation and storage of accelerator components before installation in the SwissFEL complex will be carried out in an assembly building temporarily leased by PSI. This building will be ready for use before the end of 2011. While the SwissFEL Injector Test Facility in WLHA is the test bed for most beam related components, the prototype of the main linac C-band accelerator module will be tested in an RF high-power test stand, which will be installed in the existing OBLA building on the PSI East site from beginning 2011 onwards. In 2015, the complete injector will be moved from the WLHA test hall to the SwissFEL tunnel. Thereafter, WLHA can be used for development, assembly and storage of SwissFEL components and the leased building will no longer be required. An overview of the building locations is given in Figure 1.3.2.1.

By the mid of 2016, installation of the injector, the linac and the Aramis line will be completed, and commissioning of SwissFEL will start in the third quarter of 2016, with hardware commissioning in general and RF conditioning in particular. Some initial tests, yet to be defined, will be performed beforehand, during the course of 2015, to allow debugging and improvement of critical systems before main machine commissioning. First beam tests will start in fall 2016, with the goal of having first FEL lasing of Aramis by winter 2016 and regular user operation by the mid of 2017.

The Athos undulator line will be installed during a shutdown period in end 2018 and subsequently commissioned. With this commissioning period, the SwissFEL construction project will be completed by the mid of 2019 and SwissFEL will be operated as one of PSI's large user facilities thereafter. A schematic sequence of the construction steps is shown in Figure 1.5.1.

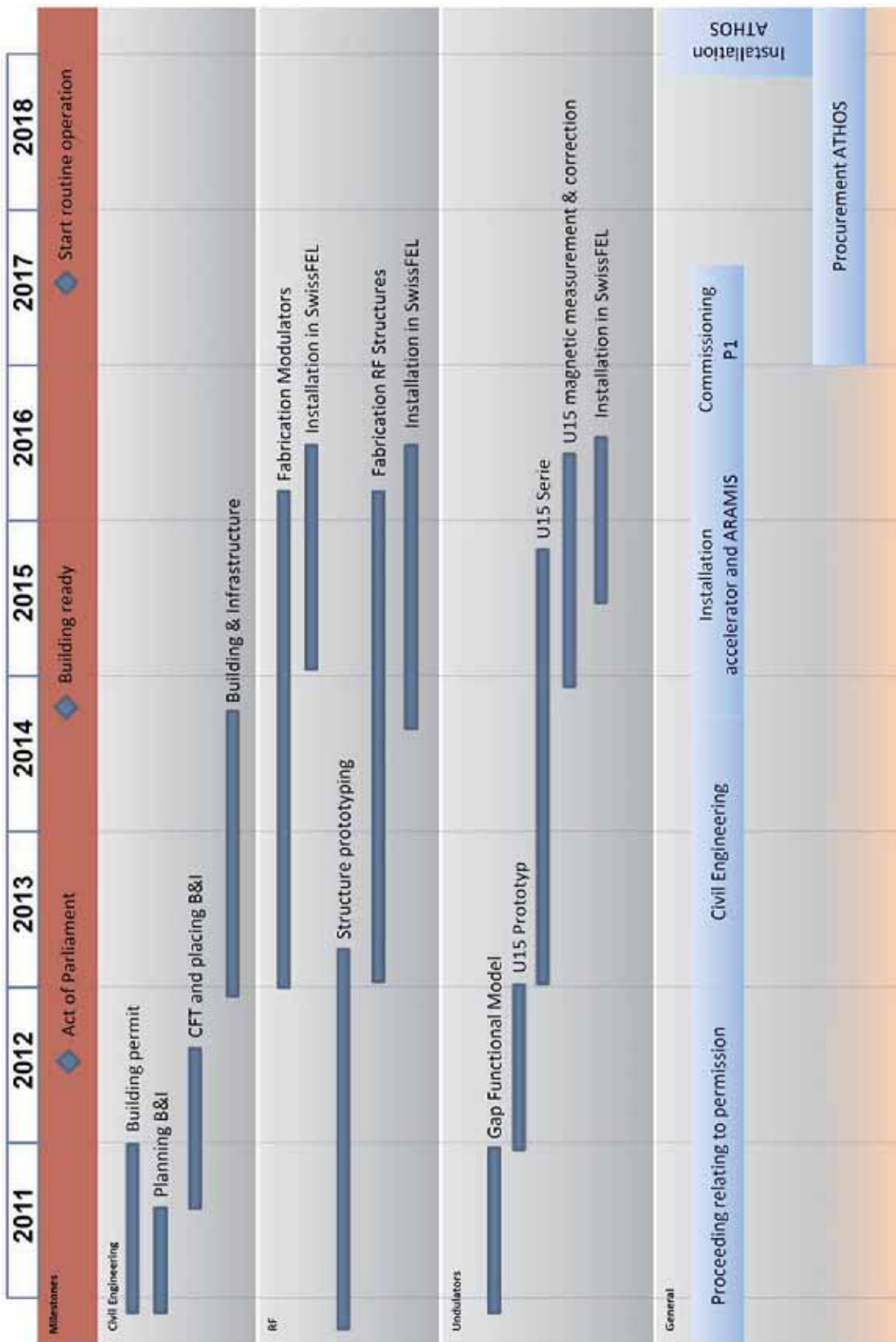


Fig. 1.5.2: Schematic of the Assembly sequence (see Chapter 6 for exact and latest building drawing)

1.5.2 Future extensions

SwissFEL will be initially built with two FEL undulator lines, each with its own experimental hall. The photon beam from each FEL line can be switched to three different experiment hutches in each hall. The baseline operation mode foresees the provision of X-ray pulses at 100 Hz repetition rate simultaneously for both undulator lines. An obvious extension of the facility's capabilities is an increase of the electron beam energy from 5.8 GeV to 6.5 GeV, extending the Aramis wavelength range from 1Å to 0.8Å. Such an upgrade is essential for studying resonant Mössbauer absorption, as described in the Science Case Report [3], p.14. This new upgrade can be achieved by adding two C-band RF stations, and space reservation for such an upgrade is part of the baseline design.

At present, there are no comprehensive plans for future extensions and upgrades, but provisions are being made in the civil engineering and site selection to allow buildings to be added for another hard X-ray FEL line and another soft X-ray FEL line, with their respective experimental halls. Both additional FELs could be driven by the existing linac.

1.6 Overview of SwissFEL Science Case

This Section gives a short overview of the experiments planned at SwissFEL and the expected scientific progress. A much more detailed description can be found in the SwissFEL Science Case Report [3], which has been published recently.

Three dominant trends in today's science and technology are 'smaller', 'faster' and 'more complex'. Nanotechnology entails the measurement and manipulation of matter on the molecular scale. The relevant time-scale for dynamic processes is then the 'ultrafast' domain, defined by the femto-second vibration of an atom in a chemical bond. Complexity, which may manifest itself as chemical diversity, lack of crystalline order and/or non-equilibrium states, holds the promise of advanced materials with enhanced functionality. The predominant tool for investigating matter is light; the SwissFEL X-ray laser will be a unique light source, which will expand the frontiers of knowledge: at the nanoscale, of ultrafast phenomena and in complex materials.

In close consultation with experts representing a wide range of scientific research, a selection was made of particularly relevant areas of application for the SwissFEL. The SwissFEL Science Case emphasizes dynamical investigations of condensed matter and the damage-free imaging of nanostructure objects. Further possible applications include time-resolved spectroscopy of plasmas and molecular gases, the study of sub-femto-second electron dynamics, the generation with intense X-ray pulses of new states of matter, and probing fundamental interactions. The SwissFEL has been conceived to address pressing scientific challenges of importance to society, in which it will doubtless make ground-breaking contributions.

The important generic types of experiment to be performed on condensed matter with the SwissFEL are:

- "pump-probe" measurements of irreversible dynamics
- "probe-probe" (split-and-delay) double-pulse measurements of equilibrium fluctuations
- lensless "flash imaging" of nanostructure objects

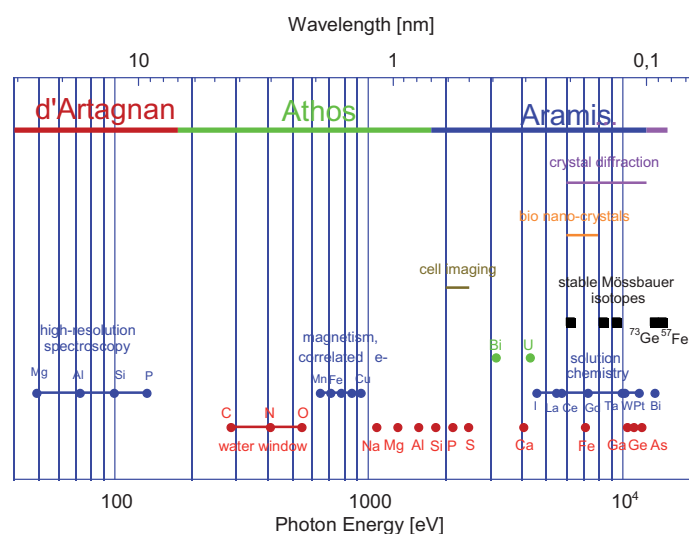


Fig. 1.6.1: An overview of photon energies accessible with the SwissFEL beamlines, and the corresponding areas of application.

The d'Artagnan undulator, used for seeding Athos, also produces soft X-rays. In the “water window“, water is transparent, but organic matter absorbs. A future upgrade of the SwissFEL will extend the Aramis spectrum from 12.4 to approximately 15 keV (violet segment). The dots indicate resonant elemental absorption features (red: K; blue: L₃; green: M₃).

An overview of the photon energy range accessible with the SwissFEL undulator beamlines and the fields of investigation are shown in Figure 1.6.1. The principal areas of application are the following:

1.6.1 Nanoscale magnetization dynamics

A wide variety of magnetic effects operate on the SwissFEL time and length scales, and the availability of circularly-polarized pulses of radiation at approximately 1 nm wavelength and a synchronized THz pump source make the planned facility an ideal instrument for the study of magnetization dynamics. Research goals include the development of high-performance devices for information storage and spintronics computing, as well as the fundamental understanding of magnetism in two-, one- and zero-dimension systems.

1.6.2 Solution chemistry and surface catalysis

Controlled catalytic reactions are the key to the efficient use of resources, the production of clean energy and the elimination of environmental pollution. Using a laser or THz trigger, followed by the scattering or absorption of SwissFEL X-ray pulses, it will be possible to produce molecular movies of fast chemical reactions, allowing detailed study of the vitally important short-lived intermediate states.

1.6.3 Coherent diffraction by nanostructures

Besides being very bright and of very short duration, the SwissFEL X-ray pulses will, in addition, have a high transverse coherence. Coupled with modern computational techniques, this opens the intriguing possibility of forming high-resolution images without the use of lenses. Radiation damage of the sample is elegantly avoided by the ultrashort pulses: the necessary information is gathered before destruction of the sample occurs. The biggest achievement will be the ability to

image individual biomolecules, thus avoiding the necessity of purifying and crystallizing large amounts of scarce material.

1.6.4 Ultrafast biochemistry

Just as a rolling ball minimizes its energy by seeking the lowest point in a bowl, biochemical reactions, which are the molecular basis of living matter, can be thought of in terms of trajectories on higher-dimensional energy surfaces. Examples are the ultrafast sequence of conformations experienced by the rhodopsin molecule upon excitation by light in the photoreceptors of the eye, and the pathways by which initially unfolded protein molecules achieve their preferred configurations. Study with the SwissFEL X-ray pulses of the detailed energy landscapes experienced by such biomolecules has great potential for the intelligent design of next-generation pharmaceuticals.

1.6.5 Time-resolved spectroscopy of correlated electron materials

After more than 20 years of intense effort, a theoretical explanation for the most prominent discovery in modern solid-state physics, that of high-temperature superconductivity, is still lacking. These oxide materials are examples of the larger class of correlated electron systems, which are distinguished by intimate interactions between the behaviour of the electronic charges, the electronic spins, the atomic orbitals and the crystal lattice. By directing the energy of a pump laser into one of these entities, and using the SwissFEL X-ray pulses to register the reaction of another one, the complex network of interactions in these materials can be untangled, paving the way for the development of novel material applications in, for example, thermoelectric devices, ultra-sensitive magnetic reading heads, spintronics and quantum computing.

Table 1.6.1: Foreseen experiments at the three beamlines of Aramis (1–7 Å) and their minimum requirements on the FEL beam pulses (in red: the most challenging parameters for SwissFEL) .

| Experiment type | System | $\Delta E / E$ | Photons / Pulse | Timescale (Pulse length) | Other |
|--|--------------------------|--------------------|-----------------|--------------------------|--------------------------------------|
| 1 – Coherent diffraction | | | | | |
| 1.1 - Nanostructures (on surfaces or in injected droplets) | | | | | |
| Lensless imaging, ptychography | 2D biocrystals | 0.1 % | 10^{10} | < 20 fs | 0.1-1 μm spot |
| Coherent diffraction | Protein nanocrystals | 0.1 % | 10^{10} | < 100 fs (?) | |
| Cross-correlation scattering | Soft disordered matter | 0.1 % | 10^{10} | < 50 fs | |
| Single molecule diffraction | Proteins in aerosol jet | 0.1 % | > 10^{10} | < 20 fs | 100 nm spot |
| 2 – Pump-Probe | | | | | |
| 2.1 – Single-shot spectroscopy (on surfaces or in liquid jets) | | | | | |
| Pump: THz, IR, vis., Probe: XES / XANES | Chem. / Biochem. systems | 1 % | 10^{10} | 60 fs | E dispersive det. |
| 2.2 – Diffraction / Scattering | | | | | |
| Pump: vis., Probe: SAXS | Solution chemistry | 0.1 % | > 10^{10} | 10 fs | Liquid jet |
| Pump: IR, vis., Probe: Bragg | Coherent phonons | 0.1-1% | 10^9 | 6-30 fs (Q = 20 pC) | Diffractometer |
| Pump: vis., Probe: Laue | Photo-excited proteins | 1% | > 10^{10} | > 100 fs | |
| Pump: X-ray, Probe: X-ray (XPCS) | Interlayer diffusion | 0.1% | 10^{10} | 50 fs | Split-delay < 2 ns |
| 3 – Other | | | | | |
| 3.1 – Mössbauer techniques (14.4 keV \pm 10⁻⁶ eV) | | | | | |
| Slow fluctuations (100 ns), Photon echoes, Inelastic scattering | Various | $2 \cdot 10^{-12}$ | > 10^{10} | > 100 fs | Pre-monoch. |
| 3.2 – Ion implantation | | | | | |
| Pump: Ion implantation Probe: diffuse scattering / diffraction | Reactor steel | 0.1 % | 10^{10} | 100 fs | Synchronized ion implantation device |

Table 1.6.2: Foreseen experiments at the three beamlines of Athos (7 Å – 7nm) and their minimum requirements on the FEL beam pulses (in red: the most challenging parameters for SwissFEL) .

| Experiment type | System | $\Delta E / E$ | ΔE step (< 5 s) | Photons / Pulse | Timescale (Pul. length) | Pol. | Other |
|--|-------------------------------|----------------|-------------------------|----------------------|-------------------------|-----------|----------------------|
| 3 – Pump-probe Imaging and Scattering | | | | | | | |
| 3.1 – External pumping (THz, IR, vis.) | | | | | | | |
| Resonant diffraction | Perovskites (3d-ions, oxygen) | 0.01 % | 0.1 eV | $5 \cdot 10^{12}$ | 10 fs | Var.lin. | Diffractionmeter |
| Holography | Magnetic thin films | 0.1 % | 1 eV | $5 \cdot 10^{12}$ | 100 fs | Circ. | |
| 3.2 – X-ray pumping | | | | | | | |
| XPCS (delay < 10 ps) | Corr. el. | 0.1 % | --- | $5 \cdot 10^{12}$ | 10 fs | Lin. | Split-delay line |
| Cross corr. scattering | Magnetic fluctuations | 0.1 % | 1 eV | $5 \cdot 10^{12}$ | 10 fs | Lin. | |
| 2 – Pump-Probe spectroscopy | | | | | | | |
| 2.1 – Monochromatic (pump: THz, IR, vis.) | | | | | | | |
| XANES, XES | Catalysis and Biochemistry | 0.01 % | 0.1 eV | $5 \cdot 10^{12}$ | 60 fs | Lin. | μ -liquid jet |
| XMCD | Magnetism and Corr. el. syst. | 0.1 % | 1 eV | $5 \cdot 10^{12}$ | 10 fs | Circ. | |
| (spin-resolved) PE spect | Magnetism and Corr. el. syst. | 0.1 % | 1 eV | $10^7 @ 1\text{kHz}$ | 10 fs | Lin. | TOF PE detector |
| 2.2 – Single-shot broadband (pump: THz, IR, vis.) | | | | | | | |
| XANES, XES | Catalysis and Biochemistry | 1 % | 10 eV | $5 \cdot 10^{12}$ | 60 fs | Lin. | No mono / seeding |
| XMCD | Magnetism and Corr. el. syst. | 1 % | 10 eV | $5 \cdot 10^{12}$ | 10 fs | Circ. | No mono / seeding |
| 1 – Inelastic scattering | | | | | | | |
| 1.1 Pump-Probe energy dispersive RIXS | | | | | | | |
| Single-shot RIXS | Molecules and Corr. el. | 1 % | 1 eV | $> 5 \cdot 10^{12}$ | 10 fs | Var. lin. | Strokov det. no seed |
| 1.2 Time-domain heterodyne spectroscopy | | | | | | | |
| FROG | Molecules and Corr. el. | 0.1 % | --- | $5 \cdot 10^{12}$ | 10 fs | Lin. | Seeded pulses |

2 DESIGN STRATEGY AND PARAMETER CHOICE

2.1 Overview and design parameters

The design parameters are defined corresponding to the specifications required to fulfil the experimental programme of the SwissFEL Science Case Report [3]. The start-to-end simulations presented in this chapter provide a more precise set of beam and machine parameters which meet the design parameters. More specific details on SwissFEL layout and optics can be found in a PSI note (FEL-RV84-002-4) [8].

The design parameters of the machine for the shortest wavelength operation (1 Å) are summarized in Tables 2.1.1 (electron beam output parameters) and 2.1.2 (photon beam output parameters). There are two nominal operation modes at 200 and 10 pC. In addition, two more special operation modes are foreseen: one that offers a large bandwidth photon spectrum and another which will produce ultra-short photon pulses (attoseconds). The wavelength of Aramis can be tuned from 0.1 nm to 0.7 nm by adjusting the energy of the electron beam in Linacs 2 and 3 (Figure 2.1.1).

Table 2.1.1: Design parameters of the electron beam output parameters for 1 Å radiation.

| Electron Beam Design Parameters | Nominal Operation Mode | | Special Operation Mode | |
|---------------------------------|------------------------|--------------|------------------------|--------------------|
| | Long Pulses | Short pulses | Large Bandwidth | Ultra-Short Pulses |
| Charge per bunch (pC) | 200 | 10 | 200 | 10 |
| Beam energy for 1 Å (GeV) | 5.8 | 5.8 | 5.8 | 5.8 |
| Core slice emittance (mm.mrad) | 0.43 | 0.18 | | 0.25 |
| Projected emittance (mm.mrad) | 0.65 | 0.25 | | 0.45 |
| Slice energy spread (keV, rms) | 350 | 250 | | 1000 |
| Relative energy spread (%) | 0.006 | 0.004 | | 0.02 |
| Peak current at undulator (kA) | 2.7 | 0.7 | 3.7 | 14 |
| Bunch length (fs, rms) | 30 | 6 | | < 0.6 |
| Bunch compression factor | 125 | 240 | | 636 |
| Repetition rate (Hz) | 100 | 100 | | 100 |
| Number of bunches / RF pulse | 2 | 2 | | 2 |
| Bunch spacing (ns) | 28 | 28 | | 28 |

Table 2.1.2: Design parameters of the photon pulses at 1 Å (Aramis) required for the SwissFEL science programme.

| FEL Beam Design Parameters | Nominal Operation Mode | | Special Operation Mode | |
|---|------------------------|---------------------|------------------------|---------------------|
| | Long Pulses | Short Pulses | Large Bandwidth | Ultra-Short Pulses |
| Undulator period (mm) | 15 | 15 | | 15 |
| Undulator parameter | 1.2 | 1.2 | | 1.2 |
| Energy spread (keV) | 350 | 250 | | 1000 |
| Saturation length (m) | 50 | 50 | | 50 |
| Saturation pulse energy (μJ) | 60 | 3 | | 15 |
| Effective saturation power (GW) | 2 | 0.6 | | 50 |
| Photon pulse length (fs, rms) | 13 | 2.1 | | 0.06 |
| Number of photons ($\times 10^9$) | 31 | 1.7 | | 7.5 |
| Spectral Bandwidth, rms (%) | 0.03 | 0.04 | 0.8 | 0.05 |
| Peak brightness (# photon/ $\text{mm}^2 \cdot \text{mrad}^2 \cdot \text{s}^1 \cdot 0.1\%$ bandwidth) | $3 \cdot 10^{32}$ | $1 \cdot 10^{32}$ | | $1,3 \cdot 10^{33}$ |
| Average brightness (# photon/ $\text{mm}^2 \cdot \text{mrad}^2 \cdot \text{s}^1 \cdot 0.1\%$ bandwidth) | $1 \cdot 10^{21}$ | $5,7 \cdot 10^{18}$ | | $7,5 \cdot 10^{18}$ |

The design parameters of the soft X-ray beamline Athos are shown in Table 2.1.3 for the long-pulse operation mode. The electron beam parameters required to achieve these FEL performances are the same as those in Table 2.1.1, except for the beam energy. In this beamline, the wavelength tuning from 0.7 nm to 7 nm is carried out by continuous variation of the undulator gap for two possible electron beam energies, 2.1 GeV and 3.4 GeV.

Table 2.1.3: Design parameters of the photon pulses from the Athos beamline (corresponding electron beam parameters are the same as in Table 2.1.1).

| Expected Parameters | Large Gap High Energy | Small Gap High Energy | Large Gap Low Energy | Small Gap Low Energy |
|--|-----------------------|-----------------------|----------------------|----------------------|
| Electron beam energy (GeV) | 3.4 | 3.4 | 2.1 | 2.1 |
| Undulator period (mm) | 40 | 40 | 40 | 40 |
| Undulator parameter K | 1.0 | 3.2 | 1 | 3.2 |
| Undulator module length (m) | 4.0 | 4.0 | 4.0 | 4.0 |
| Undulator section length (m) | 4.75 | 4.75 | 4.75 | 4.75 |
| Average b-function (m) | 10 | 10 | 10 | 10 |
| FEL wavelength (nm) | 0.7 | 2.8 | 1.8 | 7 |
| Saturation length (m) | 41.6 (*) | 22.3 | 29.7 | 16.1 |
| Saturation pulse energy (mJ) | 0.12 | 0.36 | 0.10 | 0.18 |
| Effective saturation power (GW) | 4.4 | 11.2 | 3.2 | 6.5 |
| Number of photons at saturation | $4.2 \cdot 10^{11}$ | $5.0 \cdot 10^{12}$ | $8.7 \cdot 10^{11}$ | $6.5 \cdot 10^{12}$ |
| Bandwidth (% , rms) | 0.15 | 0.19 | 0.17 | 0.25 |
| Pulse length (fs, rms) | 11.1 | 12.9 | 12.0 | 11.0 |
| Beam radius (μm , rms) | 33.4 | 40.1 | 45.9 | 56.1 |
| Beam divergence (μrad , rms) | 4.1 | 15.0 | 8.3 | 30.9 |

(*): The Athos beamline has a total length of 30 m, based on seeding operation. The value shown in the Table (41.6 m) indicates the total length required for SASE operation (§ 2.4).

With a total length of about 550 m (from gun to undulator end), the SwissFEL facility can be divided into sections, as follow:

- Gun, Booster 1 and 2 (§ 2.3.1)
- Bunch Compressors 1 and 2 (§ 2.3.2)
- Linacs 1, 2 and 3 (§ 2.3.3)
- Switchyard and collimator (§ 2.3.4)
- Undulator line Aramis (§ 2.4)
- Undulator line Athos (with d'Artagnan) (§ 2.4)
- Terahertz (THz) source (§ 2.6)

Results from simulations of each of these sections will be presented in the following Sections. As discussed in Chapter 1, it is planned to operate SwissFEL with two electron bunches per RF macropulse. The simulated parameters presented here are also valid for the second electron bunch, assuming that inter-bunch wakefield effects are negligible.

A schematic overview of the accelerator is displayed in Figure 2.1.1.

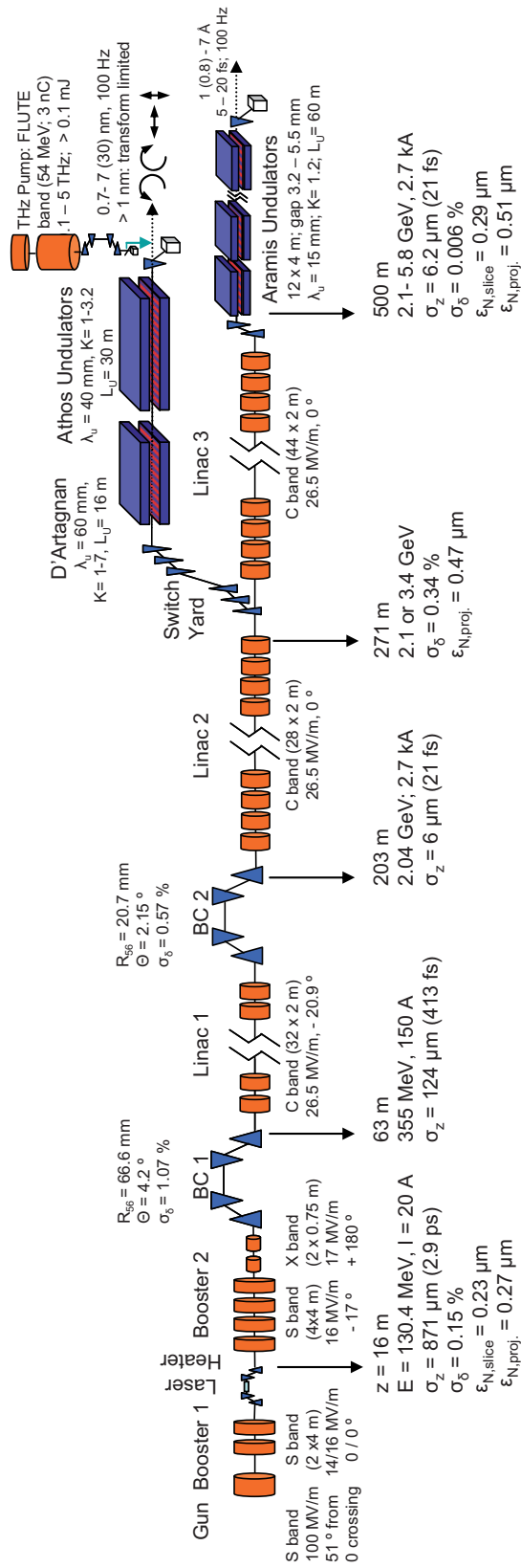


Fig. 2.1.1: Schematic of the SwissFEL Accelerator and FEL with the simulated beam parameters for the 200 pC operating mode

2.2 Simulation tools

To model the SwissFEL facility, a suite of different computer codes has been utilized. These range from simple, fast codes, to perform coarse but rapid optimization of the beam line, to highly detailed particle tracking codes to investigate subtle effects of the beam dynamics.

For the dynamics in the gun and the first accelerating structure, the particle tracking code ASTRA [1] is used, based on the detailed field maps of the RF cavities and solenoids. Faster but coarser estimates can be obtained with HOMDYN [9] and BET [2].

Tracking through the main linac is done with the code ELEGANT [10], after matching the transverse optics with MADX [11] and optimizing the longitudinal dynamics with LITRACK [12]. For the case of bunch compression, the results of ELEGANT, which uses a 1D CSR model, has been cross-checked with CSRTRACK [13].

The FEL performance is simulated with GENESIS 1.3 [14], after coarse optimization using the fast and efficient Ming Xie model [9] in MATLAB.

Once the layout is sufficiently defined, highly detailed start-to-end simulations are carried out, tracking the electron bunch from the cathode to the exit of the undulator. In order to do this, particle distributions are exchanged between ASTRA, ELEGANT and GENESIS. OPAL (Object Oriented Parallel Accelerator Library) [15,16], offers the highest level of detail and a large number of macro particles, on medium to large scale computer clusters. OPAL will be mainly used for precise beam dynamics simulation. Ongoing work however will enable OPAL to perform multiobjective optimization of the SwissFEL, using a lower dimensional beam dynamics model. This unique feature of OPAL, to gradually switch from a low dimensional model to the full 3D model, will allow us to model many relevant aspects within one simulation framework.

2.3 Accelerator simulation

2.3.1 Gun and booster section

This section describes the design considerations for the electron gun and first booster section (Booster 1) of SwissFEL (see Figure 2.1.1). It contains the electron source, a short diagnostics section, and two S-band accelerator modules, up to an energy of ~ 130 MeV. The main requirement for the gun and Booster 1 is to provide a low projected emittance below 0.4 mm.mrad, as well as a slice emittance below 0.3 mm.mrad at a peak current above 20 A.

A laser heater follows Booster 1 and is described in paragraph 2.3.1.4 (Figure 2.1.1). Since Booster 2 plays a role in the overall bunch compression scheme, it will be detailed in the next paragraph, 2.3.2.

2.3.1.1 Gun and Booster 1 layout

The electron source for SwissFEL will be a conventional RF gun, similar to the one installed at LCLS [17]. PSI plans to build a 2.5 cell normal-conducting gun in-house, based on the LCLS [18] and PHIN [19] designs, which are scaled to the RF frequency of 2998.8 MHz. The features of the gun can be summarized as follows:

- An accelerating peak gradient of 100 MV/m in the cavity, in order to minimize the effects of space charge during the first centimetres of acceleration, which is beneficial for reaching low slice emittance.
- The mode separation between the π and $\pi/2$ mode is about 16 MHz. This is guaranteed by a large iris diameter.

- The second cell (coupler cell) is coupled to two symmetric rectangular waveguides to suppress the dipole kick. A racetrack shape of the coupler cell has also been adopted to minimize the quadrupole field on the beam axis.
- In order to reduce dark current as much as possible, no cathode loading hole is foreseen (flat end wall).

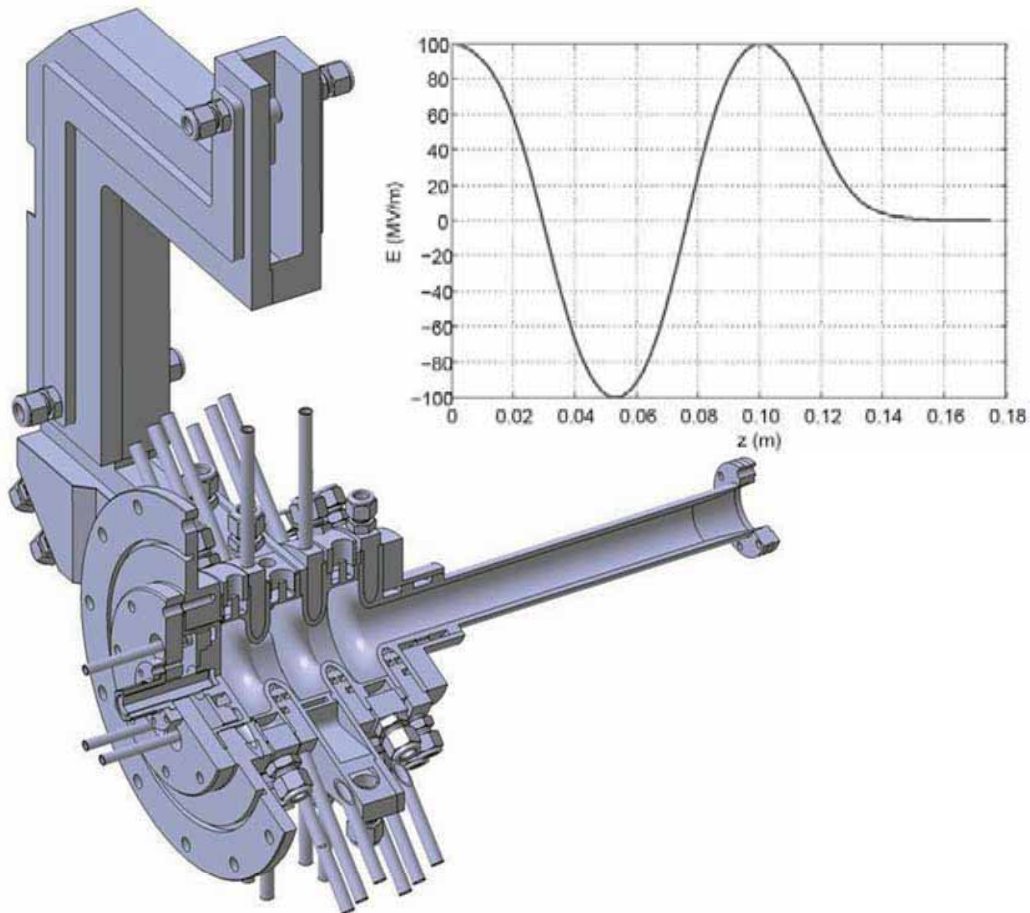


Fig. 2.3.1.1: Current design and on-axis field distribution of the SwissFEL gun.

Figure 2.3.1.1 shows a drawing of the latest design of the SwissFEL gun. Directly after the electron gun, centered at $z = 0.3$ m from the cathode position ($z = 0$ m), there is a solenoid for emittance compensation. The subsequent diagnostics section incorporates current monitors, screens, slits for emittance measurements, and a transverse deflecting cavity (TDC) for bunch length measurements. A dipole deflects the beam into a dispersive section for momentum and momentum spread measurements.

The first booster (Booster 1) starts at $z = 2.95$ m and consists of two 4.15 m-long S-band structures operated on-crest. Invariant envelope matching is applied at the booster entrance with the help of the gun solenoid, in order to apply the emittance compensation principle [20,21] and to obtain the lowest possible projected emittance at the end of the Booster 1 section (at 12.6 m from the cathode, at electron beam energies of ~ 130 MeV).

2.3.1.2 Gun and Booster 1 parameters

Beam dynamics simulations of the injector, up to 130 MeV, have been carried out using the particle code ASTRA [22]. The main concept is to use the emittance compensation principle [20,21], in which the booster entrance position and gun solenoid field are adjusted such that the electrons are accelerated on the invariant envelope. This basically freezes the low emittance obtained in the gun during the booster acceleration.

Several operation options are considered in the simulations, as presented in [23]. The following Table summarizes the main parameters obtained with simulation (in parenthesis the values obtained with ASTRA).

Table 2.3.1.1: Main parameters for the two operation modes (10pC case was only calculated with Astra).

| Bunch charge | 200 pC | 10 pC |
|---|--|---------------------|
| Gun gradient | 100 MV/m | 100 MV/m |
| Beam peak current | 20 A | 3 A |
| Laser transverse size (rms) | 215 μm | 101 μm |
| Laser longitudinal length (Full Width) | 9.9 ps | 3.7 ps |
| Intrinsic (Thermal) emittance | 0.195 μm | 0.092 μm |
| Projected normalized emittance at 130 MeV | 0.276 μm (0.275 μm) | 0.089 μm |
| Slice normalized emittance at 130 MeV | 0.250 μm (0.230 μm) | 0.070 μm |
| Energy | 129.36 MeV (130.4 MeV) | 130.5 MeV |
| Relative energy spread | 0.155% (0.162%) | 0.02% |
| Bunch length at 13 m (FWHM) | 9.87 ps (10.8 ps) | 3.68 ps |

Figure 2.3.1.2 shows the layout of the gun and Booster 1 section, together with the main simulation parameters for the standard case (100 MV/m, 200 pC; Table 2.3.1.1). All the following Figures also refer to this case.

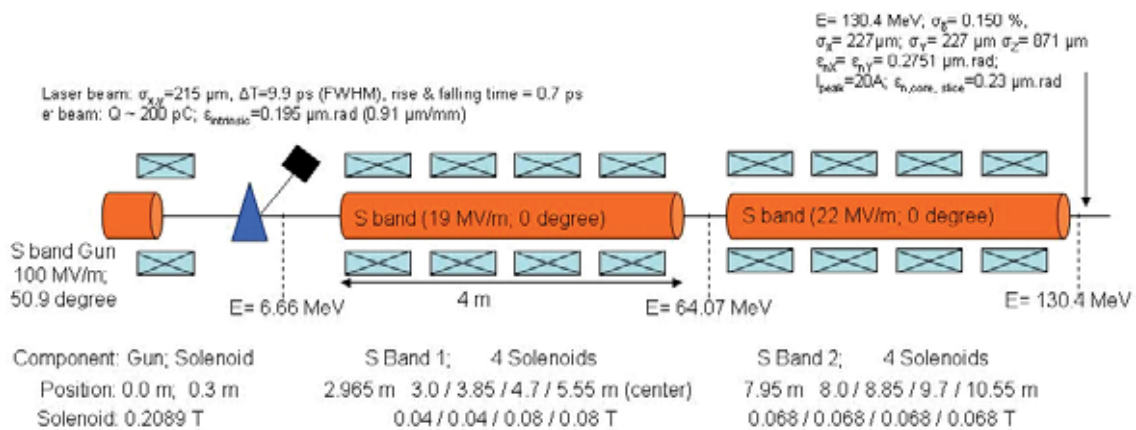


Fig. 2.3.1.2: Layout of gun and Booster 1 section with some of the simulated parameters.

Intrinsic emittance: It is necessary to comment on the intrinsic emittance values and model used in the ASTRA simulations. ASTRA applies the three-step model in which the emitted electrons leave the cathode with an average kinetic energy E_k , defined as:

$$E_k = \frac{h\nu - \Phi_{\text{eff}}}{2} \quad (1)$$

where $h\nu$ is the laser photon energy and Φ_{eff} is the effective work function (taking into account the barrier reduction due to the applied electric field).

The intrinsic emittance is then expressed as follows, where σ_{laser} is the rms laser spot size:

$$\varepsilon_{th} = \sigma_{\text{laser}} \sqrt{\frac{2E_k}{3mc^2}} \quad (2)$$

For the intrinsic emittance value used in the simulations (also quoted in the upper Table), a fixed value of $\varepsilon_{th} = \sigma_{\text{laser}} * 0.91$ mm.mrad /mm was used, according to measurements at LCLS (at a gradient of 115 MV/m) [24]. This corresponds to an average kinetic energy of 0.63 eV in the ASTRA model and was used independently of the gun gradient (100 MV/m or 120 MV/m), thus slightly overestimating the intrinsic emittance in the 100 MV/m case. Recent measurements at the SwissFEL gun test-stand [6,25,26] have demonstrated an intrinsic emittance as low as 0.41 mm.mrad / mm laser spot size, using 282 nm laser wavelength on a copper cathode for 1 pC charge.

2.3.1.3 Gun and Booster 1 simulation results

The following graphs in Figure 2.3.1.3 represent the ASTRA simulation results for the standard case (100 MV/m, 200 pC, and 20 A). Simulations for a higher gun gradient and lower charges have been presented elsewhere [17,23,27].

As can be seen from the transverse emittance curve (Figure 2.3.1.3), the invariant envelope matching results in a continuous decrease of the projected emittance during the booster acceleration. Solenoid compensation around the two S-band structures maintains the beam size below 0.3 mm rms along Booster 1. The beta-function directly after the gun (i.e. in the gun solenoid) is relatively large, resulting in a potentially higher chromatic effect. The slice emittance along the bunch (at $z = 13$ m) is displayed and reaches values as low as 0.23 mm.mrad at the centre of the bunch. The Twiss matching parameter at the end of the section ($z = 13$ m) is almost flat, which means the mismatch over the central 80% of the bunch corresponds to $\xi \leq 1.1$. This is also shown with the slice phase space ellipses.

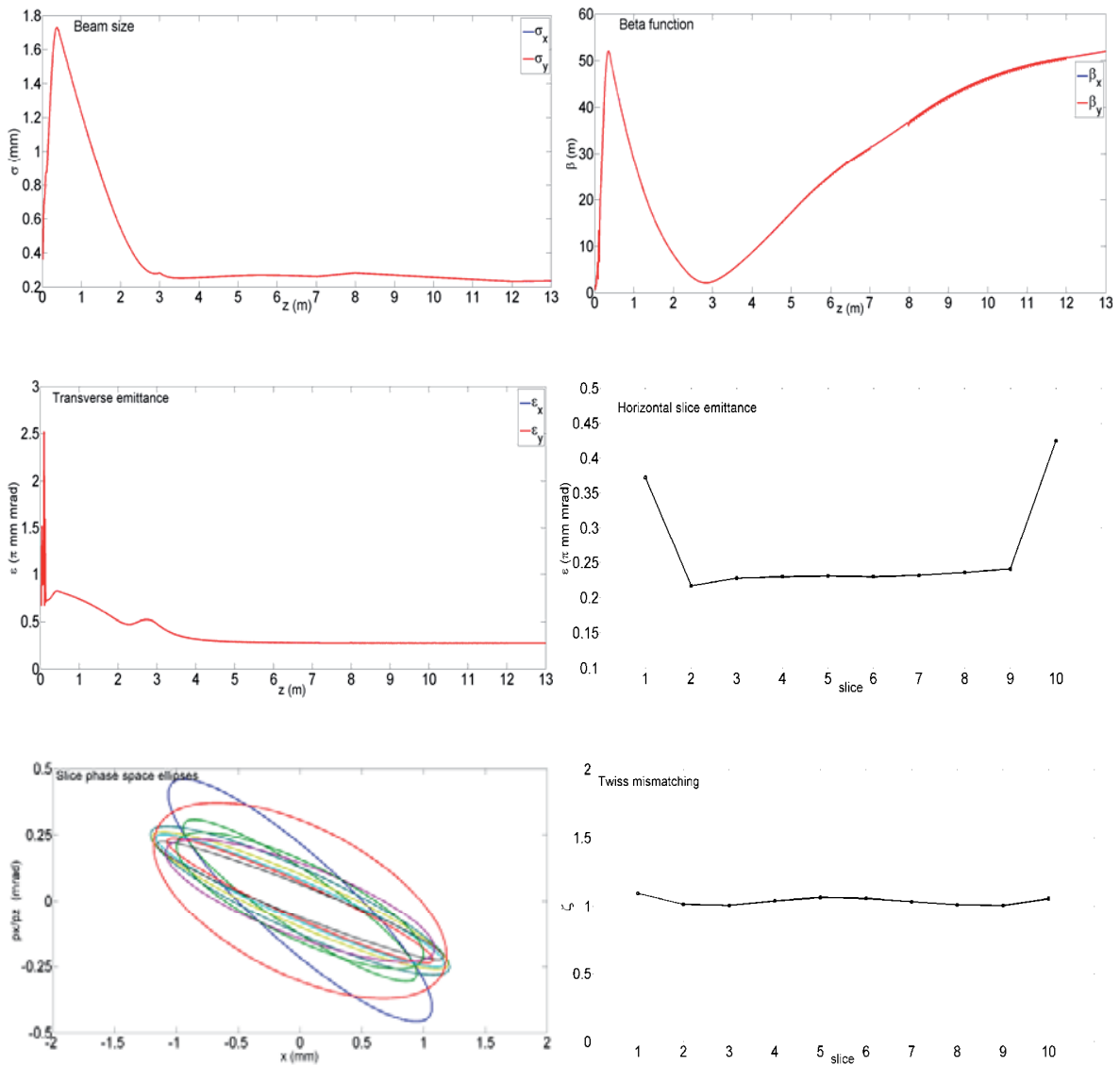


Fig. 2.3.1.3: Simulation results for the standard case (100 MV/m, 200 pC); On the right-hand side, from top to bottom: rms transverse beam size, beta-function and projected emittance development along the first 13m of the accelerator; On the left, from top to bottom: slice emittance along the bunch; Twiss mismatching parameter along the bunch and slice phase space ellipses at $z=13$ m.

Figure 2.3.1.4 shows that similar beam parameters are obtained using the full 3D OPAL simulation code for the same beam conditions.

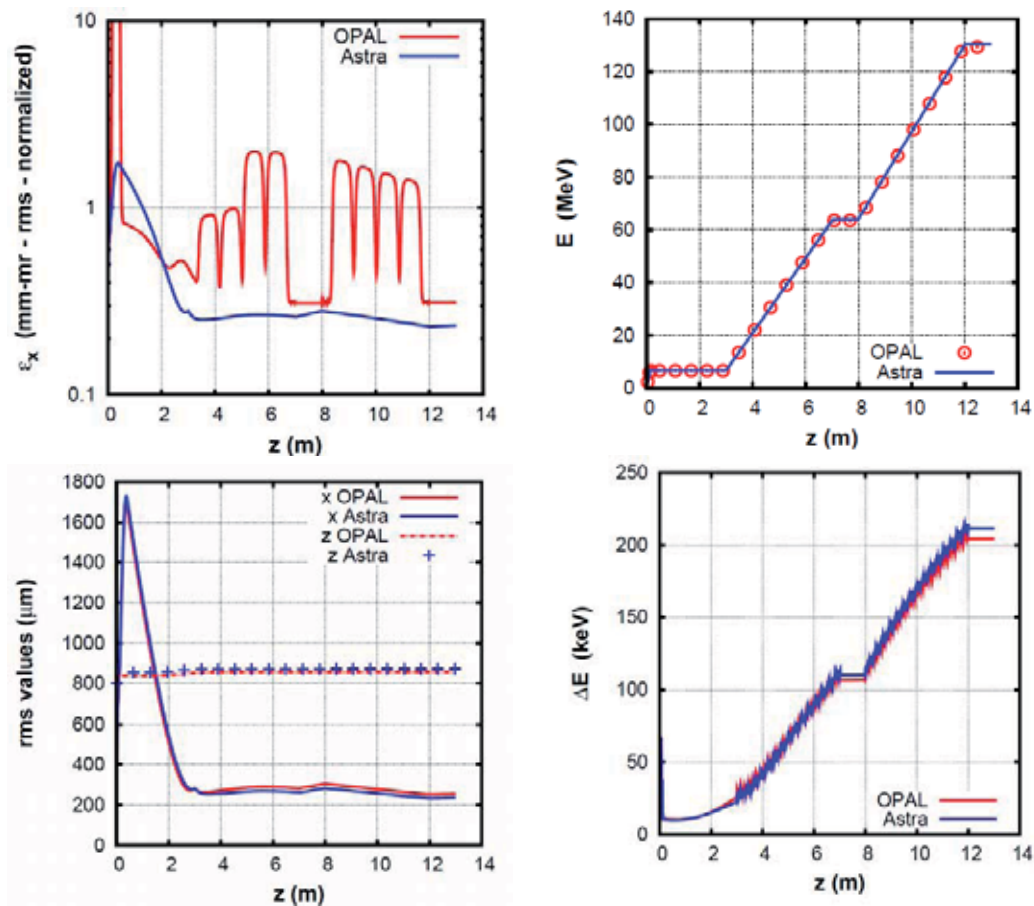


Fig. 2.3.1.4: OPAL and Astra simulation results for the standard case (100 MV/m, 200 pC). On the left-hand side, from top to bottom: normalized transverse emittance, transverse and longitudinal beam size. On the right-hand side from top to bottom: energy and energy spread.

2.3.1.4 Laser heater

Based on experience at LCLS, a laser heater is foreseen after Booster 1 (at $z = 13$ m), to damp any microbunch instability of the SwissFEL linac. For the simulations presented in this report, only a 2.5 m drift space is reserved for a laser heater, but no explicit designing has been done. If the laser heater shows significant improvement over simulated FEL performance, it will be used for operation. A first estimate of the laser heater parameter is derived from the LCLS laser heater design (Table 2.3.1.2). The total length of the LCLS laser heater is less than 1.5 m.

Table 2.3.1.2: Main parameters of the LCLS laser heater.

| | |
|---------------------------------|--------|
| Undulator length L_u | 48 cm |
| Period length λ_u | 4 cm |
| Undulator parameter K | 1.8 |
| Resonant wavelength λ_r | 800 nm |
| Dipole length L_b | 10 cm |
| Bending angle | 5.7 ° |
| Drift L_{D1} | 10 cm |
| Drift L_{D2} | 70 cm |

2.3.2 Bunch compression scheme (Booster 2, BC1, Linac 1 and BC2)

The overall SwissFEL design is motivated by the goal of 200 pC bunch charge, accelerated to 5.8 GeV and compressed to a peak current of more than 2.7 kA. A two-stage bunch compression system is used to achieve this goal. The whole bunch compression system consists, apart from the two magnetic chicanes, of two linac sections (Booster 2 and Linac 1) to imprint the energy chirp on the beam, and an X-band section to linearise the energy – time correlation along the bunch (see Figure 2.3.2.1). After the compression, the energy chirp is reduced thanks to longitudinal wakefields in Linac 2 and 3.

The overall compression scheme for each operation regime can be summarized as follow:

Normal 200 pC mode: Chirp in Booster 2 – BC1 compression - chirp control in Linac 1 – BC2 compression – wakefields remove chirp in Linac 2/3 – slight decompression in Aramis collimator

Normal 10 pC mode: Chirp in Booster 2 – BC1 compression - chirp control in Linac 1 – BC2 compression – wakefields removes partially the chirp

Large Bandwidth 200 pC mode: Chirp in Booster 2 – BC1 compression - chirp control in Linac 1 – BC2 over compression – wakefields increase chirp in Linac 2+3 – Aramis Collimator slightly compress.

Attosecond 10 pC mode: Chirp in Booster 2 – BC1 compression - chirp control in Linac 1 – BC2 compression – wakefields removes partially the chirp in Linac 2+3 – Aramis Collimator compression.

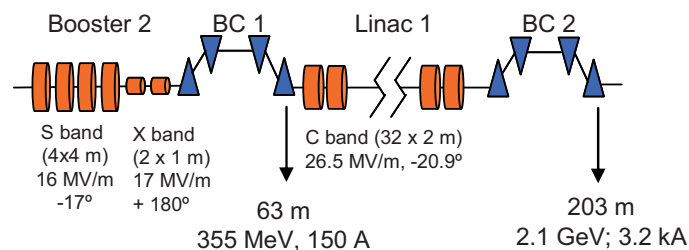


Fig. 2.3.2.1: Schematic of the components involved in the bunch compression scheme: from Booster 2 to BC2.

The RF gun and Booster 1 have been described previously, in Section 2.3.1. The second part of the booster, Booster 2 (consisting of 4 S-band cells), generates the necessary longitudinal chirp, through off-crest operation, for the bunch compression. Its parameters are summarised in Table 2.3.2.1, with a cell layout overview in Figure 2.3.2.2. The transverse beam optics is controlled by a quadrupole doublet downstream of each S-band structure. The below presented simulation results are assuming an input peak current of 22 A for 200 pC instead of the optimized value of 20 A found in section 2.3.1. This does not change the tolerances and general bunching concept. Parameters like RF gradient, RF phase or bending angle are slightly changing depending on the operation mode.

Table 2.3.2.1: Summary of Booster 2 parameters

| Cell layout | Quadrupole Doublet Lattice | | | |
|-----------------------------------|---|--------------|-------------|------------|
| Cell length | 5.9 m | | | |
| Number of cells | 4 | | | |
| S-band cavities per cell | 1 | | | |
| S-band cavity length, L_C | 4.15 m (reserved) / 4.083 m (effective) | | | |
| Drift, L_{D1} (Bellows) | 10 cm | | | |
| Drift, L_{D2} (Bellows) | 30 cm | | | |
| Quadrupole length, L_Q | 25 cm (reserved) / 15 cm (effective) | | | |
| Drift, L_{D3} | 20 cm | | | |
| Drift, L_{D4} (BPM+ Gate Valve) | 70 cm | | | |
| Operation mode | 200 pC Normal | 10 pC Normal | 200 pC (BW) | 10 pc (as) |
| S-band cavity gradient | 16 MV/m | 18 MV/m | 16 MV/m | 18 MV/m |
| S-band cavity phase (off crest) | -17 ° | -17.8° | -17 ° | -17.8° |

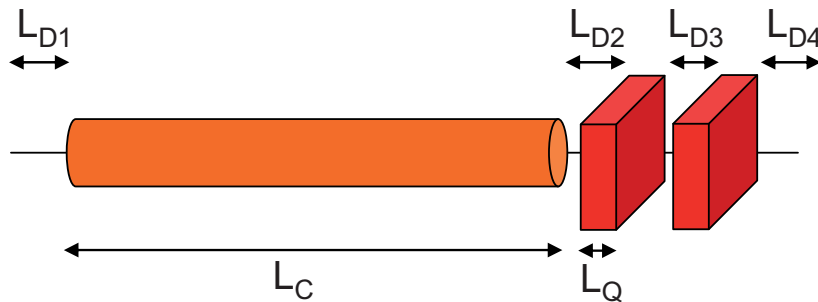


Fig. 2.3.2.2: Schematic of single-cell layout of Booster 2.

Longitudinal phase space (energy – time correlation) linearization is completed with an X-band cavity, operated at the 4th harmonic of the 2.9988GHz; that is to say, at 11.9952 GHz. The parameters of the X band structures are depicted in Table 2.3.2.2 for the two operation mode 10 and 200 pC.

Table 2.3.2.2: Summary of X-band parameters

| | | |
|------------------------|---|--------------|
| Cavity length | 0.965 m (reserved) / 0.750 m (effective) | |
| Separation of cavities | 15 cm | |
| Number of cavities | 2 | |
| Operation mode | 200 pC Normal | 10 pC Normal |
| Cavity gradient | 16.89 MV/m | 21.2 MV/m |
| Cavity phase | + 180.13 ° | 270° |

Two magnetic chicanes, BC1 and BC2 (with four dipoles arranged in D-shape), are used to generate a non-zero momentum compaction factor, R_{56} . A schematic layout and parameter summary are given in Figure 2.3.2.3 and Table 2.3.2.3. Coherent Synchrotron Radiation (CSR) effects, especially

on the slice emittance, can be mitigated when the horizontal beam size has a waist in the fourth dipole of the chicane. We have chosen beta functions below 7 m and 5 m in BC1 and BC2, respectively, while the vertical parameters are not subject to tight constraints.

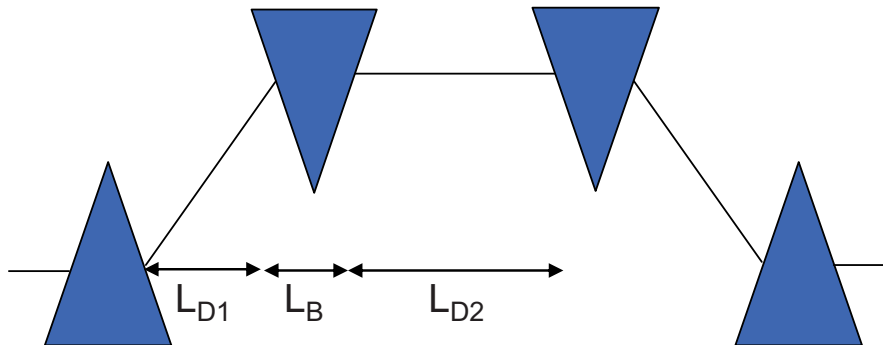


Fig. 2.3.2.3: Schematic layout of the bunch compressors BC 1 and BC 2

Table 2.3.2.3: Summary of bunch compressor BC1 and BC2 parameters for the 200 pC and 10 pC operation modes.

| BC 1 | | | | |
|---------------------------------|--|-----------------|---------------|-------------|
| Bending magnet length, L_B | 0.25 m | | | |
| Drift, L_{D1} | 6.0 m | | | |
| Drift, L_{D2} | 1 m | | | |
| Beam energy | 355 MeV | | | |
| Matching condition at last bend | $\beta_x < 5$ m, $\alpha_x = 0$, $\beta_y < 40$ m | | | |
| Operation mode | 200 pC Normal | 10 pC Normal | 200 pC (BW) | 10 pc (as) |
| Bending angle | 4.2 ° | 3.82° | 4.2° | 4.2° |
| R_{56} | 66.6 mm | 55.1 mm | 66.6 mm | 66.6 mm |
| Peak current at last bend | 150 A | | 150 A | |
| Slice norm. emittance last bend | 0.3 mm.mrad | 0.11 mm.mrad | 0.3 mm.mrad | mm.mrad |
| Bunch length, rms σ_z | 124.2 μ m | | 124.2 μ m | |
| Compression factor | 6.75 | | 6.75 | |
| BC 2 | | | | |
| Bending magnet length, L_B | 0.5 m | | | |
| Drift, L_{D1} | 7.0 m | | | |
| Drift, L_{D2} | 1 m | | | |
| Beam energy | 2040 MeV | | | |
| Matching condition at last bend | $\beta_x < 3$ m, $\alpha_x = 0$, $\beta_y < 40$ m | | | |
| Operation mode | 200 pC Normal | 10 pC Normal | 200 pC (BW) | 10 pc (as) |
| Bending angle | 2.15 ° | 2.15° | 2.245 ° | 2.15° |
| R_{56} | 20.7 mm | 20.7 mm | 22.5 mm | 20.7 mm |
| Peak current at last bend | 3200 A | 1100 A | 3700 A | 14000 A |
| Slice norm. emittance last bend | 0.3 mm.mrad | 0.11 mm.mrad | 0.3 mm.mrad | mm.mrad |
| Bunch length, rms σ_z | 6.2 μ m | 1 μ m | 6.2 μ m | 0.2 μ m |
| Compression factor | 20.1 | | 24.6 | |

Chirp adjustments between the compressor chicanes are carried out in the C-band (5.712 GHz) structures of Linac 1, with an off-crest phase of -20.9° and a gradient of 26.5 MV/m. The main purpose here is to control the compression factor in BC2 independently of BC1. Linac 1 parameters are summarised in Table 2.3.2.4.

Table 2.3.2.4: Summary of Linac 1 parameters

| | Linac 1 | | | |
|-------------------------|---|-----------------|----------------|---------------|
| Number of cavities | 32 | | | |
| Length of cavity, L_C | 2.05 m (reserved) / 1.983 m (effective) | | | |
| Cavity frequency | C-Band, 5712 MHz | | | |
| Cavity gradient | 26.5 MV/m | | | |
| Operation mode | 200 pC Normal | 10 pC Normal | 200 pC (BW) | 10 pC (as) |
| Cavity phase | -20.9° | -16.7° | -20.9° | -20.8° |

The electron bunch profile (energy spread, current and emittance) after the second bunch compressor BC2 are shown on Fig 2.3.2.4 for the two main operation mode at 10 and 200 pC.

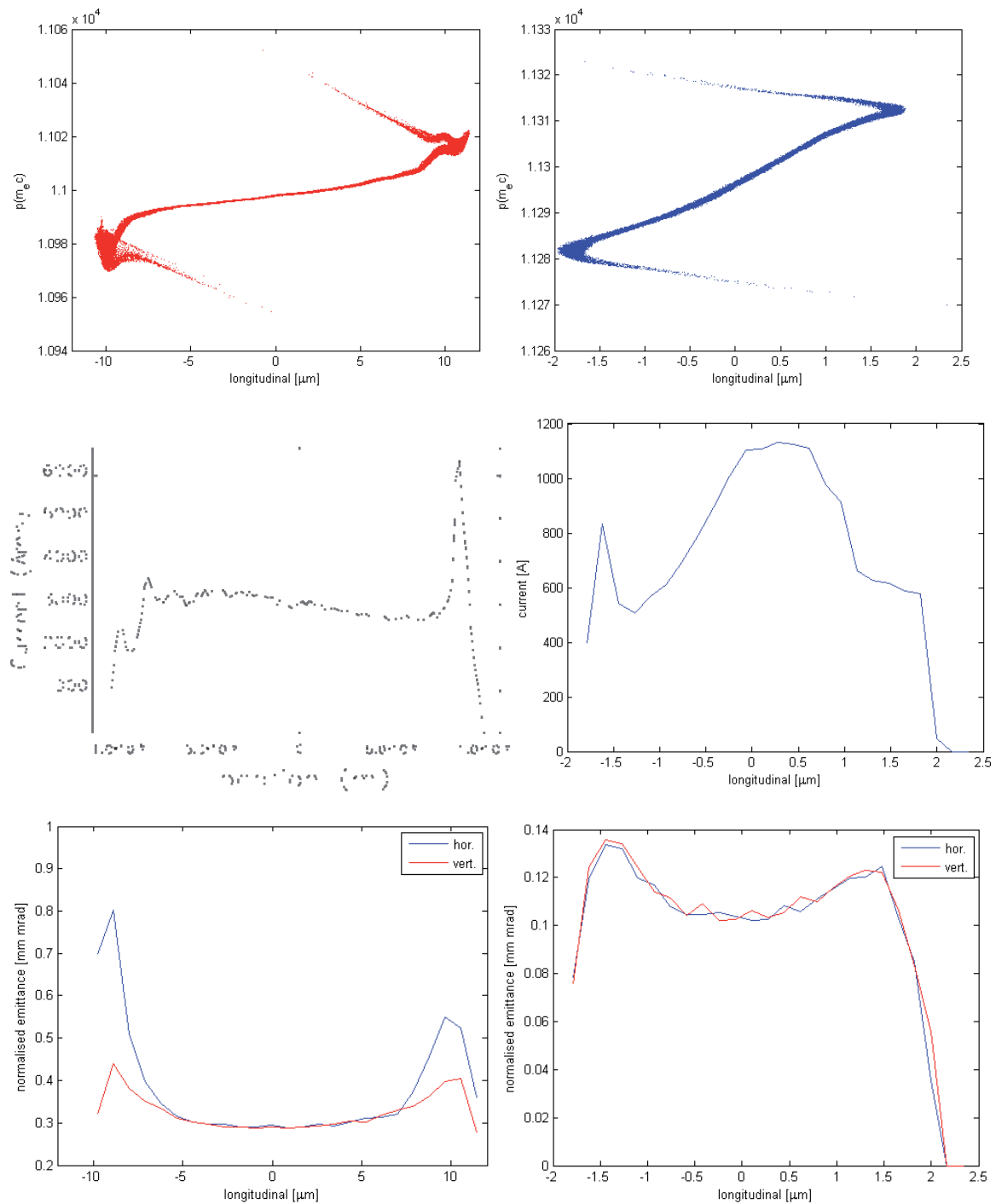


Fig. 2.3.2.4: Bunch profiles from Elegant simulations after last dipole of BC2 ($z = 203$ m) for the normal mode with 200 pC charge (left figures) and with 10 pC charge (right figures).

In the nominal operation mode of 200 pC, the bunch is compressed from initially $\sigma_z = 838$ μm , rms (or 2.8 ps, rms) to $\sigma_z = 124$ μm (413 fs) after the first chicane, and to $\sigma_z = 6$ μm (20 fs rms) final bunch length, with a peak current of 3.2 kA at 200 pC.

2.3.3 Linac layout (Linac 2 and Linac 3)

The main bunch acceleration is driven by three C-band linacs. The first of these (Linac 1) is located between the bunch compressors and has already been described in Section 2.3.2. Downstream of the second bunch compressor, Linac 2 defines the energy at the switchyard, with the extraction point to the seeded long-wavelength FEL beamline (Athos). Final acceleration to the short wavelength FEL line (Aramis) is achieved in Linac 3. The parameters of the three main linac sections are summarised in Table 2.3.3.1.

As mentioned in Chapter 3, the frequency for SwissFEL Linacs 1, 2 and 3 is 5.712 GHz, in contrast to the S-band (2.998 GHz) of the Booster.

Apart from considerations for the RF electrical consumption, C-band frequency also presents some advantages for the beam dynamics, in comparison to an S-band linac. At higher frequencies, a higher effective gradient is possible, allowing a shorter linac length. The lower iris diameter of C-band structures compared to the S-band results, however, in stronger wakefields. While wakefield effects on the transverse emittance are tolerable, the longitudinal component helps in the reduction of the energy chirp generated for the compressors, resulting in FEL bandwidth reduction. Removal of chirp in Linacs 2 and 3 would require a significantly longer linac if the frequency would be S-band.

Table 2.3.3.1: Parameters of the main linac sections for all operation modes (Linacs 1, 2 and 3).

| | Linac 1 | Linac 2 | Linac 3 |
|------------------------------------|---|-----------|-----------|
| Cell layout | FODO | | |
| Phase advance | 70 ° | | |
| Cell length | 9.8 m | 18.2 m | 18.2 m |
| Number of cells | 8 | 3.5 | 6 |
| Cavities per half-cell | 2 | 4 | 4 |
| Length of cavity, L_c | 2.05 m (reserved) / 1.983 m (effective) | | |
| Cavity frequency | C-band | | |
| Cavity gradient | 26.5 MV/m | 26.5 MV/m | 26.5 MV/m |
| Cavity phase | -20.9 °(*) | 0 ° | 0 ° |
| Drift, L_{D1} (bellows) | 10 cm | | |
| Drift, L_{D2} | 5 cm | | |
| Drift, L_{D3} (bellows) | 5 cm | | |
| Quadrupole length, L_Q | 25 cm (reserved) / 15 cm (effective) | | |
| Drift, L_{D4} (BPM & Gate Valve) | 35 cm | | |

(*) phase for 200 pC, refer to Table 2.3.2.4 for the other operation modes.

The phase of -20.9 ° in Linac 1 corresponds to maximum compression for a final peak current of 3.2 kA. The phases in Linacs 2 and 3 are chosen to remove the chirp at the end of Linac 3. Note that the choice of the phases takes into account longitudinal wakefields.

To reach 5.8 GeV, Linac 3 requires fewer RF stations than the number for which space is available in the lattice. This extra space is reserved for future energy upgrades.

The matching condition for the FODO lattice is 70 ° phase advance per cell, which is not a strong condition. It can be adjusted to different values if needed, to ease the matching from or to other sections. Only two profile monitors are foreseen per linac to measure the optical functions. For best resolution, the monitors are separated by 1.5 linac cells, corresponding to 105° betatron phase

advance. The measurement is completed by the orbit response function, measured with the BPMs along the entire linac. However for a more reliable measurement of the optical function in the lattice, three profile monitors per linacs are highly desirable. The layout of the half FODO cells of Linacs 1, 2 and 3 are shown in Figure 2.3.3.1.

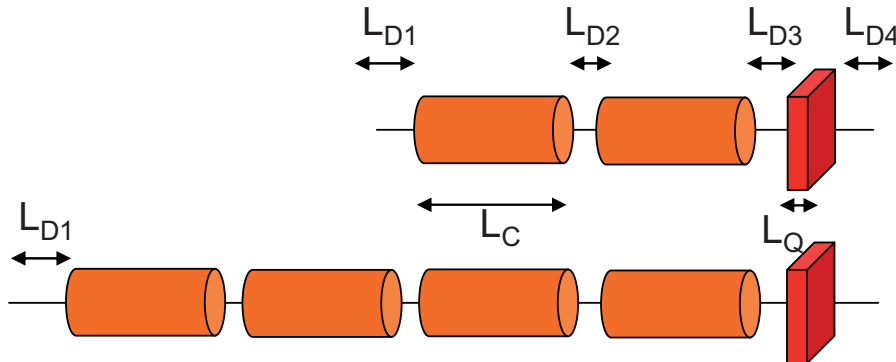


Fig. 2.3.3.1: Half-cell layout for Linac 1 (top) and Linacs 2 & 3 (bottom)

Beam optics consists of the FODO channels in each linac section, in the undulators, and in a diagnostic line downstream of BC1. Assembly of five quadrupoles between these sections enables beam matching during transition to another section and to special elements such as the chicanes or the switchyard. The overall beam optics of the full accelerator layout is shown in Figure 2.3.3.2.

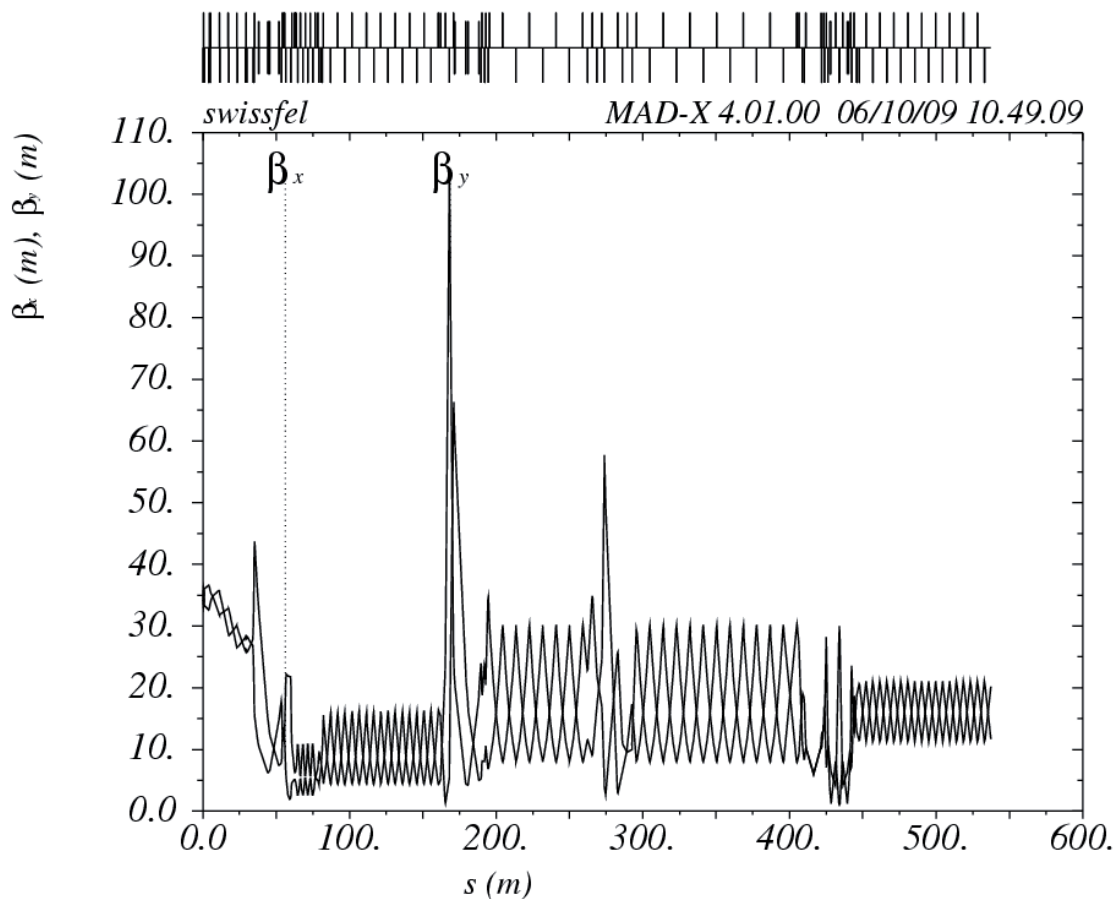


Fig. 2.3.3.2: Beam optics along SwissFEL

2.3.4 Switchyard and collimators

2.3.4.1 Switchyard Layout

The switchyard for the SwissFEL diverts the beam coming from Linac 2, with an energy of 3.4 GeV, to the long wavelengths undulator (Athos beamline). At the Switchyard entrance a fast kicker followed by a septum magnet (Section 3.4.6) will deviate the second of the two bunches accelerated in the Linac. This second bunch will then be further deviated by two double bend magnets towards Athos beamline while the first bunch continues straight towards Aramis.

Table 2.3.4.1: Electron beam parameters at Switchyard entrance

| Matching Position | Kicker Magnet Entrance |
|-------------------|------------------------|
| β_x | 5.0 m |
| α_x | 0.0 |
| β_y | 44 m |
| α_y | 6.5 |

In the present set-up of the switchyard, its total length is 77 m and the separation between the Athos and Aramis beamlines is about 4 m, with a net bending angle equal to zero, making the two beamlines parallel to each other, as shown in Figure 2.3.4.1. This design has two almost identical double-bend achromatic (DBA) sections; and each section has a total bending angle of 4° . The central dipoles in each double bend is a "micro-bend", with a bending angle of -0.2 and $+0.1^\circ$ respectively, used only to adjust the value of R_{56} , making the sector also isochronous.

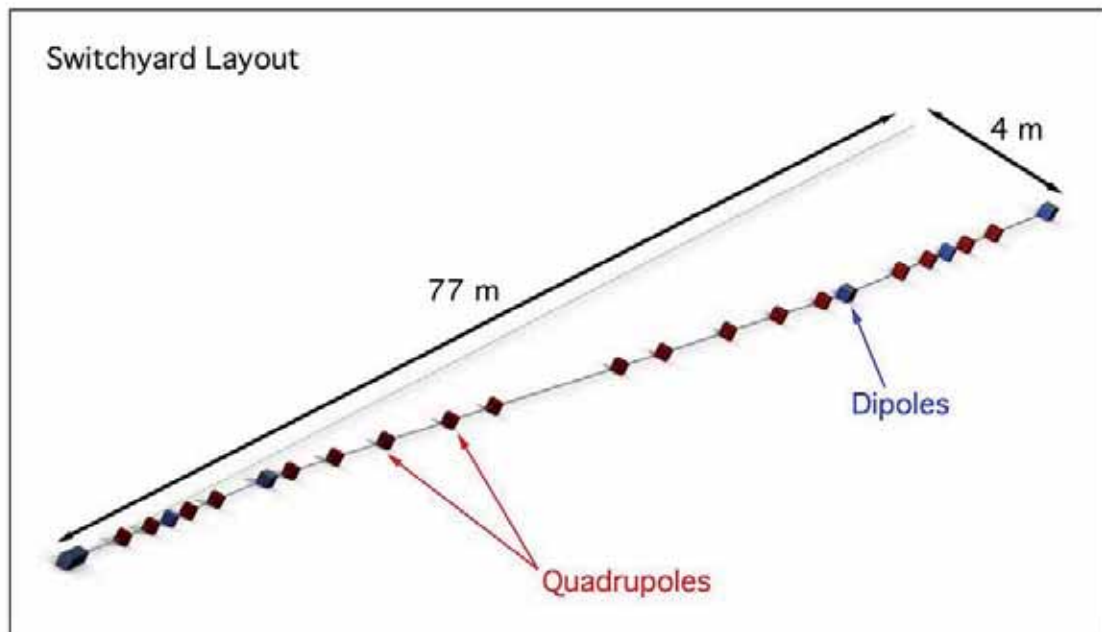


Fig. 2.3.4.1: Layout of the switchyard. The blue elements are dipoles and the red elements quadrupoles. The switchyard is composed by two DBAs and a transport line. Each DBA section has a micro-bend in the middle, so that it can be also isochronous.

The maximum beta function along the switchyard is 40 m in horizontal plane and 110 m in the vertical plane, which yields negligible chromatic effects (Figure 2.3.4.2). The phase advance between the two double bends is adjustable by changing the settings of the quadrupoles in the

transport line. The lattice functions in the two bend sets are the same, so that kicks due to coherent synchrotron radiation (CSR) act in opposite directions and, by adjusting the phase advance between them, we can compensate for the emittance dilution caused by CSR. In the transport line, the central section has 9 m which should allow for the transport of heavy equipment to the Linac area, also there is enough space for collimators.

In order to evaluate emittances and beam size changes throughout the switchyard, we have performed simulations with an electron distribution at the entrance of the kicker, which was obtained from a phase space output from an ELEGANT simulation for the 200 pC case. For the simulations, the PTC module embedded in the latest MADX version was used. CSR effects are not taken into account, but are evaluated separately using CSRTRACK (so far in 1D only). The initial beam conditions are shown in Table 2.3.4.1 and have an initial normalized emittance of $\epsilon_x = 0.47$ mm.mrad and $\epsilon_y = 0.35$ mm.mrad (according to simulations for the 200 pC case); and the bunch length is 8.6 μm .

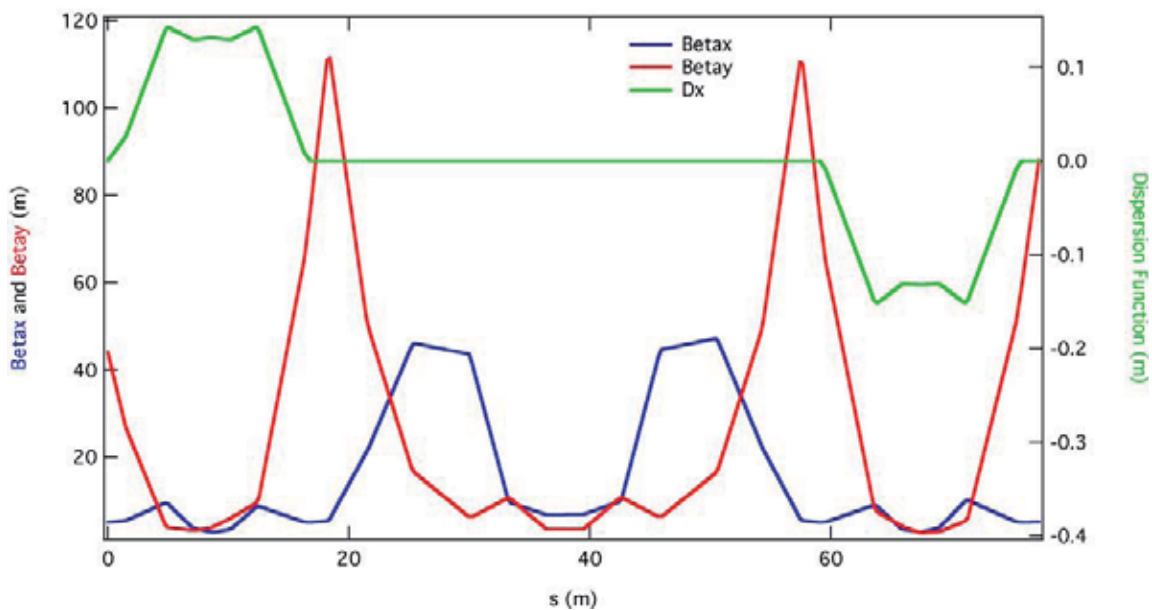


Fig. 2.3.4.2: Lattice function for the switchyard (top). Dispersion (green), (red) β_y and (blue) β_x .

The maximum dispersion is 0.15 m in the double-bend sections and, considering a total energy spread in the beam of 0.11%, the maximum beam size in the switchyard is 210 μm (1 sigma rms) in the horizontal plane, and is dominated by dispersion. Considering this beam size and a vacuum chamber of 16 mm in diameter, a centred beam would be 30 sigma from the wall. In the dispersion-free regions, the maximum beam size is 75 μm in the vertical direction and 53 μm in the horizontal. In order to keep the bunch length constant throughout the switchyard, the longitudinal parameters were chosen so that R_{56} and T_{566} were as small as possible. For the layout shown in Figure 2.3.4.1, their values are: $R_{56} = 1.8$ μm and $T_{566} = 31$ mm. The amount of bunch length variation in the switchyard is less than 1% (Figures 2.3.4.3 and 2.3.4.4).

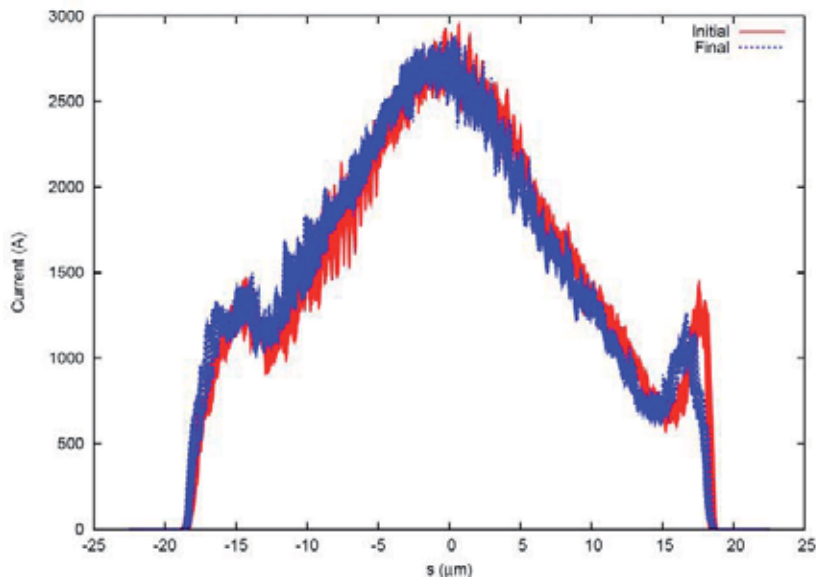


Fig. 2.3.4.3: Longitudinal profile at the beginning and at the end of the switchyard.

The total effect of CSR on the emittance is negligible, being much smaller than distortions caused by the lattice. For the case with CSR, the amount of projected emittance growth can be optimized by changing the phase advance between the two bending sets. Although the projected emittance is very sensitive to the phase advances, the sliced emittance is conserved along the whole switchyard, as shown in Figure 2.3.4.5.

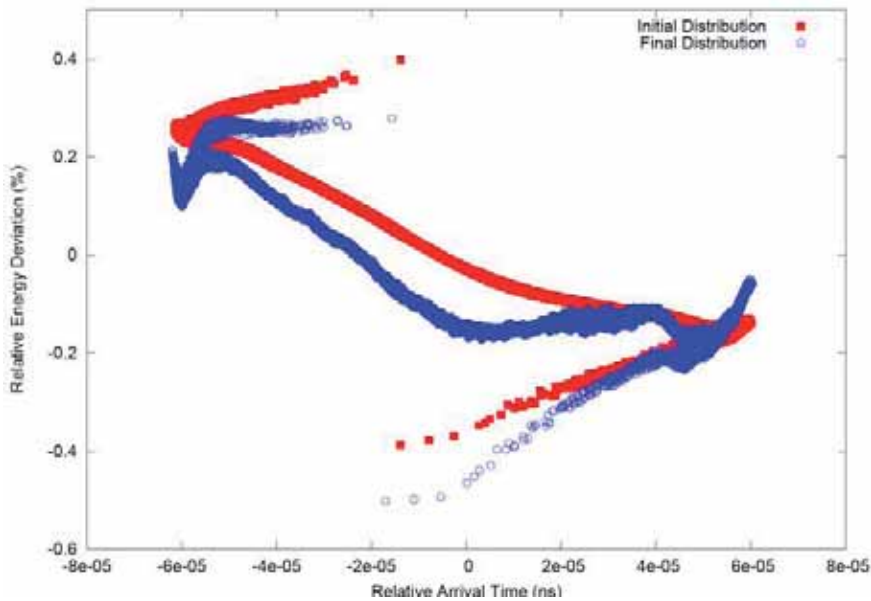


Fig. 2.3.4.4: Effect of CSR in longitudinal phase-space.

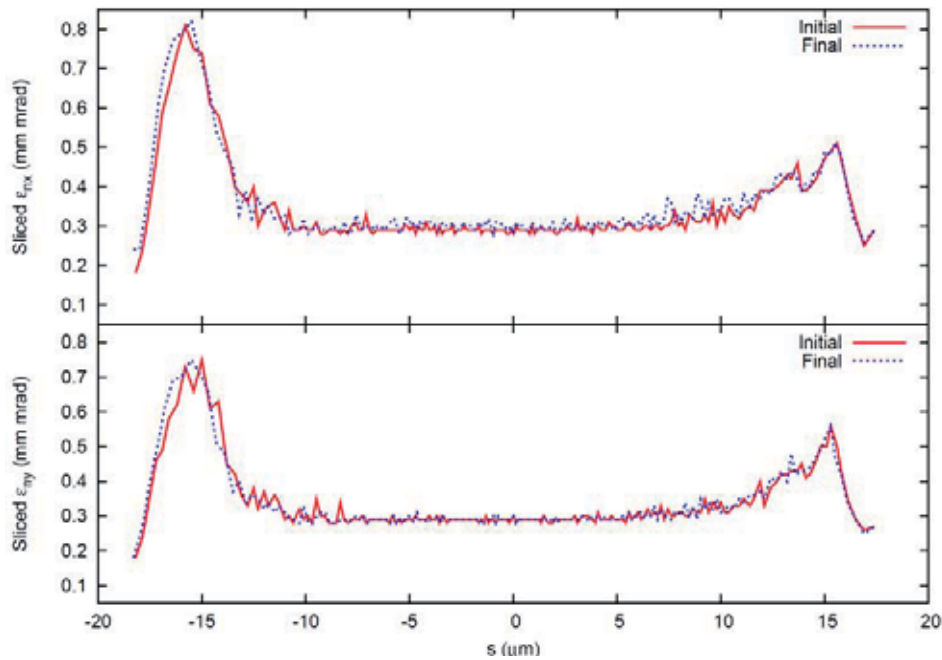


Fig. 2.3.4.5: Horizontal slice emittance at the end of the switchyard.

The misalignments of quadrupole magnets have no large impact on emittance. For a Gaussian distribution of transverse misalignments, with a width of $50\ \mu\text{m}$, the emittance grows by 6%, and if the spread is reduced to $20\ \mu\text{m}$, this growth is reduced to 2%. Although the projected emittance does not change much, misalignments can excite betatron oscillations, which can spoil the performance of the undulators. For the misalignment distributions studied, the average rms spread of offsets at the end of the switchyard is $300\ \mu\text{m}$ and $100\ \mu\text{m}$ for misalignments of $50\ \mu\text{m}$ and $20\ \mu\text{m}$, respectively. These offsets can be corrected by the use of beam-based-alignment and an orbit feedback system (see Section 3.11). Effects from multipole errors and fringe fields have not yet been addressed.

2.3.4.2 Athos Collimator design

The electron bunch deviated towards Athos will first pass through a collimator to prevent damaging of Athos undulators. The initial design for the collimator at the Athos beamline, foresees a set of transverse collimators at the dispersion free section of the switchyard and a dispersive energy collimator in the second set of DBAs, as shown in Figure 2.3.4.6. For each transverse plane a set of two collimators are separated by a phase advance of $90\ \text{deg}$ and the apertures are $12\ \text{mm}$ and $8\ \text{mm}$ for the vertical and horizontal collimators, respectively. Those apertures give an acceptance of $A_x=1.4\ \text{mm.mrad}$ and $A_y=1.3\ \text{mm.mrad}$ which is comparable to the limitation of $1.6\ \text{mm.mrad}$ at the undulators. For the energy collimation an aperture of $6\ \text{mm}$ will give a total momentum acceptance of $\pm 1.7\ \%$. Further studies including dark current and halo formation are necessary to optimize the collimators design.

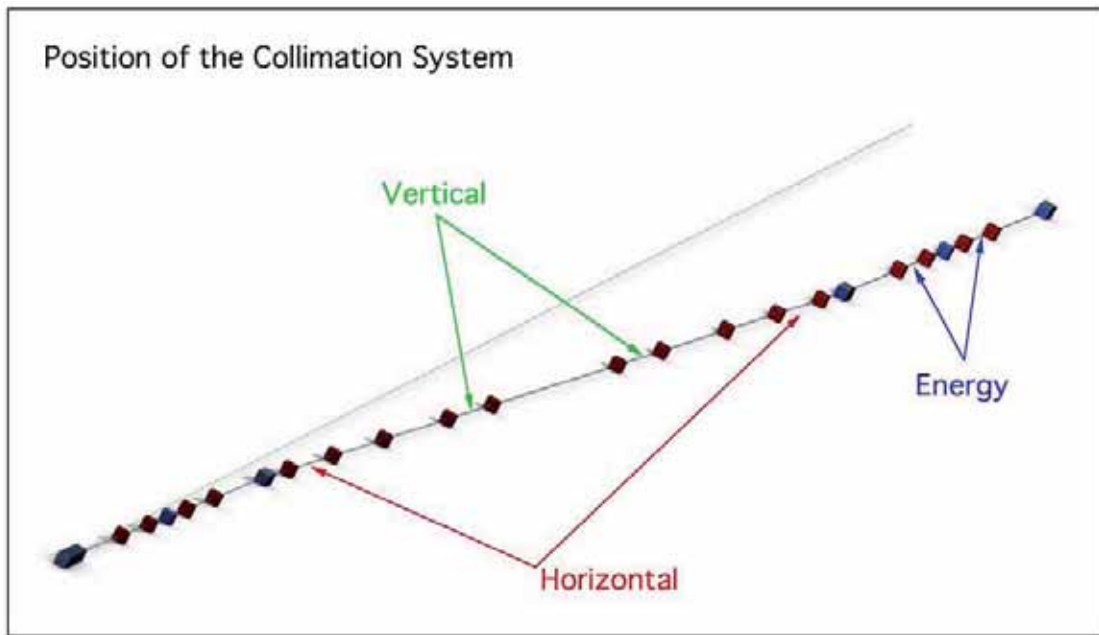


Fig. 2.3.4.6: Position of the Athos collimators along the switchyard. Red=horizontal, green=vertical and blue=energy.

Table 2.3.4.2: Athos collimator design parameters.

| | |
|--|---|
| Length of Collimator Block | 1 m |
| Number of Collimator Blocks | min. 6 |
| Length of Transverse Collimator Section L_{CT} | 50 m |
| Matching Condition (Center of T-Col.) | $\beta_x = 40 \text{ m}, \beta_y = 110 \text{ m}$ |
| Phase Advance over L_{CT} | $\mu_{x,y} \geq 0.25$ |
| Length of Longitudinal Collimator Section L_{CE} | 20 m |
| Matching Condition (Center of E-Col.) | $\beta_x = 4 \text{ m}$ |

2.3.4.3 Aramis Collimator design

The electron bunch heading straight towards the Aramis undulator will also pass through a collimator to prevent damaging of Aramis undulators. The initial design for the collimator at the Aramis beamline, foresees a transverse colimator where the beam is drifting through a waist and a dispersive energy collimator in form of a magnetic chicane. Sufficient quadrupoles have been added to let the magnetic chicane acts as two dog legs. For the 200 pC - large bandwidth mode of operation, collimator should be set as two dog legs keeping the energy chirp. For the ultra-short, low charge bunch mode the collimator is set such that it acts like a compression chicane. All other modes can be operated with both configurations. It has to be studied, which is the best in terms of emittance preservation.

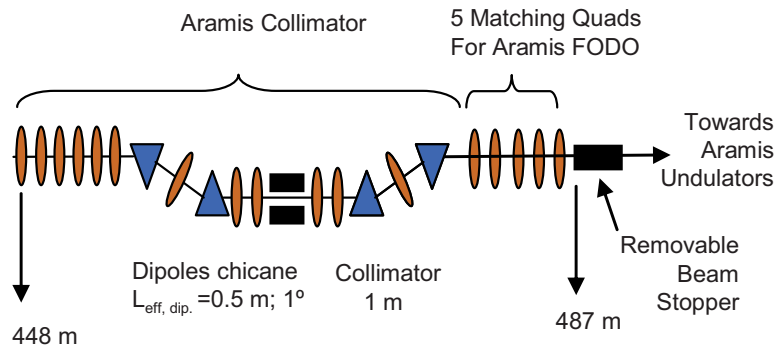


Fig. 2.3.4.7: Aramis Collimator Design (Dec 2010)

Table 2.3.4.2: Aramis collimator design parameters.

| | |
|--|---|
| Length of Collimator Block | 1 m |
| Number of Collimator Blocks | min. 10 |
| Length of Transverse Collimator Section L_{CT} | 10 m |
| Matching Condition (Center of T-Col.) | $\beta_{x,y} = 6 \text{ m}, \alpha_{x,y} = 0$ |
| Phase Advance over L_{CT} | $\mu_{x,y} > 0.25$ |
| Bend Magnet Length L_B | 0.5 m |
| Bending Angle | 0.5° |
| Length of Longitudinal Collimator Section L_{CE} | 25 m |
| Chicane Matching Condition (Center of E-Col.) | $\beta_{x,y} = 25 \text{ m}, \alpha_{x,y} = 0$ |
| Dog Leg Matching Condition (Center of E-Col.) | $\beta_x = 2 \text{ m}, \beta_y = 20 \text{ m}, \alpha_{x,y} = 0$ |

2.4 Undulator line parameters and simulations

The SwissFEL goal is to provide FEL radiation which spans the wavelength range from 1 Å to 7 nm, with a compact design. A natural cut in the wavelength is at around 7 Å, because the optics to transport the radiation differs significantly for longer or shorter wavelengths. Thus the hard X-ray beamline Aramis covers the wavelength range from 1 to 7 Å. Operation at the shortest wavelength also defines the overall compactness of the facility, because it requires the highest beam energy and has typically the longest gain length, and thus the longest undulator beamline. For the soft X-ray beamline Athos, a tuning range of from 0.7 to > 7 nm is impractical without a staged approach, with two modes of operation (2.1 GeV or 3.4 GeV).

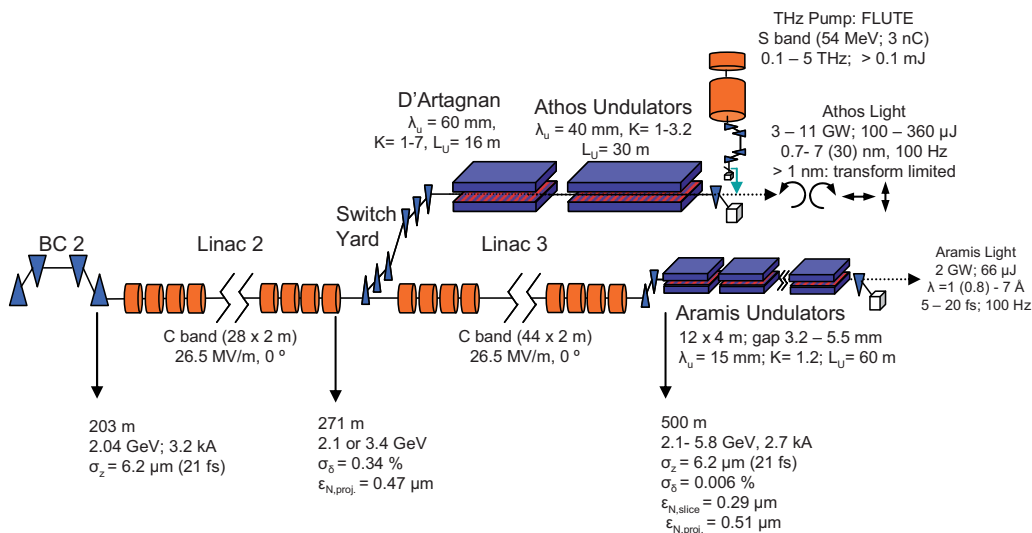


Fig. 2.4.1 Schematic of the SwissFEL accelerator (downstream of BC1) with the two undulator beamlines Aramis (0.1 – 0.7 nm) and Athos (0.7 to 30 nm)

2.4.1 Aramis

To achieve the shortest facility, the Aramis undulator is designed to provide the shortest undulator period with a reasonable value for the undulator parameter K above 1. The tuning is primarily done by the electron beam energy. However, this implies the possibility of only a single hard X-ray beamline in any future extension of the facility, due to the coupling of the FELs through the electron beam energy.

The undulator is split up into 12 modules, each of 4 m length (see Fig. 2.4.1.1). All modules have an undulator period of 15 mm and a nominal undulator parameter K of 1.2. The gap of the in-vacuum undulator is between 4 and 5 mm, to achieve the required field strength for the K parameter. The resulting wakefields for a 5 mm gap and a 2.7 kA current profile, obtained with start-to-end simulations, are shown in Figure 2.4.1.2 for aluminum and copper [28]. The expected wakefield gradient is about 50 keV/m at the core of the electron beam, which, firstly, lies within the acceptance bandwidth of the FEL at 1 Å, and secondly, can be efficiently compensated by a small taper along the undulator. The difference between aluminum and copper is miniscule.

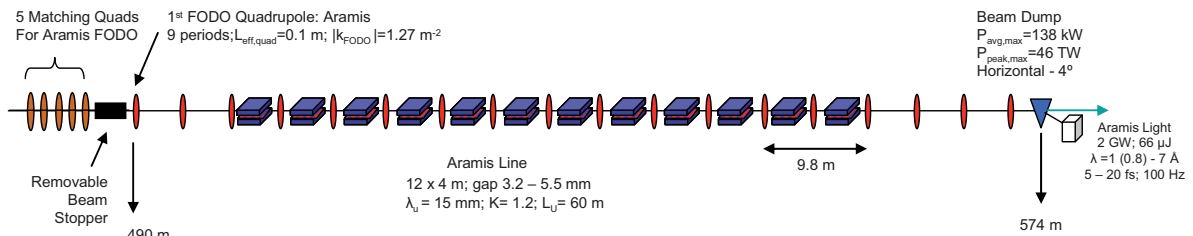


Fig. 2.4.1.1: Aramis Undulator line design

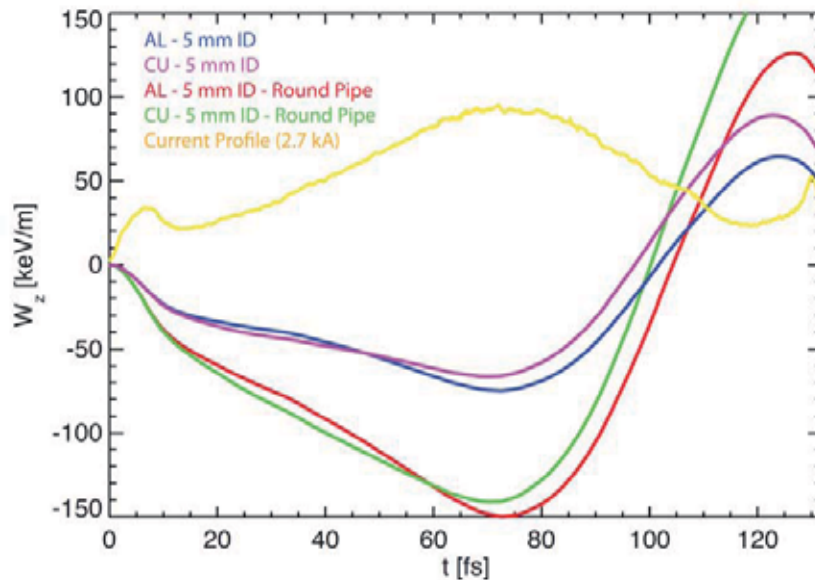


Fig. 2.4.1.2: Wake potential in the Aramis beamline for different vacuum chamber cross-sections and materials

The FEL performance of Aramis is listed in Table 2.4.1.1 and the temporal profile and spectrum at saturation for operation at 1 Å are shown in Figure 2.4.1.3. Those performances fulfill the design parameters requirements of Table 2.1.2. Results from start-to-end modelling show a better slice emittance than specifications, and thus a reduced saturation length of 30 m. However, in this case

the divergence and bandwidth is significantly larger – 2.2 μrad and 0.06 %, respectively. The latter arises from the residual energy chirp of the electron beam.

Table 2.4.1.1: Simulated performance of the Aramis hard X-ray beamline.

| Beam energy | 5.8 GeV | 2.2 GeV |
|----------------------------|----------------------|----------------------|
| Peak current | 2.7 kA | 2.7 kA |
| Charge | 200 pC | 200 pC |
| Energy spread | 350 keV | 350 keV |
| Emittance | 0.43 mm.mrad | 0.43 mm.mrad |
| Undulator period | 15 mm | 15 mm |
| Undulator parameter | 1.2 | 1.2 |
| Undulator module length | 4.00 m | 4.00 m |
| Undulator section length | 4.75 m | 4.75 m |
| Average β -function | 15 m | 15 m |
| Wavelength | 1 Å | 7 Å |
| Saturation length | 45 m | 21 m |
| Saturation pulse energy | 0.066 mJ | 0.063 mJ |
| Effective saturation power | 2.0 GW | 1.9 GW |
| Photons at saturation | $3.32 \cdot 10^{10}$ | $2.21 \cdot 10^{11}$ |
| Bandwidth | 0.034 % | 0.144 % |
| Pulse length | 13 fs | 13 fs |
| Beam radius | 22.2 μm | 37.9 μm |
| Beam divergence | 1.1 μrad | 5.7 μrad |

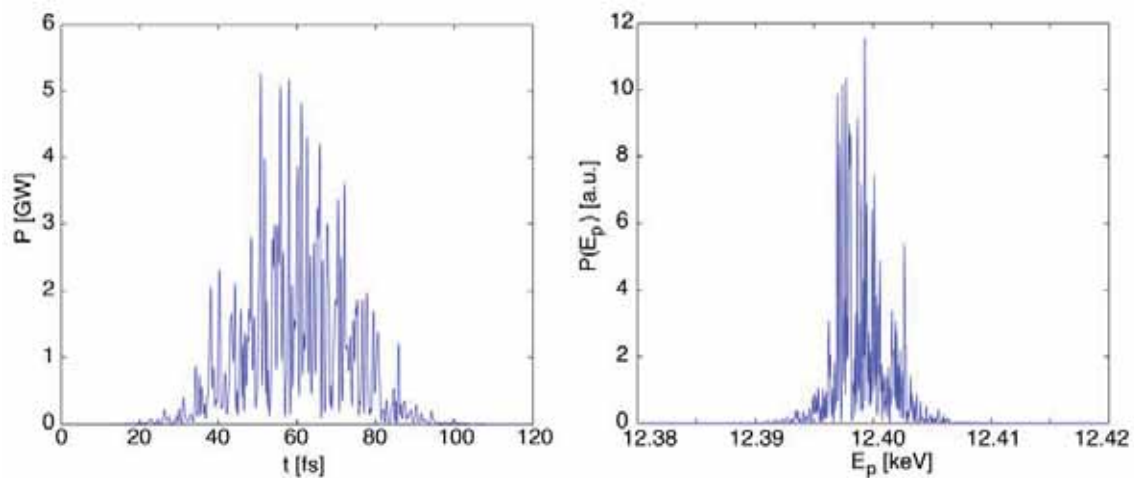


Fig. 2.4.1.3: Profile and spectrum at saturation for the Aramis beamline, tuned to 1 Å

2.4.2 Athos

To guarantee independent operation from the hard X-ray beamline, the soft X-ray beamline Athos is tuned by varying the undulator gap and thus the K-parameter. Spanning the range from 7 Å to 7 nm would require a range from 1 to 5.3 for the undulator parameter K. As a consequence, the undulator period would need to be at least 6 cm and the driving beam energy 4.2 GeV, which would result in a saturation length longer than the hard X-ray beam Aramis, tuned to 1 Å.

Therefore, Athos is operated with beam energies of either 2.1 GeV or 3.4 GeV, and a reduced tuning range of K between 1 and 3.2. In an APPLE II-type configuration with a period length of 4 cm, the minimum undulator gap is larger than 5 mm and thus sufficient to reduce the impact of

wakefields. The wavelength tuning range is about a factor of 4 for each electron beam energy, and there is some overlap in the intermediate wavelength range around 2 nm (see Table 2). Note that the minimum energy is given by the operation energy of the second bunch compressor; while an energy of 3.4 GeV and a K-value of 1 yield 7 Å, to connect with the wavelength range of the hard X-ray beamline.

Table 2.4.2.1: Performance of the Athos soft X-ray beamline without seeding

| Beam energy | 3.4 GeV | 3.4 GeV | 2.1 GeV | 2.1 GeV |
|----------------------------|---------------------|----------------------|---------------------|----------------------|
| Peak current | 2.7 kA | 2.7 kA | 2.7 kA | 2.7 kA |
| Charge | 200 pC | 200 pC | 200 pC | 200 pC |
| Energy spread | 350 keV | 350 keV | 350 keV | 350 keV |
| Emittance | 0.43 mm.mrad | 0.43 mm.mrad | 0.43 mm.mrad | 0.43 mm.mrad |
| Undulator period | 40 mm | 40 mm | 40 mm | 40 mm |
| Undulator parameter | 1.0 | 3.2 | 1 | 3.2 |
| Undulator module length | 4.0 m | 4.0 m | 4.0 m | 4.00 m |
| Undulator section length | 4.75 m | 4.75 m | 4.75 m | 4.75 m |
| Average β -function | 10 m | 10 m | 10 m | 10 m |
| Wavelength | 0.7 nm | 2.8 nm | 1.8 nm | 7 nm |
| Saturation length | 41.6 m (*) | 22.3 m | 29.7 m | 16.1 m |
| Saturation pulse energy | 0.12 mJ | 0.36 mJ | 0.10 mJ | 0.18 mJ |
| Effective saturation power | 4.4 GW | 11.2 GW | 3.2 GW | 6.5 GW |
| Photons at saturation | $4.2 \cdot 10^{11}$ | $5.0 \cdot 10^{12}$ | $8.7 \cdot 10^{11}$ | $6.5 \cdot 10^{12}$ |
| Bandwidth | 0.15 % | 0.19% | 0.17 % | 0.25 % |
| Pulse length | 11.1 fs | 12.9 fs | 12.0 fs | 11.0 fs |
| Beam radius | 33.4 μm | 40.1 μm | 45.9 μm | 56.1 μm |
| Beam divergence | 4.1 μrad | 15.0 μrad | 8.3 μrad | 30.9 μrad |

* The saturation length for the shortest wavelength is longer than the planned length of 30 m for the Athos undulator. However, the missing length can be compensated for by using the preceding undulator d'Artagnan as a SASE device, tuned to the 4th or 5th harmonic of the wavelength in Athos, and a harmonic conversion [29], [12]. This enhances the shot-noise power at the short wavelength and less undulator length is needed to reach saturation.

2.4.3 D'Artagnan and Seeding

To improve the longitudinal coherence in the soft X-ray regime, the undulator beamline Athos is seeded with an external, coherent signal. However, there is no suitable seeding source directly at 1 nm, and thus one single-stage of High Gain Harmonic Generation [30] is used to shift the seeding requirement to a longer wavelength. The undulator d'Artagnan is tuned to a longer wavelength range, with its longer period of 6 cm and large K-value of up to 5. The 4 modules of d'Artagnan have a length of 4 m, with spacing of 75 cm between.

Because the bunch length of the electron beam is short and a narrow bandwidth of the FEL signal is desired, no fresh bunch technique [31] can be used. For the harmonic conversion from d'Artagnan to Athos, a small chicane is needed, providing an R_{56} up to 5 microns. The operation modes are listed in Table 2.4.3.1.

Table 2.4.3.1: Tuning range of the soft X-ray beamline for HGHG operation

| Energy | d'Artagnan | Athos (n=2) | Athos (n=3) | Athos (n=4) | Athos (n=5) |
|---------|------------|--------------|--------------|--------------|-------------|
| 2.1 GeV | 7 - 14 nm | 3.5 - 7 nm | 2.4 - 3.5 nm | 1.8 - 2.4 nm | - |
| 3.4 GeV | 5 - 9 nm | 2.5 - 2.8 nm | 1.7 - 2.5 nm | 1.3 - 1.7 nm | 1 - 1.3 nm |

The Table indicates the wavelengths which can be reached with the smallest harmonic conversion, and thus the highest efficiency. Although d'Artagnan can be tuned down to 2.8 nm at 3.4 GeV, we assume that no suitable laser source will exist below 5 nm at the time of realization of the seeding beamline. If development is more rapid, operation at even shorter wavelength (down to 2.8 nm) would significantly improve performance. On the other hand, if there is no seed below 10 nm available, the fall-back solution is to utilize the parasitically emitted 3rd harmonics in Athos [32] to reach 1 nm. For that, Athos would be tuned to 3 nm and d'Artagnan either to 9 nm or 12 nm.

D'Artagnan is seeded either with an external radiation field or a coherent current modulation. The most promising candidate for a seeding radiation field is High Harmonic Generation [33] in noble gases. To overcome the intrinsic shot noise [34] which is present in all electron beams, the minimum requirement is an effective seeding power of about 100 kW at 12 nm, or 300 kW at 5 nm, corresponding to 5 nJ or 15 nJ at the corresponding harmonic of the HHG seed for a 20 fs long pulse, which barely covers the electron pulse and thus is extremely sensitive to beam arrival time jitter.

The profile and spectrum of the FEL output of Athos at 3 nm and 2.1 GeV are shown in Figure 2.4.3.1. The impact of shot noise is still noticeable with a seed power of 100 kW at 12 nm. Nevertheless, the bandwidth is reduced from 0.5% in SASE operation to 0.08 % when seeded.

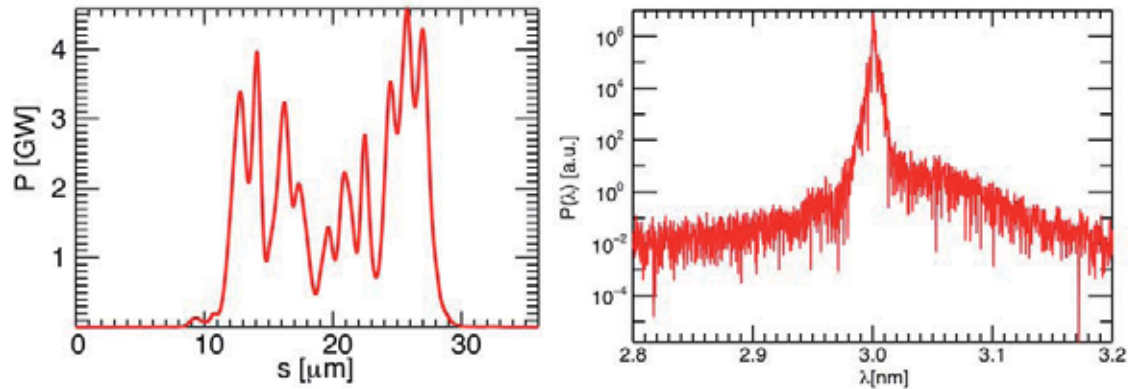


Fig. 2.4.3.1: Profile and spectrum of the Athos beamline at 3 nm, when seeded with an HHG seed.

An alternative, and much more promising, seeding scheme is echo-enabled harmonic generation [35], inducing coherent current modulation in the electron bunch. For this, the electron beam is modulated in energy at a longer wavelength and then injected into a magnetic chicane twice. With the right set of values of the chicanes, a harmonic of the modulating laser can be generated with a maximum efficiency in current bunching of $(38/n^{1/3})\%$. With the 4th harmonic of a Ti:Sapphire laser at about 260 nm, and selecting the 52nd harmonic, bunching of 10% can be achieved, which is significantly above the shot-noise bunching of the electron beam. The configuration of the seeding beamline is shown in Table 2.4.3.2, when tuned to 5 nm at 3.4 GeV.

Table 2.4.3.2: Configuration of the EE-HG seeding beamline D'Artagnan, when operated at 5 nm and 3.4 GeV;

| | First Section | Second Section |
|----------------------|---------------|----------------|
| Modulator wavelength | 260 nm | 260 nm |
| Modulator period | 20 cm | 20 cm |
| Modulator K-value | 15.1 | 15.1 |
| Modulator length | 4 m | 4 m |
| Seed power | 100 MW | 16 MW |
| Chicane R_{56} | 12 mm | 0.21 mm |

Note that this is the initial design, which can be improved significantly to reduce the length of the undulators and the strength of the chicane. Such improvements would minimize the impact of detrimental effects, such as the increase in energy spread due to emission of hard photons in the spectrum of the incoherent synchrotron radiation and the impact of R_{51} and R_{52} in the chicanes. The optimization of the seeding method is currently under study. The performance of d'Artagnan and Athos is shown in Figure 2.4.3.2.

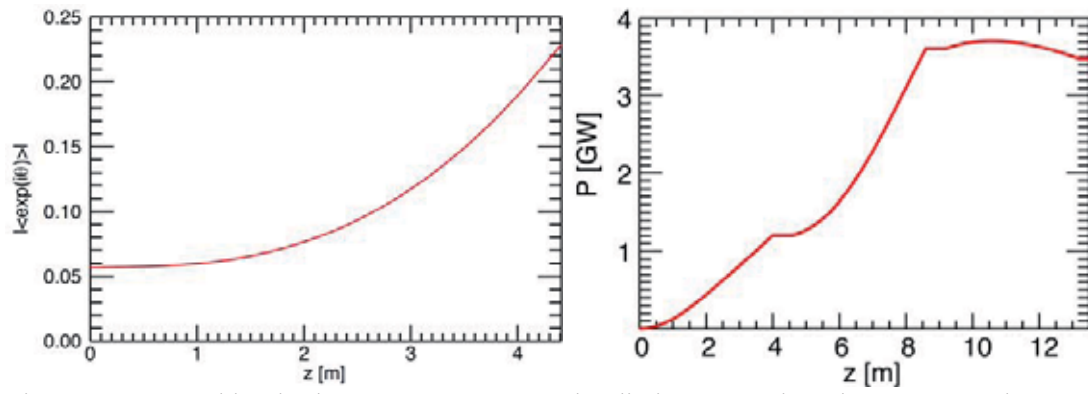


Fig. 2.4.3.2: Bunching in d'Artagnan at 5 nm and radiation power in Athos at 1 nm when seeded with EE-HG

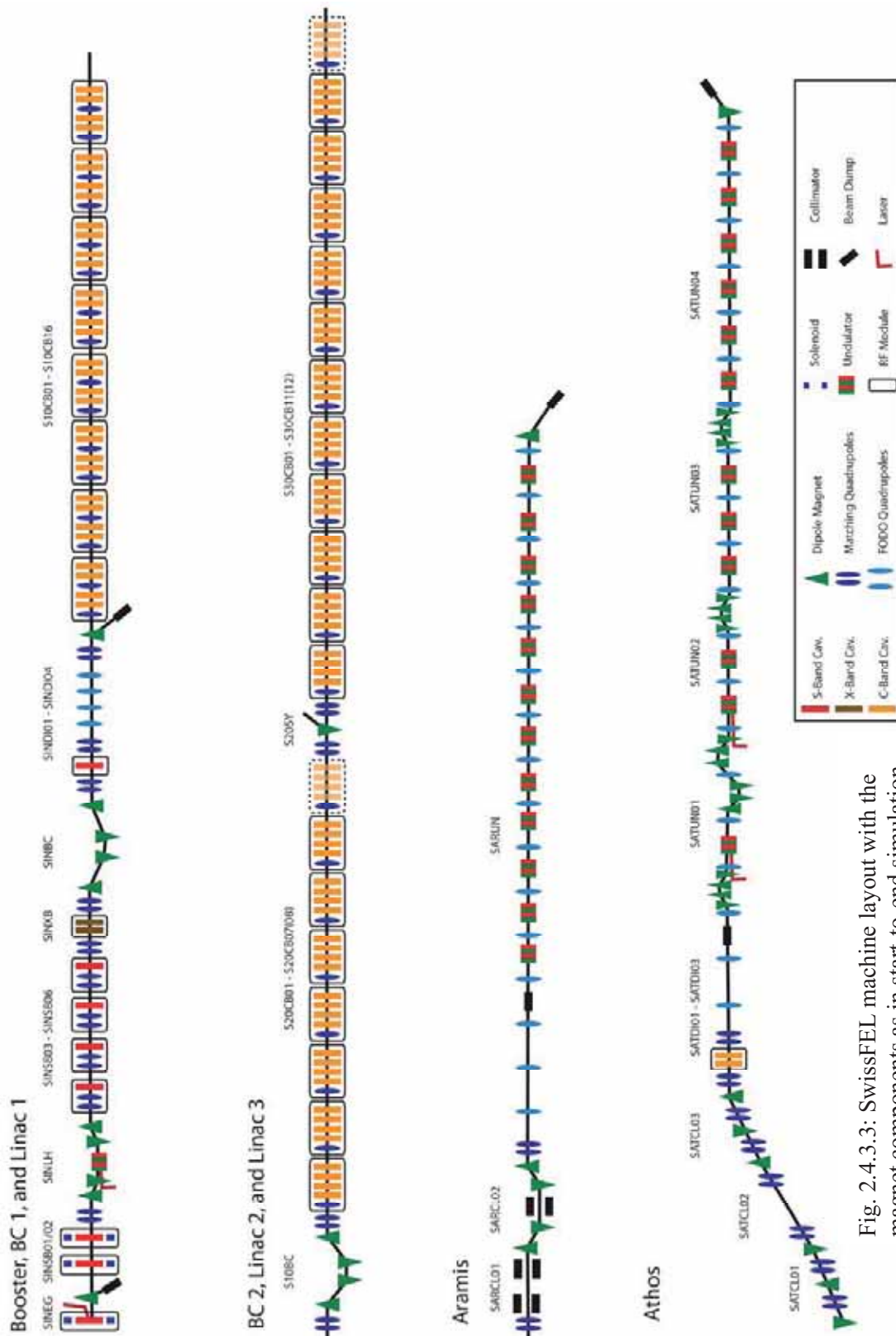


Fig. 2.4.3.3: SwissFEL machine layout with the magnet components as in start-to-end simulation.

2.4.4 Sensitivity and tolerance study for the bunch compression layout

An important factor for user facilities is the stability of the photon pulses leaving the undulator toward the user stations. Shot-to-shot jitter, as well as long-term drifts of machine parameters, such as RF phases and amplitudes, will affect the total FEL performance.

Long-term drifts induced by temperature changes can be compensated for by slow feedback systems. The main concerns regarding performance are shot-to-shot fluctuations of various subsystems. The downstream performance depends on the stability of certain subsystems. This dependence or **sensitivity** can be fitted with a first-order approximation. The sensitivities give a measure of bunch parameter variations, such as peak current, when changes occur in an upstream machine parameter. More details on the beam longitudinal tolerances can be found in a PSI note: FEL-BB84-001 [36].

The stability goals of the machine can be divided by the corresponding sensitivity to obtain the allowed deviation from the design parameter (jitter budget), assuming this is the only deviating property.

The sensitivities are obtained by a series of tracking runs from the electron gun to the undulator entrance. A set of parameters such as the magnet strength in BC 1 or the RF phase offsets are varied in a certain interval around the nominal settings. The resulting beam parameters at the undulator are then evaluated as a function of the individual deviated parameter. The linear terms of polynomial fits to these dependencies are used as the sensitivities. Since the tightest tolerances are expected from the hard X-ray line, only the performance goals of the Aramis undulator are being studied in detail.

The sensitivities are used to determine the tolerances. The required performance at the undulator is divided by the corresponding sensitivity to obtain the allowed deviation (tolerances) of a single jitter source to cause the allowed error, assuming all other error sources to be stable. Since some components are driven by uncorrelated jitter sources, such as for the linac RF stations, one can take the square root of the number of independent sources (4 klystrons for the S-band linac, 8 klystrons for the C-band linac 1, and 18 sources for C-band linac 2).

The jitter budget at the undulator entrance is determined from the SASE dynamics. Intrinsic fluctuations of the FEL process can be used to define the tightest tolerances. It will not improve machine performance to stabilize the beam on a level below these intrinsic fluctuations. This defines the level of allowed peak current fluctuations to 5%, which is the result of a series of Genesis runs. Beam arrival time is assumed to be on the order of the photon pulse length. A jitter of 0.05% in the mean energy would keep the resonant condition within the FEL bandwidth. Table 2.4.4.1 and Table 2.4.4.2 gives a summary of these tolerances for the different operation regime of SwissFEL. FEL light users might accept larger FEL jitter, which would relax the given beam tolerances by the same factor.

Table 2.4.4.1: Tolerances to ensure that FEL beam fluctuations stay within intrinsic fluctuations (Tightest Tolerances). For each electron bunch property at the undulator entrance (columns), there is a corresponding tolerance budget for every linac component (lines). The tightest tolerance are marked in each line. For example: To get 5 % peak current stability, the C-band linac 1 phase should be stable within 0.3 degree rms. This tolerance corresponds to the **200 pC nominal** operation mode.

| Beam goals Parameters requirements | arrival time 20 fs | peak current 5 % | energy 0.05 % |
|---------------------------------------|--------------------|------------------|---------------|
| S-Band Phase [deg] | 0.19 | 0.23 | 0.32 |
| S-Band Voltage [%] | 0.1 | 0.026 | 0.11 |
| X-Band Phase [deg] | 30 | 0.061 | 0.86 |
| X-Band Voltage [%] | 0.5 | 0.17 | 0.58 |
| Linac 1 Phase [deg] | 0.15 | 0.084 | 0.43 |
| Linac 1 Voltage [%] | 0.1 | 0.4 | 0.4 |
| Linac 2 Phase [deg] | 5200 | 1600 | 2200 |
| Linac 2 Voltage [%] | 15. | 87 | 0.5 |
| Linac 3 Phase [deg] | 4600 | 1800 | 2900 |
| Linac 3 Voltage [%] | 12. | 19 | 0.4 |
| Charge [pC] | 19 | 1.9 | 47 |
| Initial arrival time [fs] | 620 | 68 | 2900 |
| Initial Energy [%] | 0.097 | 0.031 | 0.11 |
| BC1 angle [%] | 5.2 | 0.11 | 1.4 |
| BC2 angle [%] | 19 | 0.11 | 1.5 |

One remark to the laser arrival time at the laser heater: ASTRA calculations show that an arrival time jitter of the laser on the cathode of 1 fs will result in an arrival time jitter of 0.81 fs at the laser heater. Therefore the value of 68 fs from Table 2.4.4.2 corresponds to a 80 fs allowed laser timing jitter on the cathode.

Table 2.4.4.2: Tolerances to ensure that FEL beam fluctuations stay within intrinsic fluctuations (Tightest Tolerances). For each electron bunch property at the undulator entrance (columns), there is a corresponding tolerance budget for every linac component (lines). The tightest tolerance are marked in each line. For example: To get 5 % peak current stability, the C-band linac 1 phase should be stable within 0.3 degree rms. This tolerance corresponds to the **10 pC nominal** operation mode.

| Beam goals Parameters requirements | arrival time 20 fs | peak current 5 % | energy 0.05 % |
|---------------------------------------|--------------------|------------------|---------------|
| S-Band Phase [deg] | 0.03 | 0.11 | 0.54 |
| S-Band Voltage [%] | 0.018 | 0.019 | 0.19 |
| X-Band Phase [deg] | >10 | 0.044 | 1.5 |
| X-Band Voltage [%] | 0.081 | 0.17 | 0.95 |
| Linac 1 Phase [deg] | 0.045 | 0.098 | 0.74 |
| Linac 1 Voltage [%] | 0.024 | 0.4 | 0.5 |
| Linac 2 Phase [deg] | >10 | >10 | >10 |
| Linac 2 Voltage [%] | 0.38 | 13 | 0.52 |
| Linac 3 Phase [deg] | >10 | >10 | >10 |
| Linac 3 Voltage [%] | 0.29 | 15 | 0.4 |
| Charge [pC] | 3.4 | 0.47 | >10 |
| Initial arrival time [fs] | 1100 | 44 | 980 |
| Initial Energy [%] | 0.02 | 0.039 | 0.23 |
| BC1 angle [%] | >0.01 | 0.069 | 2.2 |
| BC2 angle [%] | >0.01 | 0.11 | 3.5 |

Finally, to estimate the expected stability of the electron beam at Aramis, the expected stabilities of the subsystems are multiplied by the sensitivities and the square root of the number of independent sources. In this way, the contribution of each source to the final jitter is calculated. We assume uncorrelated jitter between the different sources, and therefore the total jitter is determined as their quadratic sum. A summary of these numbers is given in Table 2.4.4.3.

Table 2.4.4.3: Electron beam jitter (200 pC nominal mode) at Aramis entrance, assuming some expected jitter sources, as listed in the second column for different linac parameters. The last line is the total jitter of the linac. Critical contributions to the total jitter are shown in red.

| Beam Jitter | arrival time [fs] | peak current [%] | energy [%] |
|--|-------------------|-------------------|---------------------|
| Expected Parameter Jitter | | | |
| For 0.015 deg S-Band Phase jitter: | 1.8 | 0.2 | 0.002 |
| For 0.012 % S-Band Voltage jitter: | 2.2 | 2.1 | 0.006 |
| For 0.06 deg X-Band Phase jitter: | 0.1 | 4.9 | 0.003 |
| For 0.012 % X-Band Voltage jitter: | 0.2 | 0.2 | 0.0015 |
| For 0.03 deg Linac 1 Phase jitter: | 4 | 1.8 | 0.003 |
| For 0.012 % Linac 1 Voltage jitter: | 2.2 | 0.1 | $2 \cdot 10^{-3}$ |
| For 0.03 deg Linac 2 Phase jitter: | 0.007 | 0.001 | $5 \cdot 10^{-4}$ |
| For 0.012 % Linac 2 Voltage jitter: | 0.015 | $4 \cdot 10^{-3}$ | $1.5 \cdot 10^{-3}$ |
| For 0.03 deg Linac 3 Phase jitter: | $9 \cdot 10^{-3}$ | $9 \cdot 10^{-4}$ | $2 \cdot 10^{-4}$ |
| For 0.012 % Linac 3 Voltage jitter: | 0.02 | $3 \cdot 10^{-4}$ | $2 \cdot 10^{-3}$ |
| For 2 pC Charge jitter: | 2. | 5.5 | $2 \cdot 10^{-3}$ |
| For 30 fs initial arrival time jitter: | 1.1 | 2.1 | $7 \cdot 10^{-4}$ |
| For 0.01 % Initial Energy jitter: | 2 | 1.8 | $4.5 \cdot 10^{-3}$ |
| For 0.001 % BC1 angle jitter: | 0.034 | 0.1 | $5 \cdot 10^{-4}$ |
| For 0.001 % BC2 angle jitter: | $4 \cdot 10^{-4}$ | 0.1 | $5 \cdot 10^{-4}$ |
| total (rms) | 6.1 | 8.1 | $9 \cdot 10^{-3}$ |

Table 2.4.4.4: Electron beam jitter (10 pC nominal mode) at Aramis entrance, assuming some expected jitter sources, as listed in the second column for different linac parameters. The last line is the total jitter of the linac. Critical contributions to the total jitter are shown in red.

| Beam Jitter | arrival time [fs] | peak current [%] | energy [%] |
|--|-------------------|-------------------|---------------------|
| Expected Parameter Jitter | | | |
| For 0.015 deg S-Band Phase jitter: | 2.1 | 2 | 0.0018 |
| For 0.012 % S-Band Voltage jitter: | 3.2 | 9 | 0.0035 |
| For 0.06 deg X-Band Phase jitter: | 0.05 | 20.5 | 0.002 |
| For 0.012 % X-Band Voltage jitter: | 0.8 | 1.5 | 0.0008 |
| For 0.03 deg Linac 1 Phase jitter: | 3.4 | 5 | 0.002 |
| For 0.012 % Linac 1 Voltage jitter: | 2.2 | 1 | $1.6 \cdot 10^{-3}$ |
| For 0.03 deg Linac 2 Phase jitter: | 0.05 | 0.001 | $5 \cdot 10^{-4}$ |
| For 0.012 % Linac 2 Voltage jitter: | 0.015 | $4 \cdot 10^{-3}$ | $1.8 \cdot 10^{-3}$ |
| For 0.03 deg Linac 3 Phase jitter: | $9 \cdot 10^{-3}$ | $9 \cdot 10^{-4}$ | $2 \cdot 10^{-4}$ |
| For 0.012 % Linac 3 Voltage jitter: | 0.02 | $3 \cdot 10^{-4}$ | $1.8 \cdot 10^{-3}$ |
| For 0.1 pC Charge jitter: | 0.1 | 5.5 | $2 \cdot 10^{-4}$ |
| For 30 fs initial arrival time jitter: | 0.1 | 10 | $1.8 \cdot 10^{-3}$ |
| For 0.01 % Initial Energy jitter: | 2.2 | 4 | $2.1 \cdot 10^{-3}$ |
| For 0.001 % BC1 angle jitter: | 0.034 | 1.5 | $5 \cdot 10^{-4}$ |
| For 0.001 % BC2 angle jitter: | $4 \cdot 10^{-4}$ | 1 | $5 \cdot 10^{-4}$ |
| total (rms) | 6.1 | 27 | $5.9 \cdot 10^{-3}$ |

From the numbers presented in Tables 2.4.4.1 and 2.4.4.4, the most critical components in terms of stability requirements can be identified. In this design, it is obvious that the RF phase offsets in the S- and X-band systems upstream of the first bunch compressor chicane are the critical parts.

2.4.5 Sensitivity of FEL performance

Any disruption of the FEL process may be a combination of two effects: reduction in the transverse overlap and longitudinal synchronization between the electron beam and radiation field. These are caused by multiple error sources, such as quadrupole misalignment, detuning of undulator modules or injection errors. The hard X-ray beam Aramis at 1 Å requires the best alignment of the system, and is the point of operation which defines the sensitivity/tolerances of the SwissFEL. At longer wavelengths, in the soft X-ray beamline Athos, the sensitivity is reduced and the tolerances are more relaxed. The results of the sensitivity study are listed Table 2.4.5.1.

Table 2.4.5.1: Sensitivities of the Aramis beamline at 1 Å

| Error | RMS Sensitivity |
|---|----------------------|
| Undulator module K detuning | 0.073 % |
| Undulator vertical misalignment | 83 μm |
| Quadrupole (between undulators) field errors | 21 % |
| Quadrupole (between undulators) transverse misalignment | 4.6 μm |
| Injection offset between electron beam and undulator axis | 11.7 μm |
| Injection angle between electron beam and undulator axis | 0.78 μrad |
| Mismatch β/β_0 | 1.42 |

Note that the sensitivity corresponds to a drop by 40% in the power of the FEL at the point of saturation for the undisturbed FEL performance. The tolerance budget is the combined effect of weighted sensitivities to limit the increase in the saturation length by less than 2 m. Also, some of the sensitivities, such as mismatch or injection errors, are the results of the combined errors in the injector and linac itself.

For the seeding option of the Athos beamline, additional sensitivities are apparent; mainly the arrival time jitter and the energy jitter of the electron beam. However, the explicit seeding scheme has not yet been fully designed and optimized.

2.5 Photon beamline layout

2.5.1 Introduction

The photon beamline transports the X-rays from the undulator to the experimental station. The position of the first mirror is the key parameter for defining the space requirements for the optics and the experiment positions. The mirror acts as a filter to remove unwanted radiation, such as higher harmonics, bremsstrahlung, etc, from the X-ray free electron laser (XFEL) pulse and selects which experiments will be illuminated. The mirror must not be damaged by the intense laser pulses, and so the deposited energy has to stay well below the ablation threshold. To define space requirements, we have considered two candidate beamlines: (a) a high-flux beamline which maintains the time structure of the XFEL and simply focuses the pulses to the sample, and (b) a plane-grating monochromator beamline with 1:1 focusing for narrow spectral bandwidth.

2.5.2 Ablation and single-shot damage

A central problem at storage rings such as the Swiss Light Source (SLS) is the high heat load density, typically 1 W/mm². In contrast to this, the heat load problem at the SwissFEL is negligible (< 1 mW/mm²), but ablation is the major concern. There is no comprehensive theory or experimental data for comparable hard X-ray FELs available to date. To approach the problem, we take into account results from single-shot and multiple-shot damage experiments at FLASH [37-40], make reasonable assumptions for boundary conditions and compare the results with known quantities, to judge the feasibility. We assume 50 m distance between the end of the undulator and the first mirror. This length is at the lower limit of other comparable XFEL projects [41,42] and should be reserved anyway, to put in additional equipment, such as gas filters, diagnostics etc, which are not yet defined in detail. We assume typical grazing angles of 1 to 4 mrad for hard X-rays and 20 to 50 mrad (1 to 3 deg.) for soft X-rays, as a consequence of the X-ray reflectivity. To avoid ablation, the radiation dose must be significantly less than the dose for melting, which is of the order ≈ 1 eV/atom. With candidate materials such as C, SiC or B₄C for the coating of the first optical elements, and the grazing angles given above, we estimate a corresponding damage threshold for the fluence on the order of 1 mJ/mm².¹ It is important to note that the obvious approach to reducing the fluence by reducing the grazing angle (to spread the energy over a bigger

area) does not necessarily reduce the energy density per atom, i.e. per volume, since the penetration depth for X-rays decreases for small grazing angles. This is the reason for preferring light elements, with greater penetration depth, as coating materials.

Table 1 summarizes the relevant machine parameters and the resulting thresholds for SwissFEL in comparison with other XFEL projects. We emphasize the maximum fluence in normal incidence as the important value for the comparison. This value has to be multiplied by the grazing angle to obtain the fluence at the optical surface². In conclusion, all FEL's keep the maximum fluence at the optical surface $\ll 1 \text{ mJ/mm}^2$, which means a 50 m distance between undulator and optics is reasonable and gives some security margin.

Note 1: In other words, ablation will be observed with a dose of $\sim 1 \text{ eV / atom}$ or fluence of $\sim 1 \text{ mJ/mm}^2$

Note 2: Alternatively, the fluence limit is inversely proportional to the grazing incidence angle; that is to say, for $\alpha = 1.3$ to 4 mrad , the fluence limit (1 mJ/mm^2) is reduced by a factor of 770 to 250.

Table 2.5.1: Comparison of relevant machine parameters and deduced damage thresholds for the optics of SwissFEL and other hard X-ray XFELs. The parameters always reflect the worst case. Aramis: SwissFEL hard X-ray undulator, SASE2: European XFEL in Hamburg, LCLS: Stanford, SCSS: Japan

| FEL | | Aramis | SASE2 | LCLS | SCSS |
|---|---------------------------------|--------|-------|------|------|
| Photon energy | (keV) | 12.4 | 12.4 | 8.3 | 12.4 |
| Pulse energy | (mJ) | 0.06 | 2 | 2.5 | 1.5 |
| Beam size | ($\mu\text{m rms}$) | 22 | 36 | 30 | 50 |
| Beam divergence | ($\mu\text{rad rms}$) | 0.95 | 0.35 | 0.42 | 0.4 |
| Position of first mirror | (m) | 50 | 500* | 100 | 100 |
| Beam size @ 1 st mirror | ($\mu\text{m rms}$) | 52 | 178 | 51 | 64 |
| Max. fluence @ 1 st mirror ** | (mJ / mm^2) | 3.5 | 10 | 153 | 62.5 |
| Max. fluence @ 1 st mirror *** | ($\mu\text{J} / \text{mm}^2$) | 7 | 20 | 306 | 125 |

* approximation or assumption

** normal incidence

*** grazing angle: 2 mrad

2.5.3 Conceptual beamline layout

The conceptual beamline layout defines the space requirements and gives a feasible layout for the optical system and the experiments. The key input parameters are the position of the first mirror s_1 and the possible grazing angles from the previous section. In addition, we assume a 1:1 focusing with the first mirror, to minimize aberrations, and reserve about the same length for refocusing and experiments, i.e. the total beamline length is $s = 3 \times s_1$. With $s_1 = 50 \text{ m}$, the beamline length is about 150 m. Each undulator shall serve 3 experiments in separate hutches, to allow access for installation and maintenance etc, while another experiment receives beam. For each experimental hutch, we reserve an area of about $100 \text{ m}^2 \approx 7 \text{ m} \times 15 \text{ m}$. The achievable transverse separation with mirrors is small, due to the possible grazing angles, in particular for hard X-rays. Therefore, the experiments have to be arranged more or less in a row. We considered two candidate layouts for beamlines. First, the high-flux beamline type shown in Figure 2.5.1 takes direct advantage of the unique properties of the FEL radiation. The minimum number of optical elements preserves the transverse coherence of the radiation and does not lengthen the pulses. The beamline consists of the flat mirror 50 m downstream of the undulator and a strong focusing system directly upstream of the experiment. The Figure assumes a 100:1 focusing with an ellipsoidal mirror. Alternatively, one can use a KB [43] system with plane elliptical mirrors, or even retract the mirror(s) for direct unfocused FEL radiation. The second type is a monochromator beamline, as shown in Figure 2.5.2. We choose a plane grating monochromator (PGM) beamline in collimated light, similar to the successful beamlines at SLS [44] but scaled to FEL dimensions.

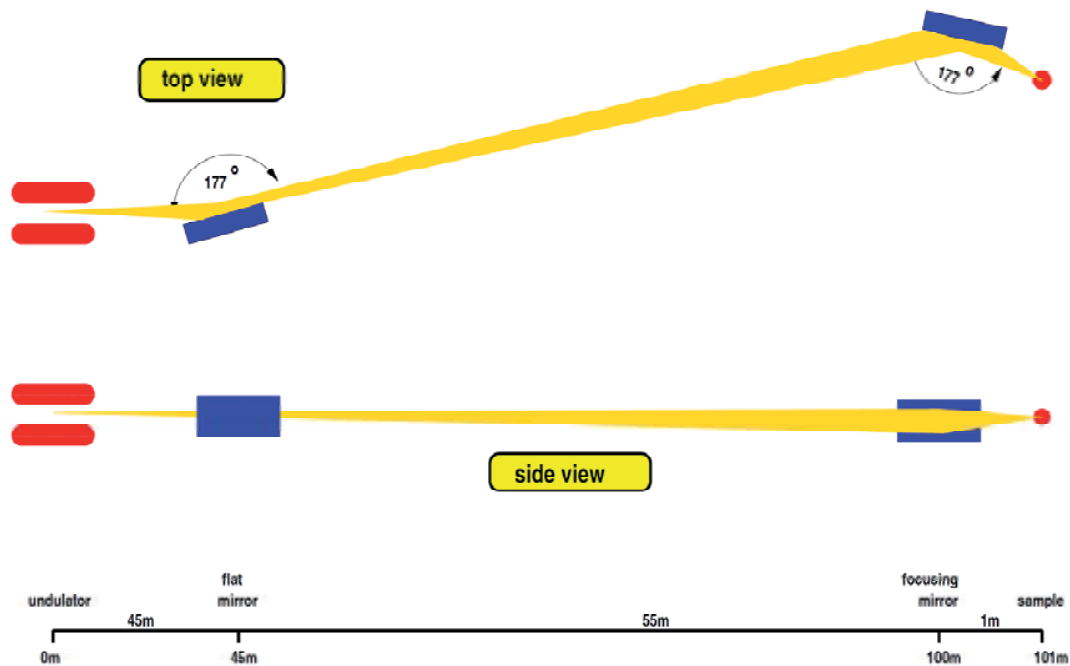


Fig. 2.5.1: Conceptual layout for a high-flux beamline for soft X-rays. A hard X-ray beamline can be built identically, but with other angles.

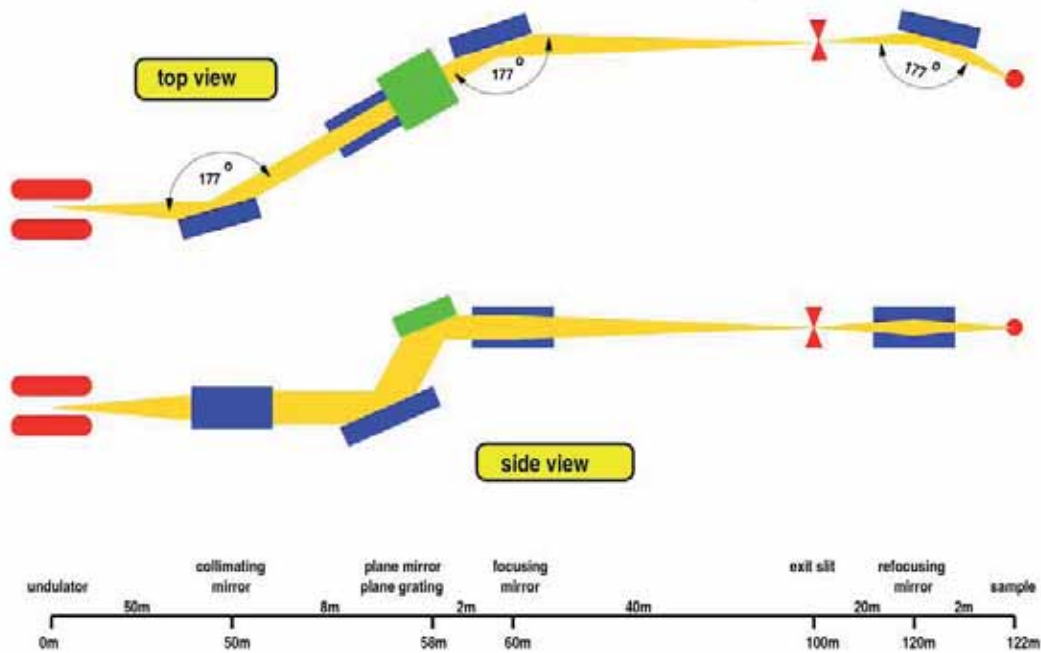


Fig. 2.5.2: Conceptual layout for a soft X-ray monochromator beamline for narrow bandwidth.

Monochromator beamlines are required if the spectral bandwidth of the undulator is not sufficient for the experiment. A monochromator increases, of course, the number of optical elements which may influence the coherence properties or extend the length of the pulses. The acceptable pulse length extension can be, to some extent, traded with the resolving power by different operation modes of the PGM (variable grating orientation, gratings with different line density). A feasible floor layout is shown in Figure 2.5.3. This shows the end of the undulators, the beam distribution

system and the layout of the experimental area. The hard X-ray branch is on top and bounces the beam to the left, while the soft X-ray branch is on the right. The chosen layout with the experiments (almost in one line) minimizes the volume of the experimental hall.

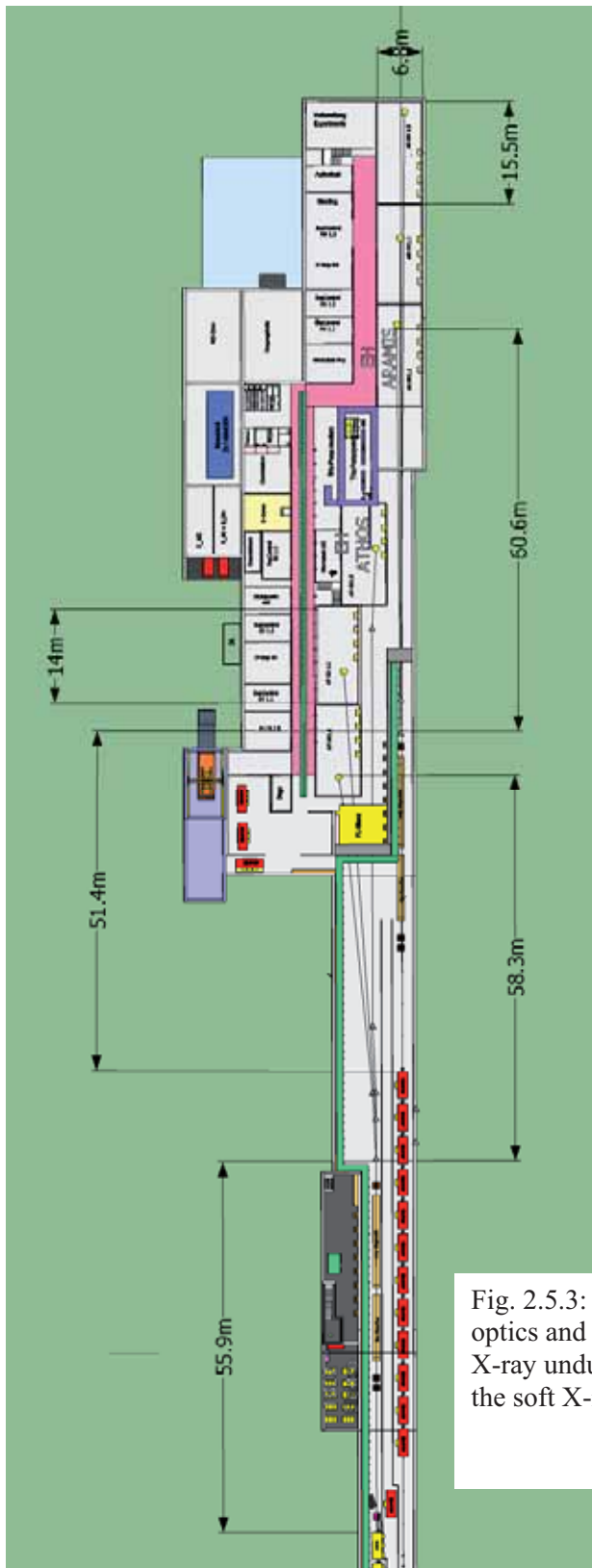


Fig. 2.5.3: Floor layout for X-ray optics and experiments. The hard X-ray undulator is coloured red, the soft X-ray undulator yellow.

2.6 THz pump source at the SwissFEL

This chapter describes the design considerations for a powerful THz source called FLUTE considered for THz pump / X-ray probe experiments at the SwissFEL Athos beamline (see Fig. 2.6.1). The source should deliver half-cycle pulses of less than 1 ps duration, with a pulse energy of 100 μJ in a focal region of 1 mm^2 . More details on the FLUTE THz source can be found in [45]

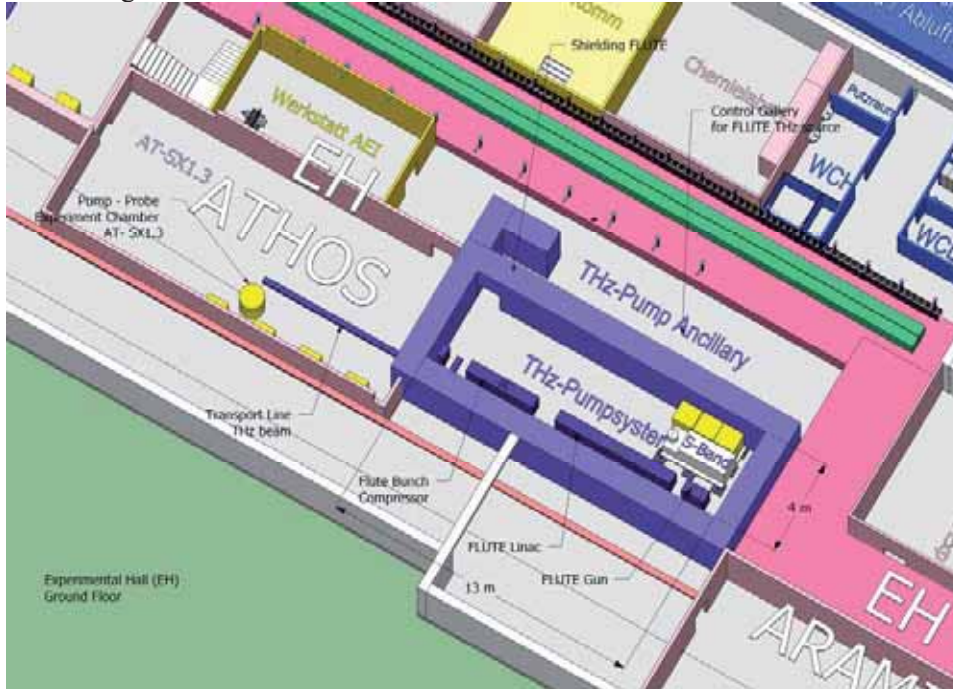


Figure 2.6.1: Layout of the THz linac bunker beside the Athos experimental hutch AT-SX1.3

2.6.1 Motivation

The design of SwissFEL foresees a separate source of THz radiation, delivering high-energy electromagnetic pump pulses of THz bandwidth which are synchronized to the sub-ps X-ray probe pulses of SwissFEL Athos beamline. The combination of THz pump and X-ray probe pulses permits real-time investigations of ultrafast magnetic interactions, as well as exploring non-ionizing heating phenomena and catalytic processes at the nm scale [3].

In order to allow such experiments to be performed, the THz pump source at SwissFEL has to fulfil the following specifications:

- A photon beam with a **pulse energy of 100 μJ and more, focused down to 1 mm^2** , allowing localized heating of materials faster than the relaxation time (i.e. without heat expansion). The achieved electric field strength would be $\sim 10^8$ V/m and can be used to displace atoms in polar solids, to probe structural phase transitions, ferroelectricity, etc. The magnetic field is of the order of 1 T, which allows the creation of magnetic / spin excitations and the following of magnetization dynamics on a ps time-scale.
- A **half-cycle pulse with a duration of less than 1 ps** provides unidirectional electromagnetic fields that create unidirectional surface distortion or polarization, opening up, for example, exciting possibilities for the detailed study of catalytic processes.
- Experiments require the arrival of the **THz pump pulse up to 1 ns prior to the X-ray probe pulse**. This is hard to realize by deriving the THz pump pulse from the FEL drive beam. Generating the THz pump signal independently from the X-ray probe signal by means of a separated THz source is therefore preferred, and has the additional advantage that a very compact THz source (in particular, also tunable by the users) with high electron-bunch charge (compared to the ≤ 200 pC of the FEL drive beam) can be built.

2.6.2 Basic considerations

When passing an electron beam with the proper beam parameters through a bending magnet, synchrotron radiation (SR) in the THz range can be produced. A sketch of such a SR spectrum is shown in Figure 2.6.2.

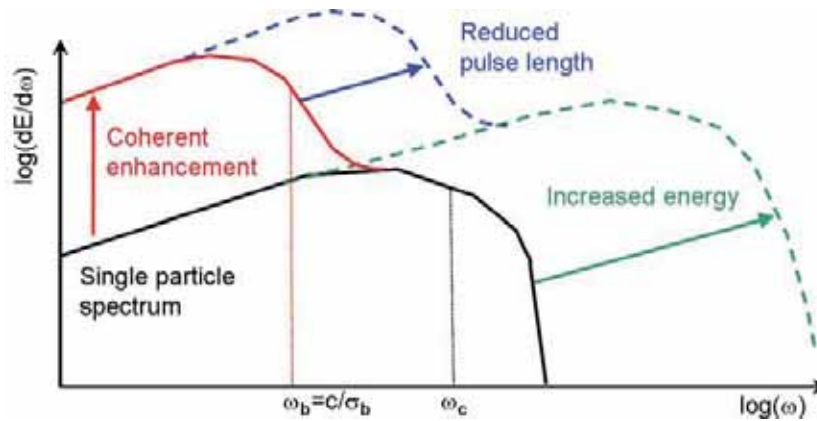


Fig. 2.6.2: Sketch of the synchrotron radiation spectrum.

Compared to transition radiation (TR), SR has the advantage of well-defined polarization, though its single-particle emission is less efficient at long wavelength than TR. For single-particle emission, the cut-off in the spectrum is given by¹ $\omega_c = 3c \gamma^3 / r_{bend}$, the maximum amplitude is proportional to the electron beam energy and the emitted power for $\omega \ll \omega_c$ is independent of the electron beam energy. For short bunches (i.e. bunch length smaller than the wavelength of observation), multiparticle coherent enhancement occurs. The most promising approach is therefore coherent emission from a relativistic electron beam, where the radiation process in the forward direction can be described by

$$P_{total}(\omega) = P_e(\omega) \cdot |F(\omega)|^2 \cdot N^2$$

with the single-particle emission spectrum $P_e(\omega)$, the form factor F , which is the Fourier transform of the longitudinal bunch profile, and N , the number of electrons in the bunch. When considering the three terms of the equation, the radiation process can be maximized by:

- (i) Using a particle energy high enough to guarantee that $P_e(\omega)$ is broader than the width of the form factor F ;
- (ii) Reducing the bunch length such that the bunch emits coherently in the THz range ($F \sim 1$ for coherent emission, while $\langle |F(\omega)|^2 \rangle = 1/N$ for incoherent emission);
- (iii) Increasing N , i.e. the bunch charge Q .

2.6.3 Design parameters

The FLUTE THz source presented in this report can fulfill the requirements of experiments as described in chapter 1 and [3]. The main parameters of the THz light delivered by the FLUTE source are given in Table 2.6.1. The characteristic of FLUTE which makes it different from other facilities is the high electron bunch charge (up to 5 nC) that will be used. Such high electron bunch charge leads to a high flux of THz photons of up to 1 mJ integrated over the whole spectrum from 0.1 to 10 THz. This unique flux of THz photons will allow the different experiments presented in chapter 1. Such high amount of photons does not only allow to reach high electromagnetic field

¹ This frequency is twice the critical frequency, which divides the emitted power spectrum into two parts of equal energy content: $\omega_{critical} = 3/2 c \gamma^3 / r_{bend}$

when focused to a small spot, but it enables also the irradiation of large sample areas with relatively good intensities (for example to activate surface reactions).

The FLUTE facility consists of a radio-frequency (rf) photoinjector gun followed by an accelerating rf structure which bring the electrons to an energy of up to 60 MeV (see Fig. 1.1). In order to produce electromagnetic radiation the electron bunch must follow a curved trajectory that is obtained with dipole magnets. In FLUTE, four dipole magnets are used to compress longitudinally the electron bunch and to radiate in the THz frequency range. The last dipole serves as a THz radiator (see Figure 2.6.3). There are actually two effective ways to extract THz radiation and both can work in parallel. First the electron bunch will emit coherent synchrotron radiation (CSR) in the dipole magnet if the bunch duration is shorter than the desired wavelength (for example 1 mm bunch length corresponds to 0.3 THz). The advantage of CSR over normal synchrotron radiation is that the intensity of CSR goes with the square of the number of electrons N^2 (SR is only proportional to N). The other method of extracting THz radiation from a Linac is to insert a metallic screen in the path of the electron beam. The change of medium from vacuum to metal will generate transition radiation which can also be coherent (N^2) if the observed wavelength is of the same length or longer than the electron bunch. This type of radiation is called the coherent transition radiations (CTR).

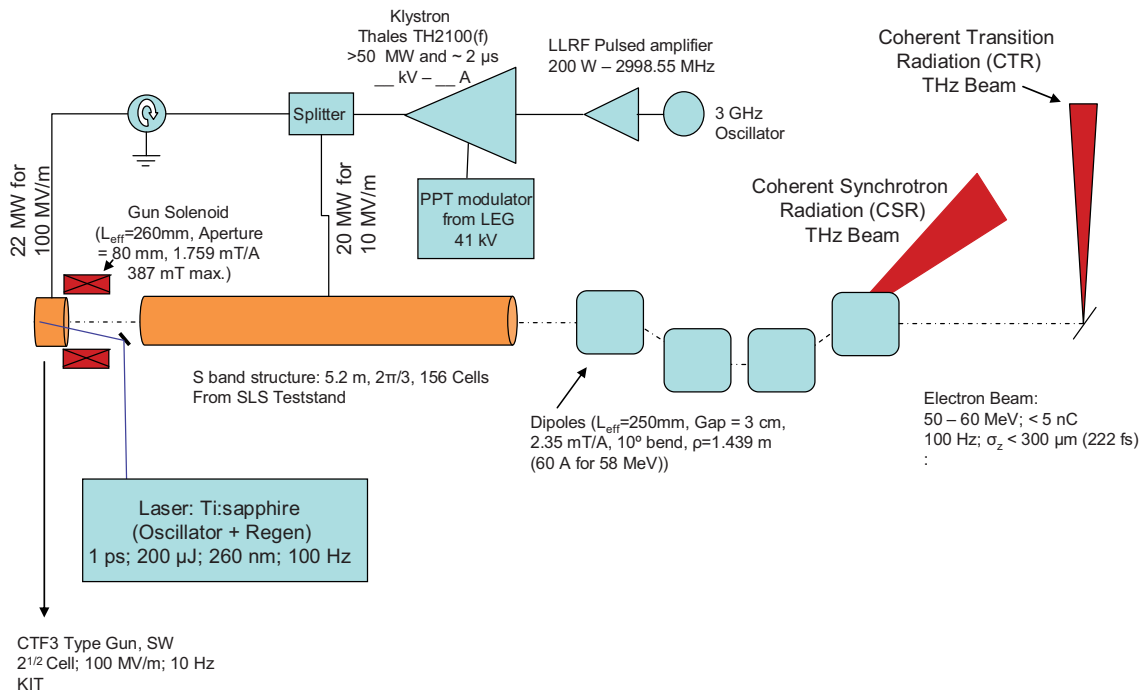


Figure 2.6.2: Schematic of the FLUTE facility with key parameters.

As explained above, some of the design parameters are already fixed by the hardware which will be used to build the FLUTE facility (see Chapter 4). The electron source is an S-band RF gun, originally designed for high-charge operation of up to 20 nC at CTF3 [46,47], and was used to generate a 5 nC electron beam (laser parameters: 10 mm spot radius, 1 -3 ps pulse length). The accelerating section is an S band structure from the Linac II Desy Type [48] with an effective length of 5.2 m and 156 cells.

The compression and CSR extraction is accomplished with a four dipoles magnetic chicane. The last dipole is also used to extract the CSR THz pulses. Two modes of compression are foreseen: use of the RF linac to create a negative linear bunch chirp followed by a compression with 4 dipoles 1)

or with ultra short laser pulse one let the bunch develop naturally a positive chirp which is then compressed with only two dipoles and quadrupoles (dog leg 2).

2.6.3.1 Compression with negative chirp and positive R56

In this mode of compression, the 4 dipoles are required to compress effectively the beam.

Table 2.6.1: Design Parameters of the FLUTE THz source

| | |
|---|---------------------|
| Charge Q | 3 nC |
| Laser pulse duration $\sigma_{t,\text{laser}}$ (rms) | 4 ps |
| Laser Longitudinal Shape | Gaussian |
| Laser Transverse size $\sigma_{r,\text{laser}}$ (rms) | 2.5 mm |
| Laser Transverse Profile | Gaussian |
| Peak Current | 3 kA |
| RF Gun Peak Field | 100 MV /m |
| Gun Solenoid Field | 40 - 280 mT |
| Gun Solenoid Length | 260 mm |
| Accelerating Structure Position z_{acc} | 1300 mm |
| Accelerating Structure length l_{acc} | 5200 mm |
| Beam Energy at Gun exit | 7 MeV |
| Beam Energy at End | 45 - 54 MeV |
| Peak Accelerating gradient in Linac F_{acc} | 10 MV/m |
| Linac Phase Φ_{acc} | 0 -25 deg |
| 1 st Dipole Bending Angle α | 10 deg |
| Effective length dipole magnet l_{eff} | 250 mm |
| Bending radius of dipole magnet r_{bend} | 1439 mm |
| Distance between dipole d | 500 mm |
| R56 four dipole chicane | 34 mm |
| Compression Factor | 10 |
| Final Bunch Length $\sigma_{\text{bunch},f}$ | < 150 μm |
| Total Spectral Energy (0.1 to 10 THz) | > 100 μJ |
| THz Radiation divergence | 150 mrad |

In order to tune the THz radiation frequency one has to vary the bunch compression factor.

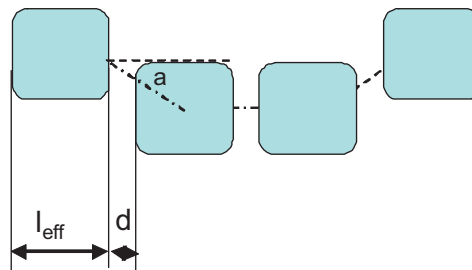


Fig 2.6.3: Bunch compressor magnetic chicane (α being the bending angle)

The compression factor of the FLUTE facility can be expressed as follow [49]:

$$C = \frac{1}{1 + A.R_{56}} \quad (2.1)$$

The linear chirp factor A being:

$$A = -\frac{2\pi e V \cdot \sin \Phi}{(E_{\text{gun}} + eV \cos \Phi)\lambda}$$

With V being the maximum voltage gain across the linac accelerating structure ($V=F_{\text{acc}} \cdot l_{\text{acc}}$), Φ the rf phase in the linac, E_{gun} the energy at gun exit and λ the period of the linac structure (3 GHz).

For a four dipole magnet chicane the R_{56} parameter is defined by:

$$R_{56} = 4r_{\text{bend}}(\tan \alpha - \alpha) + 2d \frac{(\tan \alpha)^2}{\cos \alpha}$$

With α and r_{bend} being the bending angle and the bending radius respectively. A factor 10 compression can be obtained then by using a bending angle of 10 degrees and a linac phase 25 degrees off – crest.

2.6.3.2 Compression with positive chirp and negative R_{56}

Beam simulations for the described generic setup have been done with the particle tracking program ASTRA [22]. As electron source, an S-band RF gun, originally designed for high charge operation up to 20 nC at CTF3 [47], was used to generate a 5 nC electron beam (laser parameters: 10 mm spot radius, 1 ps pulse length) (Fig. 2.6.3.2a).

Due to the high charge density in the bunch, space charge forces strongly distort the longitudinal and transverse phase space during the acceleration process, although a high acceleration gradient (100-120 MV/m) is applied at the cathode and a focusing solenoid (280 mT) is placed directly after the gun such that the magnetic field extends up to the cathode plane. Fig. 2.6.3.2b displays the longitudinal phase space at the gun exit.

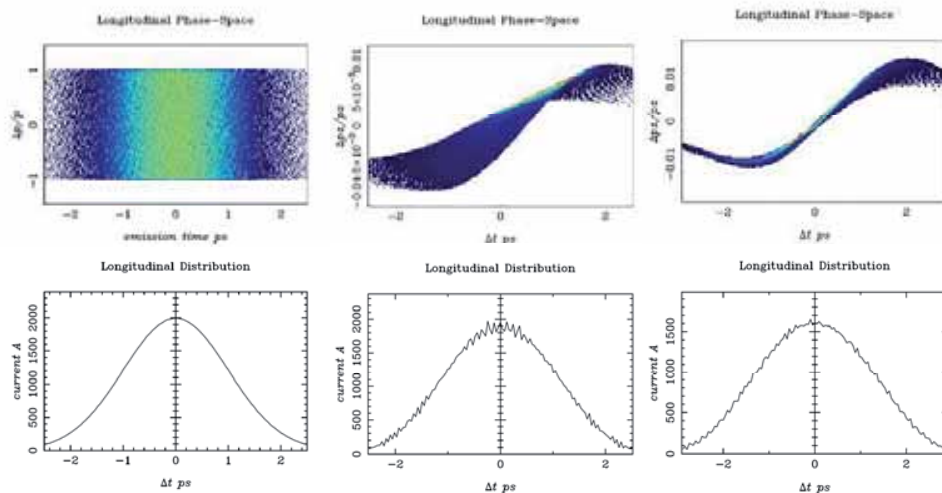


Fig. 2.6.3.2: Longitudinal phase space distributions (top line) and their projections (bottom line). a) at the cathode plane ($\sigma_t=1$ ps) (left); b) after the gun (center), c) after the booster (right).

In order to avoid further beam blow-up and bunch lengthening, an S-band booster cavity (1.25 m long, 38 cells) starting at $z=0.5$ m after the cathode increases the electron beam energy from about 8 MeV to 30 MeV. Since emittance is no concern, no envelope matching was applied at the entrance of the booster cavity, thus avoiding additional space charge problems induced by strong focussing. RF focussing occurs in the booster cavity and leads to a nice beam size development, as shown in

Fig. 2.6.3.3 (left). The beam size reduction after the gun indicates clearly the two regimes: solenoid focussing at the gun exit and RF focussing in the booster.

After the booster, the influence of space charge becomes negligible and the phase space (Fig. 2.6.3.2c) is frozen. The bunch length at this position is 1.24 ps, or 370 μm .

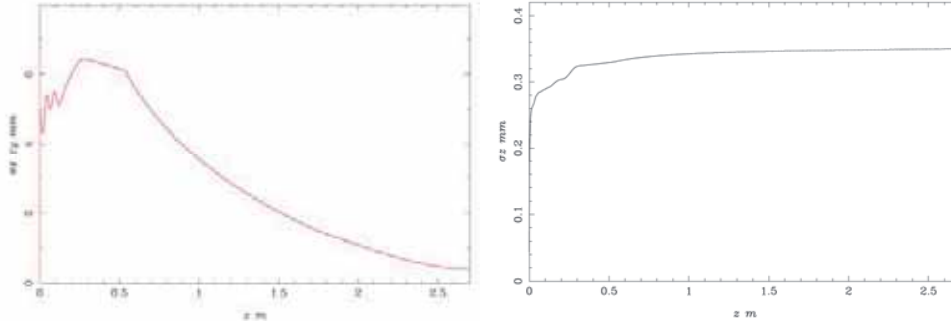


Fig. 2.6.3.3: Beam size (left) and rms bunch length (right) development of the electron beam along the accelerator.

Bunch compressor design

Let's assume that the electron bunches, produced by the presented compact linac layout, can be compressed to 100 μm . This corresponds to a compression factor of ~ 3.5 and should be feasible. For bunches of this length, the calculated spectral distributions look very promising and the spectral energy contained above 1 THz reaches the required 100 μJ . It is clear that larger bunch compression factors (e.g. a factor of 10, resulting in a bunch length of 37 μm) may cause trouble at the bunch charge used, due to increased space charge forces.

We can conclude that the installation of a bunch compressor is essential to reach the envisaged photon beam parameters. The precondition for bunch compression is the existence of an energy chirp in the longitudinal energy profile of the bunch. This condition is fulfilled for the majority of particles in the simulated bunch, see Fig. 2.6.3.2c: here, the head electrons have higher energy than the tail electrons. They experience consequently a stronger deflection in the dipoles of a magnetic bunch compressor and should have a longer path length in the compressor in order to compress the bunch. This requirement is fulfilled by a bunch compressor with negative R_{56} . The design of such a bunch compressor is described in [50] and design simulations following the dogleg-based scheme have been done with the matrix based particle code elegant [10]. A short matching section (1 m long) before the compressor, consisting of four quadrupoles, allows for adjustment of the β -functions at the bunch compressor entrance. The compressor itself is, in the present design, 2 m long and consists of 2 dipoles (combining the functions of

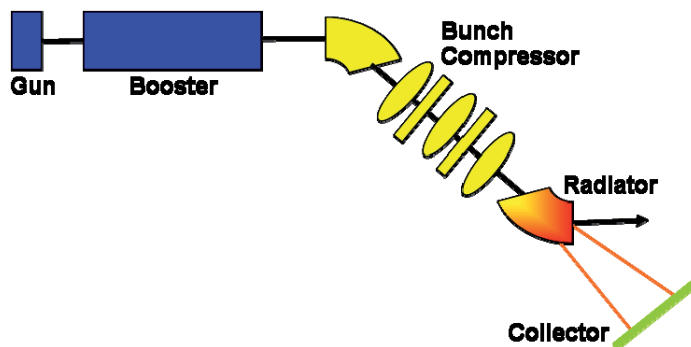


Fig. 2.6.3.4: Schematic layout of the THz source with the bunch compressor. The complete setup is 5 m long. The quadrupoles in the matching section are not drawn.

bending magnet and radiator²), 3 quadrupoles (to assure a dispersion-free path), and 2 sextupoles (for linearization of the compression process, not in use in the current design), arranged symmetrically around the compressor's midpoint, as sketched in Fig. 2.6.3.4.

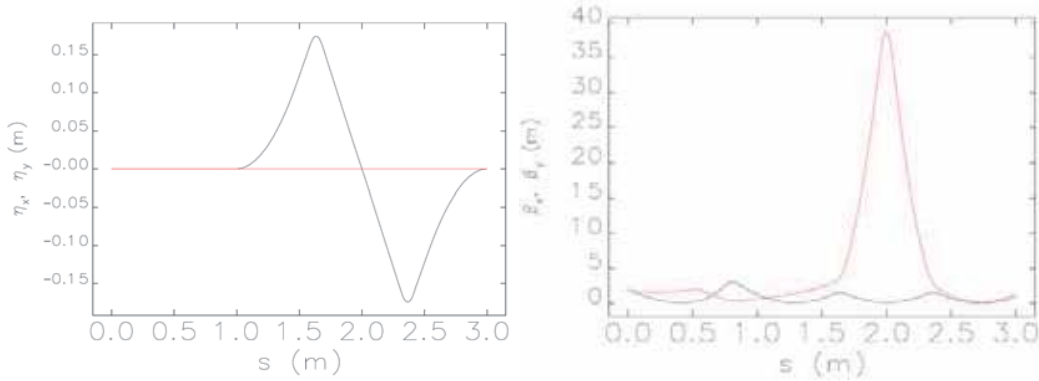


Fig. 2.6.3.5: Dispersion (left) and β -functions (right) along the matching section and in the bunch compressor.

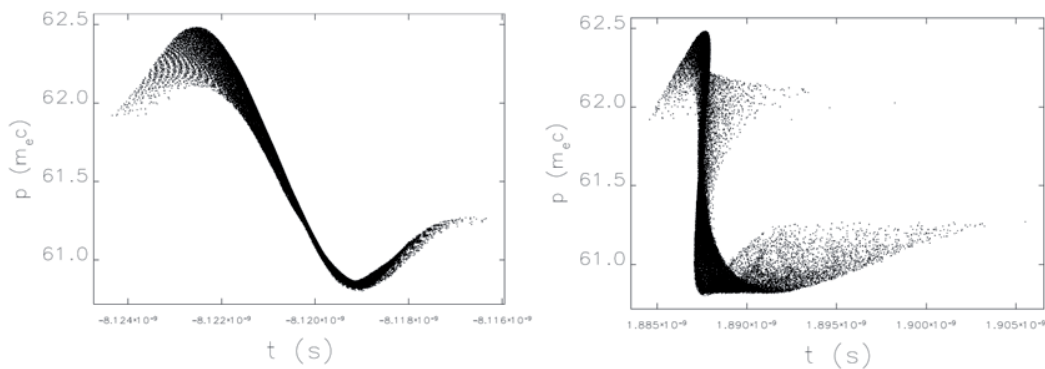


Fig. 2.6.3.6: Longitudinal phase space before (at $z=2$ m; left) and after ($z=5$ m; right) the compression.

The distributions of dispersion functions and β -functions along the matching and compressor sections are shown in Fig. 2.6.3.5. Fig. 2.6.3.6 displays the longitudinal phase space at the entrance of the matching section (at $z = 2$ m from the cathode) and at the exit of the bunch compressor (3 m further downstream, i.e. at $z=5$ m from the cathode). Fig. 2.6.3.7 (left) shows the time projection of the electron bunch at these position, i.e. before and after compression. A peak current of ~ 6.7 kA is reached after compression, and a fit of the time distribution results in a final bunch length between 155 fs (47 μm) and 222 fs (67 μm). A large part of the charge is contained in ± 0.5 ps (3.6 nC out of 5 nC).

² in that case, the radiation from the uncompressed beam, generated in the first dipole, comes for free

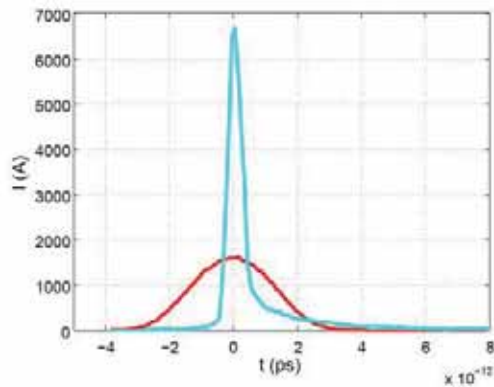


Fig. 2.6.3.7: Left: Current distributions of the electron bunch before and after compression. $Q=5$ nC; $E=30$ MeV, $r_{bend}=1$ m. Collection angle: 100 mrad.

2.6.4 THz radiated energy per pulse

Let it be assumed that the electron bunches produced by the presented compact linac layout can be compressed to 100 μm . This corresponds to a compression factor of ~ 3.5 and should be feasible. For bunches of this length, the calculated spectral distributions look very promising and the spectral energy contained above 1 THz reaches the required 100 μJ . It is clear that larger bunch compression factors (e.g. a factor of 10, resulting in a bunch length of 37 μm) may cause trouble for the bunch charge used, due to increased space charge forces.

Assuming that a final bunch length between 155 fs (47 μm) and 222 fs (67 μm) is reached after compression. A large part of the charge is contained in ± 0.5 ps (3.6 nC out of 5 nC). These numbers are used to calculate the expected THz photon spectra; results are displayed in Figure 2.6.4 and Table 2.6.2.

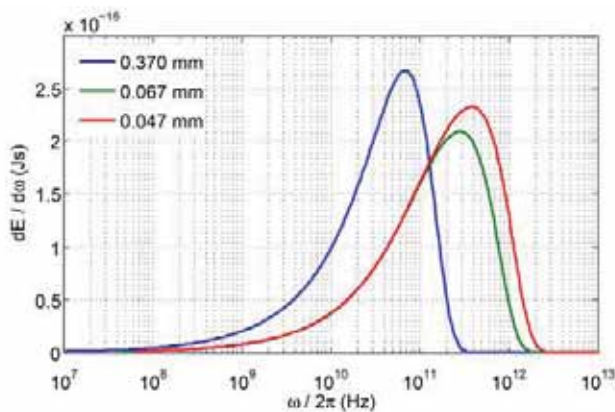


Fig. 2.6.4: Synchrotron radiation spectrum from the analytical model for the expected electron bunch lengths before compression ($Q=5$ nC; blue curve) and after compression ($Q=3.6$ nC; green and red curves). $E=30$ MeV, $r_{bend}=1$ m. Collection angle: 100 mrad.

Table 2.6.1: Calculated photon pulse energies for the expected electron bunch lengths before compression ($Q=5$ nC) and after compression ($Q=3.6$ nC), corresponding to Figure 2.6.4., $E=30$ MeV, $r_{bend}=1$ m, collecting aperture: 150 mrad. The total spectral energy as well as the spectral energy contained above 1 THz are displayed.

| Bunch Length | Total Spectral Energy | Energy >1 THz |
|-------------------|-----------------------|----------------------|
| 370 μm | 1.57 mJ | $4 \cdot 10^{-8}$ mJ |
| 67 μm | 15.1 mJ | 1.15 mJ |
| 47 μm | 23.7 mJ | 5.85 mJ |

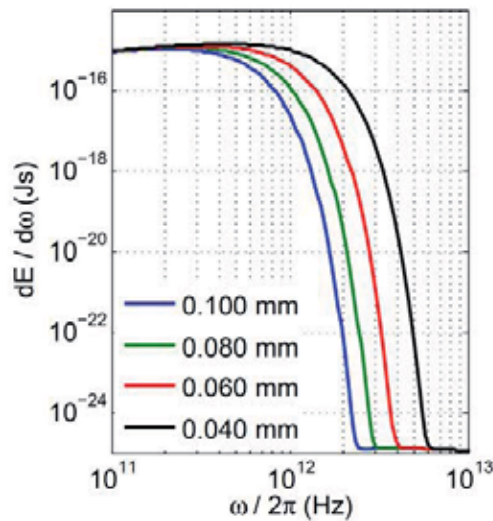


Fig. 2.6.5: Synchrotron radiation spectrum from the analytical model for different bunch lengths after compression, for a reduced charge of $Q=3$ nC. $E=30$ MeV, $r_{bend}=1$ m. Collection angle: 100 mrad.

It is clear that there is enough power contained in the spectrum for the planned experiments. After taking into account losses in the THz transport line (at least factor 10), that decrease mainly the low-frequency part of the spectrum, a possibility to further decrease the total energy is to reduce the bunch charge, e.g. from 5 nC to 3 nC, or even 1 nC. This would also facilitate the setting up of the machine since the space charge influence is enormously decreased. With the lower charge, the bunch could possibly be further compressed, allowing for a certain tuning of the output radiation up to a few THz, as Figure 2.6.5 shows. Further studies are, however, needed in order to understand in detail the possibilities for tuning the machine with the help of changes in the bunch compression factor and bunch charge.

3 ELECTRON BEAM COMPONENTS

3.1 Laser system

3.1.1 Gun laser system

A copper photo-cathode is presently the base-line electron source candidate fulfilling the SwissFEL injector requirements in terms of beam brightness. For the operation of the SwissFEL, a laser system capable of generating 200pC of photo-electrons is required. A minimum energy per pulse of 100μJ at 266nm is required to produce 200pC of photoelectrons from a copper surface, assuming a QE of 10^{-5} . Such pulse energies can easily be achieved with current Ti:Sa amplifier systems. In addition, Ti:Sa laser systems provide pulses as short as 50 fs, so that it becomes possible to generate uniform longitudinal profile (square profile) with a rise time of a few 100 fs by frequency-domain pulse shaping.

Ti:Sapphire systems are commercially available and have reached high technological maturity, due to their widespread use in research laboratories throughout the world. In addition, many diagnostics tools and pulse-shaping techniques are available for the near-IR/visible spectral region, and frequency-tripling of the fundamental laser wavelength allows easy access to the UV.

Table 3.1.1: Gun laser characteristics for SwissFEL

| Laser specifications | |
|--|---------------|
| Maximum pulse energy on cathode | 60 μJ |
| Central wavelength | 250-300 nm |
| Bandwidth (FWHM) | 1-2 nm |
| Pulse repetition rate | 100 Hz |
| Double-pulse operation | yes |
| Delay between double pulses | 50 ns |
| Laser spot size on cathode (rms) (10 pC / 200 pC) | 0.1 / 0.27 mm |
| Minimum pulse rise-time | < 0.7 ps |
| Pulse duration (FWHM) | 3-10 ps |
| Longitudinal intensity profile | various |
| Transverse intensity profile | Uniform |
| Laser-to-RF phase jitter on cathode (rms) | <100 fs |
| UV pulse energy fluctuation | < 0.5% rms |
| Pointing stability on cathode (relative to laser diameter) | <1% ptp |

Conventional Ti:sapphire amplifiers, however, suffer from spectral narrowing due to the limited gain bandwidth, yielding spectra of 30-40 nm (FWHM) at the mJ level and making wavelength tuning impossible. The scheme presented here overcomes this limitation and furthermore offers enhanced pulse energy stability and direct UV pulse shaping. This should help to produce electron bunches with lowest emittance at the gun.

3.1.2 General layout

The laser system consists of 4 subsequent amplifier stages. As seed laser, a Rainbow oscillator (Femtolaser, Inc.) delivering 380 mW is used. This seed is an ultra-broadband source needed for further amplification while maintaining short pulses.

The pre-amplified (10 μ J) and temporally stretched (\approx 500 ps) pulse seeds the regenerative amplifier, which is followed by sequential multi-pass amplifiers. An acousto-optic programmable gain-control filter (Mazzler, Fastlite Inc. [51]) situated in the regenerative cavity is used as an adaptive spectral filter, providing broad spectra with up to 120 nm (FW). Wavelength selection is performed by a Dazzler. The current amplifier scheme allows continuous variation of the central wavelength within a range of 755 to 845 nm, with a spectral width of 30 nm. The compressed pulses (20 fs, up to 21 mJ) are frequency-converted from the near-IR to the UV by second-harmonic generation (SHG) and subsequent sum-frequency generation (SFG) in β -barium borate (BBO) crystals. The expected wavelength tunability covers 260-280 nm, with pulse energies up to 1 mJ.

The large number of six identical diode pump lasers helps to increase stability, since pump-laser induced energy fluctuations can be significantly reduced by mixing different pump sources.

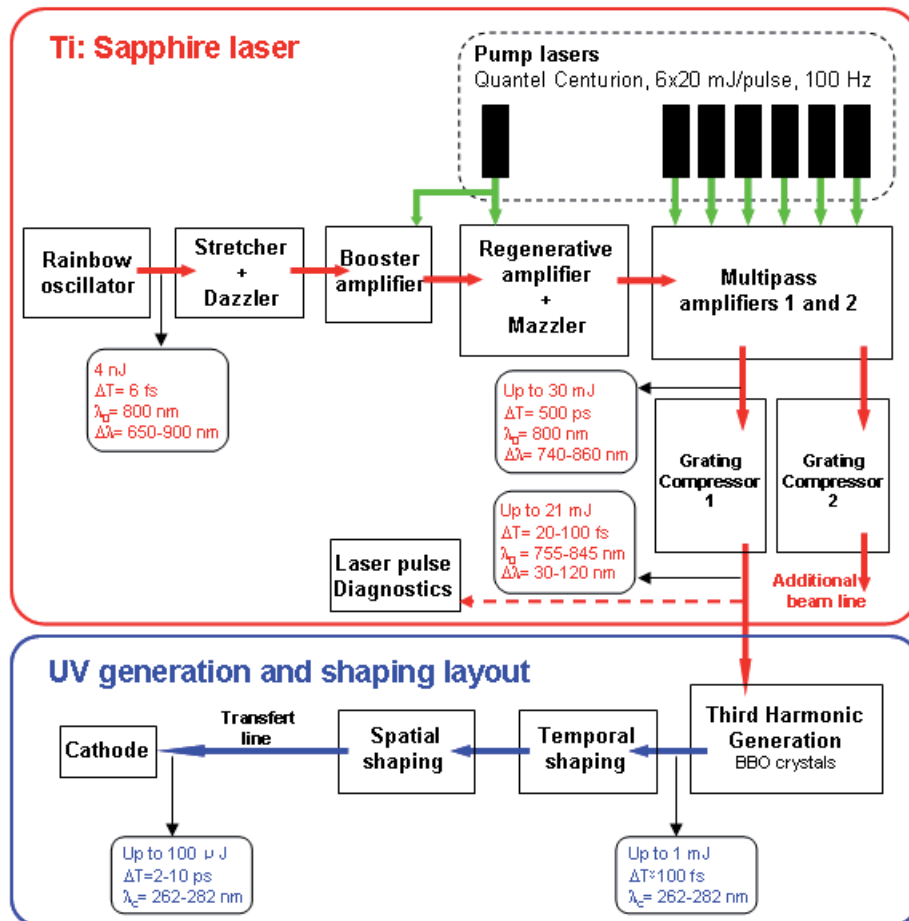


Fig. 3.1.1: Schematic drawing of Ti:Sapphire gun laser .

3.1.3 UV temporal and spatial pulse shaping

The spatial and temporal shape of the amplified laser pulse is nominally Gaussian. Electron beam dynamics simulations indicate that a flat-top-like pulse shape helps to generate uniform temporal and spatial electron distribution, resulting in lower transverse emittance at the gun. Since other simulations show that a Gaussian-like electron distribution is less sensitive to timing jitter in the undulator, it is more likely that an intermediate pulse shape will be optimal for best FEL

performance[52]. Our approach for achieving high-quality shaped UV pulses is based on direct UV pulse stretching and shaping. A UV stretcher based on highly efficient transmissive UV gratings (Ibsen Photonics Inc.) allows the stretching of Gaussian pulses (see Fig. 3.1.2). This setup is very compact and gives the possibility of temporal shaping by using spectral filtering in the Fourier plane of the stretcher. The pulse length can be continuously varied from 2 to 10 ps FWHM by changing the distance between the two gratings.

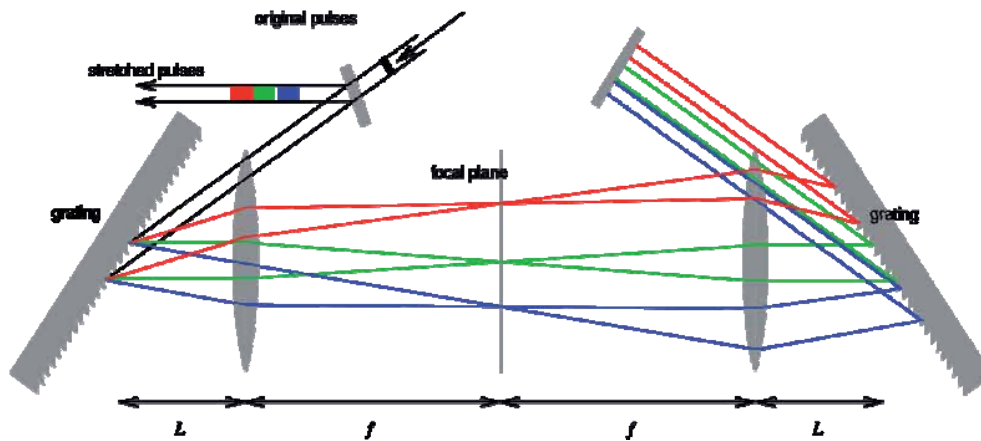


Fig. 3.1.2: UV pulse stretcher based on a UV transmissive gratings.

An alternative technique that is considered for producing ps flat-top-like pulses is the so called “pulse stacking technique”. α -cut β -barium borate (BBO) crystals of length L are used to generate replicas of the initial pulse. Each crystal generates two orthogonally polarized replicas separated in time by a delay $\Delta t = \frac{L}{c}(n_o - n_e)$ as can be seen in Fig. 3.1.3. The use of several crystals of adequate lengths allows the generation of flat-top-like ps pulses with an efficiency of 70% (or 30 % energy loss). Temporal pulse characterization will be performed by cross-correlation with the fundamental laser pulse.

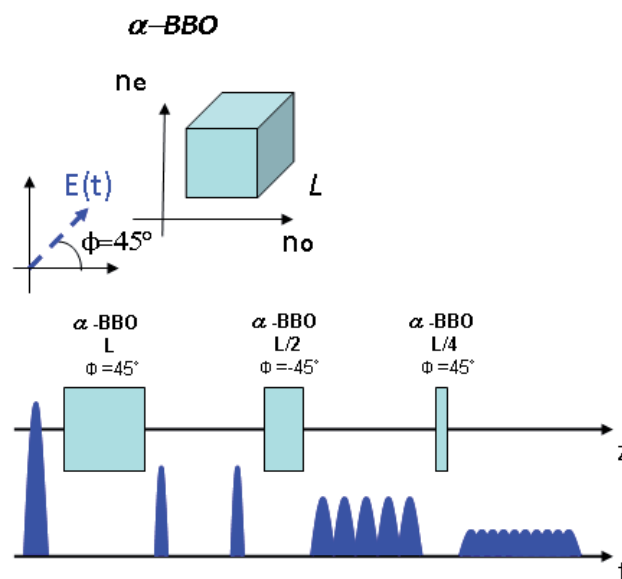


Fig. 3.1.3: Pulse stacking with α -cut BBO crystals for the production of ps flat-top-like pulses.

In order to produce a homogeneous flat-top electron beam profile (transversally) on the cathode surface, the laser intensity profile must also be flat-top. Laser transverse homogenization techniques are described below. In order to quantify the quality of the laser intensity transverse profile we defined some key parameters and developed an analysis tool. The tool is computing the beam ellipticity as well as the beam transverse and radial uniformity:

- the ellipticity is computed doing the ratio of the beam diameter measured over two orthogonal axis.
- the beam transverse and radial uniformity calculations are based on the following method: the beam is divided in transverse (Fig. 3.1.4 in blue) and radial (Fig. 3.1.4 in red) sections, each section having the same area. Then, the normalized average intensity in each section is estimated. Finally, the RMS and standard deviation for transverse and angular uniformity is computed.

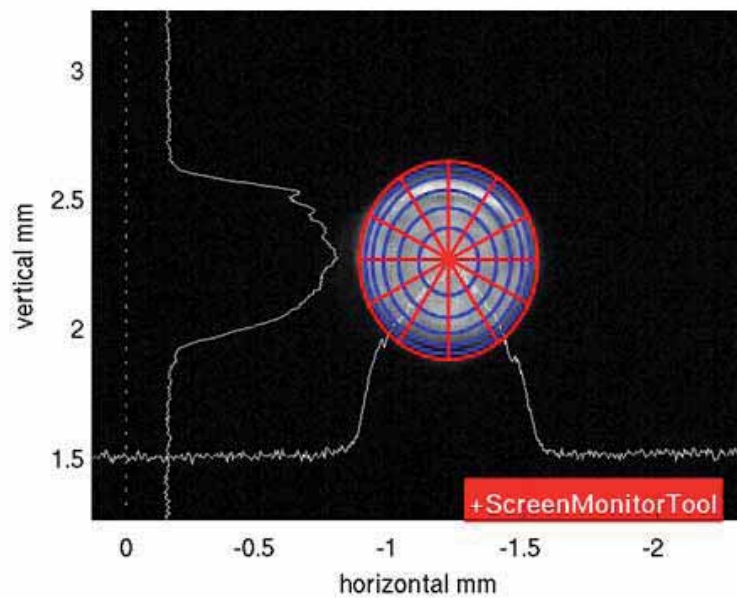


Fig. 3.1.4: Schematic of the beam sections used by the analysis tool. The blue concentric circles are used for transverse beam homogeneity calculations while the red ‘pizza portions’ are used for radial intensity homogeneity.

Fig 3.1.5 shows a screenshot of the analysis tool. As can be seen, other interesting parameters like the integrated beam profiles over x and y axis, as well as the plot of transverse and radial average intensity versus beam section are displayed.

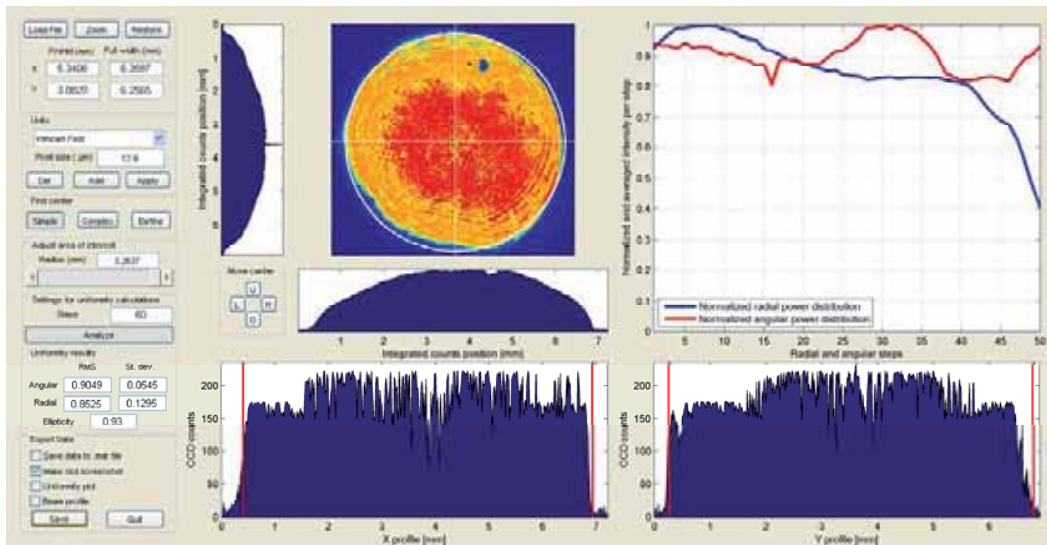


Fig 3.1.5: Screenshot of the beam analysis tool.

The optical technique for transverse beam shaping consists in selecting the core part of the intensity profile by a spatial mask, which is relay-imaged onto the cathode surface. Prior to this, the UV beam passes through a beam homogenizer for reduction of intensity hot spots arising during third-harmonic generation process. The beam homogenizer consists of a 15-30 cm-long glass waveguide with a 400 μm air-filled core. For appropriate beam parameters, the waveguide acts as a low-pass filter, since strong coupling is only achieved for the fundamental HE_{11} mode.

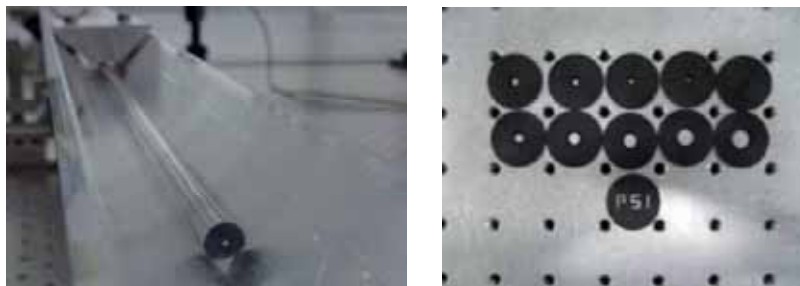


Fig. 3.1.6: Left: glass capillary for beam homogenization; right: set of apertures for transverse flat-top beam generation

3.1.4 Laser room for the SwissFEL injector

The amplitude stability of laser systems is highly dependent on environmental conditions (temperature, air turbulence, humidity). In order to provide the best environmental quality for the laser system, the SwissFEL injector will include a temperature and humidity controlled clean room. The room provides a Class 10000 environment with a temperature stability of $\pm 0.1^\circ\text{C}$. The humidity is limited to a maximum of 45%, in order to avoid condensation on optical components.

The analogue and optical Master Oscillator also requires a stable environment. For this reason, both will be hosted in the laser room.

3.1.5 HHG-based seeding laser system

A promising approach for seeding a FEL is based on high-order harmonic generation (HHG) in gases by an intense femtosecond laser system. HHG yields fully coherent XUV radiation in very short pulses, ranging from femtosecond to attoseconds. It is planned to seed the soft X-ray beamline

of the SwissFEL with both a 12 nm and a 5 nm seeding source. While HHG at 12 nm is feasible with a state-of-the-art Ti:Sapphire laser system ($\lambda_{\text{laser}}=800$ nm), the generation of 5 nm coherent radiation by HHG requires the development of a powerful mid-IR driver (e.g. ($\lambda_{\text{laser}}=3000$ nm)).

Table 3.1.2: Parameters of the laser for High Harmonic Generation (HHG) seeding

| Seed laser | Unit | |
|--------------------------|------|---|
| Harmonic wavelength | nm | 12 (5) |
| Driving laser wavelength | mm | 0.8 (3) |
| Laser energy | mJ | 20 (10) |
| Conversion efficiency | | $1.0 \cdot 10^{-6}$ ($1.0 \cdot 10^{-6}$) |
| Photon energy | eV | 103.3 (248) |
| Minimal average power | kW | 50 (100) |
| Pulse duration, rms (s) | fs | <35 |
| FEL gain bandwidth, Dw/w | | 0.003 (0.001) |
| Temporal pulse form | | train |
| Size of e beam, rms (s) | mm | 25 |
| Mode size, rms HHG | mm | >25 |
| Loss beam transport | % | 50 |
| Loss in HHG-FEL coupling | % | 90 |

3.1.6 Laser system for laser heater

An electron beam with a small energy spread may introduce micro-bunching instabilities in the electron beam and subsequent problems for electron beam diagnostics equipment, due to coherent synchrotron radiation.

Table 3.1.3: Parameters of the laser heater laser

| Laser heater | Unit | |
|------------------------------------|---------------|----------|
| Pointing stability, rms | μm | < 20 |
| Laser energy | μJ | 10...100 |
| Laser spot-size, rms (\square) | μm | 300 |
| Transverse profile | | Gaussian |
| Laser peak power | MW | 10...20 |
| Laser wavelength | nm | 800 |
| Rayleigh range | m | 0.5 |
| Pulse duration | ps | 10...100 |
| Longitudinal profile | | Gaussian |
| Pulse energy stability, rms | % | <2 |
| Repetition rate | Hz | 100 |

To avoid this, the uncorrelated energy spread of the electron beam needs to be increased. This can be done with the help of a powerful infra-red laser beam, which is overlapped with the electron bunch in an undulator situated in a chicane. The laser heater laser is a split from the gun laser system, since this system provides enough power to drive the gun and the heater synchronously. The transport from the laser hutch to the laser heater will be performed in vacuum tubes, to provide the required beam pointing stability at the laser heater. The required laser parameters are listed above.

3.2 RF systems

3.2.1 Main parameters of different SwissFEL RF Structures

Table 3.2.1: Summary of the key parameters of the different accelerating structures of SwissFEL

| | S-band photogun | S-band cavities (injector) | X-band cavities (injector) | C-band cavities (Linacs 1, 2 and 3) |
|-----------------------------------|----------------------|----------------------------|----------------------------|-------------------------------------|
| Frequency (MHz) – $f_b=142.8$ MHz | 2998.8 (21 x f_b) | 2998.8 (21 x f_b) | 11995.2 (84 x f_b) | 5712 (40 X f_b) |
| Phase Advance | π | $2\pi/3$ | $5\pi/6$ | $2\pi/3$ |
| Active Length | 162 mm | 4070 mm | 750 mm | 1920 mm |
| Total Length | | 4150 mm | 965 mm | 2050 mm |
| Number of Cells | 2.5 | 122 | 72 | 110 |
| Operating Temperature | 40 ° C | 23 ° C | 40 ° C | 40 ° C |
| Operating Gradient | 100 MV/m | 20 MV/m | 20 MV/m | 26.5 MV/m |
| Required Peak Power per structure | 19 MW for 100 MV/m | 36.5 MW for 20 MV/m | 7.2 MW for 20 MV/m | 27 MW for 26.5 MV/m |
| Klystron maximum performance | 35 MW – 4.5 μ s | 45 MW – 4.5 μ s | 50 MW – 1.5 μ s | 50 MW – 2.5 μ s |
| Filling Time | 490 ns | 955 ns | 100 ns | 300 ns |
| Number of structures | 1 | 6 | 2 | 104 |
| Number of structures per klystron | 1 | 1 | 2 | 4 |

3.2.2 RF photogun design

The RF gun for Swiss FEL consists of $2\frac{1}{2}$ cells operating in the π mode. The simulations presented here are for a European S-band frequency of 2997.912 MHz. However, the final RF frequency choice for all S-band cavities present in the injector will be 2998.8 MHz, in order to have a common sub-harmonic ($f_b=142.8$ MHz) with the American C-band linac (C-band linac frequency is 5712 MHz) (see Table 3.2.1). The second cell is coupled to two waveguides, which leads to cancellation of the dipole fields by symmetry. To minimize the quadrupole field component, the second cell has a racetrack shape. To reduce the thermal stress and to decrease the pulsed surface heating, the coupling ports to the waveguide are optimized by adopting coupling along the length of the cell (z-coupling) and by increasing the radius on the inside surface of the coupling aperture. The dimensions of the coupling port have also been optimized, so that the coupling factor β is equal to 2. This allows faster filling of the cavity. The frequency separation between the operating mode and the next lower mode ($\pi/2$ mode) is more than 15 MHz. This feature, achieved by increasing the radius of the irises between the cells, should minimize the impact of the neighboring modes on potential emittance degradation.

Optimizing the radius of each cell allows field balance in the cells to be obtained (Figure 3.2.1).

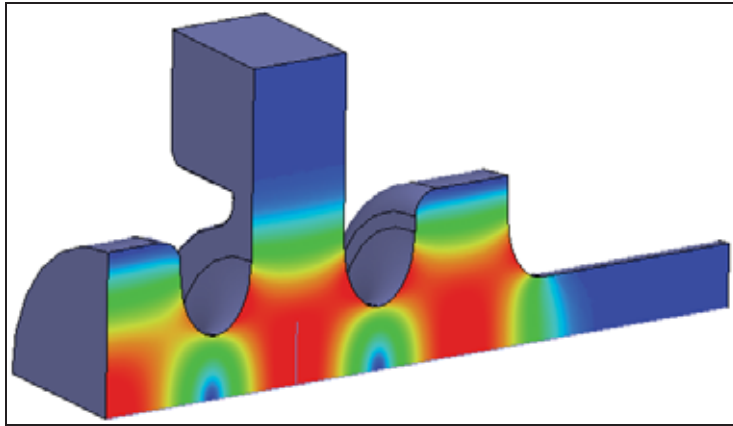


Fig. 3.2.1: 3D field map of the complex amplitude of the accelerating electric field.

For multibunch operation, flat-topping of the accelerating field can be obtained with amplitude modulation of the klystron input power. To achieve a flat-top accelerating field of 100 MV/m for 150 ns with a total pulse length of 1 μ s, the input power from the klystron has to be set to about 19 MW for 850 ns, and then decreased to about 13 MW for 150 ns (Figure 3.2.2). In addition, care has to be given to the phase of the accelerating field.

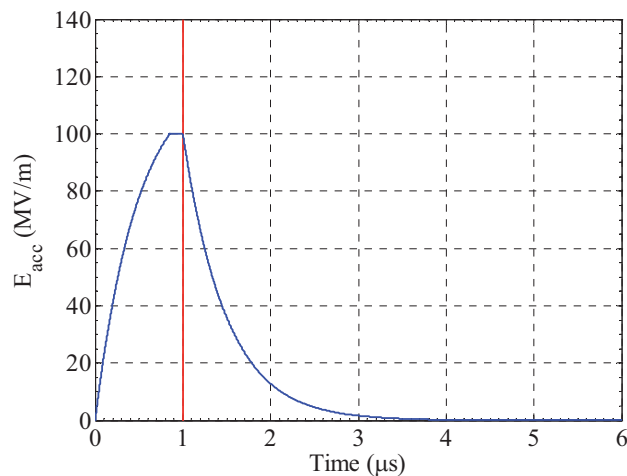


Fig. 3.2.2: Peak accelerating electric field vs. time.

Operating with a pulse length as small as 1 μ s, and in the amplitude modulation mode, substantially decreases the average power of the RF gun and therefore reduces the thermal stress. For an accelerating field of 100 MV/m, a repetition rate of 100 Hz and a pulse length of 1 μ s, the dissipated average power is as low as 0.9 kW (Figure 3.2.3). The maximum temperature rise due to pulsed heating, located at the coupling ports, is as low as 17°C – well below the 50°C considered acceptable.

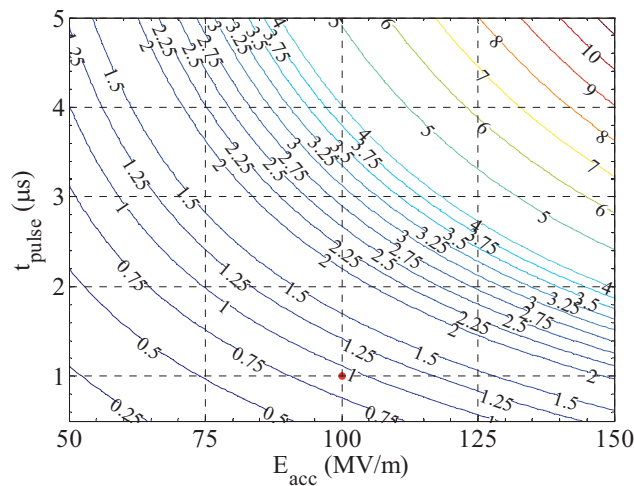


Fig. 3.2.3: Contour plot of dissipated average power vs. accelerating field and pulse length (for a repetition rate of 100 Hz).

Three RF pick-ups, one per cell, are foreseen to monitor and control the RF field in the gun during operation. The operating temperature will be 40°C. However, dimple holes on each cell are also foreseen, to allow tuning to reach the required frequency during cold measurements. The back plane of the $\frac{1}{2}$ cell, which is used as cathode plate, is also longitudinally adjustable, giving another degree of freedom for the tuning of the gun.

3.2.3 RF systems of the SwissFEL injector

The RF systems for the SwissFEL injector are already installed at the SwissFEL Injector Test Facility currently undergoing commissioning at PSI. The RF hardware will be moved in the SwissFEL building in 2015. The main difference between the SwissFEL Injector Test Facility and the final SwissFEL injector is that two additional S-band structures, as well as one more X-band structure, will be installed before the bunch compressor (see Section 2.3.1). The SwissFEL Injector Test Facility is currently operated on the European frequency (S-band: 2997.12 MHz; X-band: 11991.648 MHz), but soon tests at the SwissFEL design frequencies (Table 3.2.1) will be performed.

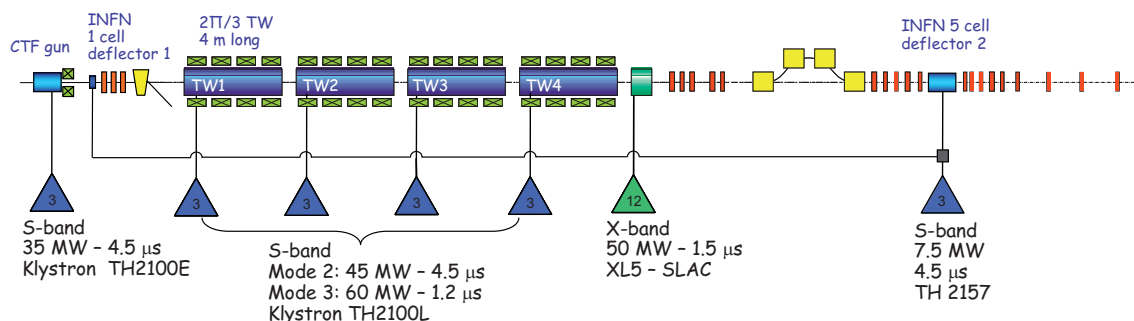


Figure 3.2.2.1: General layout of the RF systems for the SwissFEL Injector Test Facility. The SwissFEL injector will have two more S-band modules and one more X-band module.

The general layout of the RF system for the Injector Test facility is shown in Figure 3.2.2.1. The accelerator starts with the S-band rf-photoinjector described in Section 3.2.1. A booster linac composed of 4 S-band structures, 4 m long, provides the required acceleration and energy chirp for

the magnetic compression. A 12 GHz cavity is placed in front of the compression chicane for linearization of the longitudinal phase space. Two S-band deflecting cavities are implemented for diagnostics purposes, in order to characterize the longitudinal phase space and slice parameters of the beam. For maximum flexibility, each accelerating structure will be powered by a dedicated power station. This choice will allow fine control of the RF focusing (gradient optimization) for optimal invariant envelope matching, avoiding any cross talking between cavities. SLED compressors have not been considered for the initial phase, in order to suppress any additional complication. The modulator and the klystron run in a short-pulse mode for maximum gradient tests (25 MV/m), and in long-pulse mode (45 MW) to later allow RF compression tests.

3.2.3.1 S-band structures

Booster linac

As mentioned above, the actual SwissFEL booster linac consists of six constant-gradient $2\pi/3$ travelling-wave accelerating structures separated by short drifts, where corrector, BPM and screen monitor are located. The structure RF design derives from the Linac II DESY structures and was re-optimized by compromising between maximum shunt impedance to decrease the power requirement at 25 MV/m and short-range wakefield considerations. For small correction of the transverse focusing, each cavity is surrounded by four solenoid magnets, each 70 cm long (operated with peak magnetic field between 40 and 80 mT (cf. Section 3.4.1)).

The design parameters of the S-band accelerating structures are summarized below in Table 3.2.2.1.

Table 3.2.2.1: RF parameters for the booster cavities of the SwissFEL Injector Test Facility. (SwissFEL injector S-band structures will later be operated at 2998.8 MHz)

| | |
|--|---|
| Operating frequency (at 40 °C) | 2997.912 MHz |
| Phase advance | $2\pi/3$ |
| Flange-to-flange total length | 4150 mm |
| Number of cells | 122 |
| Operating temperature | $38-42^{\circ}\text{C} \pm 0.1^{\circ}\text{C}$ |
| Input coupler, double-feed type, | racetrack geometry |
| Output coupler, double-feed type, | racetrack geometry |
| Nominal accelerating gradient (guaranteed) | 20 MV/m |
| Targeted accelerating gradient | 25 MV/m |
| Targeted shunt impedance per unit length | 62 M Ω /m |
| Peak power for an accelerating gradient of 25 MV/m | 57 MW |
| Filling time | <1 μs (955ns) |
| RF pulse length (60 MW) | 1.2 μs |
| Optional RF pulse length (45 MW) | 4.5 μs |
| Maximum pulse repetition rate | 100 Hz |
| Material of the cavity | Cu-OFE |
| Material of the flanges, supports and cooling connectors | 316LN |
| Concentricity tolerance | +/- 150 μm |
| Design pressure of the cooling channels | 16 bar |

The iris design has been optimized by introducing an elliptical shape to reduce the maximum surface electric field (Figure 3.2.2.2). The iris aperture ranges from 12.695 mm upstream to 9.31 mm downstream. The input and output coupler cells have been symmetrized with dual feed and racetrack geometry. The maximum surface electric field and the accelerating field along the structure are described in Figure 3.2.2.3.

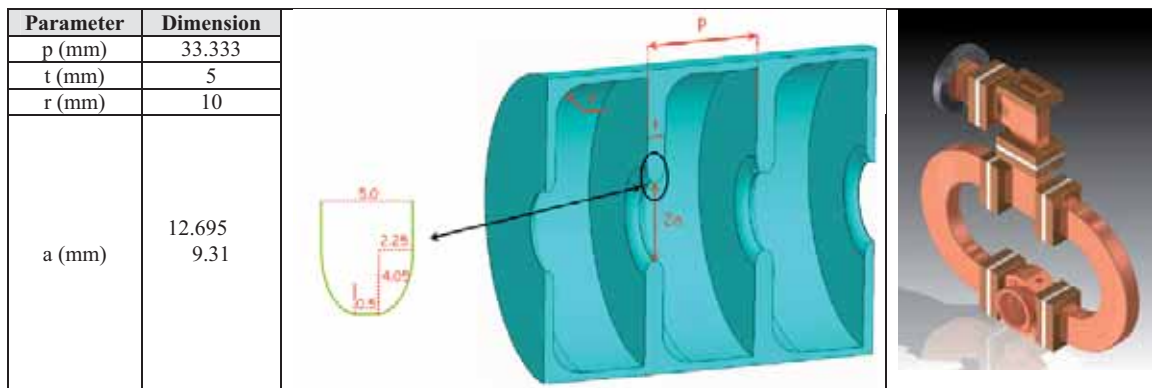


Fig. 3.2.2.2: Detail of the iris design of the booster cavities and 3D model of the wave guide system at the input coupler (only the first cell is shown here)

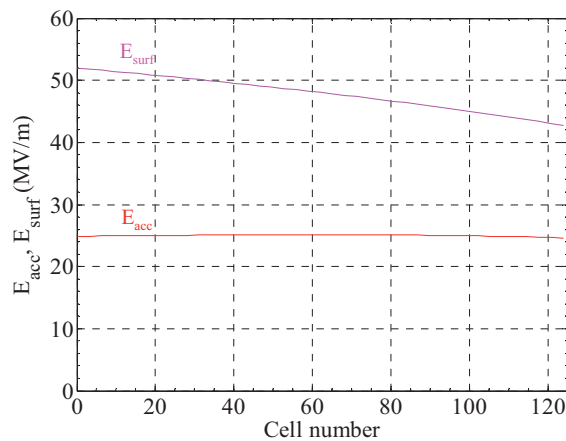


Fig. 3.2.2.3: Accelerating gradient and maximum peak surface electric field along the booster structure

3.2.3.2 X-band structures

The X-band harmonic structure is a modification of the SLAC H75 structure. This structure is being developed in collaboration with CERN, where it will be tested for high-gradient applications within the CLIC high-gradient R&D program. Two structures will be manufactured for PSI, while the FERMI project is also interested in joining the collaboration for two structures. The operating frequency for the SwissFEL Injector is 11995.2 MHz (see Table 3.2.1), with a temperature around 23 °C. The SwissFEL Injector test facility will, however, initially operate the X-band structure at 11991.648 MHz and 40°C. This travelling-wave structure is of the constant-gradient type, with a $5\pi/6$ phase advance and 72 cells, including the matching cells [53]. The active length is about 750 mm.

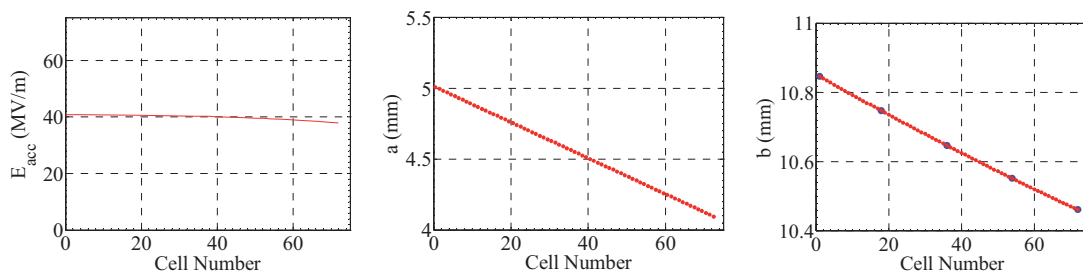


Fig. 3.2.2.4: Gradient, iris radius and cell radius along the harmonic X-band cavity.

In the SwissFEL Injector Test Facility, the structure will be operated at the nominal average gradient of 40 MV/m, resulting in a total decelerating voltage of 29 MV. The iris aperture (see Fig. 3.2.2.4) ranges from 4.993 mm upstream to 4.107 mm downstream. With such a small aperture, this structure will dominate the impedance budget of the entire injector. Misalignments larger than 10 μm can generate large transverse kicks, with catastrophic consequences on the final emittance. For this reason, cell numbers 36 and 63 have been radially coupled to four wave guide systems (Figure 3.2.2.5), to extract dipole mode signals which will give an indication about the cavity misalignment.

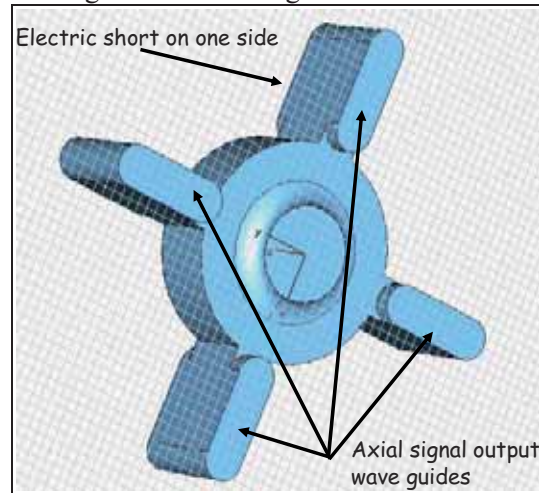


Fig. 3.2.2.5: Special cell design with output port for dipole mode monitoring

Table 3.2.3.2.1: Summary of X band structures specifications

| Operating frequency (at 40 °C) | 11995.2 MHz |
|--|--|
| Phase advance | $5\pi/6$ |
| Flange-to-flange total length | 1120 mm |
| Number of cells | 72 |
| Operating temperature | $23^{\circ}\text{C} \pm 0.1^{\circ}\text{C}$ |
| Input coupler | Mode launcher |
| Output coupler, last cell | |
| Maximal accelerating gradient (guaranteed) | 40 MV/m |
| Targeted accelerating gradient | 20 MV/m |
| Targeted shunt impedance, central cell R/Q | 9.3 k Ω /m |
| Peak power for an accelerating gradient of 20 MV/m | 7.2 MW |
| Filling time | 100ns |
| RF pulse length (50 MW) | 1.5 μs |
| Maximum pulse repetition rate | 100 Hz |
| Material of the cavity | Cu-OFE |
| Material of the flanges, supports and cooling connectors | 316LN |
| Concentricity tolerance | +/- μm |
| Design pressure of the cooling channels | bar |

A mode launcher is used to couple the RF power into the cavity, and a similar structure will be implemented at the end of the structure to couple out the residual power (Figure 3.2.2.6).

The manufacturing process will require a machining precision better than 2 μm . According to the experience accumulated at CERN and SLAC in this field, such a specification can be reached with modern temperature- and vibration-stabilized micro-machining tools (diamond turning).

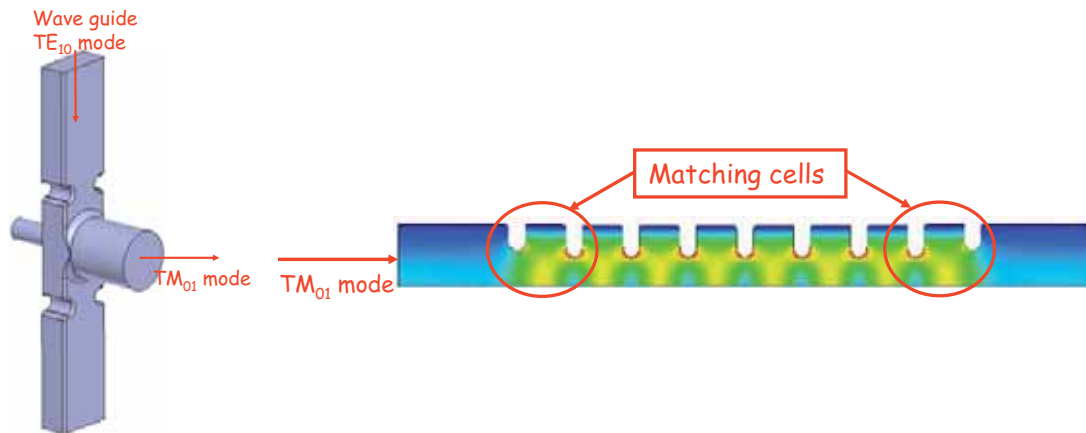


Fig. 3.2.2.6: X-band cavity 3D model of the mode launcher and EM simulation of the input/output matching cells with electric field amplitude

3.2.3.3 Deflecting structures

The first deflecting cavity at low energy will be a single cell pill box cavity developed in collaboration with INFN (Italy). A wave guide port will be used as input coupler and a small antenna as a pick up. The RF parameters are summarized in Table 3.2.3.3.1

Table 3.2.3.3.1: Specification of the low energy one cell deflector

| | |
|---|-----------|
| No. of Cells | 1 |
| Frequency (MHz) | 2997.912 |
| Nominal / Maximum deflecting voltage (kV) | 300 / 440 |
| Nominal / Maximum input power (kW) | 90 / 200 |
| Repetition rate (Hz) | 100 |
| Filling time (μ s) | ~0.8 |
| Nearest mode - different polarity (MHz) | 50 |
| Length flange to flange (m) | 0.1 |
| Quality factor - Q0 | ~15000 |
| Shunt Impedance deflecting mode R_{\perp} ($M\Omega$) | 0.5 |
| Aperture Beam pipe (diameter) (mm) | 38 |
| Working temperature | 40° |
| Temperature range (°C) | 35 - 50 |
| No. Pickups | 1 |

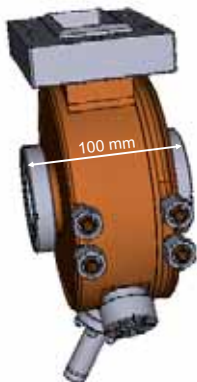


Figure 3.2.3.3.1: 1 Cell RF deflecting cavity for 7 MeV Beam

The high energy deflector is scaled from the structure developed for the SPARC project. It will be manufactured by INFN within a collaboration framework with FERMI at ELETTRA and PSI. The cavity is a 5 cell standing wave structure (see Fig 3.2.3.3.2); the operating mode is the $TM_{110,\pi}$ like hybrid mode. The RF parameters of this structure are summarized in Table 3.2.3.3.2.

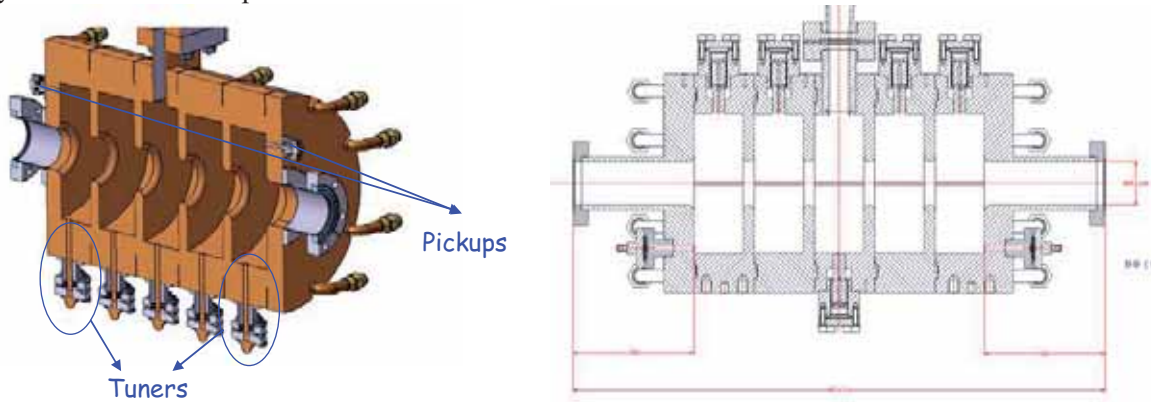


Figure 3.2.3.3.2: 3D model of the deflecting cavity designed by INFN for the FERMI project and the PSI version with the tuners displaced on the upper side.

Table 3.2.3.3.2: Specification for the 5 cell RF deflector to be installed at 250 MeV

| | |
|---|--------------|
| No. of Cells | 5 |
| Frequency (MHz) | 2997.912 |
| Nominal/Maximum deflecting voltage (MV) | 4.5 / 4.9 |
| Nominal/Maximum input power (MW) | 4.2 / 5 |
| Operating mode | π |
| Repetition rate (Hz) | 100 |
| Filling time (μ s) | ~ 0.8 |
| Nearest mode - different polarity (MHz) | 50 |
| Length flange to flange (m) | 0.5 |
| Quality factor - Q_0 | ~ 15000 |
| Shunt Impedance deflecting mode R_{\perp} ($M\Omega$) | 2.4 |
| Aperture Beam pipe – diameter (mm) | 38 |
| Working temperature | 40° |
| Temperature range (°C) | 35 - 50 |
| No. Pickups | 2 |

3.2.4 RF systems of the SwissFEL Linacs 1, 2 and 3

The Swiss FEL linac is composed of 104 two-metre-long accelerating structures, to boost the beam energy from 410 MeV at the injector to the final energy of 5.8 GeV. The accelerating structures are divided into 26 groups, so-called RF modules, each module being composed of four accelerating structures, one pulse compressor, one 50 MW klystron and one solid-state modulator (Figure 3.2.3.1). The 26 modules are distributed over three linacs: Linac1, composed of 8 modules and inserted between the two-bunch compressors; Linac2, composed of 7 modules, between the second bunch compressor and the switchyard; and Linac3, composed of 11 modules after the switchyard. The design frequency of these C-band structures is 5712 MHz, as in the Linac of the SCSS project [54].

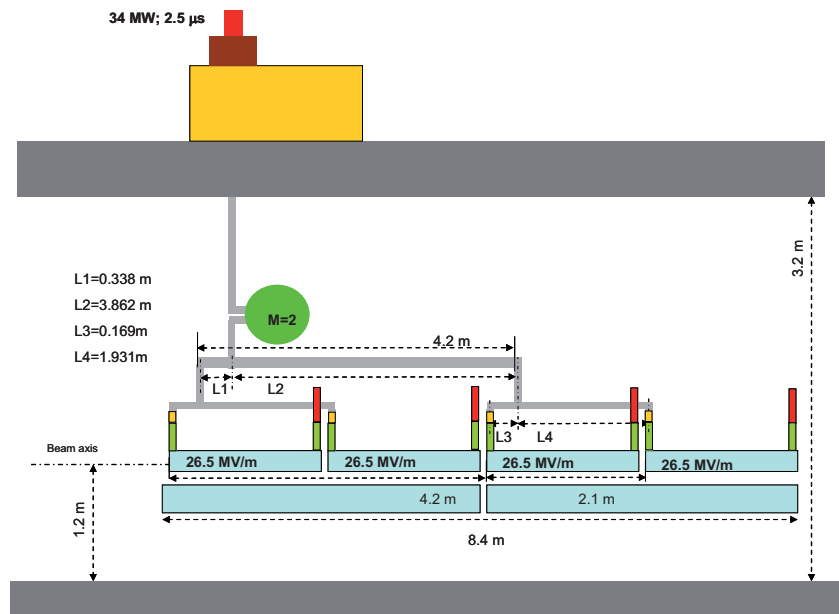


Fig. 3.2.3.1: Layout of a C-band RF module: 4 C-band structures; 1 pulse compressor cavity; 1 klystron and 1 modulator.

The peak power of the klystron is 50 MW, with a 2.5 μ s pulse length. Single-bunch operation requires 34 MW. The power requirements are determined by the required average gradient (26.5 MV/m), the accelerating structure design, the energy multiplication factor of the pulse compressor (indicated as M in Figure 3.2.3.1), and the overall losses in the waveguide network. The waveguide network is based on an asymmetric design, in order to better synchronize the compressed pulse with the bunch; the average RF path length from the klystron output to the accelerating structure input is roughly 9 metres, which ideally corresponds to 7% losses. Taking into account the pulse compressor and all the flanges, a value of 20% has been assumed for the losses.

In the case of two-bunch operation mode with a bunch spacing of 50 ns, the required power is between 40 and 44 MW, and depends on the accelerating structure design and on the pulse compressor design.

The C-band accelerating structures consist of 110 cells, including the two coupler cells of the J-type, and operate with a $2\pi/3$ phase advance. The length of each cell is 17.495 mm and the active length of each structure is 1.92 m. Three cell topologies are under study: the disk-loaded cell (Figure 3.2.3.2a.), the cup-like cell (Figure 3.2.3.2b.), and the rounded-wall cell (Figure 3.2.3.2c). Each type of cell has elliptical-shaped iris tips optimized to minimize the peak surface electric field.

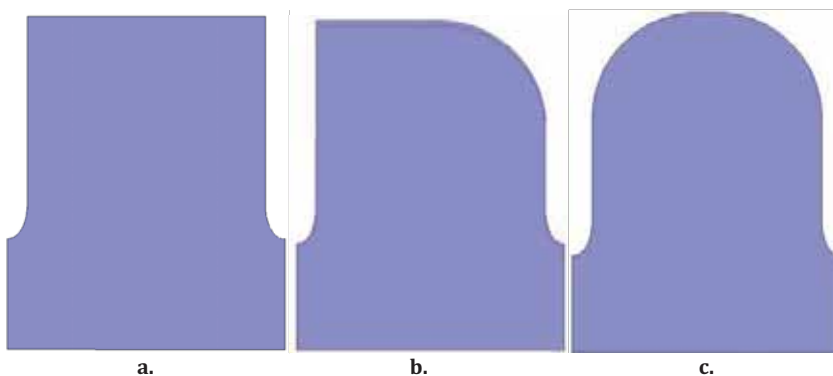


Fig. 3.2.3.2: Different cell topologies under study

The variation of the group velocities and of the r/Q function on the iris radius (Figure 3.2.3.3) for an iris thickness of 2.5 mm (the minimum achievable for mechanical rigidity reasons) is about the same for all three types of cell. However, for a given iris radius, the quality factor of the disk-loaded cells is 4 % lower than for the cup-like cells. The quality factor of the cup-like cells is 6 % lower than for the cells with double rounding of the walls.

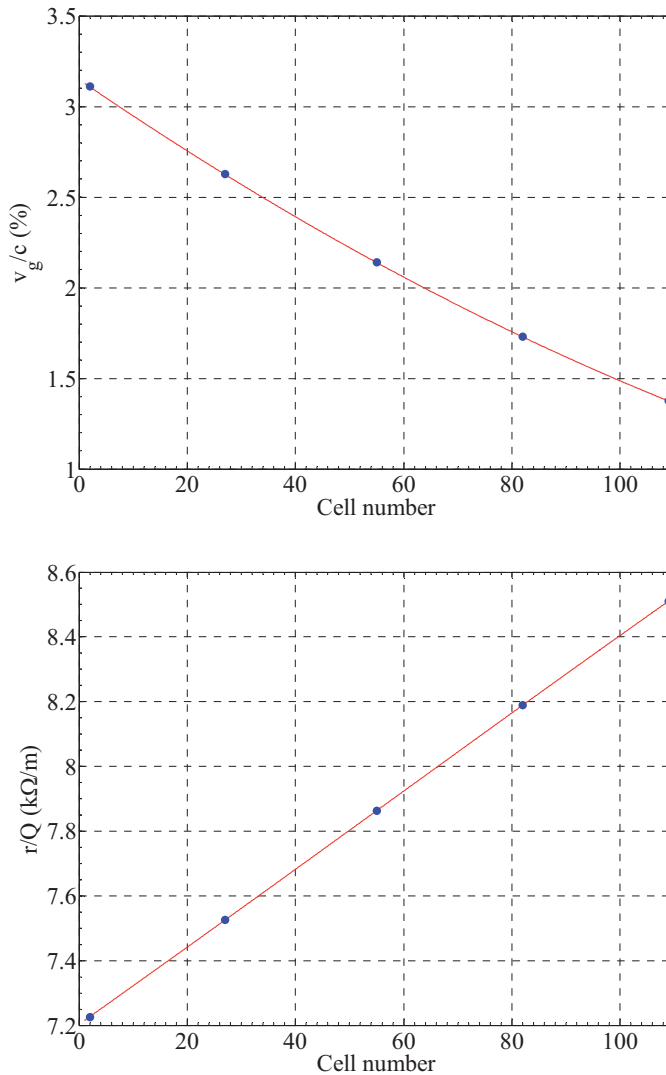


Fig. 3.2.3.3: Variation of v_g/c and r/Q vs. cell number, for structure with rounded-wall cells

Three types of constant-gradient accelerating structure, one for each type of cell, have been synthesized, with an average iris radius of 6.437 mm, this choice being dictated by longitudinal short-range wakefields issues and beam-dynamics requirements. For these structures each elliptical iris tips have been optimized to ensure minimum surface electric field..

The variations of iris apertures for all three structures are as follows:

- Disk-loaded structure: iris radius, a , varies from 7.341 mm to 5.532 mm
- Structure with cup-like cells: iris radius, a , varies from 7.313 mm to 5.56 mm
- Structure with double rounding of the cell walls: iris radius, a , varies from 7.267 mm to 5.606 mm

The power requirements without pulse compressor, to achieve an accelerating gradient of 26.5 MV/m, are similar for all three structures and are about 27 MW. Ultimately, the choice of cell

type will be dictated by manufacturing issues, each type of structure having different brazing planes of the cells, and by the RF efficiency of a whole module.

The key device of the RF power distribution is the pulse compressor. Two possible designs have been studied and compared: the SKIP, which is the pulse compressor for SUPERKEKB (Figure 3.2.3.4), and a C-band version of the Barrel-Open Cavity (BOC) (Figure 3.2.3.5).



Fig. 3.2.3.4: SKIP pulse compressor used at KEK

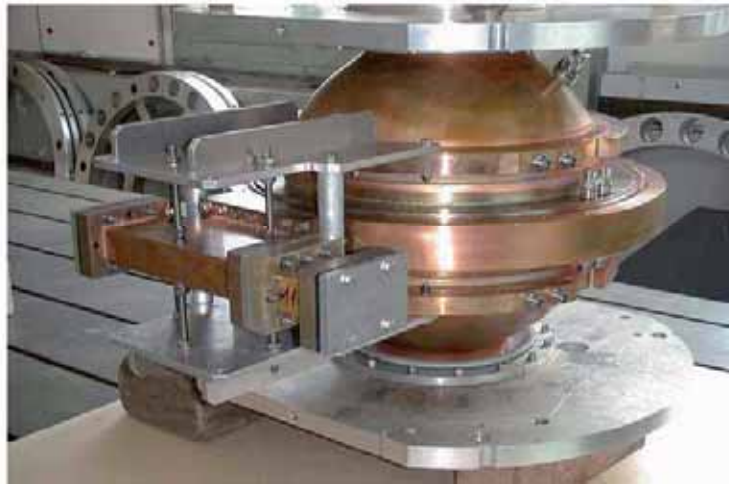


Fig. 3.2.3.5: 3 GHz BOC used at the CLIC Test Facility (CERN)

The SKIP is a conventional LIPS-based design using the $TE_{0,3,8}$ mode. However, studies have showed that to operate in the $TE_{0,3,11}$ mode results in a quality factor Q approximately 10 % larger than for the $TE_{0,3,8}$ mode. Note that care has to be taken to ensure that in both cases the $TM_{1,3,8}$ mode and $TM_{1,3,11}$ mode are not degenerate with the operating modes. This is achieved by designing, in both cases, the base plane of the cavities with grooves. The BOC is a redesign at C-band of a 3 GHz BOC operated at CERN in the CLIC Test Facility. This new design used the whispering-gallery mode $TE_{18,1,1}$ and provides very large Q ($\sim 220,000$), as well as being compact (single cavity). The electric field configuration of this BOC is shown in Figure 3.2.3.6, in the symmetry plane.

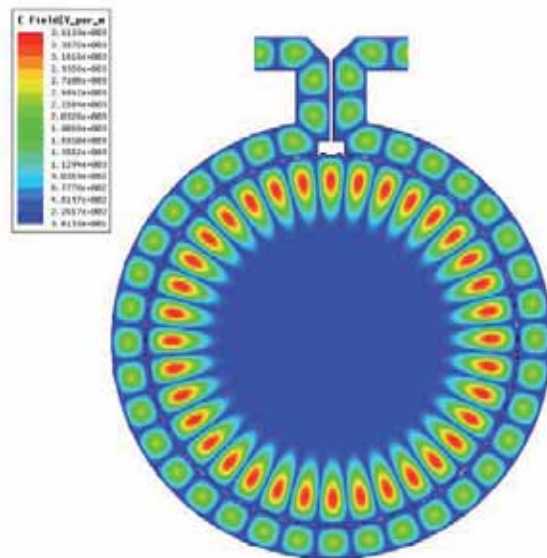


Fig. 3.2.3.6: Electric field amplitude at a given time of the BOC in its symmetry plane

For each type of accelerating structures, the RF efficiency of each module is conditioned by the quality factor and by the coupling factor β of the pulse compressor. Figure 3.2.3.7 shows that there is a clear advantage operating with a BOC-type pulse compressor instead of a SKIP-type.

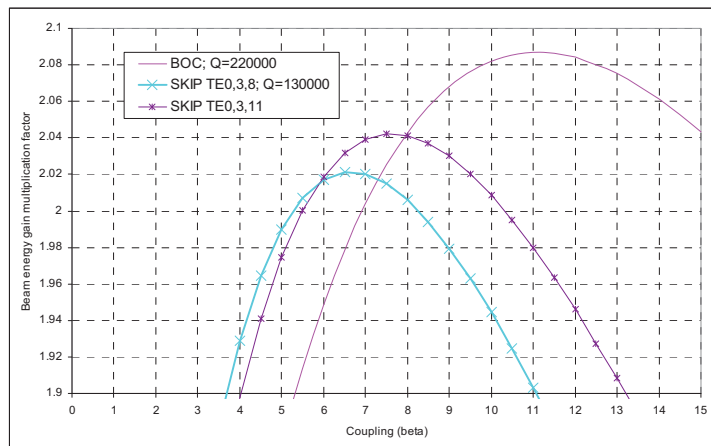


Fig. 3.2.3.7: Energy gain multiplication factor for SKIP-based pulse compressor and BOC vs. coupling factor for an accelerating structure consisting of cup-like cells

For single-bunch operation, and for all possible combinations of accelerating structures and pulse compressor, an energy gain per structure higher than 53 MeV is achievable (Figure 3.2.3.8) with a klystron power of 40 MW.

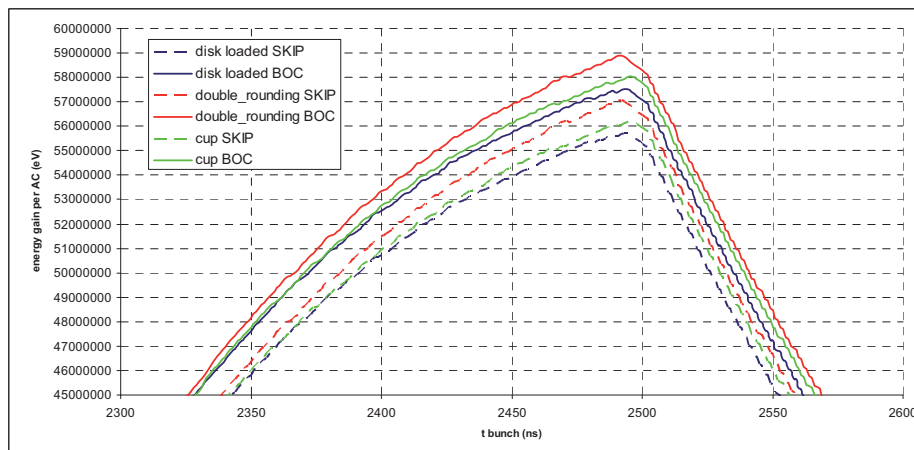


Fig. 3.2.3.8: Energy gain per accelerating structure for all three types of accelerating structures and for SKIP-type and BOC-type pulse compressors vs. bunch arrival time— single-bunch operation

For two-bunch operation and a 28 ns bunch spacing, the favoured option consists of creating a plateau in the curve of energy gain per accelerating structure vs. bunch arrival time. This can be achieved by performing a phase modulation on the klystron drive signal. Operating with a BOC-type pulse compressor and with the structure which has rounded cell walls allows the required 53 MeV energy gain per structure to be reached with 40 MW klystron power, the other combinations requiring more klystron power.

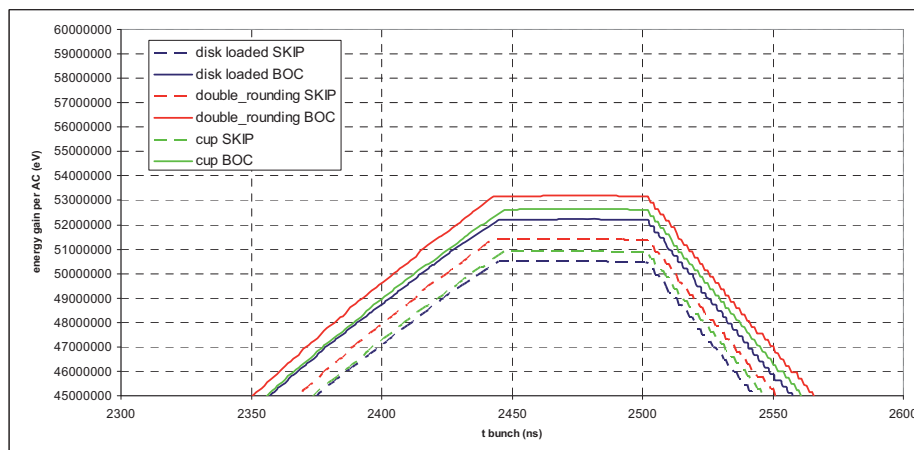


Fig. 3.2.3.9: Energy gain per accelerating structures for all three types of accelerating structures and for SKIP-type and BOC-type pulse compressors vs. bunch arrival time – two-bunch operation

One issue related to the accelerating structures requiring further study is the effect of longitudinal and transverse long-range wakefields on the beam dynamics in the multi-bunch regime. An accelerating structure with a detuning of the two fundamental dipole bands is under consideration.

3.2.5 Power systems for SwissFEL Injector

The power sources provide the high-voltage pulsed power for the klystron amplifiers in the system. These different sources are characterized by their peak power, pulse width, and high voltage and current capabilities. A detailed description of power system parameters is still under study. In any case, the klystrons will be powered by solid-state modulators, as in the existing SwissFEL Injector Test Facility. The maximum electrical parameters of the modulator power sources installed at the SwissFEL Test Facility are given as an example in Table 3.2.4.1.

Modulators that provide this high power are connected to the klystron loads through low leakage inductance and low stray capacitance high-voltage step-up pulse transformers. The flat top of the voltage pulses produced are approximately equal to the RF pulse width of the klystron. The modulator energy efficiency is mainly determined by the rise and fall times of the voltage pulses, which will be approximately 1 μ s and 2 μ s (10 to 90%), respectively.

Table 3.2.4.1: Modulator operational parameters of the klystron amplifiers at the SwissFEL Injector Test Facility (European frequencies)

| | 3 GHz RF gun K2-1L | 3 GHz Linac - mode 1 to 3 K2-2S | | | 12 GHz K2-3X | 3 GHz TDC K1-2S | Unit |
|-----------------------------|--------------------------|------------------------------------|------|------|-----------------|--------------------|-------------|
| | | 30 | 45 | 60 | | | |
| RF peak power | 30 | 30 | 45 | 60 | 7.5 | 50 | MW |
| RF average power | 15 | 4.5 | 22.5 | 9 | 3.75 | 5 | kW |
| Peak power klystron | 71.4 | 69.7 | 104 | 146 | 15.7 | 107 | MW |
| Average power klystron | 53.1 | 19.6 | 65.2 | 42.5 | 10.2 | 26.5 | kW |
| Klystron voltage range | 266 | 261 | 307 | 351 | 148 | 410 | kV |
| Klystron current range | 268 | 267 | 340 | 416 | 106 | 262 | A |
| Pulse length (top) | 5 | 1.5 | 5 | 1.5 | 5 | 1 | μ s |
| Max pulse length (at 76%) | 7.4 | 3.9 | 7.4 | 3.9 | 7.4 | 3.4 | μ s |
| Repetition rate | 10-100 | 10-100 | | | 10-100 | 10-100 | Hz |
| Flat-top flatness (dV) | < \pm 0.2 | < \pm 0.2 | | | < \pm 0.2 | < \pm 0.2 | % |
| Rise rate (at 50% voltage) | 170/270 | 250-360 | | | 300-420 | 148 | kV/ μ s |
| Fall rate (at 50% voltage) | 170/270 | 250-360 | | | 300-420 | 70-148 | kV/ μ s |
| Amplitude stability (rms) | < \pm 0.02 | < \pm 0.2 | | | < \pm 0.02 | < \pm 0.02 | % |
| Pulse-to-pulse jitter (rms) | <5 | <5 | | | <5 | <5 | ns |
| Pulse length jitter (rms) | < \pm 10 | < \pm 10 | | | < \pm 10 | < \pm 10 | ns |

The primary energy storage in each modulator can be either a pulse-forming network (PFN) or a capacitor. The PFN line-type modulator method (Figures 3.2.4.1 and 3.2.4.2) provides a fixed pulse width voltage pulse having a source impedance that is matched to the klystron impedance. The stored energy in the PFN is made just sufficient to satisfy the klystron load requirements. In this case, the high-voltage switch on the primary side of the pulse transformer needs to be only an ON device, such as a Thyatron or SCR assembly.

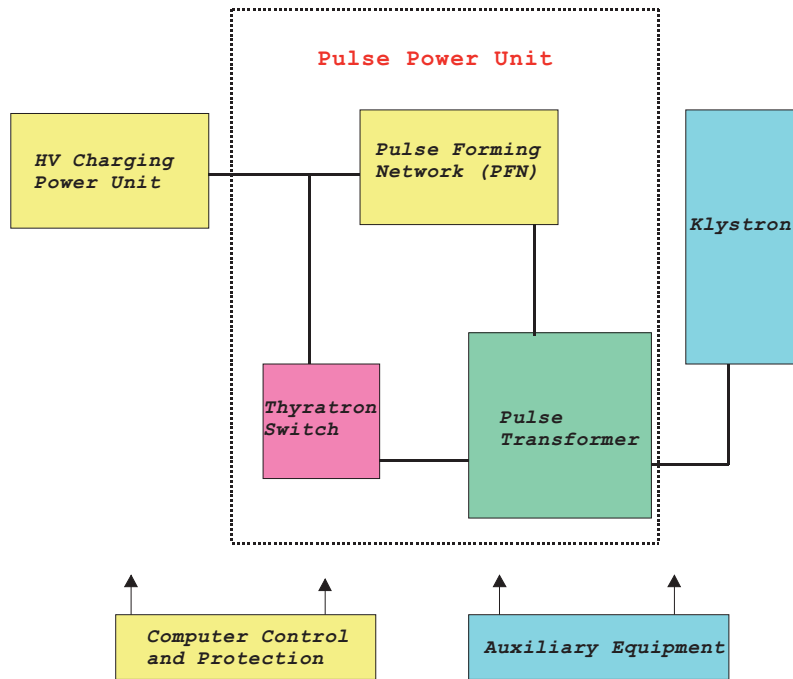


Fig. 3.2.4.1: Line-type modulator block diagram

In the second method (see Figure 3.2.4.3), where a capacitor discharge source is used, the stored energy has to be very much larger than that required by the klystron load, to ensure a voltage flat-top region with a small percentage voltage drop. Additional protection is needed in this case, to protect the klystron from receiving excessive energy from the storage capacitor in the case of a gun arc. This type of modulator mostly uses an IGBT solid-state on-off switch to define the voltage pulse duration. Since these devices operate in a lower voltage region (3 to 6 kV), the step-up ratio of the pulse transformer needs to be a higher ratio than when a Thyatron switch is used (30 to 40 kV), and consequently requires special transformer technology to ensure that the rise and fall times mentioned above can be achieved.

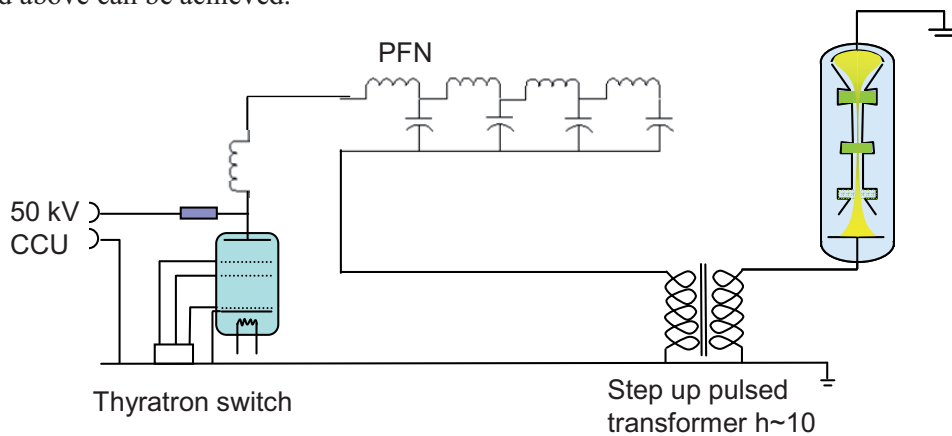


Fig. 3.2.4.2: Typical scheme of a PFN modulator

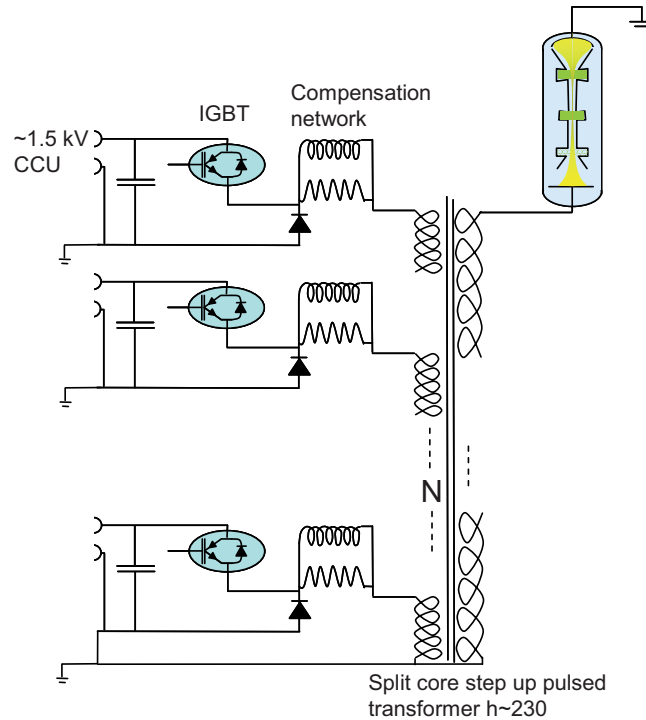


Fig. 3.2.4.3: Electrical schematic of a solid-state modulator

Both these types of modulator have been investigated from the point of view of performance specification, reliability, maintainability and cost.

A few PFN modulators using conventional Thyatron switch technology are already in operation at the SwissFEL Gun Test Facility and the SLS, with known reliability and running experience. The main weakness of this approach, especially at high repetition rates, is the relatively short lifetime of the Thyatron switch (15,000 to 20,000 hours), which substantially contributes to the operational costs and reliability. The pulse behaviour is fixed by the number of cells in the PFN and can be modified only by changing the capacitor configuration inside the modulator rack. The size of the components and the mechanical assembly is adapted to the relatively high voltages of the PFN line, fixing a physical limit to the compactness of the HV cabinet.

A low-power solid-state modulator has been purchased for the SwissFEL Gun Test Facility (LEG), introducing a new technology to PSI. This very compact device has been tested, with extremely fast installation and commissioning times. The modulator is composed of a series of low voltage (~ 1 kV) switching modules connected in parallel to the step-up transformer (see Figure 3.2.4.3). Experience at PSI with the solid-state modulator has shown the following advantages:

1. Fast installation (only three main connections for electrical power, cooling and controls)
2. Modularity (the same switch modules can be stacked in different configurations, i.e. fewer spare components needed)
3. Reliability (70,000 hours without failures recorded by the suppliers; a few modules can fail without perturbing modulator operation)
4. Compactness
5. Adjustable pulse length
6. KHz repetition rate

At a comparable investment cost, and based on the positive experience obtained so far, PSI has decided to explore the solid-state option for the SwissFEL Injector Test Facility. The 3 GHz and 12 GHz modulators will produce a much higher peak power, and the design needs a large amount of parallel-operating solid-state IGBT devices with a high-ratio step-up pulse transformer, in order to handle the same power as a PFN modulator with a single Thyatron or SCR assembly could handle.

The new modulators have been delivered as “single rack” amplifier units, integrating the tank, water distribution and power supplies for the klystron solenoids and heater (see Figure 3.2.4.4).



Fig. 3.2.4.4: Drawing of the high-power modulator K2 from the company SCANDINOVA (10–60MW; 200–450 kV) (top), and photograph of the installed prototype at the SwissFEL Injector Test Facility (bottom).

The klystron loads for the modulators are high-gain RF power amplifiers that usually have a narrow bandwidth (10%) at the fundamental frequency. The Thales TH2100 klystron shown below (Figure 3.2.4.5) is a typical example.

The RF output pulses from each klystron are transmitted via an RF window that is conditioned to operate with an SF₆ gas pressure of about 2 bars. This electro-negative gas enhances the voltage hold-off capability in the presence of high forward and reflected power occurring in phase together at the window. If this should occur, the used gas is recovered in a closed-circuit system and the window volume is flushed with clean gas and re-filled.



Fig. 3.2.4.5: High-power klystron amplifier TH2100 (Thales)

As mentioned above, the shot-to-shot RF phase and amplitude stability are particularly critical, because they can potentially generate large FEL fluctuations (arrival time, power, wave length). Assuming a stable distribution network, the RF phase and amplitude are mainly driven by the modulator voltage stability. To meet the FEL tolerance specifications (~ 0.03 deg rf in Table 2.4.4.2), the relative voltage stability must be of the order of 10^{-5} . This will require an effort in ameliorating the capacitor charging scheme, which usually reaches values one order of magnitude larger than those specified. To overcome this problem, we are developing at the injector facility, and in collaboration with the modulator suppliers, an R&D programme to improve the performance of the commercially available hardware. Recent encouraging measurements of achievable phase stability have been carried out at the SwissFEL Injector Test Facility. The experimental data reproduced below in Figure 3.2.4.6 indicates that a solid-state-based S-band power plant is able to reach shot-to-shot phase stabilities below 0.02° . A slow feedback system is nevertheless needed to correct slow phase fluctuations which might be induced by thermal drifts of the power plant components.

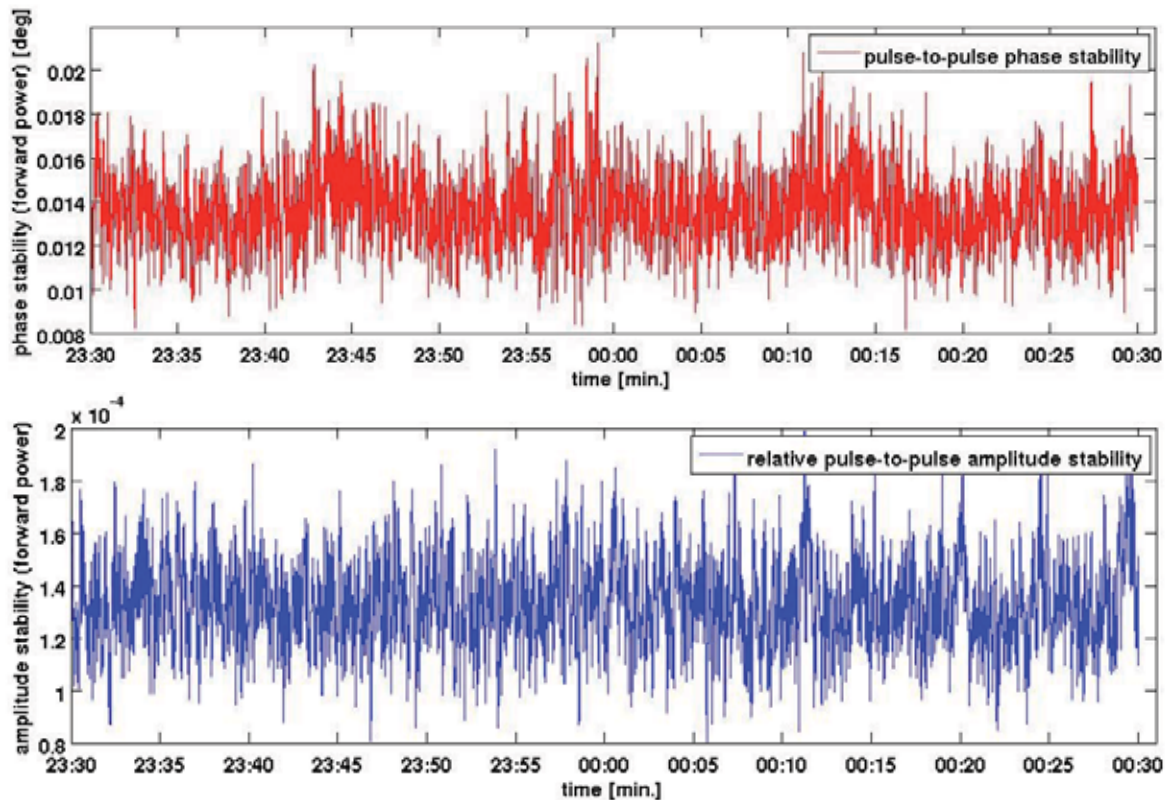


Fig. 3.2.4.6: Top: Pulse-to-pulse phase stability of the incident RF power as standard deviation over the last 40 pulses (repetition rate 10 Hz). At each pulse, the phase is averaged over 400 ns. Bottom: Pulse-to-pulse amplitude stability of the incident RF power as standard deviation over the last 40 pulses, measured at the S-band power plant of the SwissFEL Injector Test Facility.

3.2.6 Power systems for the C Band SwissFEL linac

The basic idea for the linac RF power system is to keep it identical to the injector systems as far as possible.

3.2.6.1 C-Band Klystron

Due to the frequency choice the available klystron types are limited. Toshiba has an existing type at the required frequency but this type is still too low in average power. Toshiba is designing an improved version compliant with the requirements of the SwissFEL project.

Table 3.2.6.1: Technical data of the C-Band klystron types

| | Existing Klystron E37202 | Upgraded Version E37210 | Unit |
|-------------------------------------|-----------------------------|----------------------------|---------|
| Nominal Frequency | 5712 | 5712 | MHz |
| RF peak power | 50 | 50 | MW |
| Peak Cathode Voltage | 370 | 370 | kV |
| Peak Klystron Current | 344 | 344 | A |
| High Voltage Pulse Width | 6.2 | 6.2 | μ s |
| RF Pulse Width | 2.5 | 3 | μ s |
| Average RF Power | 7.2 | 15.6 | kW |
| Average Collector Power Dissipation | 35 | 78 | kW |
| Pulse Repetition Rate | 60 | 100 | pps |
| RF Bandwidth @ -1.5 dB | +/- 5 | +/- 5 | MHz |
| Gain | 50 | 50 | dB |



Fig. 3.2.6.1: Similar C-Band klystron (Toshiba E3748)

3.2.6.2 C-Band Modulator

The modulator technical requirements are very close to the data of the S-Band systems. The modulator baseline design is an updated version of that system. The redesign of the modulator will be required in order to optimise the system for the linac operation. The modulators shall be built in such a way to allow transportation in the technical building and installation with only a small local crane at the modulator final position. The modulator will have to be built with an integrated power factor compensation in order to limit the harmonic current and asymmetric phase currents on the mains.

Table 3.2.6.2: Target parameters for the C-Band Modulator

| | Value | Unit |
|---|-----------|---------|
| Peak Voltage | 370 | kV |
| Peak Current | 344 | A |
| Pulse Repetition Frequency | 100 | Pps |
| Pulse-to-pulse stability (Std. Deviation) | 10^{-5} | |
| High Voltage Pulse Width @76% | < 6.2 | μ s |
| Flattop Ripple (peak-peak) | < 0.4 % | |
| Mains Supply | 400 | V |
| Mains Power Factor | > 99 % | |

The modulator will be separated in two or more mechanical units in order to allow transportation and installation inside the SwissFEL technical building. Figure 3.2.6.2 shows the reference design for the modulator mechanics. The tank with the transformer and the klystron socket will be a separate unit. The racks with the electronics and auxiliaries will be placed close to the modulator on a double floor.

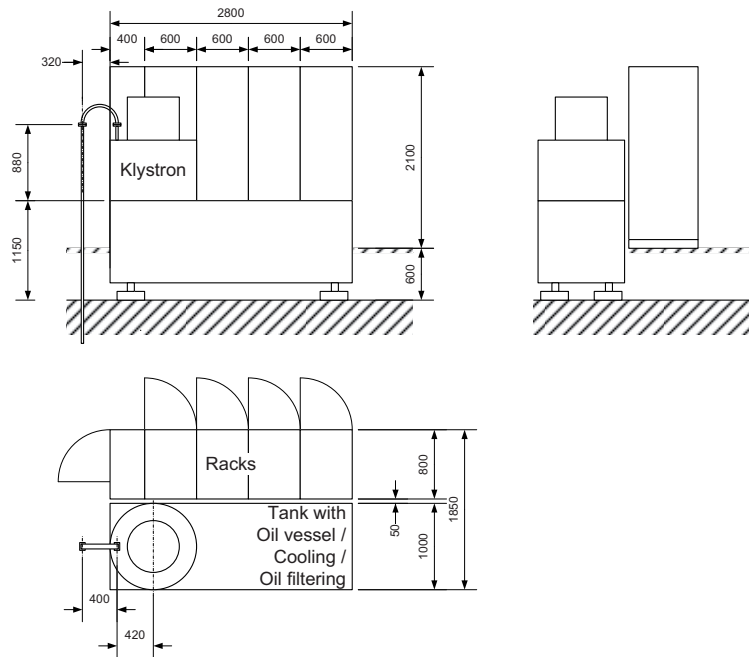


Fig. 3.2.6.2: Modulator Mechanics Reference Design

3.2.7 Low-Level RF

The Low-Level RF (LLRF) system has to synchronize and control the RF fields in the accelerating structures to the tight tolerances specified in Section 2.4.4. In the SwissFEL injector, each RF structure, namely the 3 GHz RF gun and the S-band and X-band travelling wave structures, is likely to be fed by a separate klystron, in contrast to the main linac, where a single klystron and an RF pulse compressor delivers RF power to four C-band structures (see Section 3.2.3). A generic overview of one RF station in the main linac is given in Figure 3.2.5.1. The controller therefore has to regulate amplitude and phase of the vector sum of a string of four accelerating structures.

The LLRF system is based on modern FPGA technology and floating point processing platforms. Such a system allows the required flexibility for different RF stations, especially for the necessary

phase switch for the RF pulse compression in the main linac. The RF signals from pick-ups and directional couplers are down-converted to common intermediate frequencies (f_b), which are digitized by high-resolution, low-noise analogue-to-digital converters (ADC). Thus, the digital signal processing hardware and main parts of the firm- and software are generically independent of the RF frequency (f_{RF}). Local phase-locked loops generate a phase-stable, low-noise RF signal, with the frequency which is required at each RF station to drive the vector modulator (see Section 3.3.1). The IF frequency has to be chosen so that it is a sub-harmonic of the RF frequency (f_{RF}), in order to alleviate the frequency generation. In addition, it has to be high enough to allow for a sufficient detection bandwidth of the RF signal, but finally also low enough to avoid performance degradation due to clock jitter of the successive ADCs. Today's state-of-the-art technology can provide 16 bit ADCs with sampling rates well beyond 100 MHz. The application of the non-IQ algorithm [55] for the I/Q detection in the LLRF digital signal processing part implies the use of IF frequencies of the order of a few 10's of MHz up to a maximum of 100 MHz. The definition of the exact ADC sampling and IF frequencies, including their generation, is part of the R&D process.

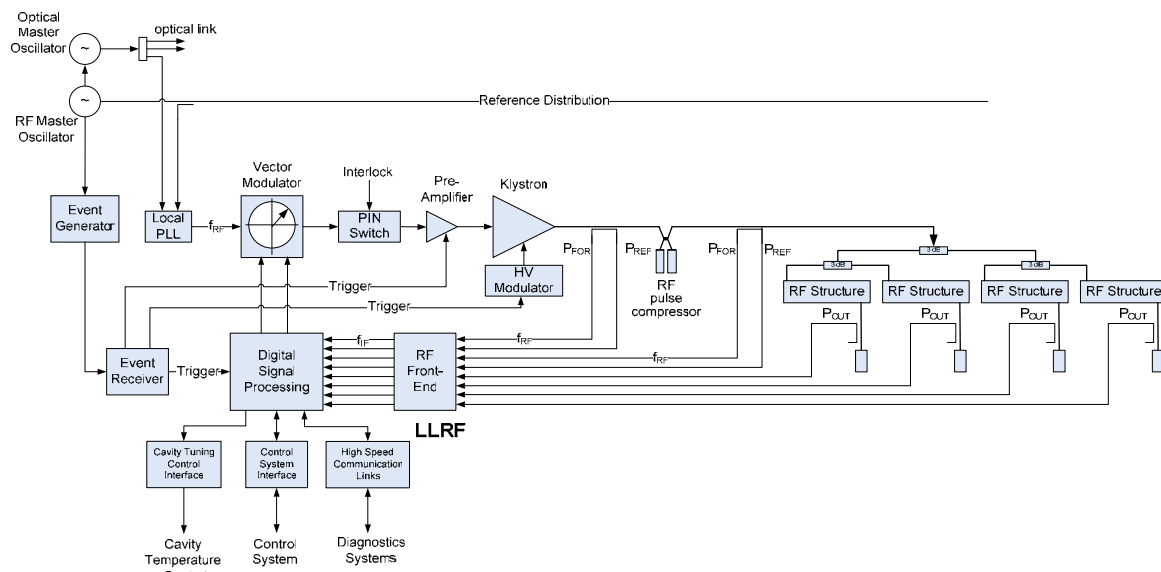


Fig. 3.2.5.1: RF system overview of one RF station in the main linac with RF pulse compression

All frequencies of the LLRF system (ADC/DAC clocks, local oscillator frequencies for the RF front-ends) are derived from the reference distribution and thereby tightly locked to the master oscillator. The trigger signals for pre-amplifier, modulator and digital signal processing are generated by an event-receiving unit which is directly coupled to the global event generator. The RF pulse duration is of the order of a few μs , which is too short for efficient intra-RF pulse feedback, due to the inherent latency of the digital system. In case the high-voltage modulators or the pre-amplifiers do not provide the necessary short-term stability, which may result in pulse-to-pulse phase jitter, the implementation of fast analogue intra-pulse phase stabilization loops around the amplifier chain may be necessary. Pulse-to-pulse feedback corrects slow drifts in amplitude and phase, while adaptive feed-forward techniques provide the ability to reduce repetitive distortions. In order to compensate for drifts, it is therefore of utmost importance to minimize the drift of the components in the measurement path. To achieve this goal, all measurement cables from the directional couplers to the LLRF system, and the LLRF electronics itself, will be placed in a temperature-stabilized environment, with temperature variations not exceeding $\pm 0.1^\circ\text{C}$. During the R&D phase, the application of pulse-to-pulse calibration techniques will be explored, to minimize any remaining drifts and low-frequency jitter in the measurement of amplitudes and phases. In addition, the LLRF electronics provides optical high-speed Gigabit communication links to other sub-systems, which allow the implementation of beam-based feedbacks, such as longitudinal

feedback. Pulse-to-pulse stability is then solely determined by the stability of the actuator chain, which consists of the reference distribution, the local phase-locked loops, the vector modulator, the pre-amplifier and the high-voltage modulator, together with the klystron. Each of these components has to provide stability such that the required short-term amplitude and phase stability of a RF station (as given in Section 2.4.4) is reached.

3.3 Timing and synchronization

3.3.1 Reference distribution system

3.3.1.1 Purpose of the timing and synchronization system

In an accelerator (and particularly in a free electron laser (FEL)) the electron bunches to be accelerated and linearly compressed demand extremely stable field phases in the RF accelerating cavities (with respect to the time they have been emitted from the gun photocathode by the gun laser). The SwissFEL RF structures, which will be operated at frequencies around 3, 6 and 12.0 GHz (S-, C- and X-band, respectively), need reference signals with the property that the temporal position of their zero-crossings, measured over a certain time (some ms) at different points in the machine, has to achieve a stability level below 10 fs. Moreover, the temporal stability and synchronization of laser systems at the experimental stations of the SwissFEL facility need to be kept within the lengths of the X-ray pulses over the duration of pump probe experiments (several minutes to hours). A number of diagnostics systems, such as, for example, beam arrival time monitors (BAM) and electro-optical bunch length monitors (EOM), will be able to measure the longitudinal properties of the electron bunches with reference to a temporally stable timing and synchronization system. Such beam-based information may be used to further improve the temporal stability of SwissFEL through longitudinal feedback systems. Although some other “clients”, such as the master event generator for the timing system and the beam position monitors (BPMs) for measuring transverse beam positions, may not need such high timing stability, the SwissFEL timing and synchronization system will be designed to provide fs stability, during short time periods of some μs up to some ms, to the majority of the “critical clients” along the accelerator and at the various experimental stations.

3.3.1.2 Concept of reference generation and distribution

The SwissFEL with its extreme jitter and stability demands (cf. Section 2.4.4) poses new challenges for the synchronization system, i.e. the reference signal generation as well as its distribution. Our concept is based on optimized microwave fiber-optic links, which is a well established, cost effective, low risk and reliable technology and also offers the best potential performance and flexibility. Systems with less critical jitter and drift requirements, as, for example, beam positioning monitors, will be synchronized with coaxial electrical links. Temperature-insensitive cables with drifts as low as a few fs/K/m will be used for short coaxial links. Uncritical systems can be fed with sub-distributions based on coaxial cable trunk lines with local phase-locked oscillators. The reference signal generation and most critical links of the reference distribution system will be optimized to achieve a benchmark jitter performance of around 10 fs, and a long-term (few hours) drift stability of a few 10's of fs in the most critical parts of the machine. Frequency stability will be $< 10^{-10}/\text{yr}$. Less than 10 fs in jitter and in long-term drift are being targeted with this fiber-optics-based system. Figure 3.3.1.1 shows a generic block diagram of the synchronization system. The RF frequencies to be distributed are derived from a common subharmonic, f_b . This subharmonic should be around 100 MHz, to enable optimum performance of the pulsed laser (optical master oscillator) and the pulsed optical receivers. The optical master oscillator laser's repetition rate is ideally chosen to be equal to this subharmonic frequency. Higher flexibility could be achieved if a single frequency standard (European only or US only) could be used for the RF systems in the machine. However, SwissFEL will mix two standards and has to find the minimum common sub-harmonic (see Section 3.3.5). A higher repetition-rate laser can be locked to this basic repetition rate, using optical cross-correlation.

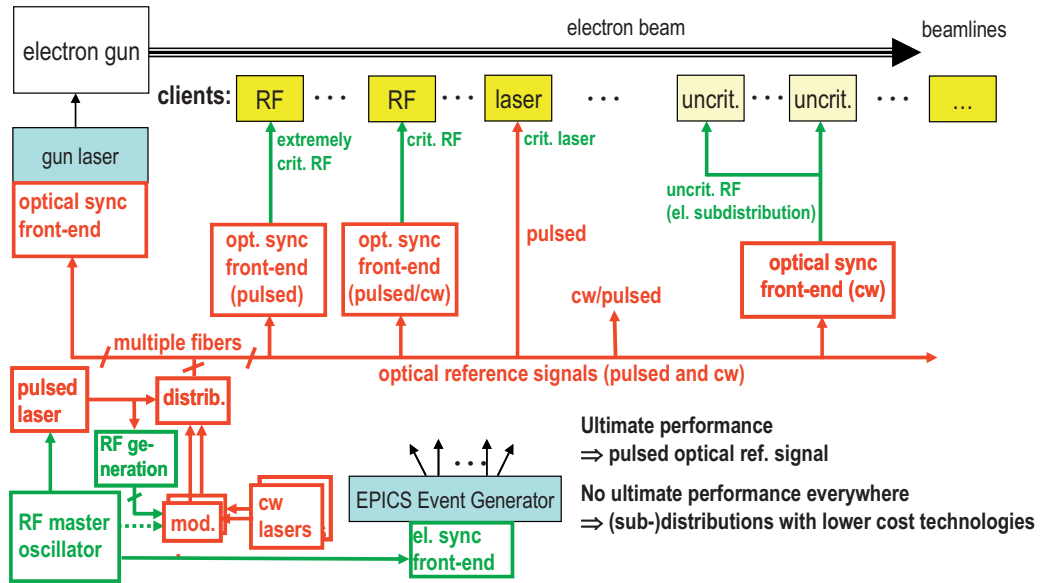


Fig. 3.3.1.1: Generic layout of the hybrid optical/electrical reference distribution system planned to be implemented in SwissFEL.

3.3.1.3 Most critical jitter and drift requirements

The most critical clients with respect to jitter and drift are located in the injector, as well as in the experimental areas. In addition, BAMs located at various points in the machine and the seeding laser also require extremely stable reference signals. Table 3.3.1.1 summarizes the requirements and Table 3.3.1.2 shows the expected performance, using various principles.

Table 3.3.1.1: Most critical jitter and drift requirements (BAM: beam arrival time monitor).

| | |
|--|--|
| Most critical parameters for sync system: Jitter (RMS, 10Hz..10MHz) and long-term drift (hours) | |
| <u>Gun laser:</u> | ≈30 fs expected (goal: 10 fs), to be measured with BAM |
| <u>Most critical RF stations:</u> | goal is "0.02° phase jitter at 3GHz (18.5 fs)" for SwissFEL RF system contributes >10fs (far out) intrinsic jitter, <5fs (diff. mode) is the requirement for the sync system |
| <u>Experiment (pump-probe) lasers:</u> | <10 fs (optical sync combined w. BAM for sorting of jittery experimental data) |
| <u>Seeding laser:</u> | <10 fs (optical sync combined w. BAM for drift FB) |
| <u>E/O sampling lasers:</u> | <50 fs |
| <u>BAM (opt. sync only):</u> | approximately 6 fs timing resolution/stability (down to 10pC) |
| "Differential mode jitter" between stations is critical, "common mode jitter" (all clients jittering with ref.) is uncritical. | |
| <u>Many drift/jitter specs for SwissFEL are not yet clear today</u> <u>→ a flexible & future-proof ref. system is required!</u> | |
| 10 fs is equivalent to 3 μm in air! | |

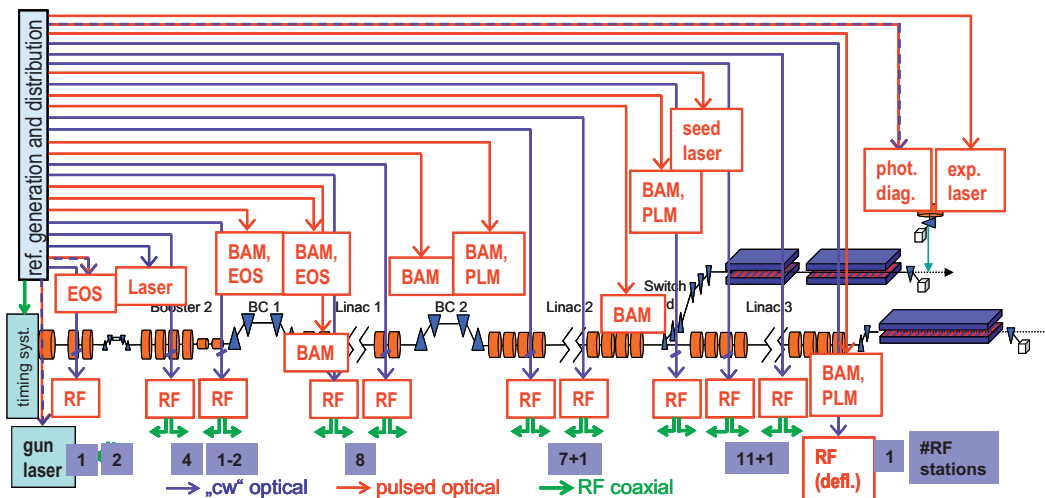
Table 3.3.1.2: Expected jitter and drift performance for different synchronization systems

| Link technology | Jitter ¹ | Drift ² | Principle |
|-------------------------------------|---------------------|--------------------------|---|
| RF/coax (temp. stab. ³) | some fs (potential) | ≈ps, ≈50 fs ³ | RFMO, power amp., trunk, taps, (RF phase det., thermal phase control ³) |
| optical pulsed (≈200fs) | <1 fs (potential) | <10 fs | OMO (RF sync), disp. compens., opt. x-corr.-based link stab. |
| optical cw (interferom. link stab.) | some fs (potential) | <20 fs | RFMO, ultra-stable cw laser, E/O modulator, lin. stage/vector mod. |
| optical cw (RF based link stab.) | <10 fs (potential) | ≈ps, ≈50 fs ³ | telecom DFB laser, E/O modulator, RF phase det., lin. stage/vector mod. |

¹ 10 Hz – 10 MHz rms with respect to reference, ² drift over some hours; ³ with RF link stabilization

3.3.1.4 Reference distribution layout for SwissFEL

Ultimate performance, particularly drift stability, and open/future-proof design can only be achieved with optical technologies. These offer extremely low drift (the possibility of using sophisticated link stabilization techniques), easy configurability and flexibility, EMI immunity, and simple and cost-effective installation. A star distribution will give the highest flexibility and can easily be realized with optical fibers (Figure 3.3.1.2).

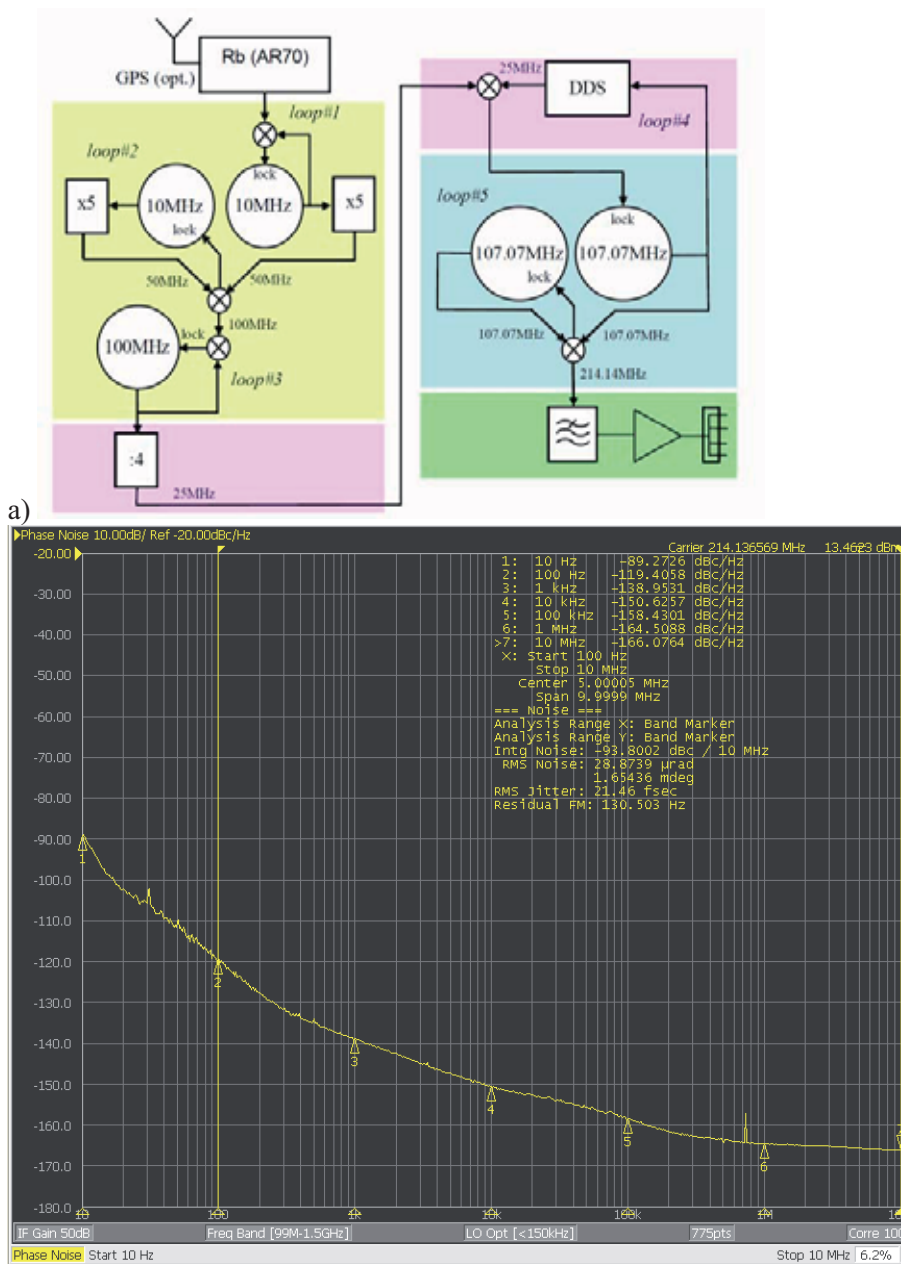


An RF station gets its reference signal over a dedicated optical link.
 An "RF" block in the drawing represent the number of RF stations indicated below.

Fig. 3.3.1.2: Proposed layout of the SwissFEL synchronization system (a block "RF" represents a group of RF stations, each of which requires an individual stabilized optical link).

3.3.1.5 RF master oscillator

A low phase noise RF master oscillator operating at a reference frequency of 214.1366 MHz (14th subharmonic of Eu S-band RF frequency) has already been implemented in the SwissFEL Injector Test Facility. The master oscillator consists of a cascade of mutually phase-locked, ultra-low, phase-noise oscillators, each optimizing a certain range of the phase-noise spectrum (Figure 3.3.1.3). Integrated absolute timing jitter between 100 Hz and 10 MHz is < 21.5 fs. If phase-lock loops (electrical or optical) are locked to this oscillator, jitter contributions below the loop bandwidth (some 100 Hz up to ≈ 1 kHz) are "common mode" and therefore almost synchronous for all clients. This means that its integral influence on the electron bunch is strongly suppressed.



b) Fig. 3.3.1.3: SwissFEL Injector Test Facility RF master oscillator [56]. a) Block diagram, b) Phase noise spectrum.

3.3.2 Optical synchronization system

3.3.2.1 Pulsed optical synchronization system

High-gain free-electron lasers are capable of generating UV and X-ray pulses in the fs range. To fully exploit the high temporal resolution offered, appropriate linac stability has to be achieved. In addition, user experiments have also to be synchronized to the machine with the corresponding accuracy. In order to secure long-term stability in the sub-10 fs range, an optical reference system is foreseen. Best performance can be achieved with such a system if pulsed links are used, similar to

the ones developed at MIT [57,58] and DESY [59,60]. The reference pulses of a highly stable low phase-noise, mode-locked laser optical master oscillator (OMO) are distributed point-to-point (star configuration) to the remote client stations of the accelerator. The different stability requirements (from an ultra-low to a low-drift and ultra-low timing stability) over long distances and extended periods of time leads to a hybrid optical system with tailored performance, to optimize cost. This utilizes the advantages of both: the ultimate-performance pulsed links and the cost-effective “cw” links. There are several key components along the accelerator, in the diagnostics and in the experimental areas which are more naturally stabilized optically.

3.3.2.2 Critical components of the pulsed optical synchronization system

a. Laser master oscillator

One prerequisite for high-accuracy synchronization is a stable optical master oscillator. Its timing jitter in the high-frequency range should be in the fs range. This is necessary due to the limited bandwidth (< 50 kHz) for locking of a mode-locked laser to an RF reference. Whereas the low-frequency noise is determined by the stability of the RF reference, the high-frequency part beyond the locking bandwidth follows that of a free-running mode-locked laser. In addition, stabilized fiber links have an intrinsic bandwidth limitation, determined by the round trip of the reference laser pulse. For a 1 km fiber, the round-trip travel time is ~ 10 ns. Any fluctuations in the pulse train faster than this can not be compensated. Low-jitter hybrid (Er-Yb fiber/solid state) lasers are already commercially available [61]. An integrated timing jitter in the range 1kHz-10MHz as low as 3.3 fs (rms) has been measured on the 14th harmonic of the laser repetition rate of 214.1366 MHz [56], making the laser an ideal candidate for an optical master oscillator (Figure 3.3.2.1).

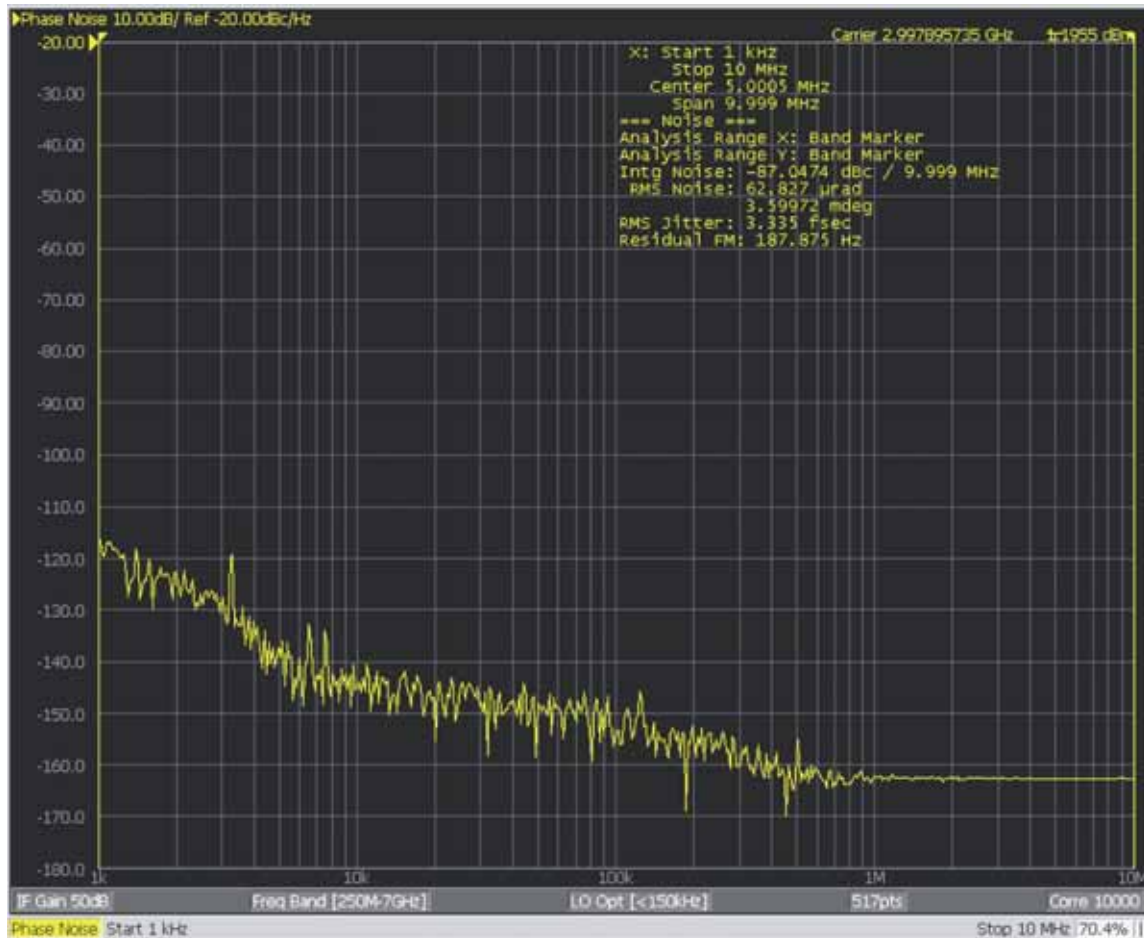


Fig. 3.3.2.1: Optical master oscillator laser jitter measurement (measured with harmonic extraction photodetector).

b. Optical cross-correlation for laser synchronization and group delay measurement

Balanced optical cross-correlation [62,63] allows optical synchronization of a wide diversity of lasers – from mode-locked [59,62] to Q-switched [64] – as well as group delay measurement for length stabilization of optical fiber links [58,63,65]. The principle is illustrated in Figure 3.3.2.2.

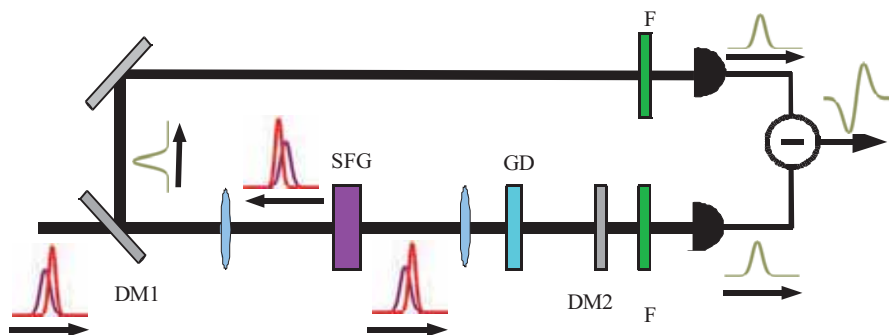


Fig. 3.3.2.2: Principle of balanced optical cross-correlation [63]. DM-dichroic mirror, SFG - nonlinear crystal for sum-frequency generation, F- filter, GD- group delay control

In such a scheme, 4.4 fs jitter over 12 hours has been achieved [65]. When the wavelengths are different, a phase-matched BBO crystal with an appropriate cut angle can be used [59,64]. Here the most efficient is the Type I interaction (parallel input polarizations), which is not background free, but nevertheless efficient when appropriate bandpass filters in front of the photodetectors are used. In this scheme, pulse swapping in the backward direction is achieved either by the group delay in the available optical elements (lenses, dichroic mirrors, etc) [59], or, if the bandwidths of the interacting optical pulses are orders of magnitude different, by a delay stage [64].

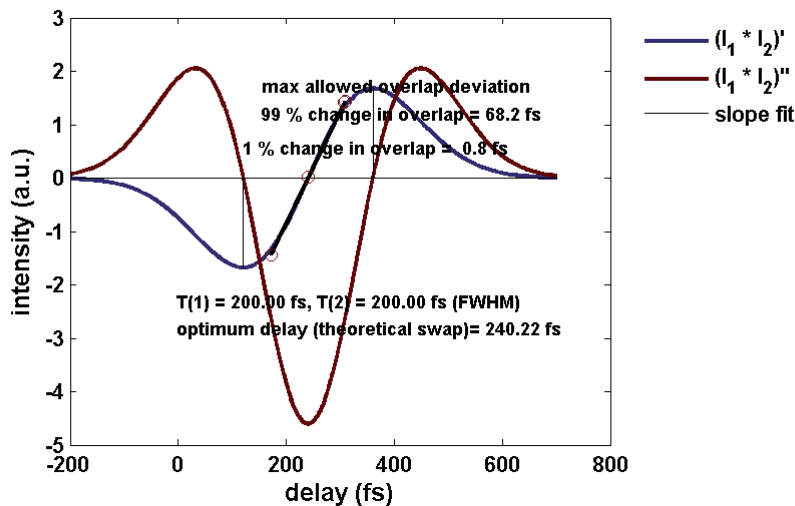


Fig. 3.3.2.3: Sensitivity of an optical cross-correlator to changes in signal overlap (blue curve). The delay between the incoming and back-reflected Gaussian pulses is chosen such that maximum sensitivity to overlap changes is achieved (red curve). The sensitivity of the scheme is theoretically sub-fs, as illustrated in Figure 3.3.2.3.

c. Length-stabilized fiber links for pulse transmission

A layout of an optical link, length-stabilization system for ultra-low drift transmission of the reference laser pulses is illustrated in Figure 3.3.2.4. The distribution after the master oscillator laser might be either free space or in fiber multiplexers. Acoustic noise and thermal fluctuations may cause variations of the optical path length in the fiber, which leads to arrival time deviations in the transmitted reference laser pulses. Therefore, active stabilization of the link length through optical cross-correlation is necessary [58,63,65]. Part of the reference pulse is back reflected from the link end through a Faraday rotating mirror. The arrival time of this pulse in the link front-end is sensitive to changes in the link length. Through an appropriate phase-lock loop (PLL), the error signal, proportional to the overlap mismatch of the pulses in the balanced optical cross-correlator, can be used to compensate for the short-term (jitter) and long-term (drift) fiber length variation. The jitter is compensated with a fiber piezo-stretcher and the drift by a free-space optical delay.

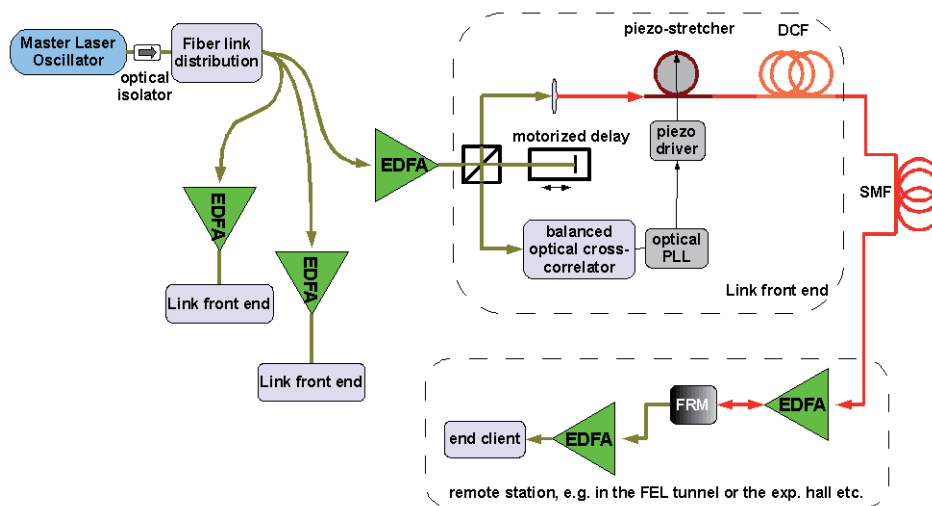


Fig. 3.3.2.4: Layout of the optical link length stabilization for drift-free distribution of the reference laser pulses: EDFA - Erbium-Doped Fiber Amplifier; PLL - Phase-Lock Loop; DCF - Dispersion Compensating Fiber; SMF - Single-Mode Fiber (standard single-mode fiber); FRM - Faraday Rotating Mirror.

Several effects have to be taken into consideration:

- Optical cross-correlation is sensitive to pulse length and polarization changes. Fiber chromatic dispersion is mitigated using dispersion compensating fibers (DCF), whereas polarization has to be controlled at the link input and output.
- Polarization mode dispersion (PMD) also leads to pulse broadening in long fibers. The effect can be minimized using low-PMD fibers [66] ($\text{PMD} \leq 40 \text{ fs}/\sqrt{\text{km}}$).
- In order to reduce undesirable non-linear effects in the link, pulse energy has to be kept below 100 pJ. On the other hand, sufficient power should be secured for optical cross-correlators. Therefore, cascade pulse amplification at both ends of the link is necessary, e.g. with Erbium-doped fiber amplifiers (EDFA), with carefully balanced seed and pump parameters to reduce the added integrated timing jitter [65].
- Radiation-hard (if required) as well as low temperature drift, non-actively stabilized fibers (for short links) are commercially available.

3.3.2.3 Alternative optical link concept: optical “cw” link

The pulsed optical links described above are those with the potentially best drift and jitter performance.

Besides “pulsed” links, another type of optical link will be used: the “continuous wave” (cw) optical link. Both technologies offer the possibility of implementing link group delay stabilization. Without this stabilization possibility, the required long-term phase/timing stability could not be achieved.

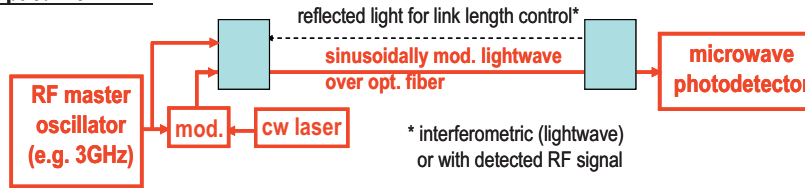
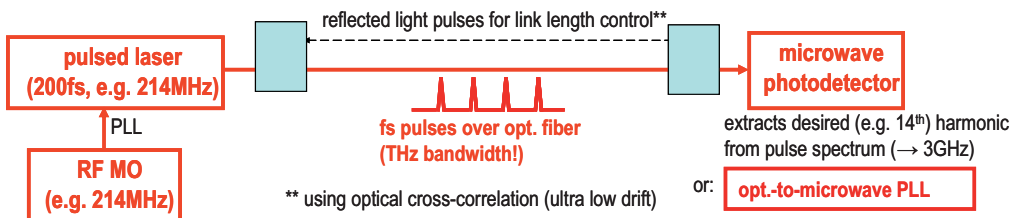
Optical “cw” link**Optical “pulsed” link**

Fig. 3.3.2.5: Comparison of optical link types to be used in the SwissFEL synchronization system.

With optical “cw” links, very low jitter (<10 fs) and relatively low drift (some tens down to about 10 fs avg. p-p per day) can be achieved, whereas pulsed links offer ultimate (approx. 1 fs) jitter and drift performance (some fs avg. p-p per day). The simplicity, potentially lower cost and proven reliability of “cw” links makes them a candidate as workhorse in the optical reference distribution system (e.g. [67]). Interferometric or RF phase detection can be used. In the former case, phase instead of group delay is stabilized, and therefore a correction has to be applied.

3.3.3 Stabilization of lasers

3.3.3.1 Ultimate stability: optical cross-correlation

There are several laser systems along the accelerator, which have to be synchronized to the master laser oscillator. Among them are: the gun laser (Ti:Sa at 800 nm or Nd:YLF at 1047 nm), the laser for longitudinal bunch electro-optical diagnostic (Yb- fiber at 1030 nm or Ti:Sa), the seed laser (typically Ti:Sa), the laser for pump-probe experiments (Ti:Sa), the laser heater (Ti:Sa) and, optionally, the laser for the optical replica (Ti:Sa). In addition, the arrival time of the photo-injector laser on the cathode can be stabilized via active stabilization of the optical transfer line (propagation in free air). For optical-to-optical synchronization, a balanced optical cross-correlator can be used, with which a 300 as rms jitter in the range 0.01 Hz-2.3 MHz has been demonstrated [62]. Because of the different wavelengths of the master laser oscillator (Er fiber laser @ 1560 nm) and the client (Ti:Sa or Yb fiber), a cost-effective, two-colour balanced optical cross-correlator, based on a single BBO crystal, can be used [59,64]. The synchronization scheme is similar to the one shown in Figure 3.3.2.2, with the exception that Type I interaction (parallel input polarizations) is used. The layout is illustrated in Figure 3.3.3.1. The laser which is to be stabilized optically has to be initially locked to the reference laser with an RF PLL. This secures initial temporal stability between the two optical pulses, necessary to achieve overlap in the balanced optical cross-correlator. After the sum frequency pulse, proportional to the overlap mismatch, has been achieved, the optical cross-correlator PLL may take over.

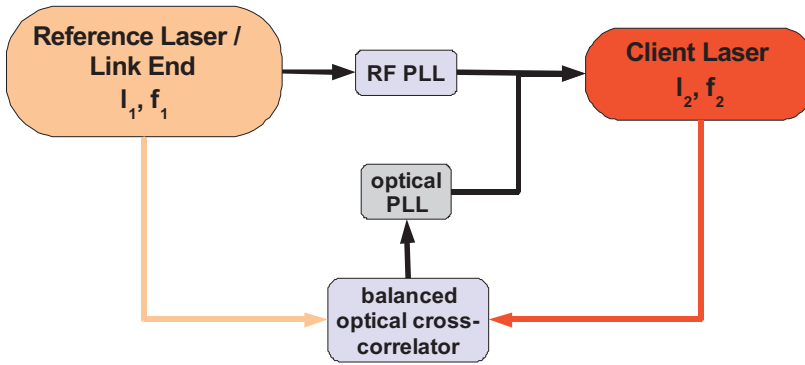


Fig. 3.3.3.1: Layout of direct optical-to-optical laser stabilization: PLL - Phase Lock Loop

3.3.3.2 Laser synchronization with relaxed drift stability

Long-term fs stability can be achieved by means of two-wavelength optical cross-correlation alone. Long-term stability of the order of some 10 fs (for laser clients with somewhat relaxed requirements) and fs jitter is possible using optimized classical PLL techniques with harmonic extraction (see, for example, [68]).

3.3.4 RF generation

3.3.4.1 Balanced optical-to-microwave phase detector

Ultimate drift (a few fs) and jitter (a few fs) performance can potentially be achieved with a technique developed at MIT, the so called “balanced optical-to-microwave phase detector”-based PLL [58]. This method has been successfully demonstrated for RF frequencies above 10 GHz. For lower RF frequencies, some problems still have to be solved [69]. A drawback of the method is its high cost.

3.3.4.2 Direct harmonic extraction photodetector

If excellent jitter, but not ultimate drift, performance is required, and cost has to be significantly minimized (e.g. synchronization of RF stations with a pulsed optical reference), the RF frequency can be directly extracted from the photo-electron current of a photodetector, illuminated with the reference pulses, which occur with a repetition rate that is a subharmonic of the RF frequencies (Figure 3.3.4.1). It has been demonstrated that jitter of some fs can be achieved with this scheme (Figure 3.3.2.4). Using optimized photodetectors and stabilization techniques, long-term drift stability of the order of 10 fs can be achieved [56,69-71].

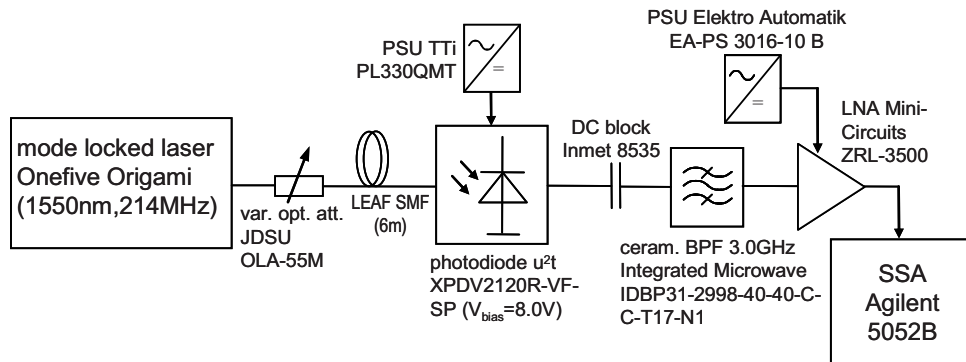


Fig. 3.3.4.1: Block diagram of a direct harmonic extraction receiver [56].

An advantage of direct harmonic extraction is the fact that jitter is (as opposed to PLL-based solutions) synchronous for all clients served by the same laser pulses (common-mode jitter only).

3.3.5 Synchronization system for mixed European/US RF frequencies

For cost reasons, RF systems operating at European and US frequencies will both be used simultaneously in SwissFEL (European: S-band and X-band; US: C-band). This poses some restrictions on the synchronization system. A common subharmonic has to be found, from which both European and US frequencies can be derived:

$f_b = 142.8$ MHz (common subharmonic)

C-band 5712 MHz = $40 \times f_b$ American Frequency

S-band 2998.8 MHz = $21 \times f_b$ detuning from 2997.912 MHz: + 0.888 MHz

X-band 11995.2 MHz = $84 \times f_b$ detuning from 11991.648 MHz: + 3.552 MHz

Figure 3.3.5.1 shows a block diagram of a possible synchronization system. The balanced optical-to-RF phase-detector-based PLLs are synchronized with the common (subharmonic = repetition rate) optical signal and guarantee extremely low drift (ultimately of the order of some fs) between the RF frequencies. The latter are then further distributed within the accelerator tunnel by means of cost-effective optical “cw” links.

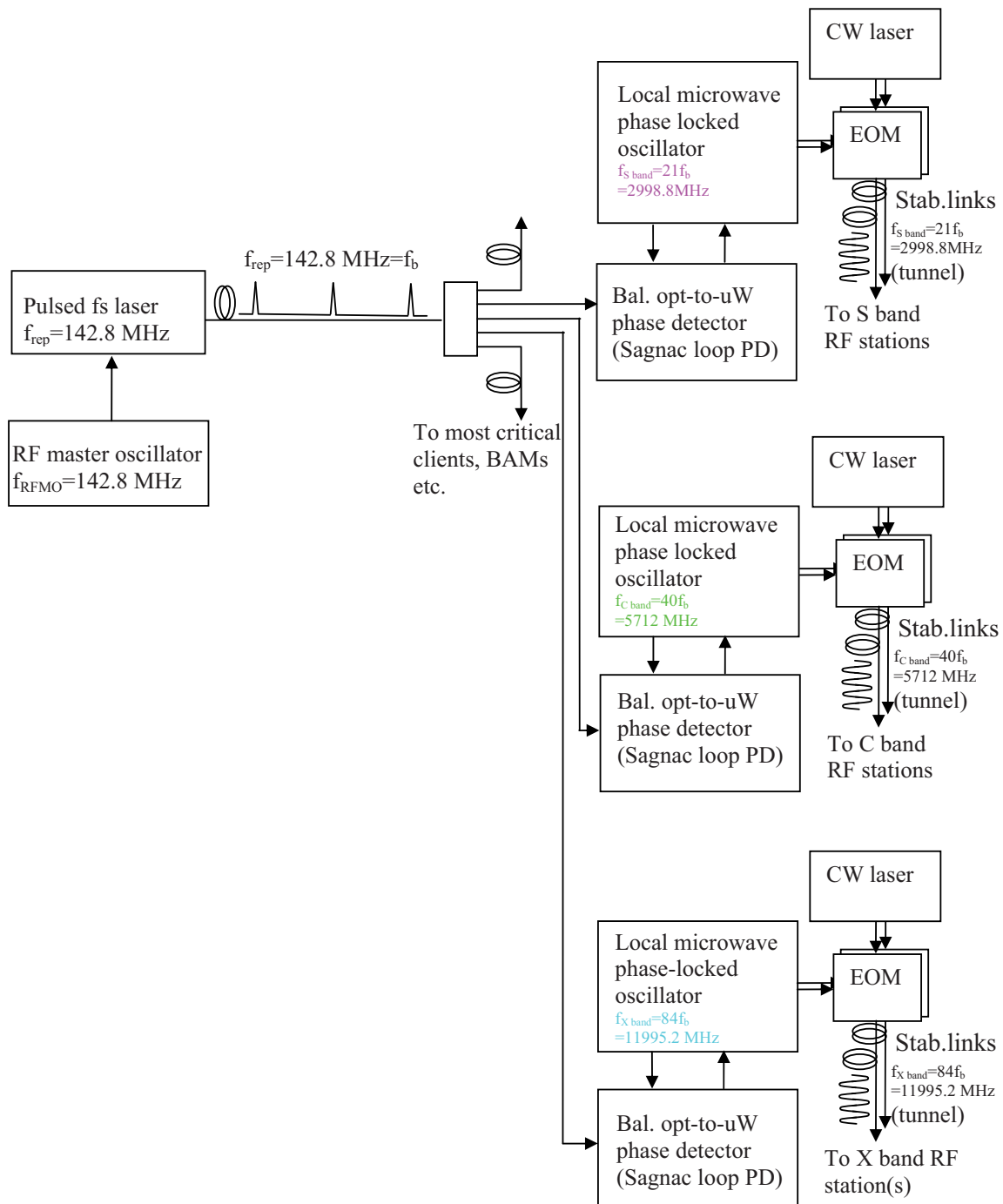


Fig. 3.3.5.1: Reference generation and distribution for mixed European and US RF frequency standards.

3.4 Magnets

Beamline magnets (solenoids, bending dipoles, quadrupoles and correctors) will be used all along the accelerator, to focus (solenoids, quadrupoles) and longitudinally compress the beam (bending dipoles in chicanes) and to correct the field quality (correctors, quadrupoles). An overview of the accelerator layout with the foreseen magnets is presented in Chapter 2. The 24 quadrupoles, the 4 bending dipoles of the Bunch Compressor 1 and the 16 solenoids for the S-band booster sections have already been built for the SwissFEL Injector Test Facility [72]. The same magnets will be used for SwissFEL, and an additional 165 quadrupole magnets, another bunch compressor chicane, and dog-leg beam-line dipoles are planned. The characteristics of the magnets will now be reviewed, type by type.

3.4.1 Solenoid magnets

In the SwissFEL Injector Test Facility, a gun solenoid right after the electron gun and 16 solenoids for the S-band accelerating structures have already been built and measured. The same magnets will be installed at the SwissFEL Injector. Below is the description of those injector magnets. More parameters (for example measurements reports) are available at PSI magnet group database (<http://magnet.web.psi.ch>).

3.4.1.1 Gun Solenoid System:

The Gun Solenoid system consists of 4 magnet elements:

- the main Gun Solenoid ($z=0.3$ m) which focuses the beam at gun exit.
- the bucking coil: (positioned at $z = -60$ mm upstream cathode plane) to cancel the fringe magnetic field of gun solenoid at cathode plane (no magnetic field should be present on photocathode surface).
- the quadrupoles and skew quadrupoles (1 layer loops around vacuum chamber) correctors to compensate imperfection in the gun solenoid.
- the correctors dipoles (on each end of solenoid's iron yoke) to steer the beam horizontally and vertically.

The parameters of those magnets are summarized in the table 3.4.1.1 and Fig. 3.4.1.1 represents the gun solenoid.

Table 3.4.1.1: Parameters of gun solenoid system

| | Bucking Coil | Quad. Correctors | Steerers | Gun Solenoid |
|--|------------------|-------------------|--------------|----------------|
| Location | $z = -60$ mm | Concentric to WFG | On WFG faces | $Z = 0.3$ m |
| Aperture | 220 mm | 46 mm | 80 mm | 80 mm |
| Outer Diameter | | | | 385 mm |
| Strength | 4.3 mT @ cathode | 27 mT/m | 0.25 mT | 0.35 T |
| Mechanical Length | | 70 mm | 10 mm | 0.26 m |
| Calibration (Gauss/A) | | | 0.25 G/A | 17.59 G / A |
| Linearity $\int_{AB/B.ds}$ | | | | 10^{-4} |
| Magnetic axis measured accuracy | | | | 0.1 mm |
| Maximum Current | 10 A | 10 A | 20 A | 220 A |
| Resistance at 50°C | | | | 110 m Ω |
| Cooling Art | air | | | Water |
| Ref. PSI Drawing | 1-50022.41.338 | | | 0-50022.41.169 |
| Magnet Interface Data | | | | FEL-SS88-004-0 |
| Reference name for Magnet Measurement Data | WFB | | SFD | WFG |

The gun solenoid, positioned just after the RF gun, aims to focus the beam immediately downstream of the cathode. Indeed, the beam experiences strong RF and space charge defocusing forces that are radially symmetric. The focusing force must also be radially symmetric or the beam will not be optimally compensated. Therefore, a solenoid is required to contain the beam. The basic solenoid specifications are listed in the Table 3.4.1.1. The solenoid consists of two coils with 161 turns/coil (double solenoid) covered with an iron yoke. Each coil consists of 14 layers glued with glass-epoxy. The solenoid axial position must be correct to approximately 0.1 mm. Therefore, the measurement of the axis of the solenoids was accurately made with a Hall-probe measuring machine, and the 0.1 mm accuracy was achieved. It was also desired that the solenoid field varies linearly with current, and the field must be radially symmetric and also axially symmetric to within 2 % about the centre of the magnet. Quadrupoles and skew quadrupoles are installed within the solenoid aperture to correct beam asymmetries.



Fig. 3.4.1.1: Gun solenoid on his test bench (the steerers V and H are visible on front plane).

3.4.1.2 S-Band solenoids

The S-band solenoids (WFS) surround the S-band cavities along the injector. They will provide additional focusing, to reduce emittance enlargement due to space charge effects during booster 1 acceleration. Specifications are shown in Table 3.4.1.2. Accuracy on the knowledge of the magnetic axis was also 0.1 mm. The solenoid consists of two adjacent coils (150 turns /coil)

Table 3.4.1.2: Requirements for the solenoids installed in the SwissFEL Injector Test Facility

| | S-band Solenoid |
|--|------------------|
| Location | injector |
| Quantity | 8 |
| Aperture | 220 mm |
| Outer Diameter | 345 mm |
| Max. Strength | 103.52 mT |
| Mechanical Length | 750 mm |
| Calibration (Gauss/A) | 0.518 mT/A |
| Linearity $\int_{AB/B.ds}$ | 10^{-4} |
| Magnetic axis measured accuracy | 0.1 mm |
| Maximum Current | 200 A |
| Resistance at 50°C | 141 mΩ |
| Cooling Art | Water: 4.1 l/min |
| Ref. PSI Drawing | 1-50022.41.043 |
| Reference Interface | FEL-GR06-39_0 |
| Reference name for Magnet Measurement Data | WFS |



Fig. 3.4.1.2: S band solenoid on his test bench.

3.4.2 Quadrupole Magnets

3.4.2.1 Quadrupoles in the Injector

The SwissFEL gun and booster section contains 3 types of quadrupole magnets with an aperture of 45 mm. These are already built, and Table 3.4.2.1 and 3.4.2.2 shows their parameters.

Table 3.4.2.1: Specifications of the quadrupoles installed in the injector

| Magnet Name: | QFB | QFC |
|--|--------------------|-------------------|
| Location | Bunch Compressor 1 | Diagnostic region |
| Quantity | 2 | 3 |
| Aperture | 45 mm | 45 mm |
| Max. Gradient G | 1.5 T/m | 0.5 T/m |
| Yoke length | 0.08 m | 0.08 m |
| Magnet effective length | | |
| Gradient measurement accuracy | $\pm 10^{-3}$ | $\pm 10^{-3}$ |
| Multipole measurement accuracy @ $r=17$ mm | $<10^{-3}$ | $<10^{-3}$ |
| Max. Current | 10 A | 10 A |
| Turns / coil | | |
| Cooling Art | air | air |
| Resistance at 50°C | | |
| Weight | | |
| Ref. Interface | | |
| Ref. Drawing | 1-50022.41.132 | 1-50022.41.152 |

The QFB quadrupoles are placed in the bunch compressor region for residual dispersion correction, and the three QFC quadrupoles are in the gun region for diagnostic purposes. The yoke design of QFB and QFC is the same only the number of turns per coil is different.

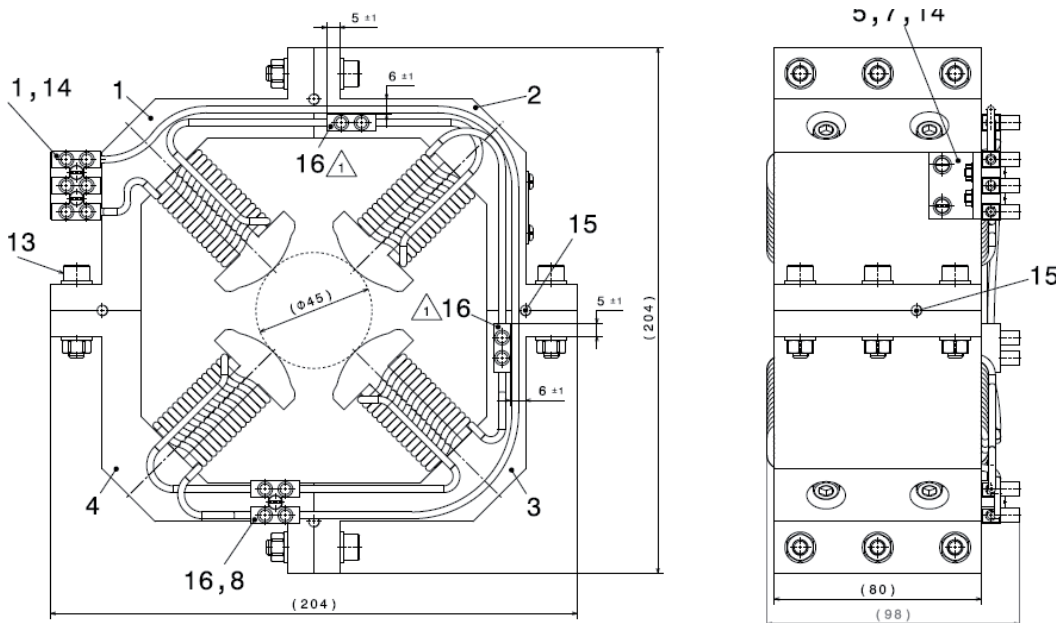


Figure 3.4.2.1: Drawing of the QFC and QFB magnets used after the gun for diagnostic purposes.

Table 3.4.2.2: Specifications of the QFA quadrupoles installed between injector and Linac 1

| | |
|---|---------------------|
| Magnet Name: | QFA |
| Location | After Injector |
| Quantity | 28 |
| Aperture | 45 mm |
| Measured avg. Gradient G at max. current | 31.74 T/m |
| Gradient measurement accuracy | $\pm 10^{-4}$ |
| Gradient reproducibility quad to quad (rms) | $1.2 \cdot 10^{-3}$ |
| Yoke length | 0.15 m |
| Measured Magnetic effective length | 0.171 m |
| Meas. multipole / main field amplitude at $r=17\text{mm}$ | $1.3 \cdot 10^{-3}$ |
| Multipole measurement accuracy at $r = 17 \text{ mm}$ | $< 10^{-3}$ |
| Max. Current | 150 A |
| Turns / coil | 45 |
| Cooling Art | Water: 0.6 l/min |
| Resistance at 50°C | 140 m Ω |
| Weight | 100 kg |
| Ref. Interface | FEL-SS88-003-1 |
| Ref. Drawing | 1.50022.41.080 |

The twenty-four quadrupoles named QFA (25 T/m) have also been built for the beam diagnostic section and the FODO cells of the SwissFEL Injector Test Facility. A similar concept of design and measurement techniques will be used for all SwissFEL quadrupoles. In order to ensure good reproducibility and symmetry for the magnets in the FODO cells, the iron cores were made by stacking isolated laminated iron layers of 1 mm thickness. The pole profiles were optimized by a Poisson 2D code, to minimize the unwanted higher harmonic field in the central part of the magnet. The contributions from the end sections were minimized by introducing a 45° chamfer geometry on the pole ends. The multipoles amplitudes were systematically measured in-house, using a rotating coil machine build by CERN. Tolerance on multipole accuracy was set to 10^{-3} at 17 mm radius (close to the radius of the measuring machine).

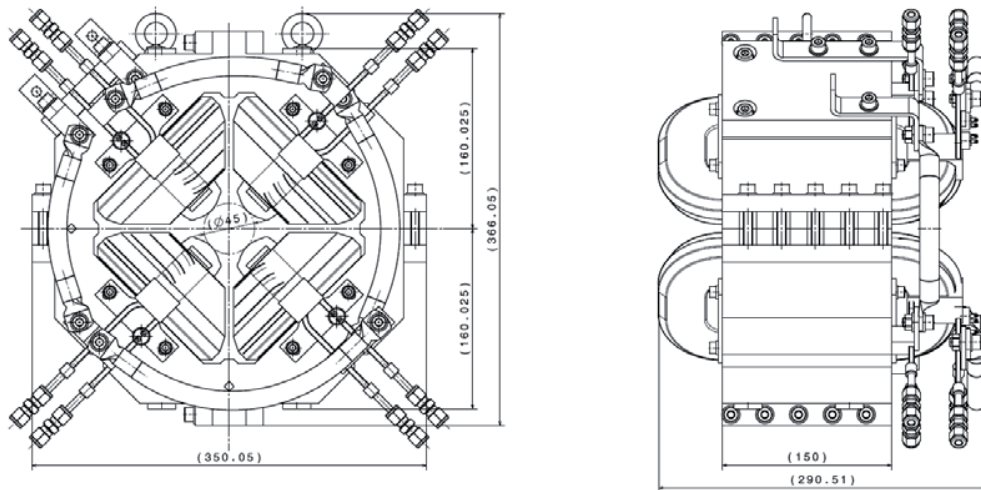
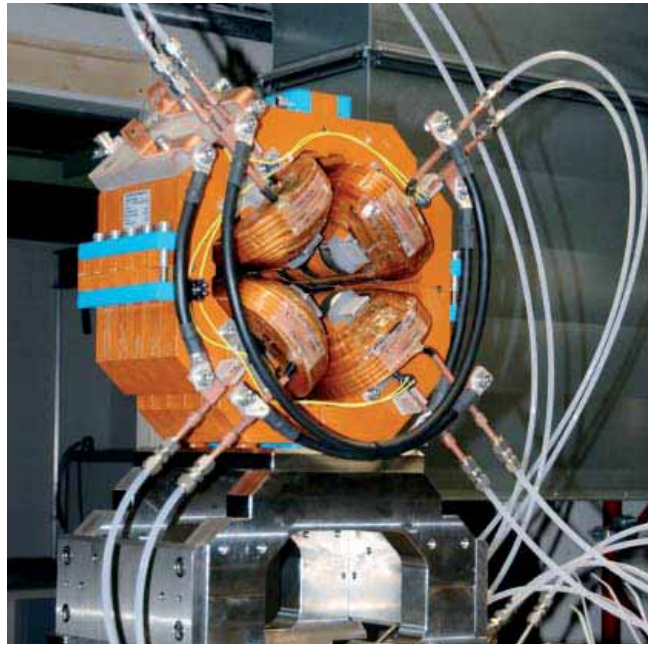


Fig. 3.4.2.2: Quadrupoles magnets in injector (QFA) on the test bench (top) and drawing showing main dimensions.

3.4.2.2 Quadrupoles in Linac and undulator sections:

For the SwissFEL, a total of 165 quadrupole magnets with apertures of 22 and 12 mm are planned. In order to avoid the plugging phenomena of the hollow magnet conductors by water corrosion and the effect of the cooling water on the magnet vibration, an air-cooled design is favoured. Table 3.4.2.3 shows the parameters of these quadrupoles.

The quadrupoles QFD and QFE will be installed in the SwissFEL linac 1,2 and 3. They will integrate horizontal and vertical steering function.

Table 3.4.2.3: Requirements for the quadrupoles used for the SwissFEL linac and in the Athos undulator beamline.

| | QFD | QFE |
|---|-------------------|----------------------------|
| Location | Linac 1,2,3 | Linac 3, SwitchYard, Athos |
| Quantity | 60 | 63 |
| Aperture | 22 mm | 22 mm |
| Gradient G | 20 T/m | 20 T/m |
| Yoke length | 0.15 m | 0.2 m |
| Gradient measurement accuracy | 10^{-4} | 10^{-4} |
| Multipole measurement accuracy at $r < 12$ mm | 10^{-3} | 10^{-3} |
| Max. Current | 10 A | 10 |
| Precision in magnetic axis positioning (rms) | 50 μ m | 50 μ m |
| Turns / coil | 104 | |
| Cooling Art | air | air |
| Resistance at 50°C | 0.5 Ω | 0.65 |
| Total Weight | 80 kg | |
| Ref. Interface | FEL-SS88-007 | |
| Ref. Drawing | 1.50023.41.001 | |
| Power Supply Type | bipolar | bipolar |
| Steering max. field (H and V) | 30 mT | 30 mT |
| Steerers maximum current | 2 x 10 A | 2 x 10 A |
| Steerers Resistivity | 2 x 0.15 Ω | 2 x 0.18 Ω |

The 22 mm-aperture quadrupoles will be used in the linac sections and beam matching sections. The shorter QFD quads (0.15 m) are foreseen for the Linac 1, 2 and 3 section. The longer QFE magnets (0.2 m) will be used in matching sections at higher beam energy where stronger focussing is required. For similar reasons to those mentioned above, the magnet cores of the quadrupoles will be made of laminations. The gradient reproducibility from one quadrupole to another has to be kept within 10^{-3} . Pole profiles have to be optimized in order to minimize the 12-poles term below 10^{-3} times the quadrupole main field. The characterization of each magnet will consist of measuring the integral field strength versus current (magnetization curve, hysteresis cycle), the field quality (integral harmonics up to order $n=10$) and the magnetic axis. These measurements are planned to be carried out using a 19 mm-aperture rotating mole currently under design at CERN and a vibrating wire system. The accuracy of the field quality measurements remains a challenge in the case of such small-aperture magnets. The challenge here is represented by the limited size of the coil to maintain the needed mechanical stability. A design using 3 coils directly wound on the shaft body may be the solution, leading also to higher winding precision. A relative accuracy of 10^{-4} appears to be achievable.

The position of the magnetic axis with respect to external fiducials has to be known within 50 - 100 μ m rms. Measurements using a vibrating wire system will be systematically performed on all the quadrupoles. The precision of vibrating wire technique together with the precision on mechanical reference positions (fiducials) leads to an overall accuracy of 50 μ m rms in the magnetic axis position.

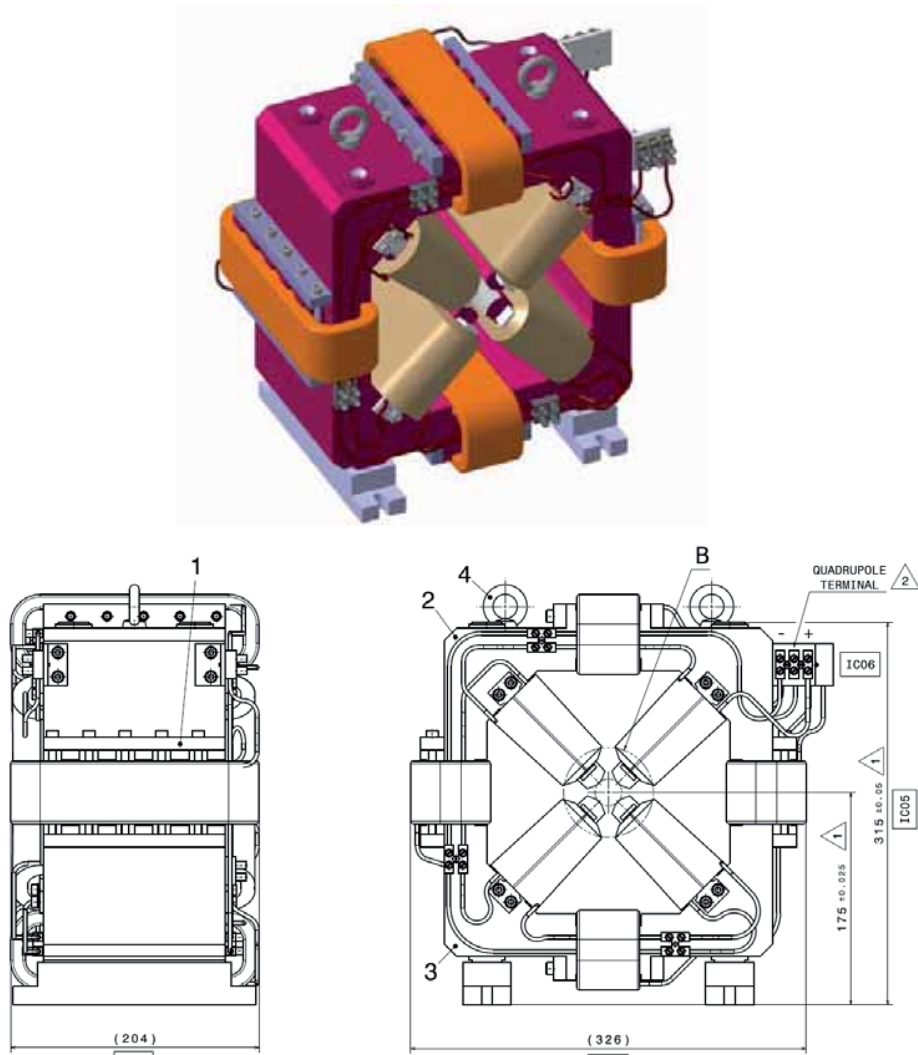


Fig. 3.4.2.3: Quadrupoles QFD drawing which integrate horizontal and vertical steering function. Four position references (fiducials) are on the top of the quadrupole yoke.

Table 3.4.2.4: Requirements for the quadrupoles used for the SwissFEL Aramis and Athos undulator beamlines.

| | QFF |
|--|--------------------|
| Location | Undulator Beamline |
| Number | 42 |
| Aperture | 12 mm |
| Gradient G | 50 T/m |
| Yoke length | 0.08 m |
| Gradient measurement accuracy | 10^{-4} |
| Multipole measurement accuracy at $r = 8$ mm | 10^{-3} |
| Max. Current | |
| Turns / coil | |
| Cooling Art | |
| Resistance at 50°C | |
| Weight | |
| Ref. Interface | |
| Ref. Drawing | |
| Power Supply Type | bipolar |

QFF quadrupoles (50 T/m, 12 mm apertures) will be placed in the undulator beamlines. The same measurement goals as for the linac quadrupoles are required and the tolerance on the field quality is at the level of one percent. The integrated field gradient and the field quality can be measured using an 8 mm-aperture rotating mole, under development at CERN. The main difficulty will be the determination of the magnetic quadrupole axis in respect to fiducials references sitting on quadrupole frame. SwissFEL will use a beam-based alignment technique to align the quadrupoles to the needed accuracy (less than 1 μm). However, an initial accuracy of the quadrupole alignment not worse than 50 μm is required. In addition, each undulator frame will incorporate two small alignment quadrupoles (specifications are still to be defined) on the same girder support (see Section 3.5.3). The fiducialization of the undulator and quadrupole will be carried out using the vibrating wire technique. A temperature-controlled environment ($\pm 0.1^\circ\text{C}$) is needed for the precise measurement of the quadrupole axis, and especially for the undulator module. To save space, all quadrupoles (QFD, QFE and QFF) will contain integrated steering functions in the horizontal and vertical directions.

3.4.3 Dipole magnets

Table 3.4.4 shows the parameter of the dipoles already built for the SwissFEL Injector Test Facility. Two magnetic chicanes will be used in the two bunch compressors BC1 and BC2 to generate a non-zero momentum compaction factor R_{56} . A schematic layout and parameter summary is given in Chapter 2. The dipoles in the bunch compressor BC1 with a magnetic gap of 30 mm are ready for installation in the SwissFEL Injector Test Facility. A good field region of ± 40 mm with a field accuracy of 0.01% in the field integral is specified and achieved in simulations. Special attention was paid to the manufacturing tolerances to insure a precise geometry. To build dipoles as similar as possible to each other, all dipole yokes will be cut and machined from one piece of iron so as to avoid differences in the material composition. The tolerance on the pole parallelism and flatness will be tightened to 10 μm and 5 μm respectively. Each dipole winding will integrate one loop more separately powered, to correct possible differences between dipoles. Two dipoles for beam dump and diagnostic complete the bending magnets of the injector part.

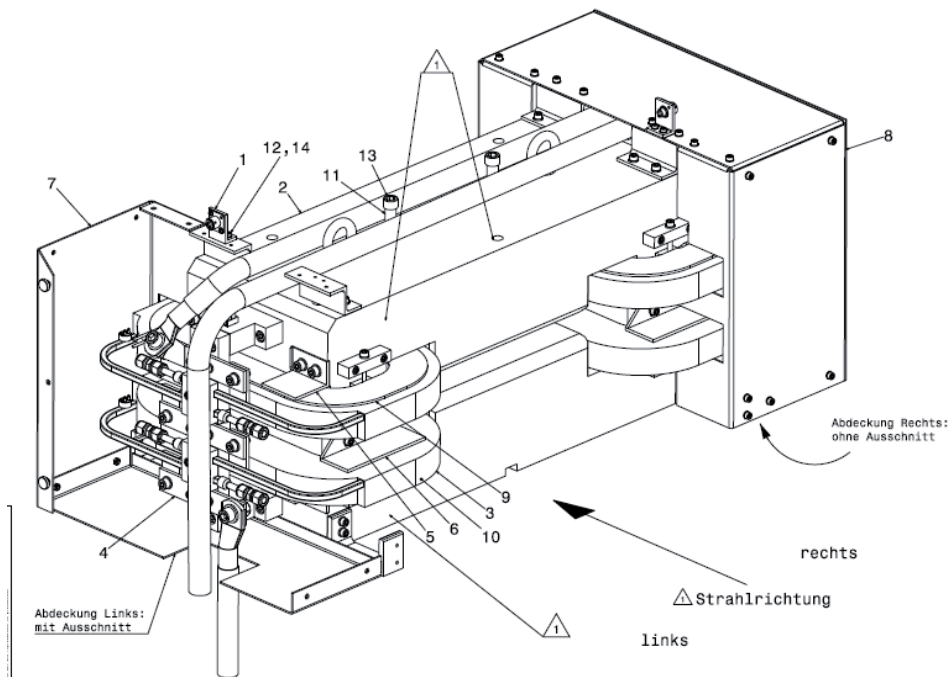


Fig. 3.4.2.4: Bunch compressor 1 (BC1) dipole, magnetic length is 0.27 m and gap is 3 cm.

For the bunch compressor 2, the dipoles with the same accuracy goals will be built. For a bending angle of 2.15° at energy of 2032.9 MeV, the dipoles will have a magnetic length of 0.5 m and a magnetic field of 0.5 T. Additional dipoles for beam dump; switchyard section and diagnostic purposes are also planned. A total amount of 43 dipoles (laser heater 4, switchyard 6, BC1 5, BC2 4, Aramis 5, Athos 19) is planned. Corresponding specifications are not yet defined in Table 3.4.5 to Table 3.4.6.

Table 3.4.4: Requirements on the dipoles used for SwissFEL: Injector to Linac 2 (laser heater dipoles are not yet defined)

| | Dipole BC1 | Dipole BC2 | Dipole Gun | Dipole Dump A45 |
|------------------------------|----------------------|-----------------------|-----------------------|--------------------|
| Location | Chicane | Chicane | Diagnostic (injector) | Dump (injector) |
| Number of magnets | 4 | 4 | 1 | 1 |
| Max. Strength | 0.4 T | 0.5 T | 0.2 T | 0.467 T |
| Effective Length | 0.27 m | 0.5 m | 0.25 m | 0.31-0.486 m |
| Fig. Type | H – Magnet | H – Magnet | Window Frame | H - Magnet |
| $\int \Delta B / B \cdot ds$ | 10^{-4} | 10^{-4} | 10^{-4} | 10^{-4} |
| Transverse good field region | 150 mm | 70 mm | 60 mm | 60 mm |
| Bending angle | 3.82 deg (407.1 MeV) | 2.15 deg (2032.9 MeV) | 30 deg (30 MeV) | 7.5 deg (250 MeV) |
| Full gap | 30 mm | 20 mm | 101.2 mm | 30 mm |
| Pole width | 280 mm | 200 mm | 108 mm | 100 mm |
| Magnet Type name | AFBC2 | | SHA | A45 |
| Calibration | 2 mT/A | | 1.686 mT/A | 5.917 mT/A |
| Maximum Current | 200 A | | 50 A | 80 A PS limited |
| Nominal Orbit radius | 4.05 m | | 0.5 m | 3.15 m |
| Turns per coil | 2*28 turns/coil | | 2* 136 turns/coil | 12*6 turns/coil |
| Cooling Art | water | | water | water |
| Flow Rate | 0.68 l/min. | | | |
| Mass | 500 kg | | | |
| Resistance | 24 m Ω | | 256 m Ω | 180 m Ω |
| Ref. Drawing | 1-50022.41.223 | | 1-00101.41.373 | 0-10010.41.034 |

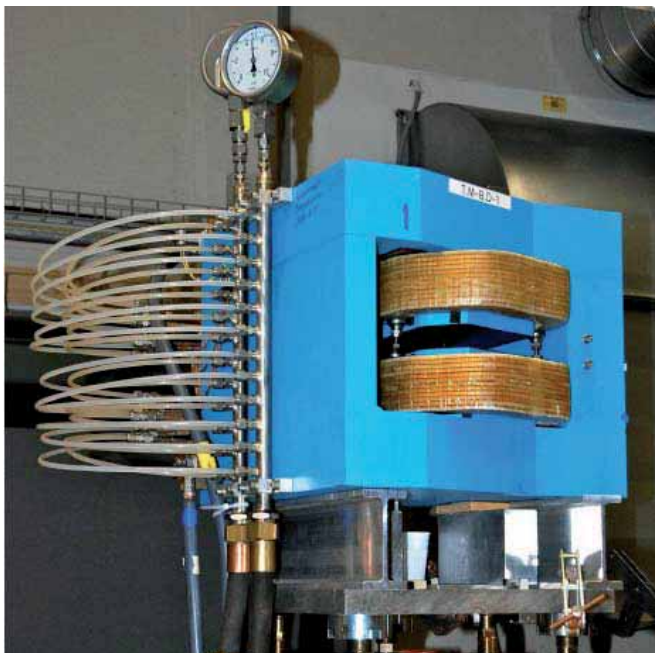


Fig. 3.4.2.5: Injector Beam Dump Dipole magnet currently installed at the SwissFEL Injector Test Facility (250 MeV)

Table 3.4.5: Requirements on the dipoles used for SwissFEL: Linac 2 to End

| | SwitchYard | Athos Modules | Athos Beam Dump Dipole |
|----------|------------|---------------|------------------------|
| Location | TBL3 | TBU2 | TBU1 |

Table 3.4.6: Requirements on the dipoles used for SwissFEL Aramis line

| | Aramis Collimators | Aramis Beam Dump Dipole | Aramis Beam Dump Dipole |
|------------------------------|--------------------|-------------------------|-------------------------|
| Location | TBU2 | ARAMIS DUMP | Aramis Dump |
| Number of magnets | 4 | 1 | 1 |
| Max. Strength | | | |
| Effective Length | | 2 m | |
| Fig. Type | | | Permanent Magnet |
| $ \Delta B/B.ds$ | | | |
| Transverse good field region | | | |
| Bending angle | | 6 deg | |
| Full gap | | | |
| Pole width | | | |
| Magnet Type name | | | |
| Calibration | | | |
| Maximum Current | | | |
| Nominal Orbit radius | | | |
| Turns per coil | | | |
| Cooling Art | | | |
| Flow Rate | | | |
| Mass | | | |
| Resistance | | | |
| Ref. Drawing | | | |

3.4.4 Corrector magnets

Twenty-six separated steering magnets for horizontal and vertical correction of the beam position have already been built and will be used for the injector part of the machine (< 450 MeV). They display “window frame” geometry with four iron yokes fitted with coils, two of which are connected in series to create a vertical and a horizontal dipole, with a deflection of 1 mrad. The yoke parts are completely machined out of ARMCO iron. They work at a nominal current of 10 A, producing a nominal field of 20 mT. The magnetic length is 0.05 m and the equivalent aperture is 80 mm.

The steering function for the new SwissFEL parts will be integrated in the 165 quadrupole magnets by additional corrector coils driven by 10 A power supplies. A deflection angle of 0.3 mrad at maximum energy is specified.

3.4.5 DC magnet power supplies

In order to drive all the magnets mentioned above, the DC Magnet Power Supplies (PS) required will be designed and tested in-house and have direct interface with the EPICS control system.

As for any particle acceleration application, PS for the SwissFEL must fulfil very high stability and precision requirements. They will consist of switched-mode converters controlled by 2nd generation PSI-type Digital Power Electronics Controllers (DPC).

A simple buck converter structure is used for the unipolar PSs (1Q), whereas the bipolar PSs (4Q) are realized with H-bridges. Depending on the current and voltage ratings of the PS, IGBTs or MOSFETs are used as semiconductor switches. Simplified block diagrams of the two PS structures are given in Figure 3.4.5.1. The DC source is either realized with a diode bridge or (for a low-power PS) with an off-the-shelf AC to DC converter. Several PS will share a common DC source, to reduce costs. The switching frequency and the output filter cut-off frequency are chosen to be as high as possible, in order to obtain a high system bandwidth, which is essential for a high-precision PS. These types of converters have been used at the Swiss Light Source (SLS) for approximately 10 years, and have proven to be very reliable.

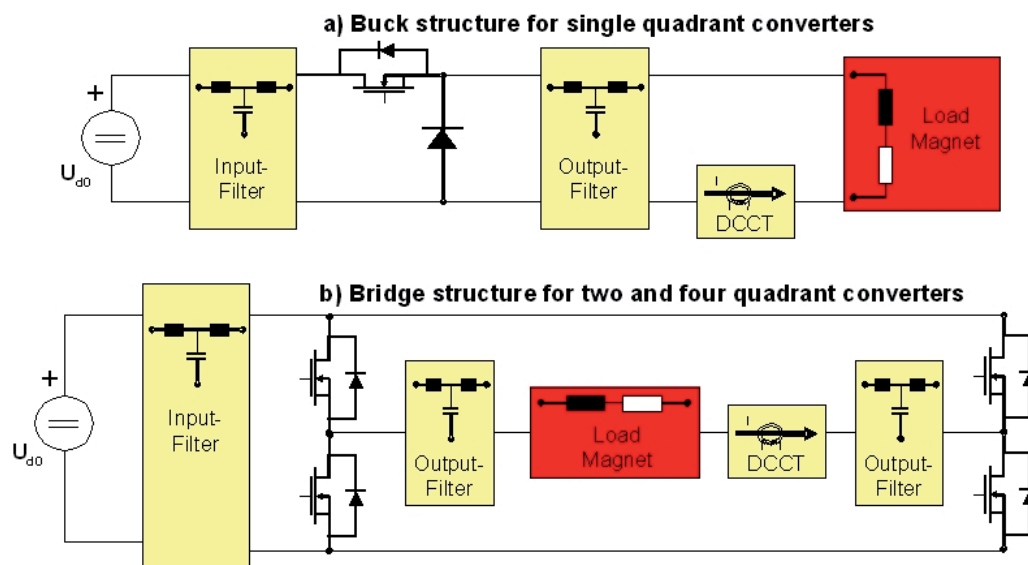


Fig. 3.4.5.1: Converter structure

For the SLS, a fully digital PS control system was developed 10 years ago. This controller has been adopted in several particle accelerators across the world, and several thousands are in service, to the complete satisfaction of their users. Based on this good experience, a second generation of this PS control system, called DPC (digital power electronics controller), has been developed and will be used for SwissFEL (refer to Figure 3.4.5.2). The DPC consists mainly of a controller board and a high-precision analogue to digital converter board. A backplane links the two boards and acts as the interface to the outside world. Compared to the first generation, computing power has been improved remarkably, allowing faster control cycles and/or more complex control algorithms.

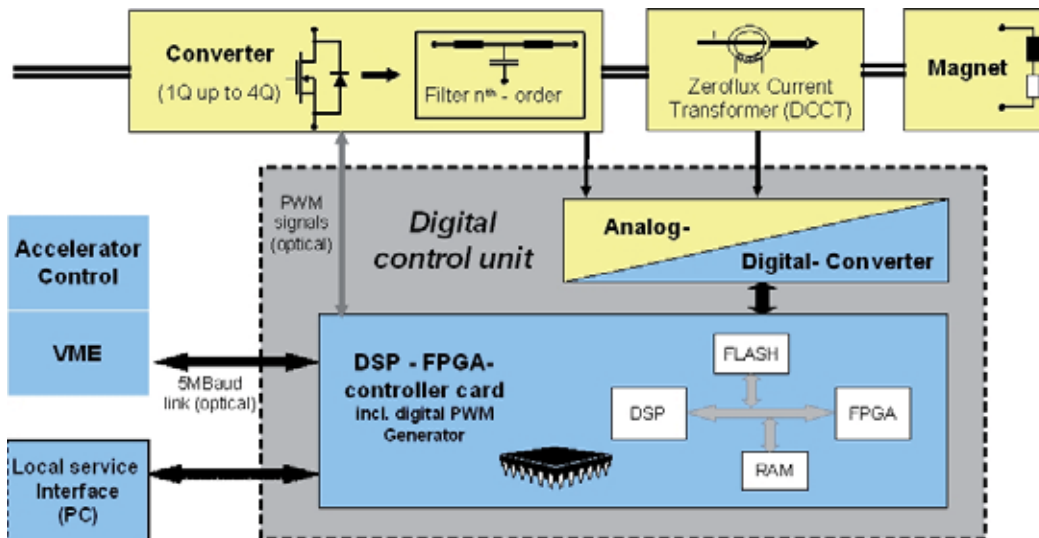


Fig 3.4.5.2: Digital Power Supply Control System (DPC)

The new controller board contains also 12 ADC channels for protection functions. For PS with released stability requirements the separate and expensive high-precision ACD can be omitted and a cheaper current measuring system can be used. The increased computing power of the controller board allows to control up to 3 independent PS with one single controller board. The current stability (noise 1...10Hz, drift over 8h, reproducibility) will be less than 200 ppm peak to peak with omitted ADC board, which will be the standard case for most of the PSs. However, by adding the high precision ADC board and selecting a more precise measuring head the current stability can be lowered down to 50ppm peak to peak. This will be necessary for sensitive magnets like the bunch compressors and some sensitive quadrupoles.

From the vantage point of the present, the power supplies listed in Table 3.4.5.1 are needed for SwissFEL. The table also shows the cooling type and the expected average power consumption per PS

Table 3.4.5.1: Preliminary power supply list for SwissFEL

| PS type | Rating | | Number | Cooling | Power |
|--------------------------|--------|----------|--------|---------|--------|
| Quadrupole and Corrector | 10A | bipolar | 570 | air | 50W |
| Corrector | 20A | bipolar | 13 | air | 200W |
| Quadrupole | 150A | bipolar | 24 | water | 2'000W |
| Dipole | 200A | bipolar | 11 | water | 6'000W |
| Solenoid | 220A | unipolar | 9 | water | 5'000W |

The 20A corrector PS, the 150A quadrupole PS, the solenoid PS and some dipole PS are already built and in operation at the SwissFEL Injector Test facility. A cost and space optimized design for the 10A corrector PS is currently under development. It is foreseen to install 3 independent PS in one 19' rack and control them from one single controller board. Optionally, a high-precision ADC board can be added for one channel if required. Such a triple PS will feed one complete quadrupole magnet, including a quadrupole winding and two corrector windings.

3.4.6 Kicker systems

SwissFEL operation is planned with 2 electron bunches with 28 ns separation per RF macro pulse, at a maximum repetition rate of 100 Hz. One electron bunch will continue through the ARAMIS undulator line, the other bunch will be deviated by the kicker system towards the ATHOS undulator line. The general approach is to use a kicker to give a small, fast deflection, then to follow with a

slow pulse or DC septum magnet, which gives the large angular change. From previous experience with septa at PSI, a beam separation at the septum entrance of 7mm or larger is feasible. The deflection is for a single bunch and therefore flat-top tolerance is not relevant.

Table 3.4.6.1: Starting parameters for system design [73].

| | |
|---|--|
| Beam energy + 10% system reserve | 3.74 GeV |
| Rise time | < 28 ns |
| Beam size | 20 μm rms (H), 50 μm rms (V) |
| Deflection angle | 2° (35mrad) |
| Deflection tolerance of system | < +/-10 ppm (under discussion) |
| Available length | < 7 m |

From Table 3.4.6.1, the deflection tolerance is extremely small and all possibilities will be explored to relax this. Using equipartition of jitter, the tolerances are divided equally between amplitude and time jitters, and inversely proportional to the deflection angle; the results are shown in Table 3.4.6.2.

Table 3.4.6.2: Septum and kicker jitter tolerances

| | |
|---|---|
| Beam separation at septum entrance | 7 mm |
| Approximate deflection for fast kickers | $\sim 7 \text{ mm}/3 \text{ m} = 2.3 \text{ mrad}$ |
| Septum amplitude jitter, peak-peak | < +/-5 ppm |
| Kicker pulse shape | sine wave |
| Kicker amplitude jitter, peak-peak | ($\sim 33 \text{ mrad}/2.3 \text{ mrad}$ of septum value) < +/-36 ppm |
| Kicker time jitter, peak-peak | ($\sim 33 \text{ mrad}/2.3 \text{ mrad}$ of septum value) < +/-7.2 ppt of full cycle time |

The parameters for the septum and kickers are found using the program MAGNET, and the results are given in Table 3.4.6.3-4. Several design parameters were chosen from experience. The kicker will be implemented as an LC resonator with a resonant frequency of $\sim 40\text{MHz}$, phase locked to the linac RF and driven by a FET switch. With this combination, the jitter specification should be achieved by avoiding the use of thyatron switches.

Table 3.4.6.3: Septum parameters

| Parameter | Given | Derived |
|----------------------------|----------|---------------------|
| Maximum particle energy, E | 3.74 GeV | |
| Magnet gap length, l | 1.5 m | |
| Angle | 35 mrad | |
| Bending radius | | 42.857 m |
| Field intensity | | 291.132 mT |
| Magnet gap width, w | 30 mm | |
| Magnet gap height, g | 20 mm | |
| Number of turns on magnet | 1 turns | |
| Magnet inductance | | 2.827 μH |
| Peak current | | 4.634 kA-t |
| Energy in magnet | | 30.352 J |

Table 3.4.6.3: Kicker parameters

| Parameter | Given | Derived |
|----------------------------|----------|---------|
| Maximum particle energy, E | 3.74 GeV | |
| Magnet gap length, l | 500 mm | |
| Angle | 2.3 mrad | |

| | | |
|---------------------------|---------|------------|
| Bending radius | | 217.391 m |
| Field intensity | | 57.395 mT |
| Magnet gap width, w | 15 mm | |
| Magnet gap height, g | 60 mm | |
| Number of turns on magnet | 1 turns | |
| Magnet inductance | | 157.080 nH |
| Peak current | | 2.740 kA |
| Energy in magnet | | 589.814 mJ |
| Pulse repetition rate | 100 Hz | |
| Power loss | | 1.800 W |
| Capacitor voltage | | 17.460 kV |

Using the estimated lengths in the septum and kicker tables above, a possible mechanical layout in the tunnel is shown in Figure 3.4.6.1.

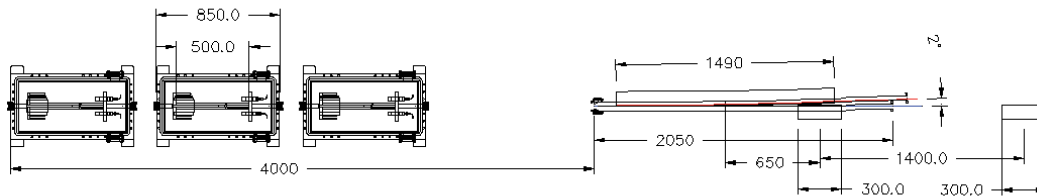


Fig. 3.4.6.1. Plan of kicker and septum layout.

3.5 Undulators

The SwissFEL will have two undulator lines. The one for hard X-rays from, 7 Å (2 keV) to 1 Å (12.4 keV), with an electron energy of 5.8 GeV, is named Aramis. The second one, covering the entire soft X-ray range, from about 200 eV to 2 keV with full polarization control, is named Athos and is supported by a planar undulator (d'Artagnan) required for seeding, but with the capability to emit up to 40 eV (30 nm).

The undulator design for the Aramis line is based on PSI's experience with short-period, small-gap in-vacuum undulators, and experience with APPLE II type (Advanced Planar Polarized Light Emitter) undulators for the Athos line.

The emitted photon wavelength is given by the following resonance condition for planer undulators:

$$\lambda = \frac{\lambda_U}{2\gamma^2} \left(1 + \frac{1}{2}K^2\right)$$

where electron energy $\gamma = E/E_0$, the period length of the undulator is λ_U and the magnetic field B . K is defined by: $K = 0.0934 \times B[\text{T}] \times \lambda_U[\text{mm}]$. For a helical undulator, the factor $\frac{1}{2}$ before K^2 disappears.

All undulators will be based on permanent magnet technology, with its well-established optimization concepts. Electromagnetic alternatives do not deliver sufficient magnetic field strength and superconducting undulators do not yet deliver the required field quality.

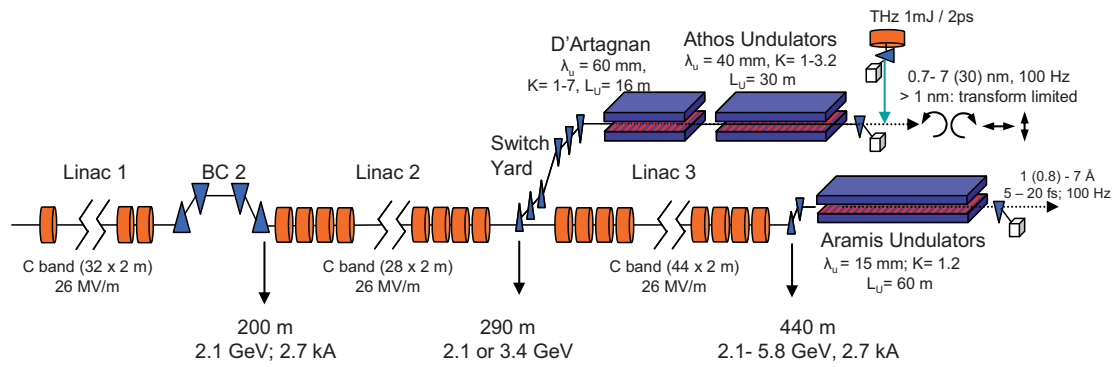


Fig. 3.5.1: Schematic layout of the undulators, with electron energies and wavelength ranges.

3.5.1 Aramis undulator

In the hard X-ray beamlines, the photon wavelength is varied by increasing the electron energy from 2.1 GeV up to 5.8 GeV, the maximum value achievable with the present linac design. In order to produce photons with wavelengths as low as 0.1 nm at this electron energy, the undulator has a 15 mm period (U15) and a small K value of 1.2. This last choice only allows small tuning of the output wavelength, because K must be larger than 1 (for $K < 1$, there is a drop in the coupling between radiation and electron beam). However, this margin is large enough for tapering the undulator modules, to compensate for electron energy loss along the undulator, or to vary the photon energy around an absorption edge. This working point demands a magnetic field of about 0.85 T, requiring small gaps, because the field scales with the ratio of the period length and gap. To minimize the undulator length, in-vacuum undulator technology has been developed. In the vacuum chamber, a 100 μm -thick copper-nickel coated foil covers the magnets, in order to provide good electrical boundaries, and hence low impedance. The minimum gap allowed is 3.2 mm.

Table 3.5.1: The main parameters of the Aramis undulators (Top: Summary Table; Bottom: Details Table)

| Type | Hybrid - In Vacuum | | | | |
|-----------------|---------------------------|-----|------|-----|----|
| # units | 12 | | | | |
| Period | 15 mm | | | | |
| # periods | 266 (including ends) | | | | |
| Magnetic length | 3990 mm | | | | |
| K-values | 1.8 | 1.4 | 1.2 | 1.0 | - |
| GAP | 3.2* | 4.2 | 4.7 | 5.5 | mm |
| Bz max | 1.27 | 1 | 0.85 | 0.7 | T |
| Br | 1.25 T | | | | |
| HcJ | >2400 kA/m | | | | |
| Magnet size | WxHxT=30x20x2.25 mm | | | | |
| Pole size | Wb/WtxHxT=20/15x16.5x3 mm | | | | |
| Max GAP | 20.0 mm | | | | |
| Δ GAP | 0.3 μm | | | | |

*Minimum magnetic GAP (Vacuum GAP=3mm)

| Requirements (Nominal Parameters for 200 pC) | | Unit | Reference |
|--|------|------|-----------------|
| Undulator Magnetic Length | 3990 | mm | FEL-RV84-002-4 |
| Number of Undulators | 12 | | FEL-RV84-002-4 |
| Period λ_u | 15 | mm | FEL-RV84-002-4 |
| Undulator parameter K value | 1.2 | mm | FEL-RV84-002-4 |
| Gap g | 4.2 | mm | CDR - July 2010 |

| | | | |
|--|----------------|-------|------------------------|
| Pole Magnetic Field Bz on axis | 0.85 | T | CDR - July 2010 |
| Magnetic Remanence Br | 1.25 | T | CDR - July 2010 |
| Beam total energy p/c [GeV/c] | 5.8 | GeV/c | CDR - July 2010 |
| Saturation length | 45 | m | CDR - July 2010 |
| Resonant Wavelength | 0.1 | nm | CDR - July 2010 |
| Photon Pulse energy at saturation at 0.1 nm | 66 | μJ | CDR - July 2010 |
| Peak Power at Saturation at 0.1 nm | 2 | GW | CDR - July 2010 |
| Photon Pulse Length (rms) | 13 | fs | CDR - July 2010 |
| Photon Beam Radius (rms) | 22.2 | μm | CDR - July 2010 |
| Photon Beam Divergence (rms) | 1.1 | μrad | CDR - July 2010 |
| Tolerances (single error source) : | | | CDR - July 2010 |
| Maximum Undulator K detuning between 2 undulators | 0.073 | % | CDR - July 2010 (Sven) |
| Maximum Undulator Vertical Misalignment between undulators | 83 | μm | CDR - July 2010 (Sven) |
| Injection trajectory offset electron beam / undulator axis | 11.7 | μm | CDR - July 2010 (Sven) |
| Injection angle between electron beam / undulator axis | 0.78 | rad | CDR - July 2010 (Sven) |
| Hardware Design Specifications: | | | |
| Type | Hybrid | | |
| Magnetic Length | 3990 | mm | CDR - July 2010 |
| Number of Undulator units | 12 | | CDR - July 2010 |
| Period | 15 | mm | CDR - July 2010 |
| number of periods (uncluding ends) | 266 | | |
| K value | 1.2 | mm | CDR - July 2010 |
| Gap | 4.7 | mm | CDR - July 2010 |
| Maximum Vertical Magnetic Field Bz | 0.85 | T | CDR - July 2010 |
| Magnetic Remanence Br | 1.25 | T | CDR - July 2010 |
| Beam total energy p/c [GeV/c] | 5.72 | GeV/c | CDR - July 2010 |
| Coercivity Hcj | 2400 | kA/m | CDR - July 2010 |
| Magnet Size (Width*Height*Thickness) | 30*20*2.25 | mm | CDR - July 2010 |
| Magnetic Material | NdFeB-Dy | | CDR - July 2010 |
| Steel Pole Size(Width / Top)*Height*Thickness) | 20 / 15*16.5*3 | mm | CDR - July 2010 |
| Thickness of Coating Foil Material Cu-Ni | 100 | μm | CDR - July 2010 |
| residual field integral | | T.m | CDR - July 2010 |
| Gap Operating range | 3.2 to 20 | mm | CDR - July 2010 |
| Typical Magnetic field | 1.3 to 0.06 | T | CDR - July 2010 |
| Beam Pipe inner diameter | 10 | mm | CDR - July 2010 |
| Cooling Art | air | | CDR - July 2010 |
| Operating Temperature (ambient) | 26 | deg | CDR - July 2010 |
| Weight | 25000 | kg | CDR - July 2010 |
| Dissipated Power | 0.4 | kW | FEL-MP06-257 |
| Expected Stability and Precision: | | | |
| Sensitivity to temperature dB/dT | -0.1 | %/K | |
| Temperature stability (ambient) | 0.1 | K | |
| Good field region width (where dB/B < 1e-4) | 2 | mm | CDR - July 2010 |
| Good field region height (where dB/B < 1e-4) | 60 | μm | CDR - July 2010 |
| Minimum Gap increment | 0.3 | μm | |
| Magnetic Field Resolution | 1 | G | |
| Corresponding minimum K increment | 0.14 | | |
| Mechanical Vertical Alignment Precision | 30 | μm | SwissFEL Jul. 1st 2010 |
| Mechanical Horizontal Alignment Precision | > 200 | μm | SwissFEL Jul. 1st 2010 |
| Straightness of inner l-beam undulator (over 4 m) | 10 | μm | SwissFEL Jul. 1st 2010 |
| Magnetic Field Measurement Art | Hall Probe | | |
| Magnetic Axis Determination Technique | Beam Based | | |
| Precision in Magnetic Axis determination (peak to peak) | 1 | μm | Thomas |
| Electrical Interface: | | | |
| Electrical Drawings | | | |
| Water Interface | | | |
| no water | | | |
| Mechanical Interface | | | |
| Mechanical Drawings | | | 50023.28.011 |
| Alignment Art | Laser Tracker | | |
| Transport Art after final alignment of magnets | Air Cushion | | |

| | | | |
|----------------------------|-----------|------|-----------------|
| Vacuum | | | |
| Vacuum Layout | | | CDR - July 2010 |
| Vacuum level | 1.00E-07 | mbar | |
| Baking maximum temperature | No Baking | | |

The magnet material has to provide a high flux density and high stability against radiation-induced demagnetization, expressed by the remanence B_r and coercivity H_{cJ} . The materials of choice are the rare-earth magnets $\text{Sm}_2\text{Co}_{17}$ and NdFeB. Samarium-cobalt is less strong, but of high stability, Neodymium-iron-boron is stronger, but generally less stable. Stability has been increased by replacing some Nd with Dy, but because the magnetic moment of Dy is opposite to Nd and Fe, remanence is lowered. One solution is to operate the undulator at cryogenic temperatures, because both parameters have a negative temperature gradient. Recently, a new fabrication technique has been developed which provides improvements at room temperature. Dy is added at a later process step by diffusion along the grain boundaries, and it can stabilize the magnet without a negative effect on the strength. The remanence can be increased from 1.08 T, as used at the SLS undulators, up to 1.25 T (with diffused Dy) or to >1.5 T (with cryogenic undulator). For the SwissFEL U15, the material with $B_r = 1.25$ T at $H_{cJ} = 2400$ kA/m seems to be sufficient and avoids the additional complications due to the cryogenic components.

For the single-pass FEL, the good field region requirement around the beam axis is smaller than that for undulators used in storage rings. This allows less-wide poles to be used, which concentrates the flux density in the centre and reduces the magnetic load by reducing the volume under the pole. With a chamfered pole, with 15 mm pole tip, and 30 mm-wide magnets, a maximum K value of about 1.5 is achievable at a gap of 4 mm, using diffused dysprosium-enriched NdFeB magnets at room temperature. The design K value of 1.2 will be reached with a gap of 4.7 mm. Using the cryogenic permanent magnet undulator (CPMU) technology, the maximum K could even be 1.75, and a K value of 1.2 could already be achieved with a 5.3 mm gap. Finally the good field region where $\Delta B/B < 10^{-4}$ is 2 mm full width in the horizontal direction and 60 μm in the vertical direction.

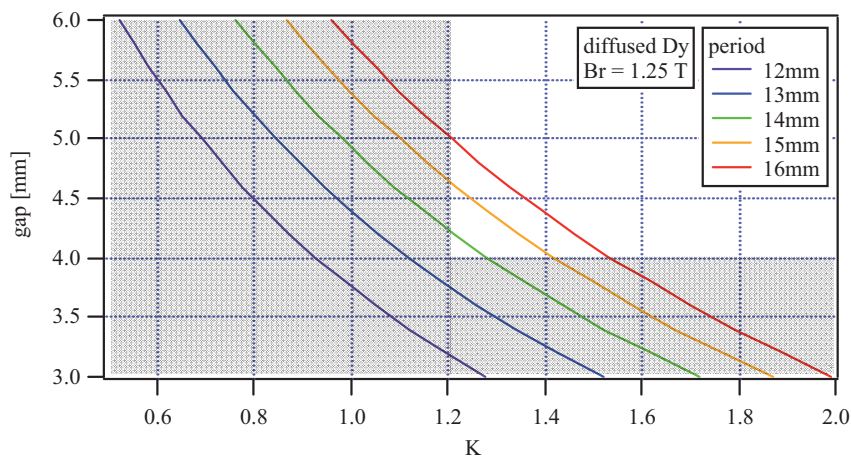


Fig 3.5.2: Gap versus K value for period length between 12 and 16 mm. It is planned to build a U15 with 15 mm period and recently developed NdFeB stabilized with diffused Dy. The white area is the working area: $K > 1.2$ with gap > 4 mm. A period of 16 mm conflicts with the demand of 1\AA with the maximum 5.8 GeV, and is given only for reference. A higher remanence would move the curves to the right, also allowing shorter periods.

Measurement and adjustment of field variations along Aramis undulators:

- 1) A laser beam going through the undulator in the gap center will define a straight line over 4 m.

- 2) A Hall probe sliding longitudinally will measure the magnetic field variation along this laser line ($B(z)$) (precision in Hall probe positioning will be less than 50 nm)
- 3) A control system will calculate the necessary height corrections to apply to the magnets where B field variations has been measured
- 4) An automatic system will act on the incriminated keepers to change locally the gap.

This method will be tested on a prototype undulator and should result in magnetic field variations of less than 1 G over 4 m.

3.5.2 Athos undulator

The basic concept in the layout of the soft X-ray beamline is to combine the tunability of the undulators with switchable extraction energy. An APPLE II type undulator with 40 mm period length (UE40), in combination with extraction energies of 2.1 and 3.4 GeV, is capable of covering the entire wavelength range from 200 eV to 2 keV on the fundamental harmonic, the first emission line of the undulator. The exact photon energy range depends on the maximum undulator parameter K in the various modes of operation: Linear polarization continuously changeable from 0-180°, as well as circular, which varies between 3.5 and 2.3. The extraction point is located at 3.4 GeV. For operation at 2.1 GeV, Linac 2 is not triggered and the beam is transported beyond 2.1 GeV through empty cavities up to the extraction point.

Table 3.5.2: The main parameters of the Athos undulators.

| name | UE40 | UE60 | U60 | U100 | U110H | |
|----------------------------|--------------|-----------|-----------|------------|-------------------|-----------------|
| period | 40 | 60 | 60 | 100 | 110 | mm |
| gap (magnetic) | 6.5 (8) - 24 | 8 - 40 | 8 - 40 | 9 - 27 | 7 - | mm |
| K | 3.5 - 0.9 | 5.2 - 0.9 | 5.2 - 0.9 | 15.2 - 4.8 | | |
| gap (vacuum) | 5 × 10 | 6 × 12 | 6 × 12 | 8 × 16 | 6 × 12 | mm |
| gap variation | 32 | 32 | 32 | 32 | 32 | mm |
| open gap / $K\text{min}^2$ | 38.5 / 0.3 | 40 / 0.86 | 40 / 0.9 | 41 / 2.5 | | |
| magnet size | 20×20×10 | 20×20×10 | 40×20×10 | 40×25×40 | 30×30×25 | mm ³ |
| pole size | - | - | - | 20×25×35 | - | |
| remanence | 1.08 | 1.08 | 1.08 | 1.25 | 1.25 | T |
| Bz / Bx | 0.94 / 0.81 | 0.8 / - | 0.8 / - | 1.63 / - | - / 1.41 | T |
| Kz / Kx | 3.5 / 3.0 | 3.2 / - | 3.5 | 15.2 / - | - / 14.5 | |
| type | APPLE II | APPLE II | PPM 4 × 1 | Hybrid | APPLE II LV fixed | |
| units | 6 | 2 | 1 | 2 | 1 | |
| unit length | 4 | 4 | 4 | 4 | 4 | m |
| number of periods | 98 | 64 | 64 | 38 | 35 | |

Operation of the APPLE II undulators is more challenging than with the in-vacuum undulators. Firstly, because of the different modes of operation, and secondly, the electron trajectory lies in the fringe field of the four magnet arrays. Although these pure permanent magnets have no iron poles, their magnets have a permeability which differs slightly from unity. This results in nonlinearities, which are the source for a variation in the field integrals when shifting the magnet arrays. Those nonlinearities also lead to distortions of the cosine behaviour of the magnetic field, which are responsible for small errors in the prediction of the energy and polarization. Samarium-cobalt shows significant smaller nonlinearities. In addition, it shows a smaller temperature dependency, so that

samarium-cobalt seems to be a serious candidate, although it is more delicate to handle because it is more brittle compared with neodymium-iron-boron.

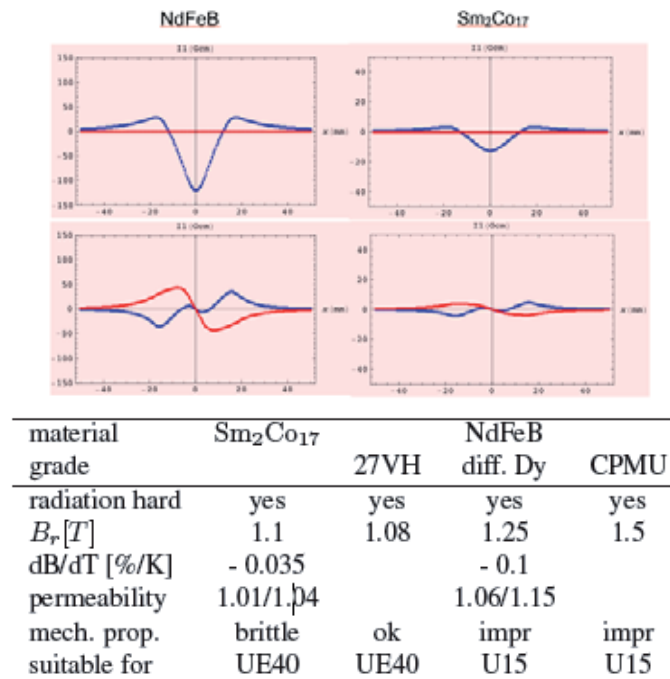


Fig. 3.5.3: Transverse variation of the first field integrals due to nonlinearity of the permanent magnet material in circular (top) and linear inclined modes (bottom), for NdFeB and Sm₂Co₁₇.

3.5.3 Undulator module

The expected saturation length of the SwissFEL varies with the electron energy, but should not exceed 45 m. Including contingency, this means for Aramis a total length of 60 m. Hence the undulator has to be segmented to allow space for focusing, beam diagnostic and electron beam corrections (see Figure 3.5.4).

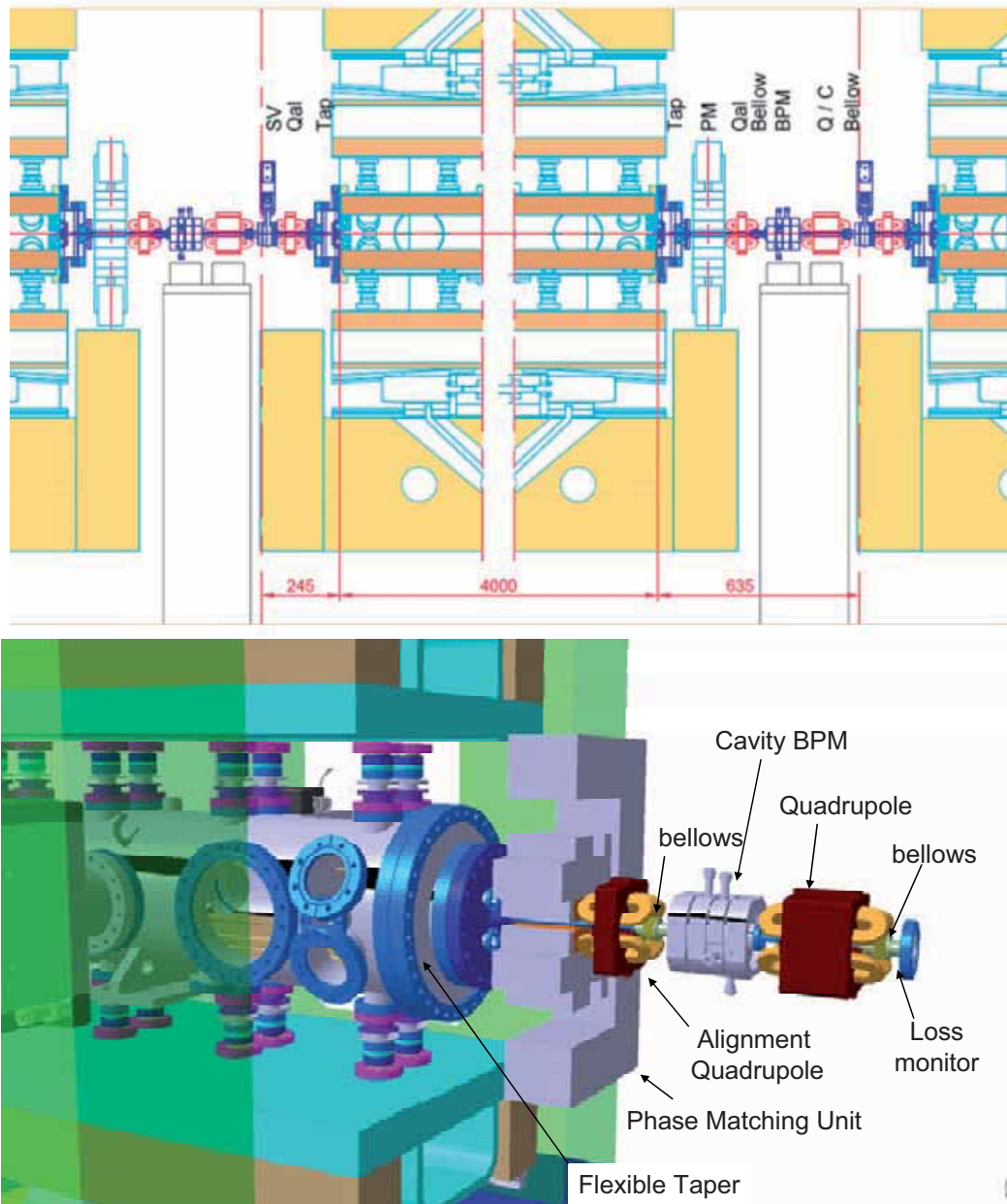


Fig. 3.5.4: Layout of the undulator module. Top: 1 module is 4.88m, from left to right: sector valve (SV), alignment quadrupole (Qal), flexible taper section (Tap), undulator for Aramis line (U15), flexible taper section (Tap), phase matching unit (PM), alignment quadrupole (Qal) and bellows. Bottom: 3D view of the undulator module entrance part.

An undulator module consists of a 4 m-long undulator, two 100 mm flexible taper sections (Tap), to guarantee a continuous change of the gap for the in-vacuum undulator, a phase-matching unit (PM), a cavity beam position monitor (BPM) and a quadrupole (Q) with an integrated correction coil (C) at the downstream side and two small quadrupoles (Qal) installed close to the undulator, one upstream and one downstream, used for undulator beam-based alignment and turned off during regular operation.

The Qal are installed on the undulator frame and aligned with respect to the undulator axis in the magnetic measurement laboratory (MML). With different gaps, the axis of the Qal can move away

from the undulator axis due to the changing forces on the common frame, hence the beam-based alignment should be performed with the same gap as during the magnetic alignment.

The module is completed by a bellows and a sector valve (SV), for a total length of 4880 mm. For the in-vacuum undulator, pumping will take place along the magnet structure. For UE40, with a vacuum chamber having a tiny cross-section of $5 \times 10 \text{ mm}^2$, the flexible tapered sections can be replaced by a pumping port, so that the total length may be identical for both modules.

3.5.4 Mechanics

SwissFEL undulators are all equipped with the same frame, see Figure 3.5.5. This consists of four units, consisting of two identical pairs: the lower and the upper “base” and the two sides. This new approach increases the symmetry with respect to the classical C frame adopted in many synchrotron light sources and allows for more compact solutions. The main disadvantage is decreased accessibility to the magnet region. The functionality of the frame is also changed, and it now plays a central role in the rigidity of final magnet configuration.

In this design, the frame transfers its stiffness to the I-beam through a wedge-based gap drive system. Because the I-beam is supported over about 70% of its total length, its height can be substantially reduced with respect to the C-frame solution.

An electron beam height of 1200 mm can be realized with this concept, allowing the hosting of the vacuum vessel of the in-vacuum undulator with all of its interior components, as well as the moveable magnet arrays of the APPLE undulator. The entire module can be aligned in 5 degrees of freedom by means of the SLAC camshaft movers, which have also been used for the SLS and LCLS.

Detailed studies carried out both in PSI and by industry have confirmed that the general concept of this new frame can be further improved by making use of mineral cast material, which has better internal damping than the more popular cast iron, is not magnetic and has a lower density.

The openings on the side of the frame allow access to the magnets and to the differential screws at the interface to the in-vacuum inner I-beam, essential for magnetic optimization.

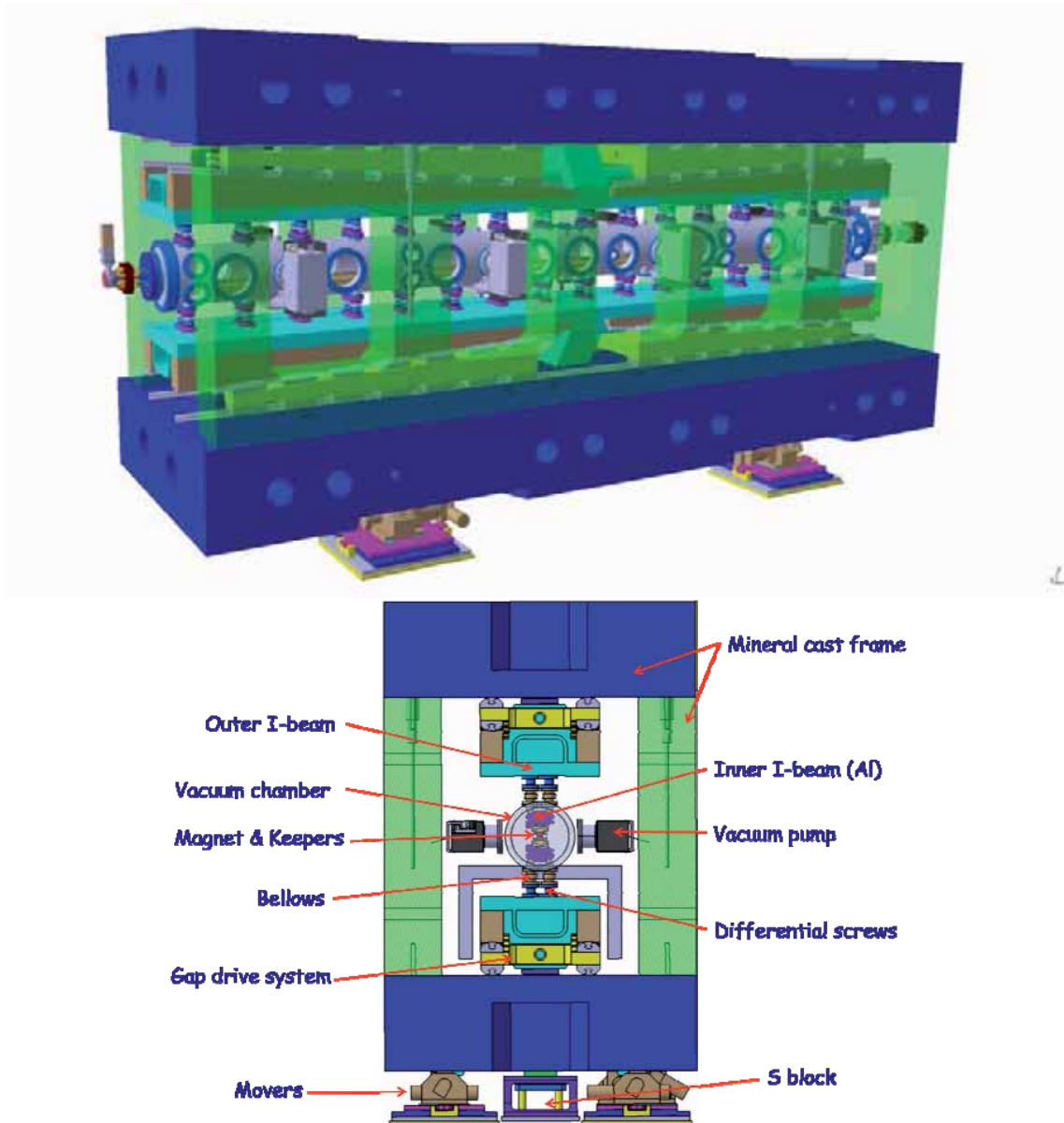


Fig. 3.5.5: Design study of the undulator frame. Above, a 3D global view of U15; below, a 2D cross-section with reference to the different components.

Besides the support structure, cost effective solutions for the keeper, which holds the permanent magnets, are also being studied. Designs of a standard keeper for planar undulators based on extruded aluminum have been carried out and have to be tested. Those designs allow adjustment of magnet position with the help of a single screw to a precision of $20\ \mu\text{m}$ and a similar design is being evaluated for APPLE II type undulators (see Figure 3.5.6).

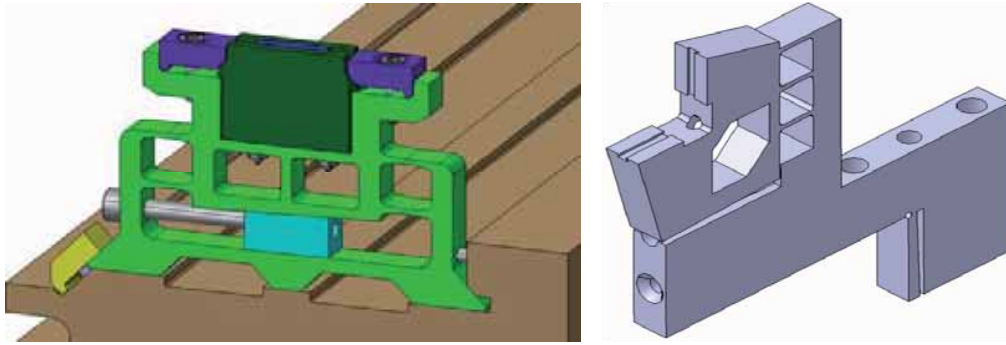


Fig. 3.5.6: Design study of adjustable and cost effective keepers made of extruded and wire eroded aluminum. On the left, the advanced design of the keeper for the hybrid in-vacuum undulator Aramis; on the right, preliminary ideas for the keepers of the PM Apple II undulator Athos.

3.5.5 Phase matching unit (phase shifters) design

In the gap, between the undulator modules, the electrons transverse velocities experience a phase shift in respect to the radiated electromagnetic wave. Such a phase mismatch causes the electrons to momentarily gain energy from the radiation field, interrupting the amplification process. The adjustable phase shifter corrects this difference before the next undulator unit.

The designs of the phase shifters for the SwissFEL hard and soft X ray beam lines are presented below, both the physical dimensions and material properties are specified together with a detail analysis of the performance. Fig. 3.5.5.1 shows the conceptual magnetic structure common to both phase shifters. It consists of five sections. The central symmetry guarantees a zero first field integral while the trajectory is optimized with respect to a nominal GAP of 14 mm.

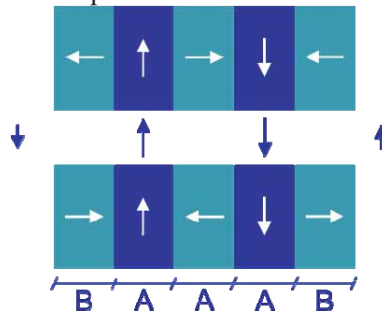


Figure 3.5.5.1 Conceptual Phase Shifter magnetic structure chosen for both the hard and soft X-ray beam lines.

Both designs have been realized with Samarium Cobalt which has a residual magnetization of 1.1 T, and lower non-linearity in comparison to the NdFeB. It is also less sensitive to temperature variations. The calculations have been made for the nominal K values of 1.2 and 3.5 for Aramis and Athos beam-line respectively.

Aramis phase shifter design

Fig.3.5.5.2 shows the 3D model of the Aramis (U15) phase shifter together with a parameter table. The overall length (along the beam line) of the device does not exceed 31.5 mm, compatible with the allocated space (about 100 mm, see Fig. 3.5.4).

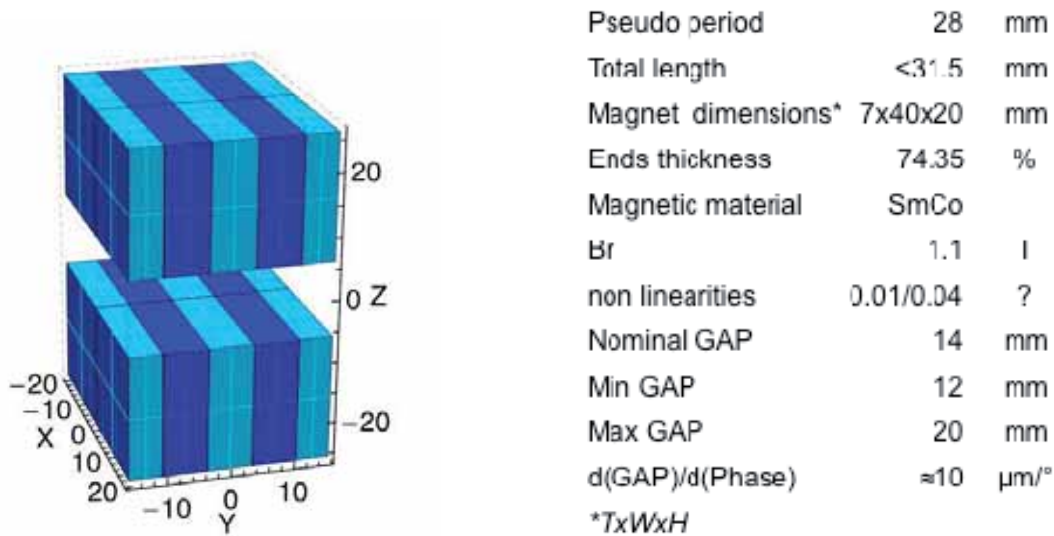


Figure 3.5.5.2: The Aramis (U15) phase shifter design, on the left the geometry of the 3D magnetic model (a) and on the right the summary table of the main parameters.

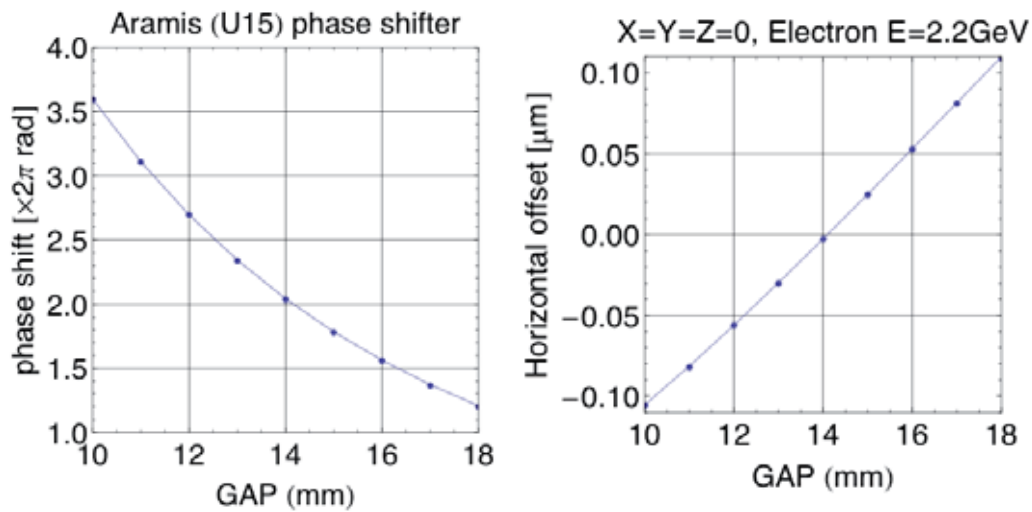


Figure 3.5.5.3 On the left side the phase shift as a function of the GAP, on the right the horizontal offset as a function of the GAP at minimum energy. The design is optimized with respect to a GAP of 14mm.

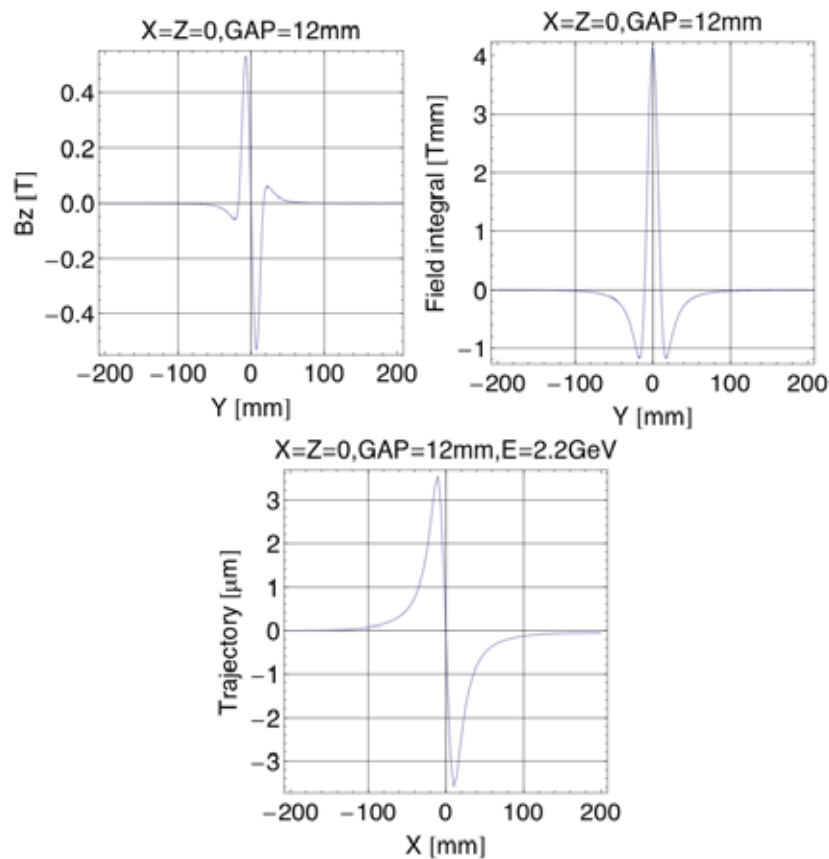
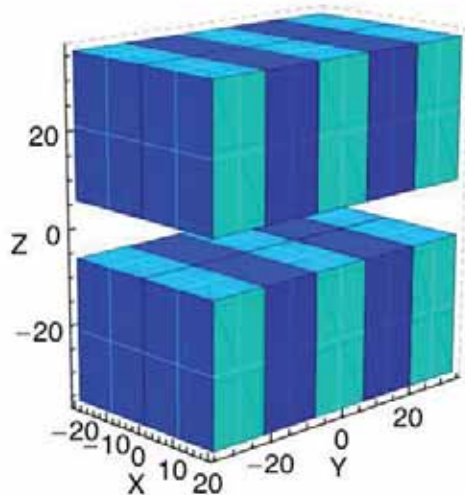


Figure 3.5.5.4 From the left to the right respectively: the magnetic field distribution, the first field integral and the trajectory (this last one for 2.2 GeV, minimum energy).

Athos phase shifter design

In Fig.3.5.5.5 shows the 3D model of the Athos (UE40) shifter together with a parameter table. The overall length (along the beam line) of the device does not exceed 31.5 mm which is compatible with the allocated space (about 100 mm).



| | | |
|---------------------------------|---------------|----------------------|
| Pseudo period | 56 | mm |
| Total length | <69 | mm |
| Magnet dimensions* | 14x40x30 | mm |
| Ends thickness | 96.27 | % |
| Magnetic material | SmCo | |
| Br | 1.1 | T |
| non linearities | 0.01/0.04 | ? |
| Nominal GAP | 14 | mm |
| Min GAP | 12 | mm |
| Max GAP | 20 | mm |
| $d(\text{GAP})/d(\text{Phase})$ | ≈ 8.7 | $\mu\text{m}/^\circ$ |
| *TxWxH | | |

Figure 3.5.5.5 The Athos (UE40) shifter design, on the left the geometry of the 3D magnetic model (a) and on the right the summary table of the main parameters.

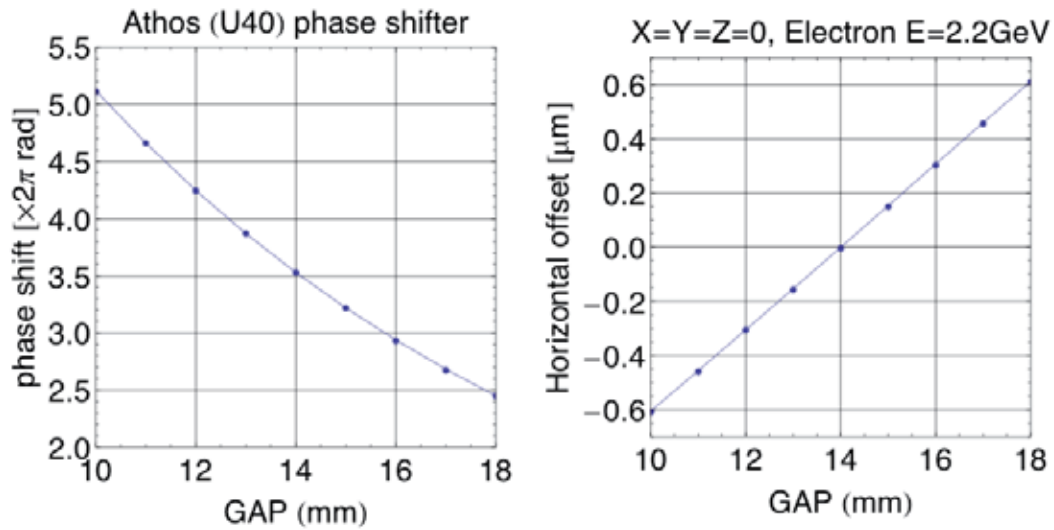


Figure 3.5.5.6 Phase shift as a function of the GAP (left), horizontal offset as a function of the GAP at minimum energy (right). The design is optimized for a GAP of 14mm.

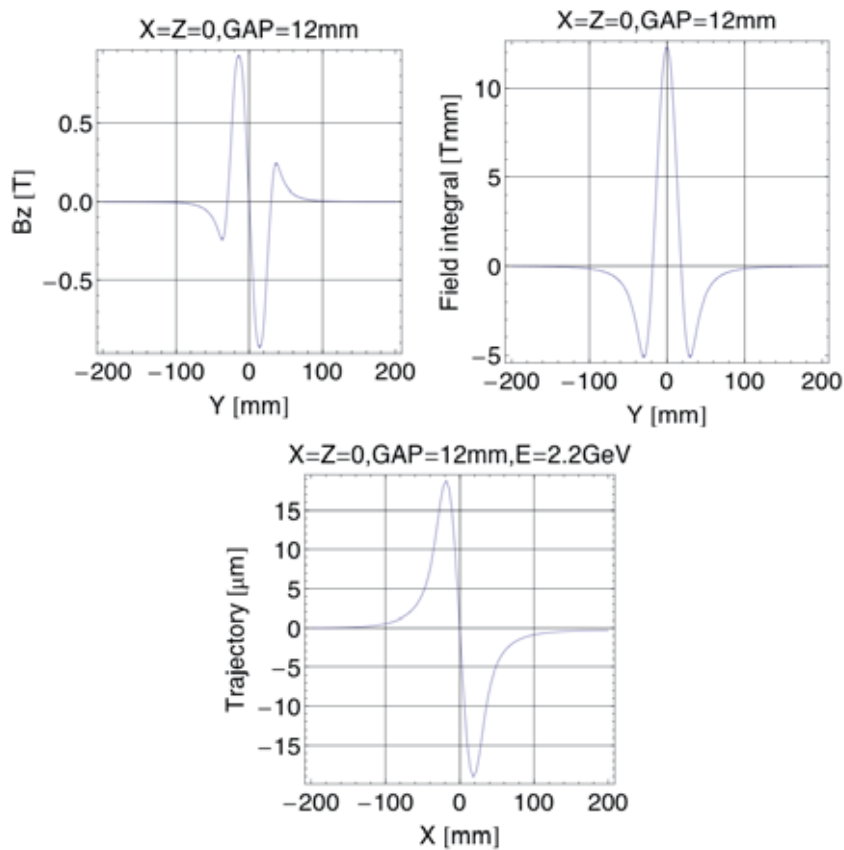


Figure 3.5.5.7 From the left to the right: the magnetic field distribution, the first field integral and the trajectory (this last one for 2.2GeV, minimum energy).

3.5.6 Undulator tolerances:

For successful lasing of the SwissFEL, there are tight tolerances on the undulators with respect to magnetic field parameters and alignment. The magnetic flux density is linked via the resonance condition to the photon wavelength, and for small K value variation we have:

$$\frac{\delta\lambda}{\lambda} \approx \frac{K^2}{1+\frac{1}{2}K^2} \frac{\delta K}{K} = \alpha \frac{\delta K}{K}$$

($K = 1 \rightarrow \alpha=0.67$, $K = 1.2 \rightarrow \alpha= 0.84$, $K = 1.4 \rightarrow \alpha= 0.99$).

Gap variation in U15: 1 μm gap change corresponds to a relative field variation of $2.5\text{e-}4$. If the gap can be controlled with 0.3 μm precision then the corresponding change in the FEL photon energy is 1.2 eV (for 12.4 keV photons). Tolerances are summarized in Table 3.5.1.

3.6 Electron beam diagnostics concept (Rasmus, Volker)

Electron beam diagnostics have to provide a full set of instrumentation for all SwissFEL operation modes, to accommodate three major tasks:

- Support accelerator commissioning and machine start-up (e.g. during SwissFEL commissioning, but also after shut-downs and future upgrades) by permitting the measurement and optimization of all electron beam parameters within an extended dynamic range.
- Provide, where possible, online information about all relevant beam parameters to the control room, to allow day-by-day operation of the SwissFEL user facility in a reliable and reproducible way.
- Provide input to a set of beam-based feedback loops, which will automatically stabilize the electron, and therefore also the photon, beam over longer time periods.

In addition, the designs of the diagnostics systems have to be robust and reliable, to enable 24h / 7d operation of the final SwissFEL user facility. Wide ranges of parameters – starting with the commissioning phase and extending to user operation modes – have to be incorporated in the designs, and full integration in the control system is a prerequisite for efficient support of machine operation. High data acquisition bandwidths, low-latency data processing and data transfer (over high-speed fiber links) have to be incorporated in all of the feedback-ready monitors (e.g. beam position monitors (BPM) or synchrotron radiation monitors (SRM)). All dedicated diagnostics sections will be designed to be an integral part of the standard SwissFEL beam optics, to allow the measurement, optimization and control of beam parameters with standard accelerator settings.

Although some of the stability requirements are still preliminary at this stage of the project, the two standard SwissFEL beam optics – the so called “200 pC” and the “low charge 10 pC” modes – provide the baseline parameter set for the design of the diagnostics systems. The design approaches not only account for the SASE operation of the hard X-ray (1 Å) Aramis beamline in the 1st phase of the SwissFEL project, but also include, from the beginning, the seeded operation of the soft X-ray Athos beamline, which will follow during the 2nd SwissFEL project phase, starting in 2018.

3.6.1 Dedicated electron beam diagnostics sections

The SwissFEL accelerator will be equipped with two dedicated diagnostics sections: one located behind the 1st bunch compressor (BC-1), and the second after final bunch compression in the electron beam transport line towards the soft X-ray Athos undulator. Both sections are an integral part of the SwissFEL accelerator optics and will allow the measurement of electron beam parameters, which are most relevant for SASE operation – namely projected transverse and “sliced”

horizontal emittances, bunch length, peak current, and “sliced” and projected energy distributions of the beam.

3.6.1.1 Low-energy diagnostics section

The first diagnostics section is located between BC-1 and Linac 1 at a beam energy of 400 MeV. Its layout follows the design approach of the SwissFEL Injector Test Facility diagnostics line [72], aiming to verify and optimize the beam parameters from the injector for matching into Linac 1. A transverse deflecting cavity (TDC), which will be operated in the vertical direction, will shear the electron beam to provide high-resolution bunch length information. Three FODO cells following the TDC generate sufficient horizontal phase advance ($\Delta\psi_{\text{hor}} \geq 165^\circ$) for measurement of the horizontal “sliced” emittance, while keeping the vertical phase advance $\Delta\psi_{\text{vert}}$ between 60° and 120° , for good time resolution ($\Delta\psi_{\text{vert}} = 90^\circ$ is ideal).

Table 3.6.1: Parameters for “sliced” horizontal emittance and electron bunch length measurements in the SwissFEL low-energy diagnostics section, using the 5-cell SW S-band TDC from the SwissFEL Injector Test Facility

| Parameter | Symbol | Value | Unit |
|---|---------------------------|-----------|-------------------|
| TDC-1 frequency | f_{TDC-1} | 2.998 | GHz |
| Number of cells | N_{TDC-1} | 5 | |
| TDC-1 shunt impedance | R_S | 2.5 | M Ω |
| TDC-1 voltage | V_{TDC-1} | 4.5 | MV |
| TDC-1 peak input power | P_{TDC-1} | 4.1 | MW |
| TDC-1 phase (crest at 90°) | Φ | 0 | deg |
| Beam energy (at TDC-1 and screens) | E_{beam} | 400 | MeV |
| RMS bunch length (200 pC) | τ_{200pC} | 180 | fs |
| RMS bunch length (10 pC) | τ_{10pC} | 35 | fs |
| β -function at TDC-1 | β_{TDC-1} | 25 | m |
| β -function at screens | β_{SCM} | 5 | m |
| Betatron phase advance TDC-1 – screens | $\Delta\Psi$ | 60 – 120 | deg |
| Normalized rms core sliced emittance (200 pC) | ε_{200pC} | 0.4 | $\mu\text{m rad}$ |
| Normalized rms core sliced emittance (10 pC) | ε_{10pC} | 0.18 | $\mu\text{m rad}$ |
| Nominal rms beam size at screens (200 pC) | $\varepsilon_{SCM-200pC}$ | 50 | μm |
| Nominal rms beam size at screens (10 pC) | $\varepsilon_{SCM-10pC}$ | 33 | μm |
| Beam sizes at screens with TDC-1 on (200 pC) | $\sigma_{SCM-200pC}$ | 376 – 435 | μm |
| Beam sizes at screens with TDC-1 on (10 pC) | $\sigma_{SCM-10pC}$ | 73 – 85 | μm |
| Number of slices (200 pC) | $n_{slice-200pC}$ | 7 - 8 | |
| Number of slices (10 pC) | $n_{slice-10pC}$ | > 2 | |
| Bunch length resolution (200 pC) | $\tau_{res-200pC}$ | 21 | fs |
| Bunch length resolution (10 pC) | $\tau_{res-10pC}$ | 14 | fs |

A total of 7 profile monitors (most likely combined OTR and YAG:Ce-type screen monitors) are placed in the FODO cells to measure the transverse beam profiles, providing sufficient phase space information for reconstruction of the (horizontal) “sliced” and projected (both planes) emittances utilizing the same beam optics, when switching the TDC off. A spectrometer magnet at the end of the diagnostics line allows the measurement of the “sliced” and projected energy distributions of the electron beam, with resolution of the order of 10^{-4} . Matching sections – consisting of five quadrupoles each – are located in front of the TDC (aiming for the largest possible vertical β -function in the TDC), the FODO cells and Linac 1. Table 3.6.1 summarizes the parameters for the SwissFEL low-energy diagnostics section, assuming the same β -functions and TDC performance as implemented in the SwissFEL Injector Test Facility. If necessary, a further improvement of the time and “sliced” emittance resolutions could either be achieved by modifying the matching optics into the TDC (for higher vertical β -function in the TDC), by increasing the number of TDC cells (e.g.: designing a 7-cell SW S-band TDC) or by using a C-band TDC, as foreseen for the high-energy diagnostics section, which is capable of providing much higher deflecting voltages. The latter option might be the preferred solution to significantly improve the time resolution for beam parameter measurements in this part of the SwissFEL accelerator.

3.6.1.2 High-energy diagnostics section

The high-energy diagnostics section is located in the beam transport line to the soft X-ray Athos undulator and can be operated at beam energies of 2.4 / 3.1 GeV. Similar to the low-energy diagnostics section, it will include two TDCs (most probably two C-band structures, following the

SCSS design), which deflect the beam in the vertical direction, and 3 FODO cells with distributed profile monitors, to allow measurements of the horizontal “sliced” emittance as well as the bunch length, for peak current of the electron beam after final bunch compression in BC-2.

Table 3.6.2: Parameters for “sliced” horizontal emittance and bunch length measurements in the SwissFEL high-energy diagnostics section using a C-band, TW TDC as currently developed by SCSS [74].

| Parameter | Symbol | Value | Unit |
|---|---------------------------|------------------------|-------------------|
| TDC-2 frequency | f_{TDC-1} | 5.996 | GHz |
| Length of TDC-2 | L_{TDC-2} | 1.7 | m |
| TDC-2 shunt impedance | R_S | 13.9 | M Ω |
| TDC-2 voltage (per deflecting structure) | V_{TDC-2} | 20 | MV |
| TDC-2 peak input power | P_{TDC-2} | 16 | MW |
| TDC-2 phase (crest at 90°) | Φ | 0 | deg |
| Beam energy (at TDC-2 and screens) | E_{beam} | 2.4 / 3.1 | GeV |
| RMS bunch length (200 pC) | τ_{200pC} | 46 | fs |
| RMS bunch length (10 pC) | τ_{10pC} | 2 – 5 | fs |
| β -function at TDC-2 | β_{TDC-1} | 60 | M |
| β -function at screens | β_{SCM} | 10 | M |
| Betatron phase advance TDC-2 – screens | $\Delta\Psi$ | 60 – 120 | deg |
| Normalized rms core sliced emittance (200 pC) | ε_{200pC} | 0.4 | $\mu\text{m rad}$ |
| Normalized rms core sliced emittance (10 pC) | ε_{10pC} | 0.18 | $\mu\text{m rad}$ |
| Nominal rms beam size at screens (200 pC) | $\varepsilon_{SCM-200pC}$ | 29 / 25 | μm |
| Nominal rms beam size at screens (10 pC) | $\varepsilon_{SCM-10pC}$ | 19 / 17 | μm |
| Beam sizes at screens with TDC-2 on (200 pC) | $\sigma_{SCM-200pC}$ | 714 – 619 536 – 464 | μm |
| Beam sizes at screens with TDC-2 on (10 pC) | $\sigma_{SCM-10pC}$ | – | μm |
| Number of slices (200 pC) | $n_{slice-200pC}$ | 24 – 21 21 – 18 | |
| Number of slices (10 pC) | $n_{slice-10pC}$ | – | |
| Bunch length resolution (200 pC) | $\tau_{res-200pC}$ | 2 / 2.1 | fs |
| Bunch length resolution (10 pC) | $\tau_{res-10pC}$ | / | fs |

A spectrometer magnet will permit the determination of the “sliced” and projected energy distributions of the electron beam. The beam dynamics layout of the high-energy diagnostics section still needs to be optimized and completed, but as for the low-energy diagnostics section, it is foreseen that both the (horizontal) “sliced” and the projected (both planes) emittances should be measureable without changing the nominal beam transfer optics to the Athos undulator. By using the fast beam distribution kicker to the Athos beamline already during the first SwissFEL operation phase, the TDC measurements in the high-energy diagnostics section could be operated in a “pulse stealing mode”, providing continuous information about the “sliced” electron beam parameters even during Aramis user runs.

3.6.2 Transverse beam profile measurements

Most of the beam properties which will be measured along the SwissFEL accelerator (see transverse profile measurement locations below) are related to emittance and peak brightness, and can be obtained by the determination of transverse profiles. Since, in reality, the bunch structure is often not of Gaussian shape, but contains important information in its tails, the transverse profile monitors

require high resolution and a high dynamic range simultaneously. Depending on the location and the transverse beam size to be measured, the profile monitors typically consist of a combination of YAG:Ce crystals (cerium-doped yttrium aluminum garnet of 20 μm and 200 μm thicknesses) for beam finding, at low beam energies and for low-charge operation and OTR (optical transition radiation) screens. They will be equipped with two types of imaging optics, providing projected pixel sizes of the order of 25 μm for an “overview path” (with up to 15 mm field of view), and $< 10 \mu\text{m}$ for the “high resolution path” (~ 2 mm field of view). Imaging will normally be performed by CCD sensors. Special CMOS sensors can image bunches separated by 70 ns, but due to rather high investment costs, these cameras will only be placed at selected locations. The screens can be inserted in the electron beam path by means of motorized linear UHV feed-throughs and absolute linear encoders (100 nm resolution) for position control. In case SwissFEL – like LCLS – also suffers from coherent OTR, all profile monitors can be equipped with wire scanners [75]. Experience with the high-brightness beam from the SwissFEL Injector Test Facility may already indicate at the start of SwissFEL commissioning if and where wire scanners will be needed.

3.6.2.1 Locations of transverse beam profile measurements

Apart from the dedicated diagnostics sections which have been described in the previous paragraphs (Sections 3.6.1.1 and 3.6.1.2), a number of additional locations for specific electron beam parameter measurements will be available along the SwissFEL accelerator.

Directly behind the RF gun, at an electron beam energy of ~ 7 MeV, the projected transverse emittances as well as beam matching conditions in the injector can be determined with gun solenoid and quadrupole scans. In the case of cathode exchanges or examination (and use) of improved cathode materials, RF photo-gun performance can be optimized by means of horizontal and vertical slit scans. The slits will be installed directly in front of the S-band injector, using the distance of ~ 4.5 m to a profile monitor behind the 1st S-band structure as a drift space, with the accelerator structure switched off. For complete characterization of the phase space, a dipole spectrometer magnet also permits the measurement of the electron beam energy distribution from the RF gun.

Transverse beam emittances, Twiss parameters and matching conditions into the bunch compressors can be determined in front of BC-1 and BC-2 by application of quadrupole scans. The corresponding profile monitors – OTR / YAG:Ce screens, or in the case of coherent OTR, wire scanners – will be equipped with high-resolution optics and camera systems to automatically perform these measurements during accelerator set-up and tuning.

Matching into Linacs 1, 2 and 3, as well as into the Aramis and Athos undulators, will be controlled by a number of transverse profile monitors (OTR / YAG:Ce screen or wire scanner) located within the matching sections, and at locations of adequate betatron phase advance along the linacs to identify beta-beating in case of unmatched beam optics.

The energy distribution of the electron beam after passing the Aramis and Athos undulators will be monitored in spectrometer arms using transverse profile monitors (OTR / YAG:Ce screens or wire scanners), which will be located in the corresponding beam-dump lines. In addition to the beam energy distribution during commissioning, this may also allow the monitoring of the energy transfer from the electron beam to the SASE radiation field during SwissFEL user operation. Figure 3.6.1 provides an overview of profile monitor locations, with related measurements.

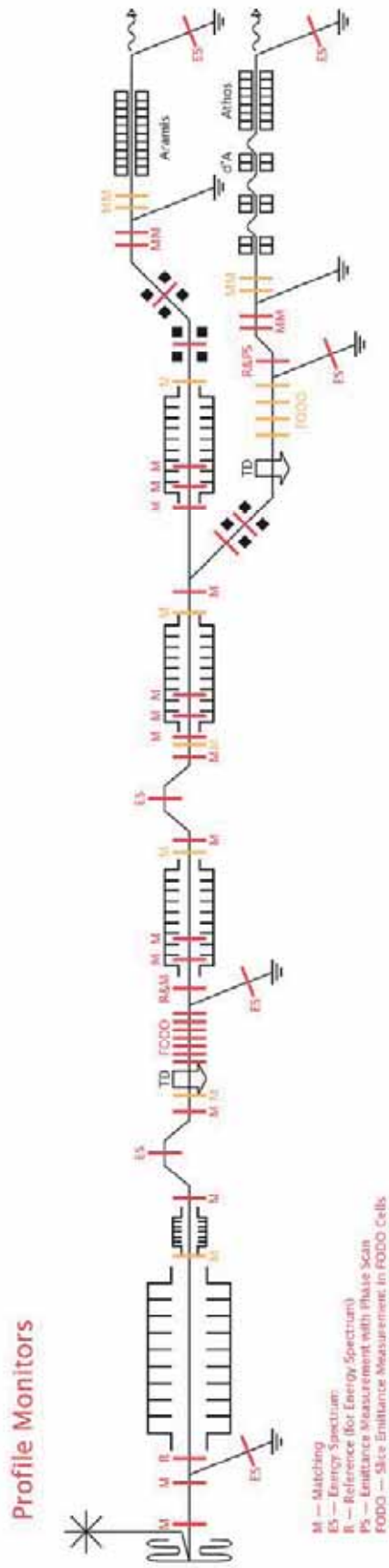


Fig. 3.6.1: SwissFEL profile monitor locations and related beam measurements

3.6.3 Bunch compressor and longitudinal diagnostics

Accurate measurement of the electron beam position in the bunch compressor permits the implementation of energy feedback for stabilization of the previous accelerator sections. Two high-resolution cavity BPMs ($< 5 \mu\text{m}$ single-shot), with a large diameter of 40 mm, will thus be installed in the round vacuum chamber sections between the 1st and 2nd and the 3rd and 4th dipole magnets of BC-1 and BC-2, respectively. Although the dispersion in the bunch compressor arcs is only about half of the value in the BC centre (between the 2nd and 3rd dipole magnet), the excellent position resolution of cavity BPMs – especially in low-charge (10 pC) operation mode – will provide sufficient energy resolution of $\sim 5 \cdot 10^{-5}$ to stabilize the beam energy in the SwissFEL injector (BC-1 feedback) and in Linac 1 (BC-2 feedback).

Synchrotron radiation monitors will be installed behind the 3rd dipole magnets of BC-1 and BC-2, allowing continuous observation of the beam energy distribution at the location of maximum dispersion in the bunch compressors. With an imaging resolution of the order of $10 \mu\text{m}$ and the application of fast, real-time (100 Hz) image processing for determination of beam centre of mass and energy distribution, as well as high-speed image data transfer, the implementation of a feedback loop for linearization of the energy chirp (e.g.: X-band cavity in front of BC-1) might be possible. The realization of such a feedback loop will be tested at the SwissFEL Injector Test Facility. For BC-1 and BC-2, additional transverse profile (screen) monitors will be installed between the 2nd and 3rd dipole magnets, at the locations of maximum dispersion.

Bunch compression and relative electron bunch length will be monitored with coherent synchrotron (or edge) radiation from the 4th dipole magnet of the bunch compressors. While complete reconstruction of the longitudinal bunch configuration can only be obtained by the determination of the coherent radiation spectrum with scanning [76], [77] (or single-shot [78], [79]) interferometers, a so-called bunching or compression monitor (BCM) will measure the integral intensity of a selected range of wavelengths which are larger than $2\pi\sigma_z$, where σ_z is the rms electron bunch length behind BC-1 and BC-2. A set of suitable transmission filters will thus be inserted in front of the far infra-red, and THz detectors of the BCMs for the 200 pC and 10 pC SwissFEL operation modes. Cross-calibration of the BCM signals with TDC bunch length measurements will allow the implementation of “peak current” (compression ratio) feedback. In the case of BC-1, the phase of the last four – operated off-crest – injector S-band RF structures can be regulated, while RF phases of selected C-band structures from Linac 1 can be adjusted with the BCM signal from BC-2.

In addition to TDC-based bunch length measurements, the non-destructive, online monitoring of the longitudinal current profile in the 200 pC SwissFEL operation mode will be provided by compact and robust electro-optical bunch length monitors applying the method of spectral decoding [80].

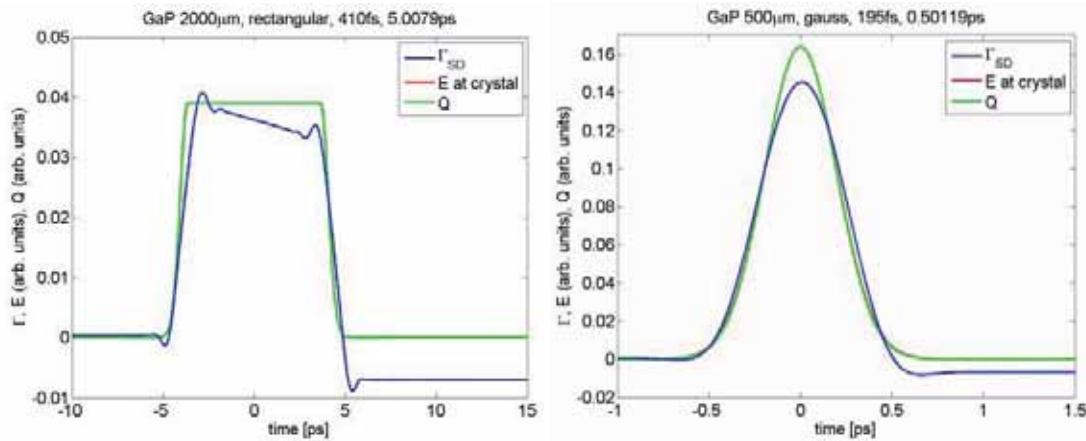


Fig. 3.6.2: Simulation of bunch length measurements applying the method of EO spectral decoding for SwissFEL longitudinal bunch distributions in front of and behind the 1st bunch compressor (simulation parameters are given in the text)

Two of these monitors are planned to be installed around BC-1. An in-house developed amplified Ytterbium fiber laser operating at a wavelength of 1050 nm, with a spectral bandwidth of about 100 nm [81], will be used in combination with a 2 mm-thick GaP crystal to observe the rectangular bunch current profile of 10 ps in front of BC-1. The use of a 500 µm-thick GaP crystal behind BC-1 will provide sufficient temporal resolution (~ 150 fs) to permit online monitoring of the compressed bunches in the control room. The EO bunch length monitors should continuously run in the background, in order to permit longitudinal feedback loops on timing, laser pulse shape and RF parameters. For non-destructive monitoring of the longitudinal bunch current profile (~ 45 fs rms) after the final SwissFEL compression stage (BC-2), the method of temporal decoding with a high-bandwidth Ti:Sa laser [82] and the use of broad bandwidth EO materials such as DAST (4-N,N-dimethylamino-4'-N' methyl stilbazolium tosylate) are presently under consideration. Tests with over-compressed bunches in the 200 pC operation mode at the SwissFEL Injector Test Facility are planned, in order to develop such a non-destructive longitudinal (bunch length) diagnostic.

Since non-destructive single-shot bunch length measurements at very low charges (< 100 pC) and below 50 fs pose a challenge which is presently not yet solved, it is so far foreseen for SwissFEL to direct the coherent THz radiation from the 4th dipole magnets of BC-1 and BC-2 to a Martin-Puplett interferometer (scanning polarization interferometer), for determination of the bunch form factor (proportional to the square of the longitudinal charge distribution) by Fourier transform spectroscopy. Single-shot spectrometers (e.g.: [78], [79], [83]) are also under consideration and will be tested at the SwissFEL Injector Test Facility.

Measurement of the electron bunch arrival time in relation to a highly stable optical reference (optical master oscillator), with anticipated time resolution in the order of 5 fs, will be performed with an electro-optical bunch arrival-time monitor (BAM) [84]. The principle of electro-optical BAM operation is illustrated in Figure 3.6.3. The reference laser pulses from the optical master oscillator (~ 100 fs-long pulses at 1550 nm wavelength and with 214 MHz repetition rate) pass through an electro-optical modulator (EOM), which modulates their amplitude according to the applied fast transient RF signal from a high bandwidth beam pick-up, which is sensitive to the bunch transverse Coulomb field. The acquisition is performed at the zero-crossing of the pick-up signal. Any deviation due to bunch arrival time jitter will cause an offset to the reference laser pulse, which will lead to its amplitude modulation. By the use of a delay line with a high-accuracy absolute position encoder, the amplitude modulation can be calibrated with time.

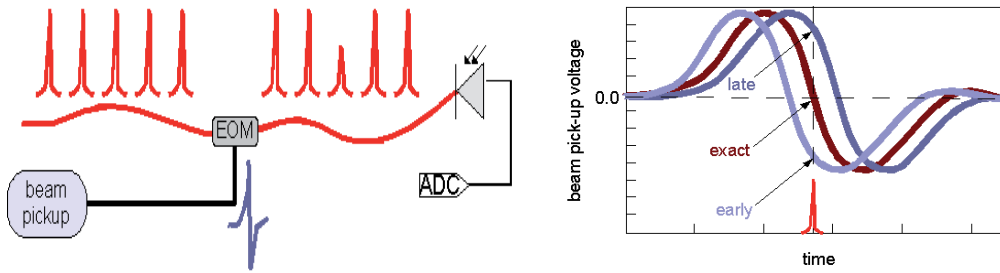


Fig. 3.6.3: Electro-optical BAM operation principle

Beam arrival-time resolutions of < 6 fs (rms) short term (10 min), and < 20 fs (rms) long term (10 h), have been demonstrated at FLASH [84]. The intrinsic resolution of the FLASH system was 20 fs/% amplitude modulation at 0.3% laser amplitude stability and $2 \mu\text{m}$ positioning accuracy of the encoder [85]. For SwissFEL, it is planned to improve the time resolution by the use of higher bandwidth beam pick-ups, higher accuracy position encoders and improved amplitude stability of the reference laser. The pick-up design can be tailored to the specific needs, e.g. long-bunch, high-charge / short-bunch, or low-charge operation modes. Two pick-up designs will be tested at the SwissFEL Injector Test Facility: a button pick-up with 60 GHz bandwidth, which according to simulations has sensitivity of 1 fs/mV at 1 nC, and a waveguide pick-up with 20 GHz bandwidth and expected sensitivity of 0.7 fs/mV at 200 pC. The bandwidth can be dynamically adjusted by the use of appropriate filters to generate pick-up slopes with different steepness. In this way, both high sensitivity and large dynamic range one be secured to compensate for possible drifts in over several tens of ps. High-precision position encoders (< 10 nm) are available on the market, which should also contribute towards improving BAM accuracy. Such improved BAM time resolution will be a helpful diagnostic to support stable operation of the low-charge (10 pC), short-pulse (< 10 fs) SwissFEL operation mode.

3.6.4 SwissFEL beam position monitor system

Although SwissFEL will only have one undulator in the first operation phase, for the generation of hard X-rays, called Aramis (U15), the machine is designed to support the future installation of up to two additional undulators for soft X-rays. SwissFEL will have bunch trains of 1–2 bunches at 50ns spacing and 100 Hz bunch train repetition rate, with a fast kicker that distributes each bunch in the train to a different undulator. The injector and main linac BPMs will be able to measure the position of each bunch in the train individually. The fast fiber-optic links of each BPM electronics and a latency below 1ms allow the integration of the BPMs into fast transverse trajectory or longitudinal feedbacks (using dispersive BPMs, e.g. in bunch compressors) that operate at bunch train repetition rates up to 100 Hz (see Section 3.11). The SwissFEL BPM electronics will allow remote-controlled selection of the beam charge / beam position range. For the commissioning of the SwissFEL with 1st beam and large orbit excursions, a ± 5 mm range, or even more (depending on the beam charge), are possible. During standard user operation, when the beam positions are usually quite close to the BPM centre, a smaller measurement range of ± 1 mm can be used for lowest (nominal) noise and drift (both scale with the range for the chosen cavity BPM type). If necessary, it is even possible to tune the range of each BPM individually, e.g. for BPMs in special locations, such as the bunch compressor or beam dump, simply by attaching an additional attenuator to the output of the position cavity resonator (see Section 3.6.4.2 and following). Figure 3.6.5 provides an overview of the number and locations of BPMs along the SwissFEL accelerator and undulator lines.

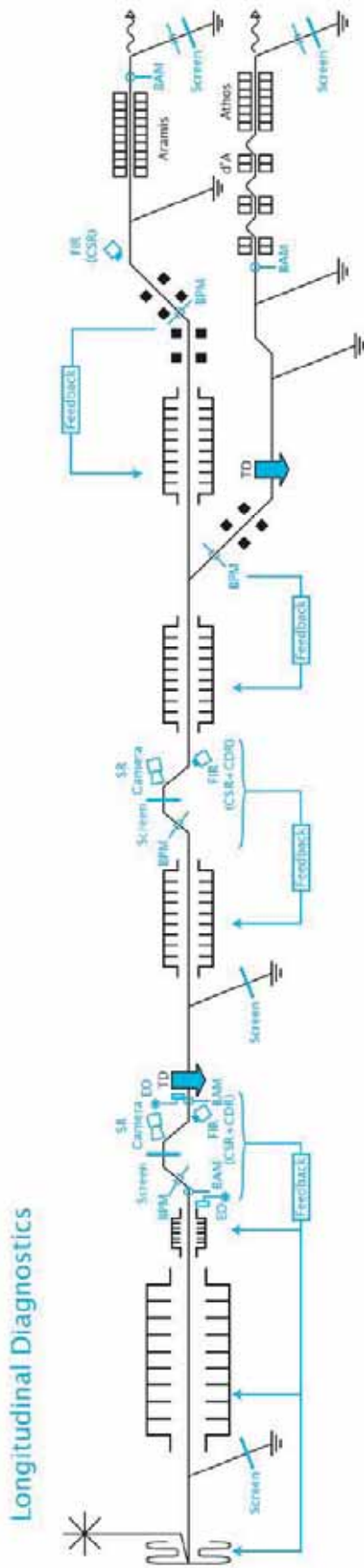


Fig. 3.6.4: Distribution of SwissFEL longitudinal diagnostics.

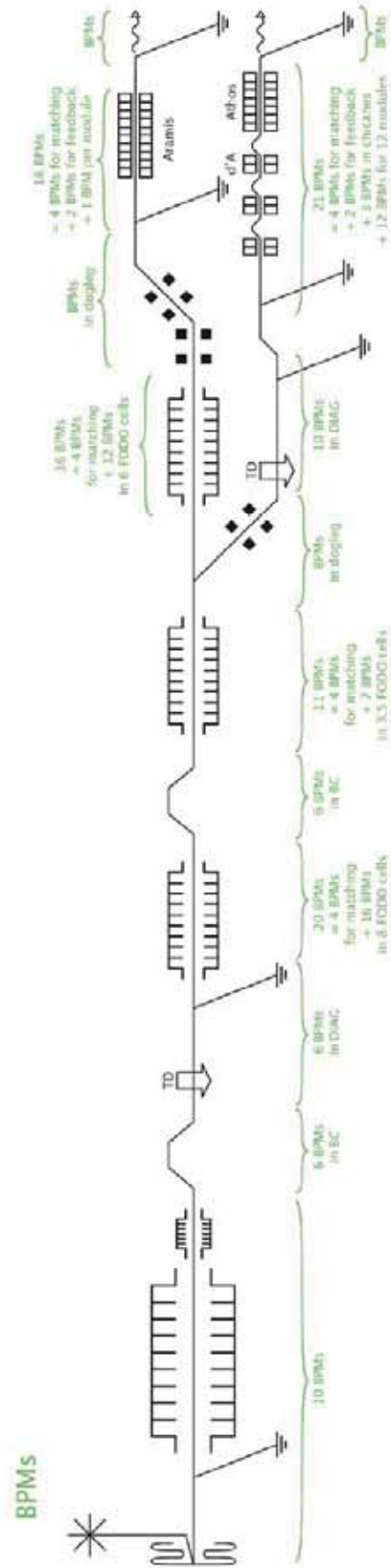


Fig. 3.6.5: Distribution of BPMs along SwissFEL.

3.6.4.1 Undulator BPM system requirements

The main challenges for the SwissFEL BPM system are the planned operation with beam charges from 200 pC down to 10 pC, and a comparatively small transverse beam dimension down to $\sigma \sim 10 \mu\text{m}$ in the U15 undulator. The noise and drift requirements for the undulator BPMs are mainly driven by the beam-based trajectory alignment, e.g. by the dispersion-free steering (DFS) method [86] as well as by the transverse trajectory feedback system. The BPM noise and drift-per-hour requirements for the DFS method are typically of the order of $\sim \sigma/10 \cdot \Delta E/E$ [87], [88], where $\Delta E/E$ is the maximum relative energy change that can be applied during the DFS procedure. For $\Delta E/E=50\%$, this corresponds to $0.5 \mu\text{m}$ BPM position noise and drift. Assuming the noise can be improved by a factor of two using low pass filters for the BPM readings (where the improvement factor is limited by systematic effects such as differential nonlinearity of the electronics), a single bunch resolution of $\sim 1 \mu\text{m}$ at 200 pC is assumed to be sufficient for the DFS method, that will be performed at the maximum beam charge for optimal resolution. The noise and drift requirements for the transverse feedback (see Section 3.11.2) are also of the order of $\sigma/10$ ($\sim 1 \mu\text{m}$), but over the whole beam charge range of 10 to 200 pC. If necessary, the amount of uncorrectable high-frequency trajectory jitter and BPM noise that is modulated onto the beam by the feedback, e.g. for machine studies below 10 pC, can be reduced by using low-pass filters or by reducing feedback loop controller gains, at the expense of a lower feedback loop bandwidth.

3.6.4.2 Undulator BPM pick-up

In order to fulfil the requirements described above, the SwissFEL undulators will be equipped with choke-mode cavity BPM pick-ups pioneered by T. Shintake et al. at SCSS/Spring8 [89]. They consist of a monopole (reference) and dipole (position) cavity that both have the same frequency for the relevant TM_{01} (monopole) and TM_{11} (dipole) modes, with the reference cavity signal being proportional to the bunch charge and the position cavity signal (with two ports per plane) being proportional to the product of charge and position. The mode-selective couplers in the position cavity suppress its undesired monopole (“common”) mode that usually limits the resolution and drift of other pick-up types. Using the same frequency for both the reference and position cavity allows the use of the same electronics design for reference and position channels. This symmetry minimizes the temperature-induced position drift that is caused by frequency-dependent drift effects of electronics components in the RF input stage, since the dipole cavity signal is normalized to the monopole cavity signal and a common-gain drift of both channels is thus averaged out.

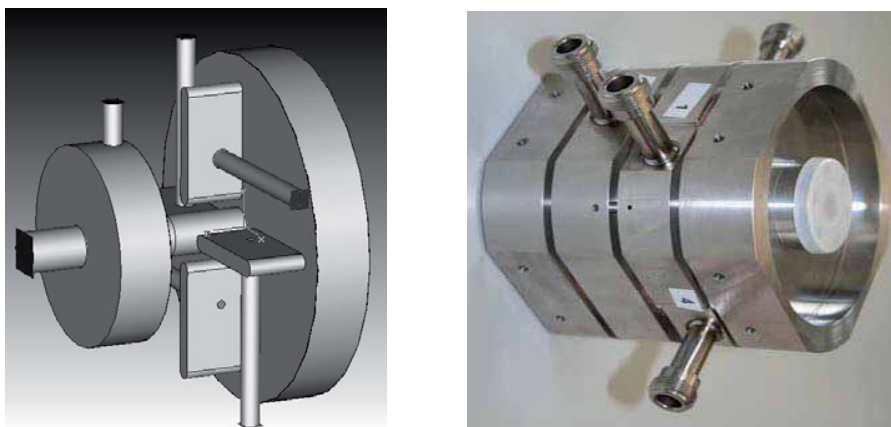


Fig. 3.6.6: E-XFEL choke-mode cavity pick-up [90]. Left: Vacuum and couplers of the reference cavity (1 port) and dipole cavity (4 ports, with mode-selective couplers). Right: 3.3GHz prototype for the E-XFEL undulators (based on an SCSS/Spring8 design by T. Shintake et al.) that will be adapted for the SwissFEL. The E-XFEL undulator pick-up has 100 mm overall length and 10 mm inner beam pipe diameter.

The pick-up and electronics will be based on a design for the European XFEL BPM (E-XFEL) that is presently being developed by a PSI-DESY collaboration within the Swiss E-XFEL in-kind contribution framework. Due to the very similar undulator BPM requirements of both machines, only a moderate adaptation of the E-XFEL system to the SwissFEL will be required in order to reach the desired performance for the 10x lower bunch charge and 4x shorter bunch spacing of the SwissFEL. First lab tests of 3.3 GHz E-XFEL prototype BPM electronics developed by PSI showed sub-micron intrinsic electronics noise at 300 pC, although the performance of the final system with beam in a real (usually more noisy accelerator environment still has to be investigated. The theoretical thermal noise limit of 110 nm RMS at 10 pC for a 3.3 GHz cavity should, in principle, allow the required SwissFEL performance to be achieved with this pick-up frequency. However, the noise of cost-efficient, real-world electronics is typically several times higher than the theoretical limit, due to electronics and interference noise, losses in cables and analogue input stage of the electronics, etc. An increase of the frequency would reduce the theoretical thermal noise limit and should thus allow higher resolution, at the expense of higher frequency-related drift effects. Therefore the choice of the optimal frequency (which has a very small impact on the electronics design), which is expected to be in the range of 3–6 GHz, will be made after beam-based noise and drift measurements of cavity pick-up and electronics prototypes at the SwissFEL Injector Test Facility, based on an overall optimization of criteria such as thermal noise, interference noise, drift, manpower, and hardware costs.

3.6.4.3 Undulator BPM electronics

The SwissFEL BPM electronics will use an RF front-end (RFFE) with IQ down-conversion of one reference and two (x/y) position pick-up signals to baseband. The RFFE IQ output signals for reference and position channels will be digitized by fast (~160 Msps) 16-bit ADCs and then post-processed by an FPGA carrier board that serves as control, timing and feedback system interface. The digitally programmable and tunable local oscillator (LO) in the RFFE, as well as the ADC clocks, will be locked to an external machine RF reference clock. Suitable design and digital processing techniques of the present prototype electronics allow the elimination of the impact of IQ phase and amplitude imbalance on position noise and drift. The electronics will also allow the suppression of an undesired dipole cavity signal component that is proportional to the beam angle (dominated by the cavity angle alignment error), thus reducing the required angle alignment tolerance to a level that can be reached with common survey-based alignment techniques. A modular cost-efficient electronics design approach, consisting of an FPGA carrier board with two ADC mezzanine modules, two RFFE cards, and a common housing with power supply and fans, minimizes the effort needed to adapt the E-XFEL system to the SwissFEL, while enabling synergies with the planned SLS BPM upgrade that will use the same FPGA carrier board and similar ADC mezzanines.

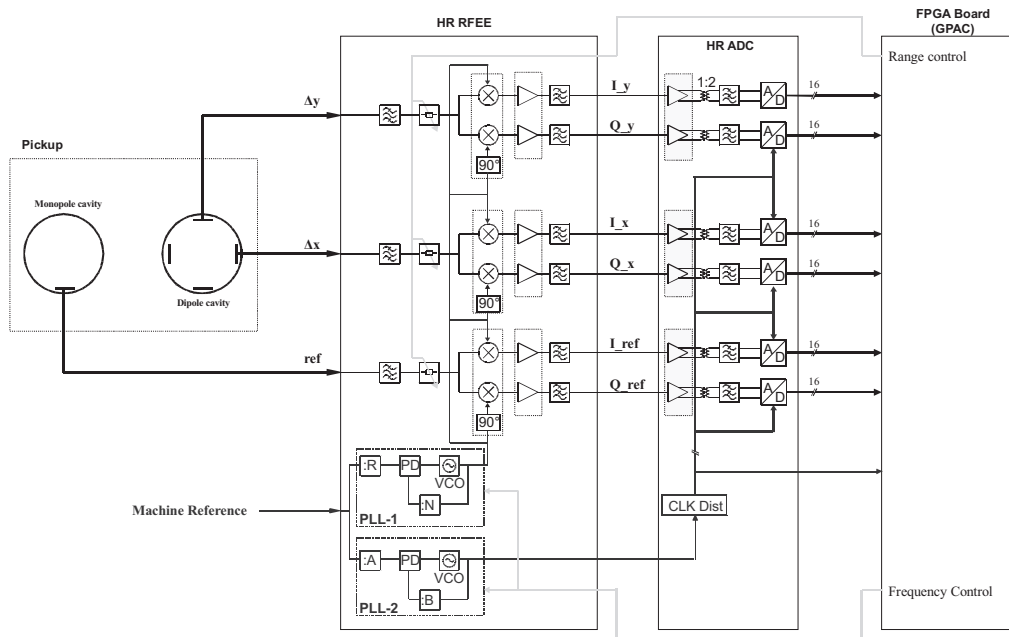


Fig. 3.6.7: Simplified cavity BPM system concept for SwissFEL and E-XFEL, consisting of cavity pick-up, RF front-end electronics, ADC and digital back-end signal processing FPGA board.

3.6.4.4 Main linac and injector BPM system

The SwissFEL main linac and injector will be equipped with the same kind of cavity BPM as the undulators (adapted to the different inner beam pipe diameter of 16 mm for the linac and 38mm for the injector), although the electronics noise and drift may be higher (up to 3 μm at 10 pC), due to higher RFFE output filter bandwidth (for low intra-train bunch-to-bunch crosstalk), higher RF cable attenuation, and a less-sensitive pick-up design with larger pipe diameter. The highly cost-efficient design and fabrication techniques of the chosen cavity BPM design still allows much better noise and drift to be attained than alternative pick-ups, such as matched or resonant striplines, at comparable or even lower costs. While the orbit trajectory alignment requirements in the main linac are relaxed compared to those of the undulators (see Section 3.11), and thus would allow the use of suitable stripline BPMs, the higher performance of cavity BPMs still has a number of advantages. These allow precise (a few 10^{-5}) energy measurements at dispersive locations in the bunch compressors, as well as the localization of possible transverse perturbations sources that cannot be suppressed by a transverse feedback system, and thus might need to be identified and eliminated in order to achieve stable FEL operation. The low thermal noise limit also allows the exploration of machine operation modes at bunch charges below 10 pC (albeit not with nominal performance), where other BPM types could no longer achieve acceptable performance. Moreover, cavity BPMs allow the precise reconstruction of the centre-of-charge at the location of wire scanners for transverse profile measurements, even at very low beam charges, and the BPM reference cavity can serve as beam current and transmission monitor. Finally, having the same cost-efficient, high-resolution BPM type in the whole SwissFEL minimizes the overall development, production and maintenance effort for pick-ups, electronics, firmware and software. For the injector, the cavity frequency will be in the range of 3.3–4 GHz, in order to stay sufficiently below the beam-pipe cut-off but above interference noise of the 3 GHz S-band linac RF, with the possibility to use a somewhat higher common frequency for main linac and/or undulator BPMs (with 16 mm and ~ 8 mm inner pipe diameter), in order to improve their theoretical thermal noise limit.

3.6.4.5 BPM pick-up supports and alignment

The SwissFEL undulators consist of a periodic sequence of ~4 m-long undulator segments mounted on individual girders, with a motorized 5D mover system. In between two undulator segments, a BPM and quadrupole are mounted on a separate girder (see Section **Error! Reference source not found.**) in order to minimize the impact of undulator gap movements on the quadrupole and BPM positions. Two additional, smaller quadrupoles per undulator are mounted on the same girder as the undulator, at its upstream and downstream ends, to allow beam-based alignment of the undulator axis, as an alternative to beam finder wires that are used, for example, at LCLS. The nominal (electric/magnetic) centres of all components on each girder will be aligned relative to each other within $\sim 30 \mu\text{m}$, using non-beam-based survey and field measurement techniques. Then the positions of these girders/supports (and thus of the BPMs, quadrupoles and undulator axis) will be corrected via remotely controlled movers, using beam-based alignment techniques (see Section 3.11). Since these techniques require only relative BPM position measurements and allow the BPM pick-up offset to be determined relative to the golden orbit, a dedicated non-beam-based system for the alignment of the BPM pick-ups, e.g. via laser, is not required.

As described in Section 3.11.1, the non-undulator BPM pick-ups have relaxed drift and alignment requirements. Their supports will only allow manual transverse position adjustment, with an initial survey-based alignment and an optional beam-based post-alignment by dispersion-free steering (energy variation) and quadrupole strength variation techniques that permit reduction of pick-up and trajectory alignment errors, and resulting emittance growth to the desired level. Section 3.11.1 contains further details about BPM and magnet alignment concepts and requirements.

3.7 Vacuum concept (Lothar)

3.7.1 Main accelerator

The detailed list of vacuum components (positions, lengths, ...) which constitute the skeleton of SwissFEL can be found in a PSI note: FEL-SL88-027 [91]. The standard inner vacuum tube diameter in the three SwissFEL Linacs will be 16 mm, with the corresponding flange size of CF 16 mm. Stainless steel will be used for the vacuum tubes and copper for the RF accelerating structures. The C-band cavities will be connected with RF shielded bellows. The space between the cavities is limited. To achieve a short and compact bellows design, the flange size will be CF 40 mm, while the inner bellows diameter is 16 mm. CuBe will be used for the RF shield in the bellows, which also allows smooth transition between different tube sizes.

A schematic layout for the Linac 1 standard cell is seen in Figure 3.7.1 and for Linac 2 and 3 in Figure 3.7.2. The common characteristic of all vacuum systems for the SwissFEL accelerator is the strong conductance limitation over the full length of the machine. In the three linear accelerators Linacs 1, 2, and 3, the vacuum pumps can only be installed in the wave guides of the C-band cavities. Due to conductance limitations, the effective pumping speed will be reduced to only a few percent of its nominal pumping speed.

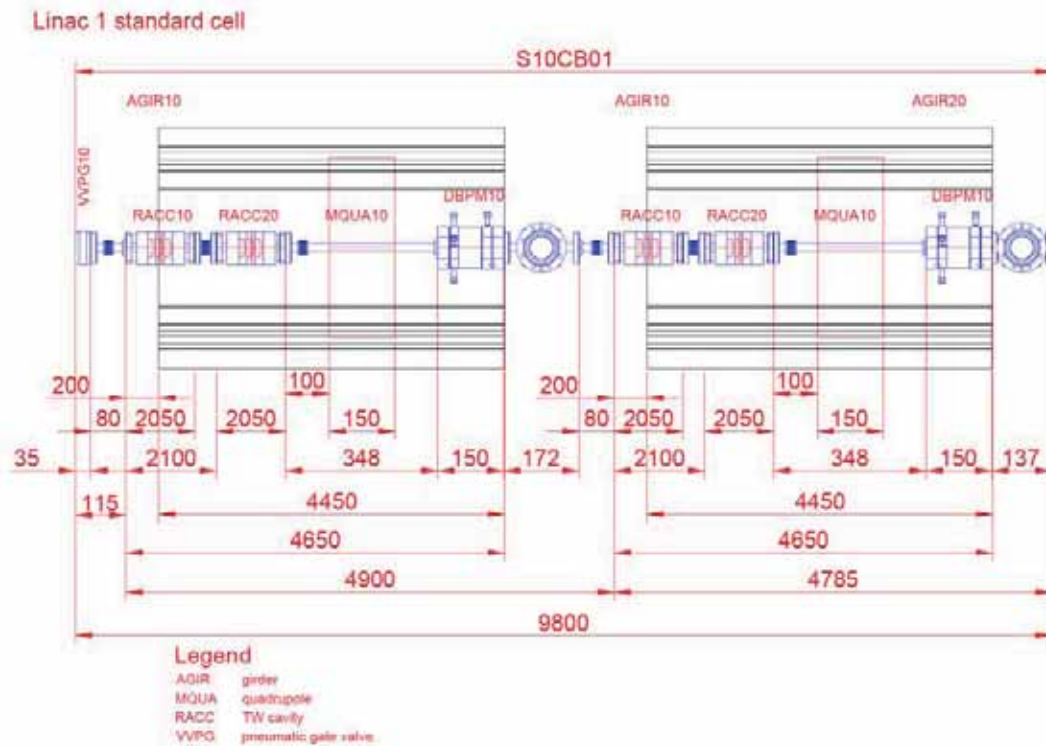


Fig. 3.7.1: Schematic layout of Linac 1 double cell (the length of the C-band cavities is compressed in this sketch) – FEL-SL88-034_0

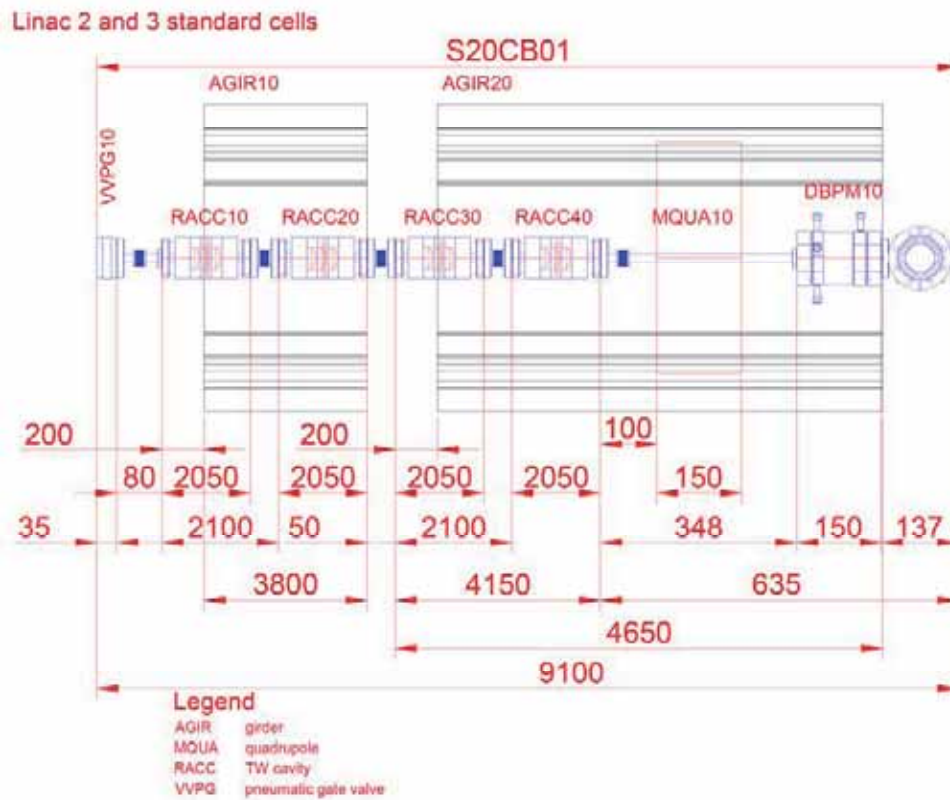


Fig. 3.7.2: Schematic layout of Linac 2 and Linac 3 cells (the length of the C-band cavities is compressed in this sketch) – FEL-SL88-035_0.

For operation of the linacs, average pressure values in the 10^{-7} mbar range are sufficient and 10^{-8} mbar are expected after baking. These pressure requirements might be relaxed, but due to conductance limitations, strict adherence to UHV standards will be essential. Therefore, in-situ bake out to remove water partial pressure will also be beneficial. Figure 3.7.3 shows the pressure distribution in Linac 1 and Figure 3.7.4 that in Linac 2. The general layout of the standard cells is equal in Linac 2 and Linac 3. A similar distribution of vacuum pressure in Linac 3 would also be expected. For pressure calculations, out-gassing rates used were 10^{-12} mbar l / s* cm^2 for stainless steel and 10^{-11} mbar l / s * cm^2 [92] for copper at 45°C operating temperature and RF power on. It can be expected that, after a long time running with RF on, the out-gassing rate for Cu can be reduced to values of 10^{-12} mbar l / s* cm^2 [93].

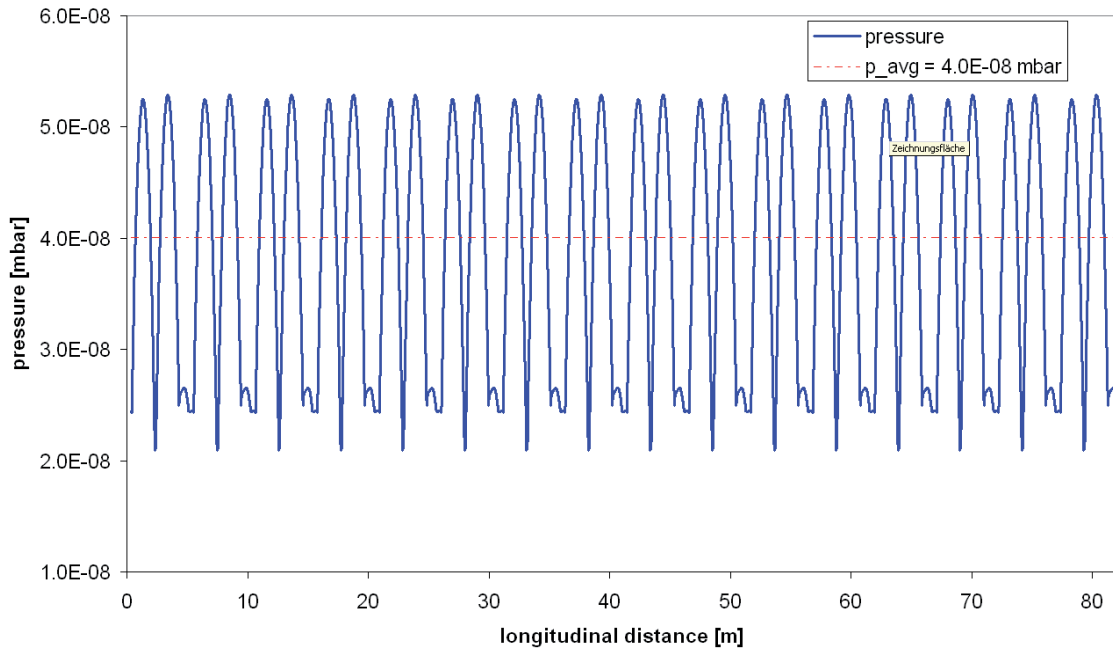


Fig. 3.7.3: Pressure distribution in Linac 1

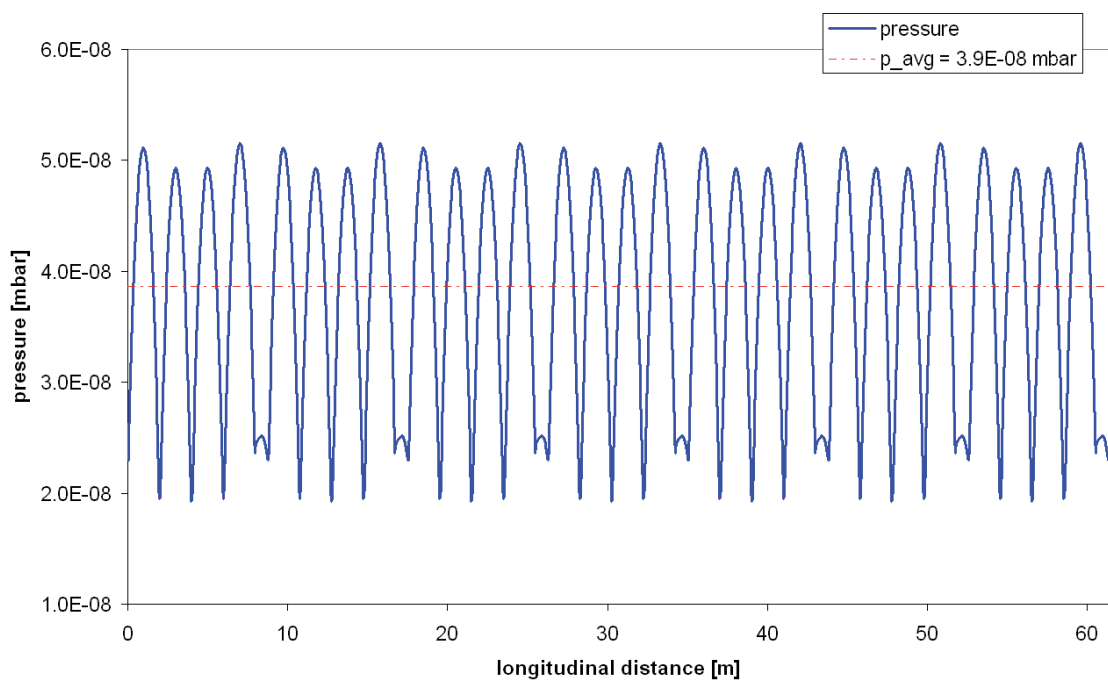


Fig. 3.7.4: Pressure distribution in Linac 2

The pressure profiles were calculated with the program VACLIN [94], which uses a matrix method to solve the linear equation system. However, the results have to be confirmed by using a program which uses Monte Carlo simulation [92].

The vacuum scheme for a Linac 1 double cell is shown in Figure 3.7.5, and for Linac 2 and 3 standard cells in Figure 3.7.6. No RF windows are installed in the RF waveguides, so that they are also part of the accelerator vacuum system. The cavities are pumped on each input and output coupler with a 20 l/s sputter ion pump, connected to a pump, T. The pump T also allows the installation of vacuum gauges and all metal cross-angle valves which are used for roughing and venting. To save costs, all 16 sputter ion pumps which will be installed in the waveguides are connected to one pump controller.

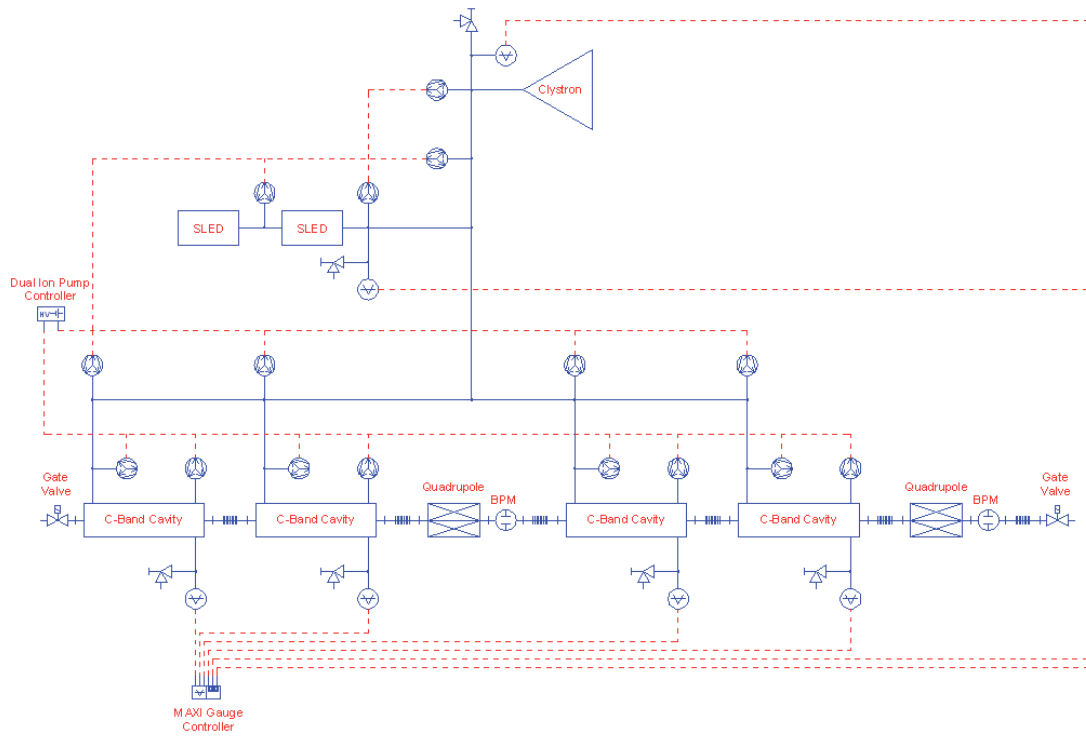


Fig. 3.7.5: Vacuum scheme of the Linac 1 double cell (The 2 SLED system is actually replaced by a BOC cavity – see Section 3.2)

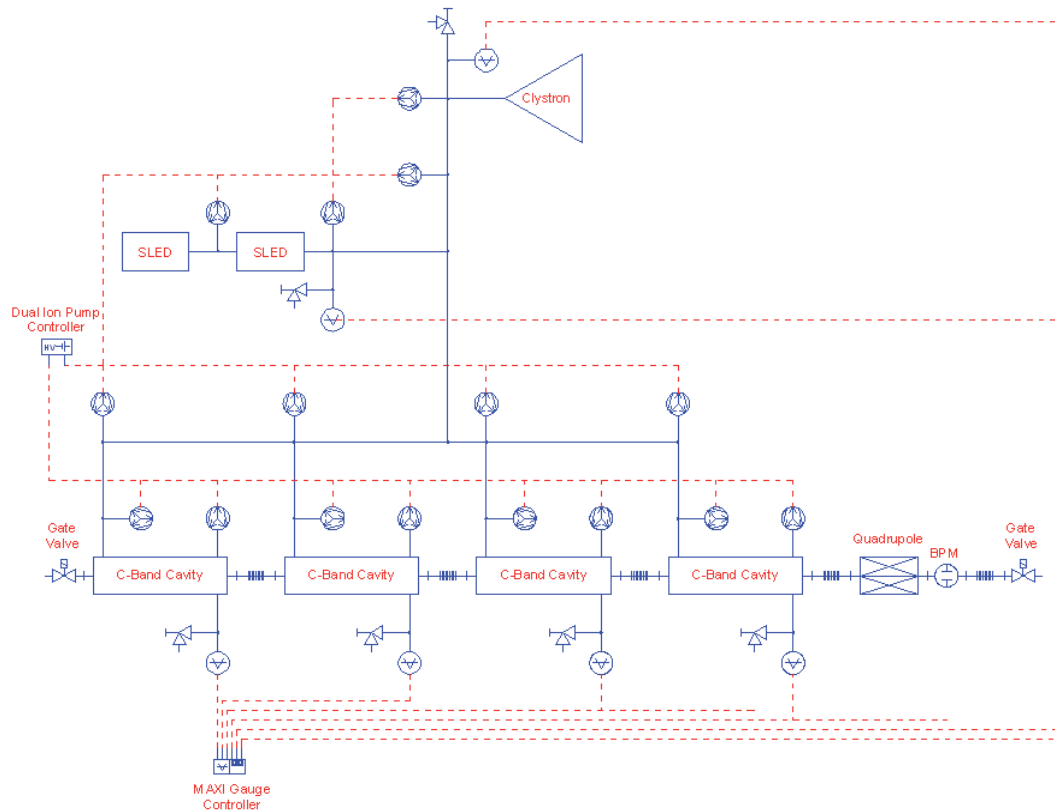


Fig. 3.7.6: Vacuum scheme of the Linac 2 and Linac 3 standard cell (The 2 SLED system is actually replaced by a BOC cavity – see Section 3.2)

For the separation of vacuum sections, rf-shielded all-metal gate valves are foreseen. For a cost optimized design, eight RF accelerating structures with two klystrons will be used for one vacuum section. The gate valve which is being considered at the present design stage has a flange size of 35 mm, but is based on a design for a DN 65 mm all-metal gate valve. It is a very large and heavy valve, which requires large installation space and high investment costs. However, the requirements for a gate valve for the SwissFEL are a little relaxed compared to those of an electron storage ring, and therefore the development of a smaller and more cost-effective gate valve has been started, based on a Viton-sealed gate valve with a simpler RF shield. For the handling and maintenance of the vacuum sections, it would be preferable to have only four cavities and one klystron in each vacuum section.

For the monitoring of vacuum pressures and for the vacuum interlock, cold-cathode gauges will be installed on one pumps T in each cavity and on some locations in the RF wave guides.

Dry turbo molecular pumps will be used for roughing and during bake-out. These pumps are installed in pump carts, which also have dry and oil-free diaphragm pumps, a vacuum control, and a venting system. The pump carts are mobile and can be connected via flexible hoses to the several cross-angle valves which are installed in each vacuum section.

3.7.2 Undulator vacuum system (Aramis)

For operation of SwissFEL, average pressure values in the 10^{-7} mbar range are sufficient and expected in Aramis undulators. No baking of the Aramis vacuum chamber will be possible.

The design of the in-vacuum undulators for Aramis strictly follows the design of SLS in-vacuum undulators. With Ni-electroplating or TiN-ionplating of the permanent magnets, UHV-compatible desorption rates can be achieved [95]. The vacuum chamber for the undulator magnets is made of

stainless steel and will be equipped with two 150 l/s sputter ion pumps and four NEG pumps delivering 1300 l/s (for hydrogen) (see Figure 3.7.7).

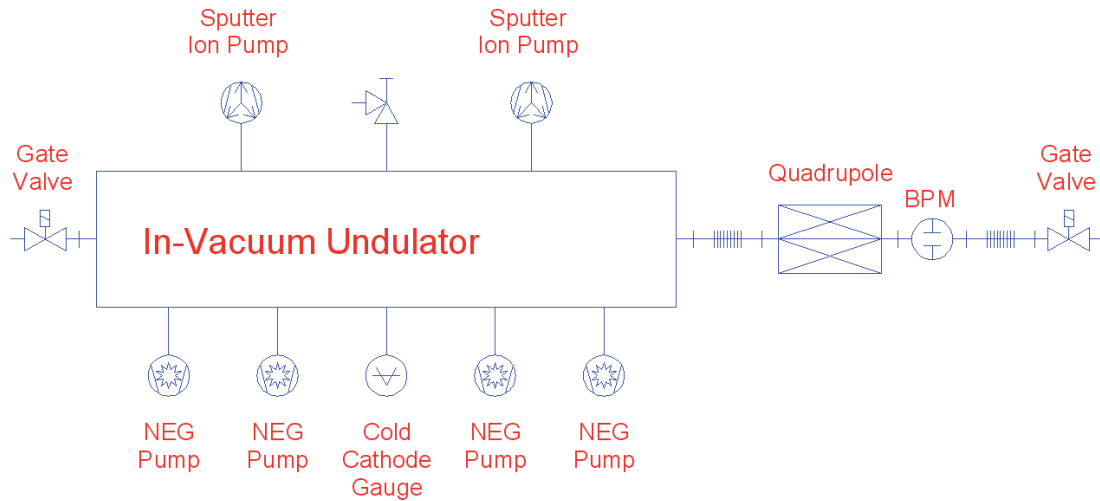


Fig. 3.7.7: Vacuum scheme of the in-vacuum undulator cell

Conductance limitations are not a problem for the in-vacuum undulators. The small magnet gap is open in the horizontal direction, giving good conductance to the undulator vessel.

Between each undulator is a short beam-tube with focusing quadrupole, BPM and rf-shielded bellows. The inner tube diameter is between 8 and 10 mm. The flange size will also be CF 16 mm.

For maintenance reasons, it would be preferable if all in-vacuum undulators could be separated by gate valves. For this, a compact Viton-sealed valve with RF shield would also be preferred.

For the monitoring of vacuum pressures and for the vacuum interlock, cold cathode gauges will also be installed on the undulator vessel.

3.7.3 Undulator vacuum system (Athos)

For the APPLE undulator Athos, a fixed-gap undulator vacuum chamber with an inner beam-clear aperture of 10 mm in the horizontal, and 4 mm in the vertical, direction is required. Depending on the small aperture dimensions, a small wall thickness is required for chamber rigidity. To guaranty small undulator magnet gaps, chamber wall thickness between 0.2 and 0.4 mm is desirable. Low electrical resistance material is necessary for the beam channel, at least for the inner surface, to obtain low resistive wall impedance. OFHC and aluminum alloy are suitable materials for the undulator chamber.

A smooth surface, with roughness values less than 300 nm, for the inner chamber wall is required to avoid a negative influence on beam performance due to wall wakefields.

OFHC is proposed to be the chamber material for the Athos undulators [96]. Chamber fabrication will be based on a galvanization method, with the following steps: In the horizontal direction, a machined and polished OFHC support plate will form the inner chamber wall on one or both sides. A smooth aluminum tube with elliptical cross-section is glued to the support plate and to the end flanges. The outer cross-section of the aluminum tube is identical with the resulting inner chamber cross-section. The thin chamber wall is then galvanized to the aluminum tube and also to the support plate and end flanges. Finally, the aluminum tube will be removed by an etching process.

A series of static structural analyses has shown that, in a chamber with two side supports, a wall thickness of 0.2 mm can be achieved, with maximum deformation of 4.3 μ m and maximum stress of 33 MPa (see Figure 3.7.8).

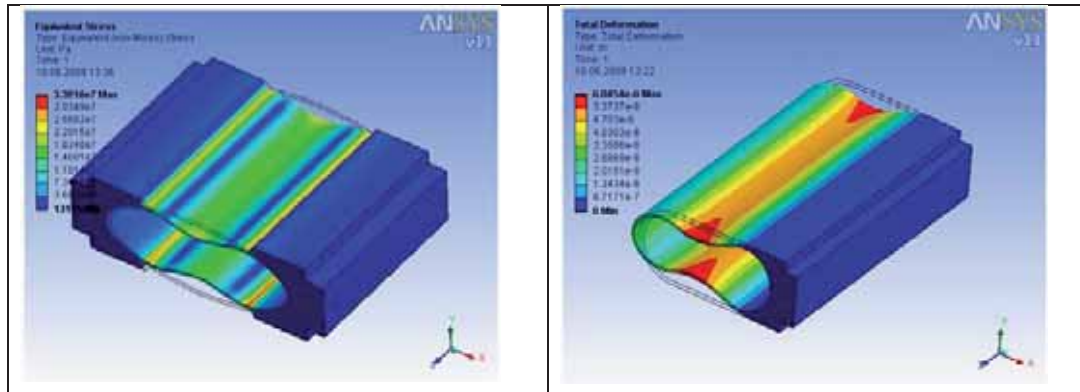


Fig. 3.7.8: Chamber deformation and stress for two-side support (left) and one-side support (right)

An average pressure of less than 10^{-7} mbar is necessary for the undulator line. The overall length of each vacuum chamber is about 4.7 m, while each undulator itself will have a length of 4 m. At the junction between undulator segments will be focusing and steering magnets, beam position monitors, bellows and pumps.

The very small chamber aperture is extremely limited in conductance. Pumps can be installed only at the junction between the undulator segments. To achieve the pressure of 10^{-7} mbar, in-situ bake-out will be required to reach desorption rates of less than 10^{-11} mbar l/s cm^{-2} .

The first design work for this new vacuum chamber type has started, and the next step is the fabrication of the first prototypes. Further investigations have to be made to calculate the photon-stimulated desorption rates and the resulting dynamic pressure. Also, the deposited radiation power over the full length has to be investigated. The first designs will be without cooling channels. If synchrotron radiation power calculations indicate large heat-up, active cooling has to be implemented in the design.

Table 3.7.1: Summary inner beam pipe size and vacuum level during operation

| SwissFEL section | Inner diameter vacuum pipe mm | Vacuum level mbar |
|------------------------------------|-------------------------------|-------------------|
| Injector | 35 mm | $< 10^{-8}$ |
| Linac 1, 2 and 3 | 16 mm | 10^{-8} |
| Aramis inter undulator sections | 8 to 10 mm | 10^{-7} |
| Athos Undulator Chamber vertical | 4 mm | 10^{-7} |
| Athos Undulator Chamber horizontal | 10 mm | 10^{-7} |
| Athos Photon Transport Pipe | | |
| Aramis Photon Transport Pipe | | |

3.8 Mechanical support systems

The mechanical support system concept is based on having pre-assembled units for the Linac and Undulator modules. For small components (e.g. single magnets, diagnostic elements, etc) individual supports are foreseen. The design concept combines optimized mechanical properties with an “easy to manufacture” design.

3.8.1 Girder Concept

Inspired by the SLS girder system, the SwissFEL girder design is conceived as an “optical table” which allows several components to be aligned with respect to one reference. The girder has a high-precision reference surface for direct vertical and horizontal positioning of components. The girder itself is then positioned on manually adjustable jacks. To achieve good stability, the jacks are mounted on concrete/granite blocks, to reduce potential leverage between the jacks and the beam axis.

The modular supports for components are mounted on the girder's reference surfaces and can be individually aligned.

Design principles for the SwissFEL linac girder and support system:

- Girder as an “optical table”, with high-precision vertical and horizontal reference surfaces for individual alignment of components
- Minimization of tolerance chain by use of fewer parts
- Kinematic “clean” solutions (preferably 3-point) for bearing arrangement of girder and component supports, to avoid “over-constraints” and to simplify alignment
- Bearings must allow free axial movement of the RF structure, to allow free thermal expansion without internal deflection during bakeout and operation
- Adjustable jacks for girder alignment with 6 degrees of freedom
- Adjustable supports for components
- Good mechanical behaviour regarding static and dynamic stabilities
- High damping properties to avoid amplification of potential vibrational excitations
- The use of non-corrosive and non-magnetic materials
- Minimization of effort for alignment procedures
- Minimization of cost for manufacturing in series
- The possibility to compensate for ground settlement by adding additional layers between concrete and adjustment jacks

To achieve the requirements for beam stability and considering the environmental conditions, design criteria are specified, and the criteria for the linac girder and support system are shown in Table 3.8.1.

Figures 3.8.1 and 3.8.2 show the girder as installed in the SwissFEL Injector Test Facility and optimized for the SwissFEL linac. Because of the smaller mass of the foreseen C-band cavity (no solenoid magnets required) in comparison with the S-band cavity (with solenoids), the SwissFEL linac girder can be optimized regarding shape and bearing configuration.

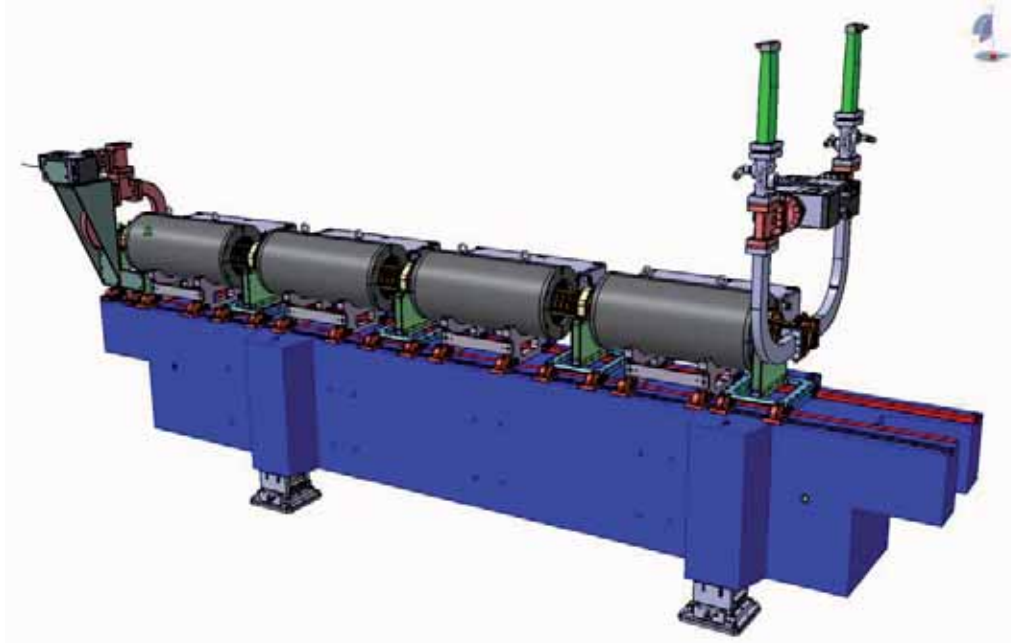


Fig. 3.8.1: S-Band Linac Girder Module of the SwissFEL Injector Test Facility.

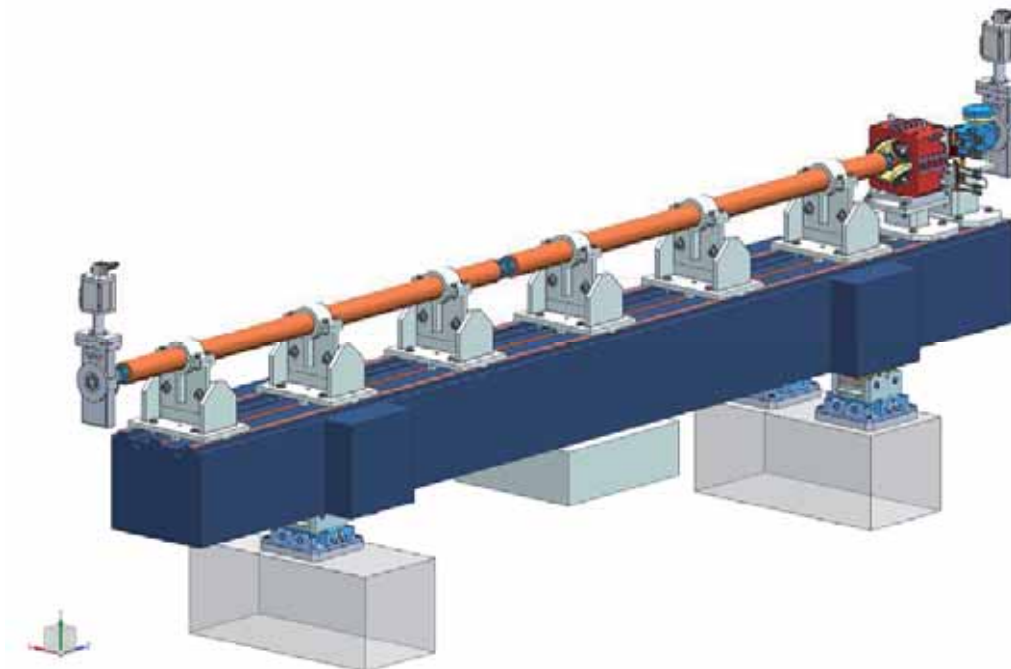


Fig. 3.8.2: Design study of C-Band Linac Girder Module for the SwissFEL Facility.

Table 3.8.1: Design criteria for the SwissFEL Linac girder and support system

| Beam stability | |
|--|--|
| - Maximum allowable orbit deviation from Theoretical beam axis | $\Delta x, y_{\text{transversal}} < 0.5 \mu\text{m}$ |
| Static stability | |
| - Maximum deformation at load (weight + thermal load ¹) | $\Delta u_{\text{vertical}} < 10 \mu\text{m}$ $\Delta u_{\text{axial, th.}} < \dots \mu\text{m}$ |
| - Maximum allowable stress values ² | $S, S_m = 0.67 R_{p0.2(T0)}$ $S, S_m = 0.3 R_{m(T0)}$ |
| Dynamic stability (derived from beam stability criteria) | |
| - Eigenfrequencies (EF) | 1. EF $> 50 \text{ Hz}$ |
| - Maximum elongation of geometric beam axis from theoretical beam axis due to dynamic excitation (vibration, shock) | $\Delta u_{\text{transversal}} < 0.5 \mu\text{m}$ $\Delta u_{\text{axial}} < 0.5 \mu\text{m}$ |
| - Internal damping ratio | c $> 4 \%$ |
| Manufacturing (girder + supports) | |
| - Tolerances (Manufacturing) global length dimensions flatness over total length parallelism (reference surfaces) inclination (reference surfaces) | $t_{\text{length}} < 100 \mu\text{m}$ $t_{\text{flatness}} < 50 \mu\text{m}$ $t_{\text{parallelism}} < 50 \mu\text{m}$ $t_{\text{inclination}} < 0.5^\circ$ |
| Alignment | |
| - Tolerances (Alignment) pre alignment final alignment beam-based alignment (BBA) | $\sigma_{\text{transversal}} \pm 1 \text{ mm}$ $\sigma_{\text{longitudinal}} \pm 1 \text{ mm}$ $\sigma_{\text{transversal}} \pm 100 \mu\text{m}$ $\sigma_{\text{longitudinal}} \pm 100 \mu\text{m}$ $\sigma_{\text{transversal}} \pm 10 \mu\text{m}$ |

¹ Maximum thermal load occurs during bakeout procedure with $T_{\text{bakeout}} = 150^\circ$

² Derived from ASME BPV, Section III, Subsection NF (supports); $R_{p0.2(T0), 316LN} = 205 \text{ MPa}$,
 $R_{m(T0), \text{Granit}} > 50 \text{ MPa}$

3.8.2 Simulation and Tests

Several numerical simulations and tests will be performed to evaluate the mechanical behaviour of the system and to optimize the design.

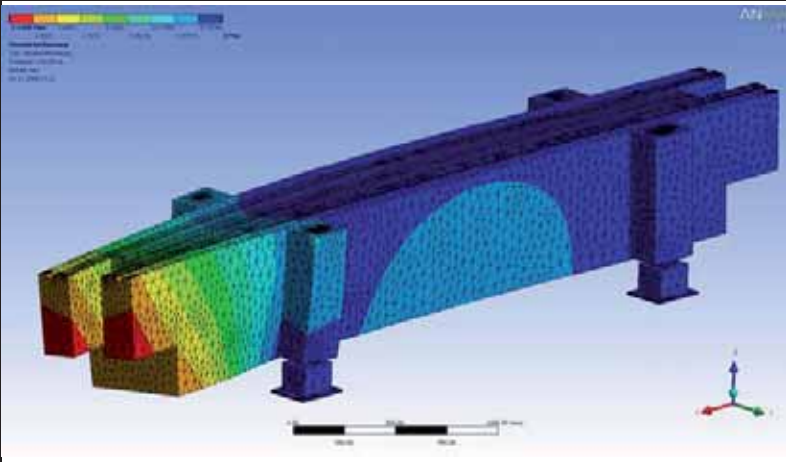
Simulations and tests (planned)

- FEA-based numerical simulation to predict the mechanical behaviour of the girder and supports regarding static, dynamic and thermal loads

- Manufacturing of prototypes, incl. quality checks in preparation for series production
- Girder test set-up (“SwissFEL Linac girder test stand”)
 - Functionality tests for single components and assembly
 - Experimental modal analysis to verify numerical simulations and to evaluate the dynamic response at the beam axis due to external excitations
 - Thermal heat loading tests
 - Alignment and pre-assembly tests

For the girder design of the SwissFEL Injector Test Facility, FEA-based numerical simulations and experimental modal analysis have already been performed.

Table 3.8.2: FEA simulation results – Girder for SwissFEL Injector Test Facility

| Mode Shape | Frequency [Hz] | Figure: Mode shape visualization of the 1 st mode shape |
|------------|----------------|---|
| 1 | 116.9 |  |
| 2 | 125.2 | |
| 3 | 147.5 | |
| 4 | 179.6 | |
| 5 | 212.2 | |
| 6 | 231.6 | |

To validate the results of the numerical simulations and the design, a number of eigenfrequency measurements have been performed, including set-ups with 3 and 4 feet and several jack set-ups.

The results of the tests confirm the simulation and show first rigid-body motion frequencies above 50 Hz, with amplitudes below 20 nm (see Figure 3.8.3 for details of the test set-up and Figure 3.8.4 for the results).



Fig. 3.8.3: Girder during eigenfrequency measurements: the arrows indicate the location of the accelerometers; test location at the SLS facility

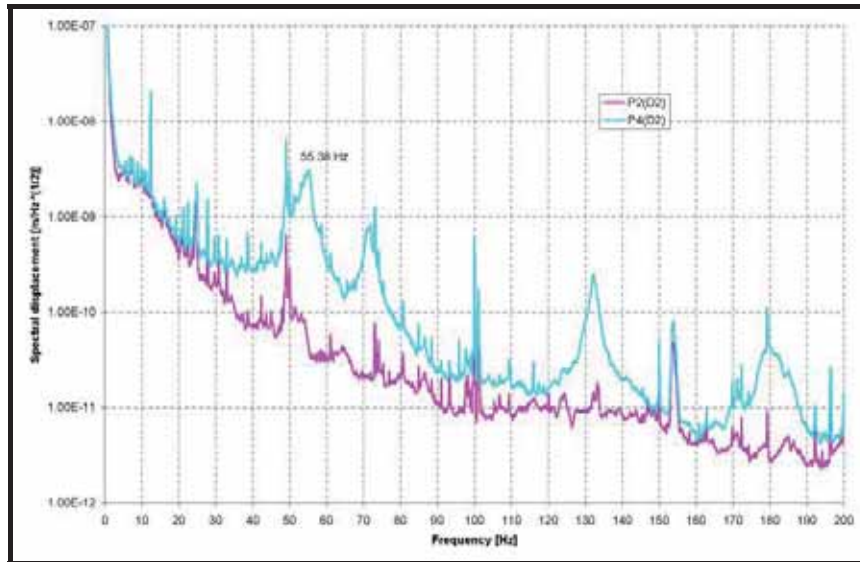


Fig. 3.8.4: Comparison between measured ground motion spectra and response spectra at the girder reference surfaces

3.8.3 Girder feet adjustment system

The relative position of the girder will be controlled by using jacks. The design of the jack should be consistent with the high eigenfrequencies of the girder; therefore the jack design relies on large surface contact. Screws or spindles in the structure that would generate a weak point for vibrations

will be avoided. The design uses commercial driving wedges for vertical adjustment and screws for horizontal adjustment.

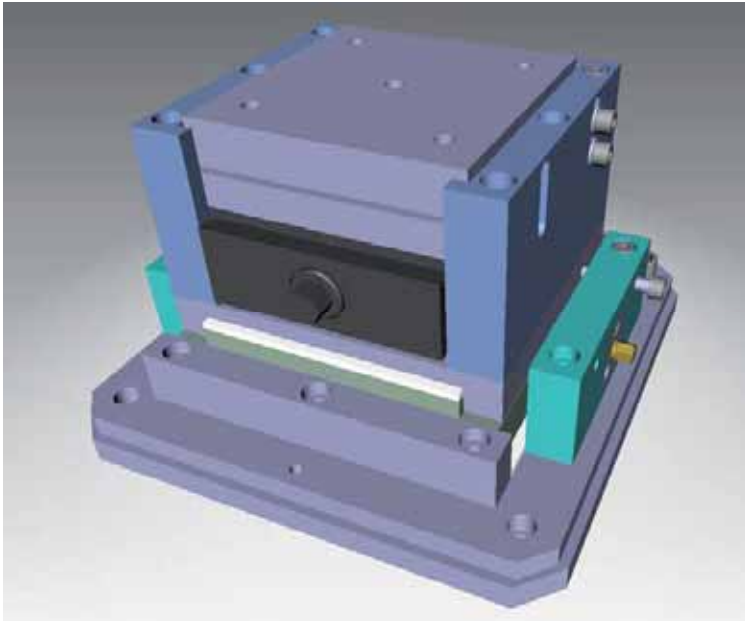


Fig. 3.8.5: The girder jack with a standard wedge located in a positioning system.

3.8.4 Local support system

For the alignment of components, single adjustable supports will be used. These supports can be placed directly on the horizontal and vertical reference surfaces of the girder. Fine adjustment of each support will be performed using shimming techniques or small driving wedges.

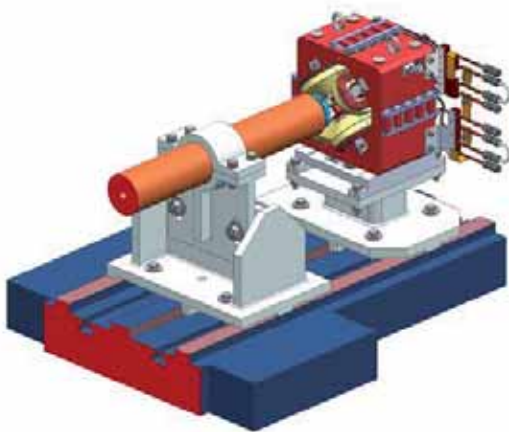


Fig. 3.8.6: Design study of local supports for SwissFEL Linac Girder Module

3.9 Control system

The control system is a central part of all large facilities. Its main task is to integrate the distributed subsystems of the facility into one coherent infrastructure. The control system provides the connection between hardware and the operators, it creates the environment that allows physicists to carry out their measurements, and it archives data to allow retrospective comparison with simulations. Guidelines for the design of the control system are reliability, ease of use, and expandability. Beyond its pure functionality, the maintainability of the whole system and the portability for new developments in computer science are basic requirements.

The hardware and software platforms, boot and archive services, configuration management and logistics developed for the other PSI accelerators will be used, as far as possible, to ensure cost efficiency and maintainability. The control system for SwissFEL will benefit from existing control systems equipment standards and know-how of the other PSI accelerators, whenever possible; in particular, the established close cooperation of the IT department and the controls section will be useful for the design and operation of the complex control system of SwissFEL. Many applications can be based on experience gained with the SwissFEL Injector Test Facility.

Developments which are required for SwissFEL have to meet the project schedule, the budget, and performance specifications, with consideration for knowledge transfer (internally and to the wider accelerator community). Results from a topical evaluation workshop on SwissFEL requirements and opportunities may influence the details of implementation.

3.9.1 Network infrastructure

The design basics for the network infrastructure of SwissFEL are the experience made by the IT department (AIT) at the Swiss Light Source (SLS) and the SwissFEL Injector Test Facility. Using PSI standard MPLS-VPN technology, it is possible to isolate networks while they share the common PSI network infrastructure and meet the ethernet design rules set up by AIT.

In the machine control network, the number of network ports needed is too high to fit into one Class C subnet, which is standard at PSI. Therefore, results from tests at the SwissFEL Injector Test Facility will be used to connect different subnets along the accelerator.

As in the SLS beamlines and SLS machine network today, the networks of the SwissFEL will be logically separated and use different address ranges. Separation is made using VLAN technology and virtual firewalls under the control of AIT. By using this standard network design, it will be possible to employ the existing centralized PSI network management method FCAPS (FCAPS is an ISO framework for network management) to monitor and maintain the SwissFEL network efficiently. It also provides connections to existing network services, such as DNS, DHCP and NTP.

The SwissFEL network will be set up in such a way that the same technology and infrastructure can be used for all of the following systems:

- SwissFEL machine networks
- SwissFEL experiment networks
- SwissFEL fire-alarm system (Brandmeldeleitsystem)
- Office networks (contains all printers, SIZ, SU network)
- Voice over IP (telephony services)

In addition, the system will be flexible and extensible, to meet new requirements from scientists or to adapt to new technologies.

3.9.2 EPICS environment

The control system will use the EPICS (**Experimental Physics and Industrial Control System**) toolkit. EPICS has been successfully applied at PSI in the SLS and in several similar large projects around the world (for example, LCLS at SLAC). Due to its collaborative nature, using EPICS enables us to take advantage of work done at other laboratories. Using a standard software toolkit will allow us to make best use of in-house know-how and to consolidate technical support services.

The basic structure of EPICS is a network-based client–server model implementing Channel Access as network protocol. At PSI, the EPICS servers are mainly IOCs (**Input Output Controller**) that can run on various hardware platforms, such as VME boards, Linux PCs, or embedded systems.

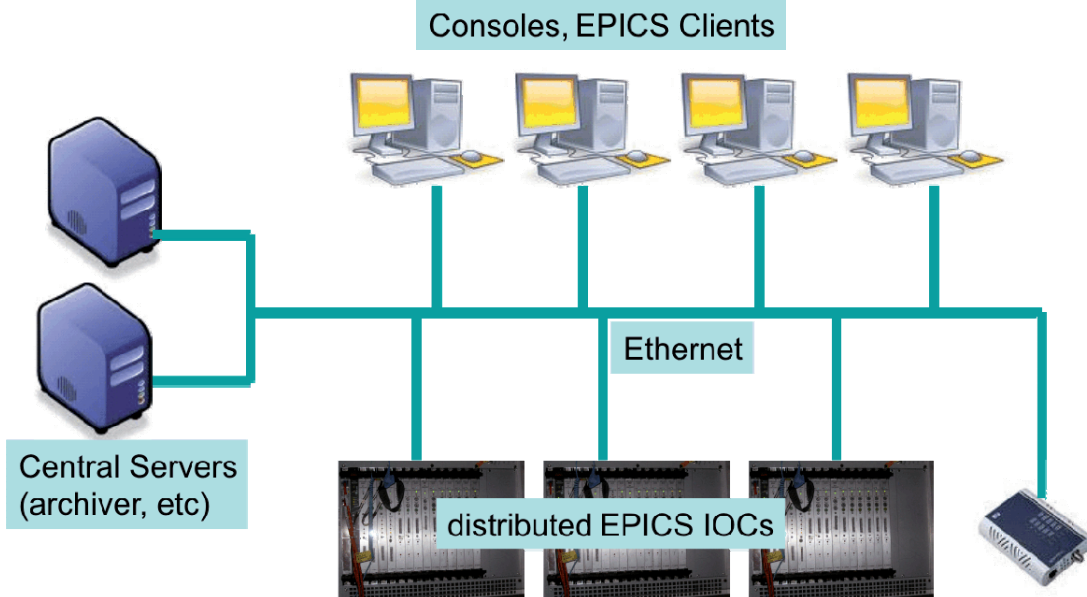


Fig. 3.10.1: Control system architecture

The IOC is configured at boot time by loading a set of configuration files, start-up scripts and drivers. The IOC may also run a sequencer process which implements a finite-state machine or customized programs.

EPICS client programs run mainly on the control room consoles and can be divided into three categories:

- System expert applications that enable experts to commission and maintain hardware systems
- Operator programs that provide control for routine machine operation
- Data acquisition programs that are used by scientists to perform and analyze experiments (on the accelerator or the experiment)

Requirements (e.g. programming language support) for the last group of programs are especially difficult to predict. Therefore, the control system will provide the flexibility and extensibility to include new developments at a later stage (during commissioning, or even later) of machine operation.

EPICS provides various interfaces to programming languages such as Java, Python, Tcl/Tk and others. To ensure maintainability of the programs and the interface itself, the controls section, in cooperation with the IT department, provides structures such as versioning systems and installation mechanisms.

An integral part of the control system is the timing system, which is covered in detail in Chapter 3.3.

The timing system provides the synchronization of all time-dependent subsystems with the electron bunch.

To connect EPICS clients and servers between the different networks (see Section 3.10.1, on Network Infrastructure), the channel access gateway application will be used. Preliminary tests of performance are organized in the SwissFEL Injector Test Facility, especially considering camera data and high measurement frequencies.

3.9.3 Software maintenance and distribution

Software development is not finished once a program works, but has to be maintained and looked after to provide reliable service. Therefore, the control system not only has to include a development environment that allows easy design and distribution of software, but maintenance and upgrade as well.

SwissFEL will be a challenge in terms of the number of controls components needed. Due to the geographical distance of the components and the installation of some systems into the beam tunnel (to minimize cable length), easy physical access to components and systems can not be expected. Therefore, automation in software distribution, installation and maintenance should be introduced wherever possible.

The general way of software distribution and installation has already been established at the SLS and will be used in the same way at SwissFEL. Further development might be needed to improve flexibility, in order to integrate new hard- and software. Experiences from the SwissFEL Injector Test Facility will be included into the concept.

The basic information needed for automated software installation is stored in relational databases. To make best usage of in-house knowledge, the environment provided by the IT department, namely Oracle databases, will be used.

All software needed for machine and experiment operation will be stored using a versioning system, to ensure accessibility and flexibility. General guidelines and support will be provided to make it easy for scientists and operators to include their programs into the control system structure.

As the control system is one of the central parts of the SwissFEL, a fault there will most probably prohibit machine operation or experiments. Therefore, control system reliability should reach 98% of the machine's operation time (the number is a little lower than the achievements of the SLS control system, to take the challenges of the SwissFEL into account). This implies similar reliability for most sub systems, such as file servers, data bases, etc.

A system can only be stable and reliable as long as malicious mischief (e.g. software viruses) is prevented. Therefore, the control system of the SwissFEL will establish close access control to the machine and the experiment networks. The security concept will be based upon the experiences and established rules at the SLS. Further developments, such as remote control of experiments, will be tested at the SLS beamlines and implemented according to the results of these tests by AIT, in cooperation with the controls section.

3.9.4 Control hardware

As far as reasonably possible, hardware used at other PSI accelerators should be preferred, to take advantage of existing expertise and cheaper stock keeping. If new hardware is used, development time and the cost for integration into EPICS (for example, for driver development) have to be taken into account and planned beforehand.

For network components, file servers and PCs, SwissFEL will use hardware based on PSI standards defined by AIT. EPICS IOC's will be the base for standard hardware control, such as analogue and digital signals and motor control (see Figure 3.10.2). A wide variety of hardware is already supported and can be adapted and extended to new developments.

Special requirements may be met by using embedded controllers (for example, FPGA-based systems or microcontrollers). Examples of such systems may include geographically isolated devices, systems that need the computing speed of a dedicated CPU, or entirely new hardware components which are not yet supported by any PSI standard hardware. However, the embedded controllers will be integrated into the EPICS framework and the software maintenance and distribution processes.

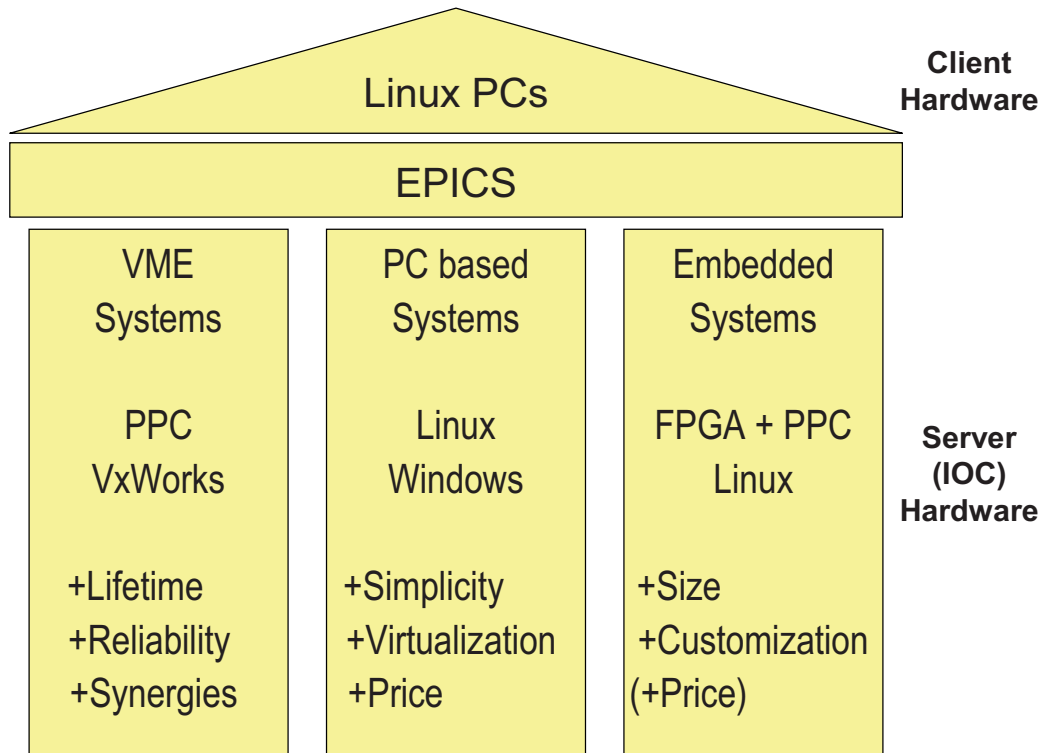


Fig. 3.10.2: The three pillars of the SwissFEL control system

With the start of experiments at SwissFEL, a large amount of data will need to be stored. At present, a volume of twenty to thirty times the data volume currently used at SLS is expected. Therefore, a server room for data storage and compute nodes for data analysis has to be planned, and the projected infrastructure provided.

3.9.5 Machine interlock concept

The interlock system can be divided into three main parts, which differ in their speed requirements, complexity and protection goal:

1. Beam Loss Interlock System for radiation protection, based on experiences from a similar system at the SwissFEL Injector Test Facility.
2. Beam Permit System for equipment protection, based on the Run Permit System used at the High-Intensity Proton Accelerator (HIPA) at PSI. A test system will be installed at the SwissFEL Injector Test Facility, to verify an upgraded design.
3. Beam Quality Verification System as part of the EPICS environment, which will be designed and realized in the course of first experiences derived from the SwissFEL Injector Test Facility. Detailed specifications will be based on the installed feedback systems and the requirements of the experiments. This system has to be flexible and easy to adapt to new conclusions derived from measurements.

Only the first two systems described are safety relevant. They are independent of the EPICS environment, in the sense that they could react reliably to situation changes without EPICS working. EPICS will be used in these systems to visualize the situation and archive the data.

In addition (but not described here) there are the vacuum system with a dedicated interlock system that disables the electron gun in the case of bad vacuum, the personal safety system (PSA), which is part of the radiation protection concept, and local routines that supervise single components, such as RF structures.

4 PHOTON BEAM COMPONENTS

This chapter describes the main components situated downstream the last undulator of Athos and Aramis lines. The photon transport can be splitted in following main areas:

- the Front End Enclosure Athos
- the Front End Enclosure Aramis
- the Experimental Hall

The purposes of the Front End Enclosure are to diagnose (arrival time, position, intensity, spectrum, ...), control (attenuate, collimate, ...) and distribute (photon switchyard, shielding) the photon pulses towards one of the three possible experimental hutches. The Front End Enclosure is separated from the Experimental Hall by a 2 m thick shielding wall.

4.1 Front End Enclosure Layout (Athos and Aramis)

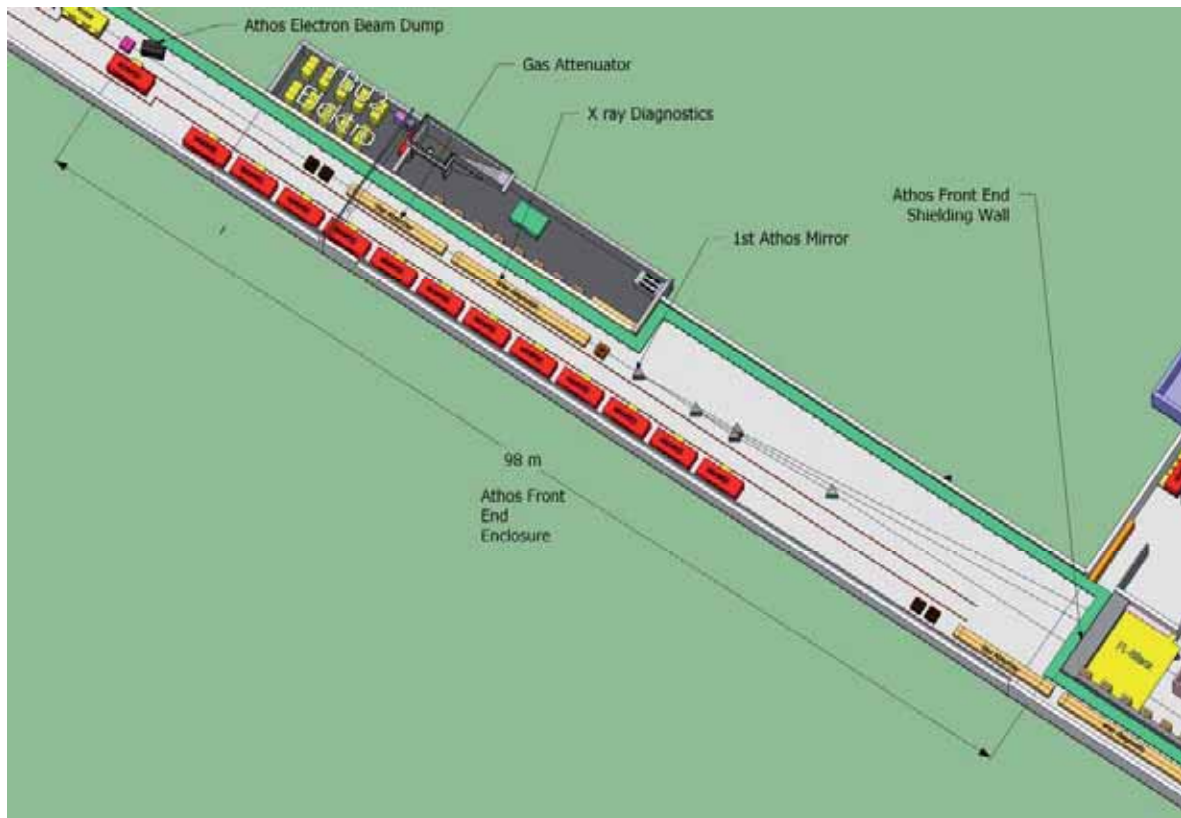


Fig. 4.1.1: Layout of the Athos Front End and Photon switchyard section.

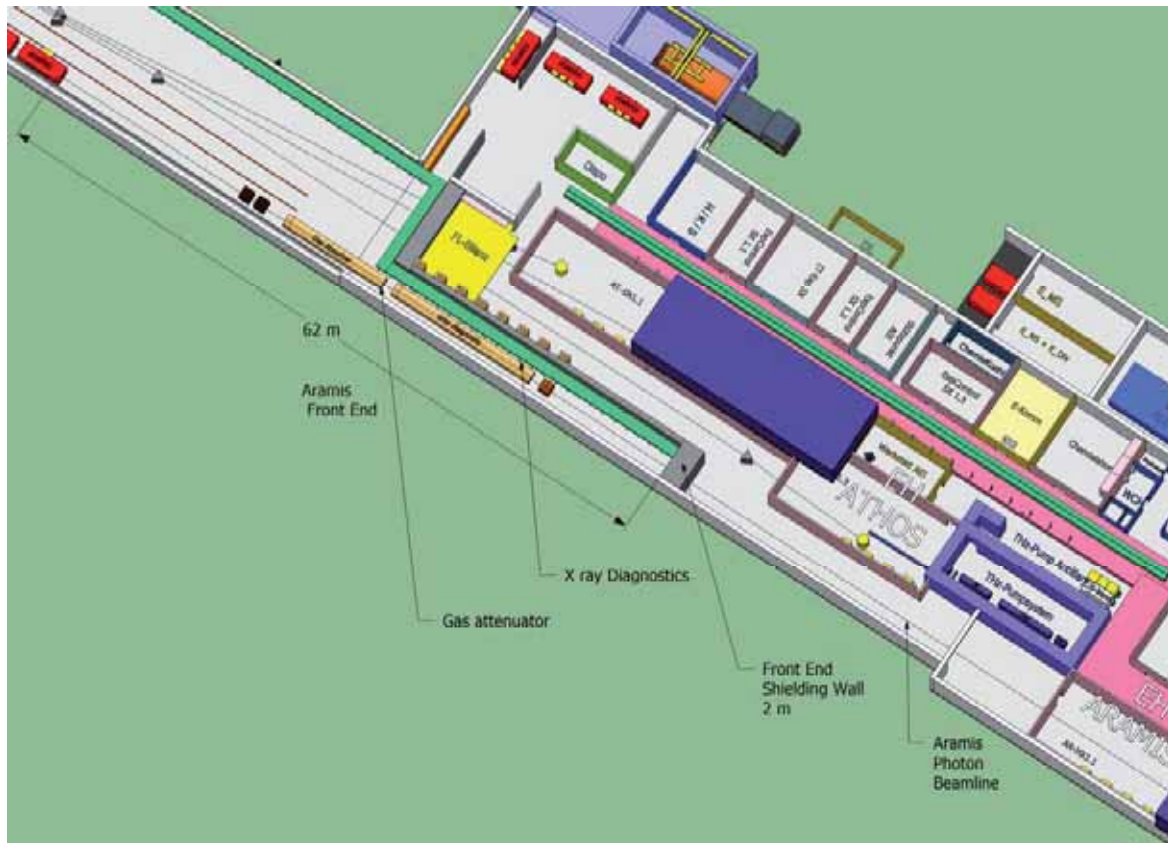


Fig 4.1.2: Layout of the Aramis Front End section

4.1.1 Gas Attenuator

4.1.2 Beam Shutter

4.1.3 Other Front End Components

4.2 Photon Beam Diagnostics

4.3 X ray Switchyard (Athos, Aramis)

4.3.1 X ray Optics Layout

4.3.2 X ray Optics Components

4.3.3 X ray Optics Mechanical Support and Alignment

4.4 Experiment Hall Layout

4.4.1 Experimental Hall general layout

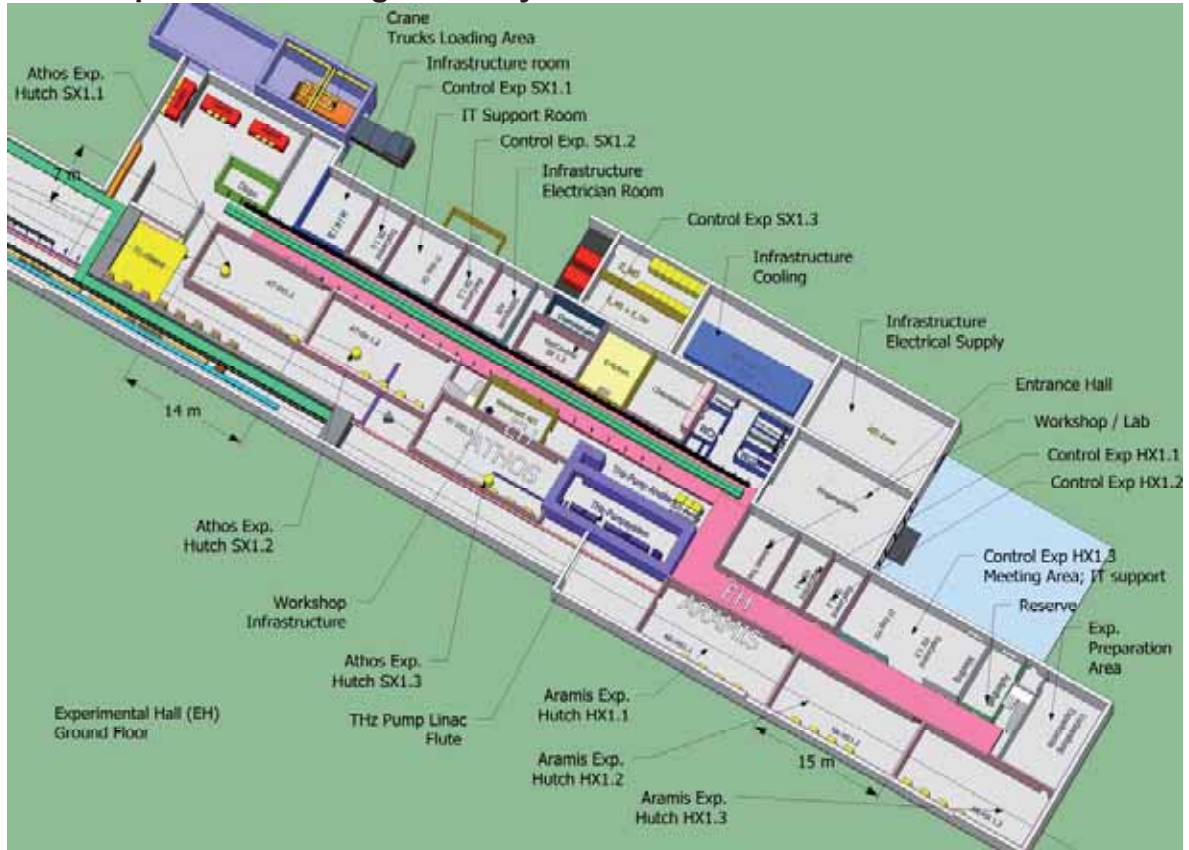


Fig. 4.4.1.1: Layout of the experimental hall (status of Jan 2011)

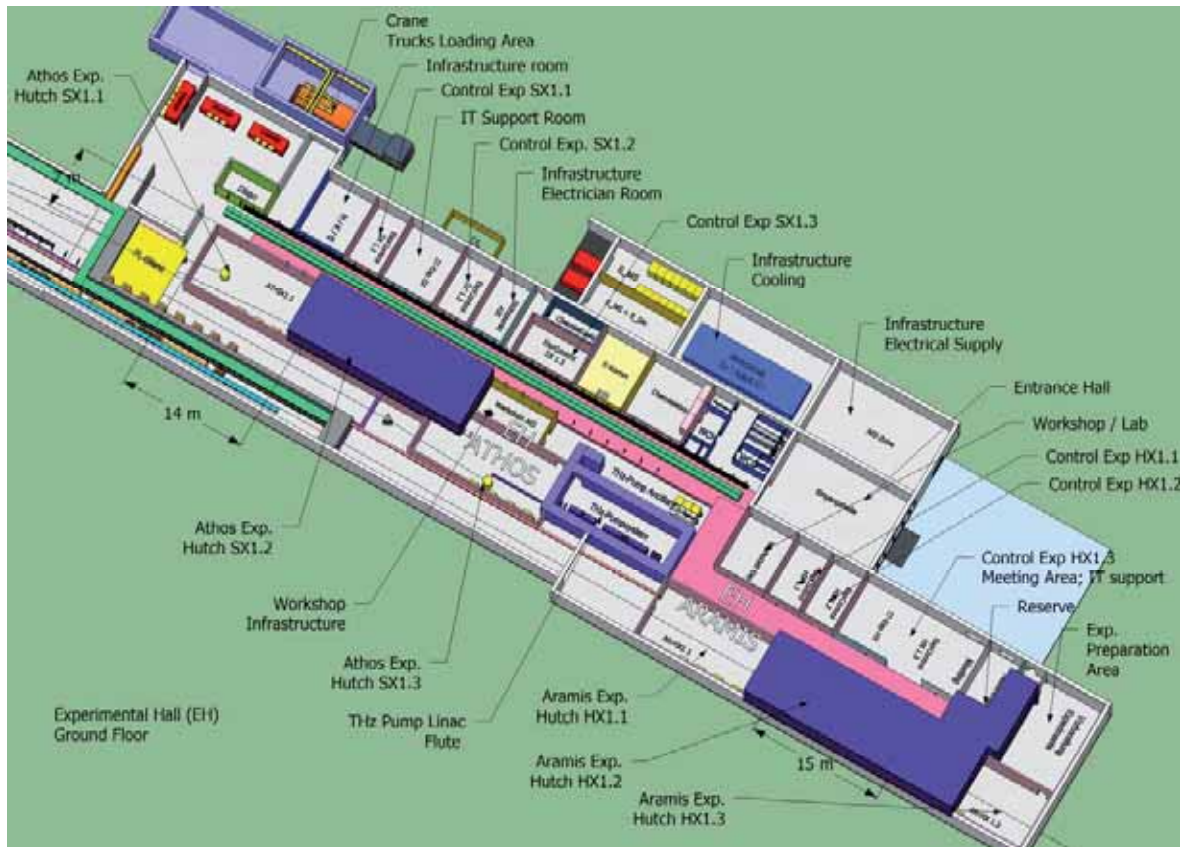


Fig. 4.4.1.2: Layout of the experimental hall showing the two laser hutch (second floor) for the pump lasers (status of Jan 2011)

4.4.2 Aramis Experimental Stations

Not yet defined.

4.4.3 Athos Experimental Stations

The design of an experimental station depends of course on the type of experiment and FEL light characteristic. Athos will consist of three experimental stations.

4.4.3.1 Pump and probe imaging and scattering: Resonant diffraction.

The basic goal of such experiments is to follow the time evolution after excitation (THz, IR, Visible) of the Lattice Orbit Charge Spin (LOCS) parameters. This should be a multi-shot experiment, non-destructive on single crystal samples (or powder). In practice, one measures the dependence of intensity (or position) of magnetic / electric Bragg peaks on pump-probe time delay. Table 4.4.3.1 compares the requirement for this type of experiment and the FEL beam parameters at the Undulator exit. Between the undulator exit and the experimental chamber, several diagnostics are planned to monitor the FEL pulses parameters. Fig. 4.4.3.1 represents a preliminary conceptual layout of the Athos front end up to the experimental chamber. The desired photons diagnostics are then depicted in Fig. 4.4.3.2.

One important parameter for the experiment is the wavelength stability which should be within 0.05 % of the resonant wavelength. In order to evaluate the consistency with

Table 4.4.3.1: FEL light requirements for resonant diffraction experiment and expected performances of SwissFEL at Athos undulator exit.

| Parameter | | Explanation | Requirement | SwissFEL |
|-------------------------------------|-------------------------------------|---|--|-----------------------------|
| Wavelength | value (λ) | Typical resonant transition range | --- | 80 – 1800 eV |
| | stability | $(\Delta n_{\text{pulse}} / n_{\text{pulse}})_{\text{mono}} < 20\%$ | $< \pm 0.25 \cdot \Delta\lambda \sim 0.05\%$ | |
| | range, scanning | $\sim (10 - 20) \cdot \lambda_{\text{res}}$ (adjustment) | 10 – 20 eV, $\Delta = 0.2$ eV | |
| Bandwidth | value ($\Delta\lambda$) | $(\Delta n_{\text{pulse}} / n_{\text{pulse}})_{\text{mono}} < 5\%$ | 0.2 % | 0.19 % @ 440 eV |
| | stability | | $< \pm 0.2 \cdot \Delta\lambda$ | |
| | range | --- | --- | |
| Beam diameter | value (d_{beam}) | --- | --- | 40 μm @ 440 eV |
| | stability | --- | --- | |
| Beam divergence | value | Beam at mono entrance small enough | 20 μrad | 15 μrad @ 440 eV |
| | stability | | $< \pm 2 \mu\text{rad}$ | |
| Beam exit position | stability | $(\Delta \lambda / \lambda)_{\text{mono}} < 0.1\%$ | | |
| Beam exit angle | stability | Beam hits mono entrance | | |
| Photons / pulse | value (n_{pulse}) | Sufficient intensity after mono | $\sim 1 \cdot 10^{12}$ | $5 \cdot 10^{12}$ @ 440 eV |
| | stability (? n_{pulse}) | $(\Delta n_{\text{pulse}} / n_{\text{pulse}})_{\text{mono}} < 5\%$ | $< 10\%$ | |
| Pulse length | value (Δt_{pulse}) | $< 0.1 \tau_{\text{physical}}$ | < 20 fs | |
| | stability | $< 0.5 \Delta t_{\text{pulse}}$ | < 10 fs | |
| Repetition rate | value ($1/\Delta t_{\text{rep}}$) | SwissFEL value | --- | 100 Hz |
| Polarization | type | Depends on transition | Variable linear | Variable linear + Circular |
| | stability | | | |
| Pulse arrival time | stability | $< 0.5 \tau_{\text{physical}}$ | < 100 fs | |
| Background tolerance (seeding only) | time domain | | | |
| | frequency domain | | | |

$\tau_{\text{physical}} = 200$ fs

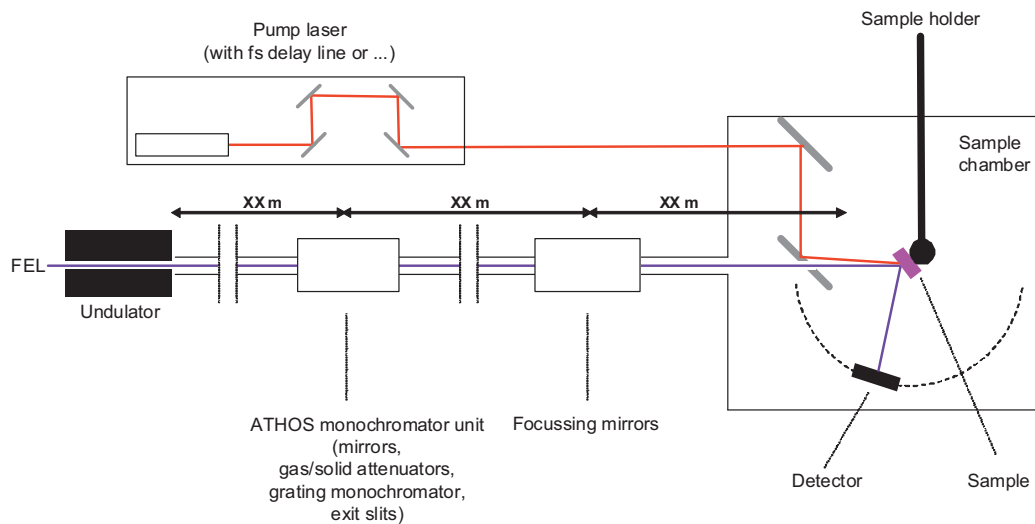


Fig. 4.4.3.1: Conceptual layout of the Athos front end including the experimental chamber.

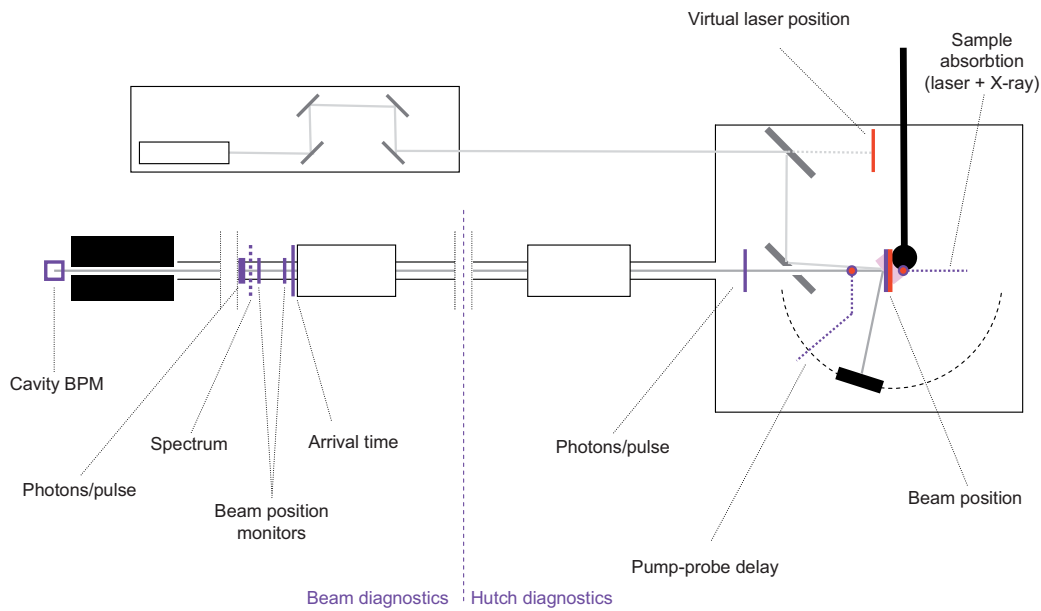


Fig. 4.4.3.2: Conceptual layout of the Athos front end and experimental chamber diagnostics.

4.4.3.2 Example of Resonant Diffraction experiment on CuO

Experiment on CuO samples were conducted by a PSI team with FEL pulses of LCLS FEL facility [4] in summer 2010 [97]. In consequence, the parameters for pump probe experiment on CuO are well known and can illustrate the typical requirements for similar experiments. Table 4.4.3.2 summarized the parameters used at LCLS in comparison to SwissFEL expectations at undulator exit.

Table 4.4.3.2: Comparison between pump probe experimental parameters used at LCLS [97] and SwissFEL expectations.

| Parameter | | Explanation of requirement criterion | Parameter value | |
|--------------------|-------------------------------------|---|-------------------------------------|-----------------------------------|
| | | | 1. CuO (LCLS) | Required to SwissFEL beamline |
| Wavelength | value (λ) | $\lambda_{\text{res}} \pm \Delta\lambda_{\text{res}}$ (resonant transition) | 932 \pm 0.75 eV | 80 – 1800 eV |
| | stability | $< 0.25 \Delta\lambda_{\text{res}}$ | ± 1 eV (wish: ± 0.2 eV) | --- (mono) |
| | range, scanning | (scanning for adjustment) | (± 10 eV, $\Delta = 0.2$ eV) | (± 10 eV, $\Delta = 0.2$ eV) |
| Bandwidth | value ($\Delta\lambda$) | $< 0.2 \Delta\lambda_{\text{res}}$ | ~ 0.1 eV | 0.1 – 0.02 % (mono) |
| | stability | $< 0.2 \Delta\lambda$ | $\sim \pm 0.02$ eV | --- (mono) |
| | range | --- | -- | --- (mono) |
| Spot diameter | value (d_{spot}) | spot well inside laser illumination | ~ 300 μm | |
| | stability | | $\sim \pm 100$ μm | |
| Spot position | stability | spot well inside laser illumination | $\sim \pm 100$ μm | |
| Photons / pulse | value (n_{pulse}) | Bragg peaks visible, radiation damage avoided ($\Delta T < 10^\circ$) | $\sim 5 \cdot 10^{10}$ (40 pC mode) | $> 1.10^{10}$ |
| | stability ($?n_{\text{pulse}}$) | $< 0.2 n_{\text{pulse}}$ | 0.8 n_{pulse} | $< 0.25 n_{\text{pulse}}$ |
| Pulse length | value (Δt_{pulse}) | $< 0.1 \tau_{\text{physical}}$ | ~ 100 fs | < 20 fs |
| | stability | $< 0.5 \Delta t_{\text{pulse}}$ | $\sim \pm 30$ fs | $< \pm 10$ fs |
| Repetition rate | value ($1/\Delta t_{\text{rep}}$) | Sample recovery ensured ($\Delta t_{\text{rep}} > 10 \Delta t_{\text{recovery}}$) | 60 Hz | 100 Hz |
| Polarization | type | Depends on resonant transition | Linear, horizontal | Variable linear |
| | stability | | | |
| Pulse arrival time | stability | $< 0.3 \tau_{\text{physical}}$ | < 300 fs | < 100 fs |

In addition to FEL light requirements, a description of the X-ray optics, the pump laser and the diagnostics used during this experiment are summarized in Table 4.4.3.3 to Table 4.4.3.4 as a possible.

Table 4.4.3.3: Soft X-ray optic parameters and Pump laser parameters requirements for CuO resonant diffraction experiments.

| | | Explanation | Set-up |
|--------------------|---------------------------|---|--|
| | | | 1. CuO |
| Monochromator unit | Pre-mirrors | Take beam to monochromator entrance | |
| | Pre-attenuator | Attenuate beam to desired fluence (sample damage !) | Gas-/solid-phase attenuators, 3-fold attenuation |
| | Monochromator | Fine tuning wavelength and bandwidth selection | VLS grating monochromator |
| | Spectrograph / Exit slits | | ± 1 eV (wish: ± 0.2 eV) |
| Focussing mirrors | | | K-B, focussing to $300 \mu\text{m} \times 300 \mu\text{m}$ |

| | | Explanation | Value / Feature |
|------------|--------------------------|--|--|
| | sample | | CuO |
| Pump laser | wavelength | Suited for pumping | 800 nm (better: 400 nm) |
| | pulse length | $< 0.1 \tau_{\text{physical}}$ | ~ 10 fs |
| | fluence | Enough to induce pump effect, no sample destruction, sample recovery ensured | 1-20 mJ cm ⁻² |
| | illumination area | $> \text{X-ray illumination area}$ | d = 0.7-1.0 mm |
| | pump-probe delay setting | | Trigger fixed, synchronised to master clock Delay by delay line |
| | Pump trigger precision | $< 0.1 \tau_{\text{physical}}$ | ~ 80 fs |

Table 4.4.3.4: Description of Soft X-ray diagnostic components used for the CuO experiment at LCLS (in grey highlighted are the on line diagnostics).

| Parameter | | Explanation | Set up |
|---------------------------|--------|--|--|
| | | | 1. CuO (LCLS) |
| Photons / pulse at sample | | Normalization of scattered intensity | Very thin Al-foil before laser mirror, drain current measurement |
| Pulse spectrum at sample | | Necessary ??? | --- |
| Beam position | coarse | Alignment of X-ray and laser beam at sample position (Monitoring fluctuations) | Insertable YAG fluorescence screen at sample position, 2 cameras $\pm 20 \mu\text{m}$ |
| | fine | (Monitoring fluctuations) | --- |
| Pump-probe delay | coarse | Approximative calibration of zero delay (Correction of nominal delay values) | Insertable coaxial antenna |
| | fine | Correction of nominal delay values | SiN ₃ -reflectivity detector |
| Sample absorption | | | Sample drain current measurement |
| Laser intensity | | Monitoring laser beam | CCD camera for virtual image on sample |
| Laser position | | | |

| | | | |
|----------------|--------------|---|--|
| | | | 1. CuO (LCLS) |
| Sample chamber | ambient | Ambient scattering minimal | Vacuum. Windows ??? |
| | holder | Orient and displace sample in the beam, for adjustment or illumination spot change. | Sample in asymmetric coplanar Bragg geometry (miscut angle $\sim 10^\circ$). Goniometer and 3D-movable holder with ??? precision. |
| | temperature | Stabilized to desired pre-pump value | $T = T_{\text{PhaseTrans}} + 5 \text{ K}$ $= 207 \text{ K}$ |
| Detector | type | Suitable for soft X-ray Bragg diffraction | Backilluminated CCD, movable in 2D |
| | readout rate | Faster than experiment repetition rate | > 60 Hz |
| | resolution | Bragg peaks resolved | Pixel size ??? Distance sample-detector ??? |
| | chamber | Ambient scattering minimal, minimal loss of scattered photons | Same as sample chamber |

4.4.4 Safety

General safety rules and concepts for the whole experimental hall are described in chapter 6.

4.5 Experiment Hall Components

4.5.1 Pump Lasers

Exact specifications of the pump laser are not yet defined. However, table 4.4.3.4 above illustrates the typical laser parameters that one need for pump probe experiment at Athos.

4.5.2 THz Pump Source

As part of the infrastructure for the users, a powerful THz source will be available for pump – probe experiment using the Athos FEL light as a probe. The THz pulses ($> 100 \mu\text{J}$, $0.1 - 10 \text{ THz}$; 100 Hz , 0.1 to 1 ps duration) should fulfill the requirements developed in chapter 2 in various experience (magnetic domain flipping, ...).

4.5.2.1 THz source layout

As shown on Fig 4.5.2.1, the THz source FLUTE is situated beside the Athos experimental hutch AT-SX1.3. The Linac required to produce coherent radiation (coherent synchrotron radiation or coherent transition radiation) has to be enclosed by a concrete shielding wall of about 1 m thickness. THz pulses are sent through a transport line to the experimental hutch. The RF modulator will be installed in the bunker to minimize the waveguide length and to keep the setup compact. All the control racks for the setup will be placed beside the bunker in the FLUTE THz Gallery.

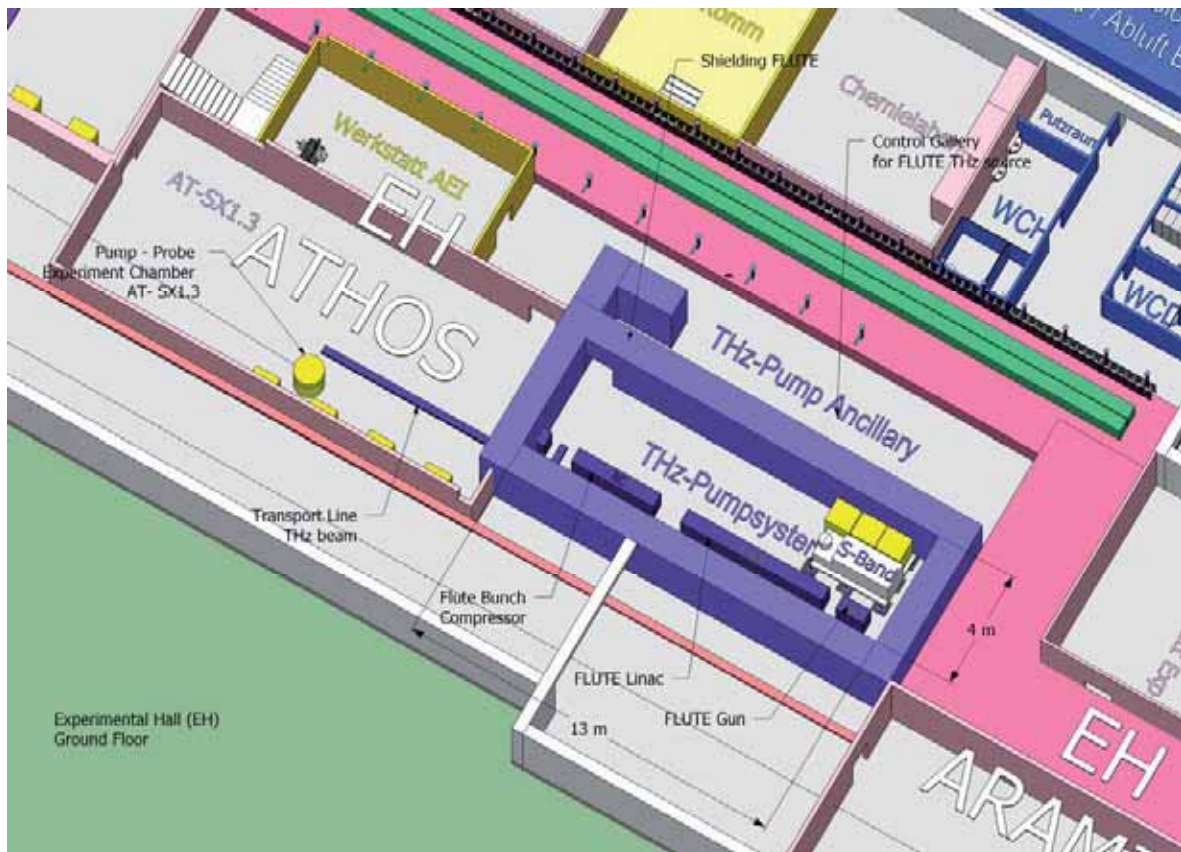


Fig. 4.5.2.1: Layout of the THz bunker situated in the Experimental Hall (EH).

The FLUTE facility consists of a radio-frequency (rf) photoinjector gun followed by an accelerating rf structure which bring the electrons to an energy of 60 MeV (see Fig. 4.5.2.2). In order to produce electromagnetic radiation the electron bunch must follow a curved trajectory that is obtained with dipole magnets. In FLUTE, four dipole magnets are used to compress longitudinally the electron bunch and to radiate in the THz frequency range. The last dipole serves as a THz radiator (see Figure 4.5.2.2). There are actually two effective ways to extract THz radiation and both can work in parallel. First the electron bunch will emit coherent synchrotron radiation (CSR) in the dipole

magnet if the bunch duration is shorter than the desired wavelength (for example 1 mm bunch length corresponds to 0.3 THz). The advantage of CSR over normal synchrotron radiation is that the intensity of CSR goes with the square of the number of electrons N (SR is only proportional to N). The other method of extracting THz radiation from a Linac is to insert a metallic screen in the path of the electron beam. The change of medium from vacuum to metal will generate transition radiation which can also be coherent if the observed wavelength is of the same length or longer than the electron bunch. This type of radiation is called the coherent transition radiations (CTR). The FLUTE design parameters are shown in section 2.6.1.

4.5.2.2 FLUTE THz components

Details on the different linac components (RF, magnets, ...) can be found in FEL-GR06-120. A drawing of the actual FLUTE is shown in Fig. 4.5.2.4. The RF gun and the S band structure will be supplied by one klystron & modulator unit. The modulator is based on a Pulse Forming Network and comes from the company PPT..

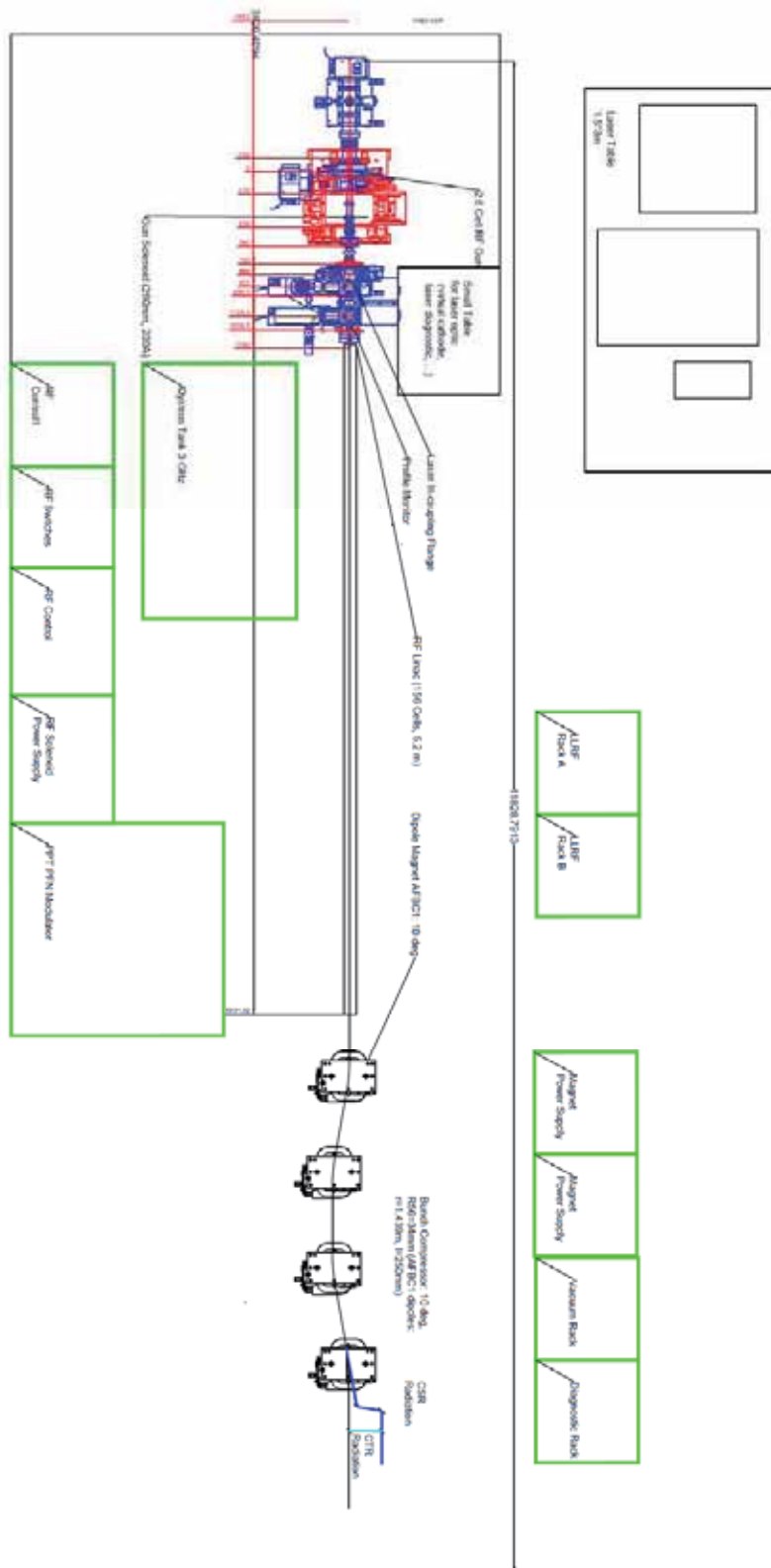


Fig 4.5.2.4: Drawing (as status of Jan 2011) of the FLUTE THz facility
 Repartition of the RF power between the gun and the structure is given in Table 4.5.2.2 for a 10 Hz operation regime.

Table 4.5.2.2: RF Power parameters

| | 3 GHz RF gun | 3 GHz Linac |
|---|-----------------|-------------|
| RF Peak Power (MW) | 22 | 20 |
| RF Average Power at 10 Hz (kW) | 1 | 0.9 |
| Peak power klystron (MW) | | 45 |
| Average power klystron at 10 Hz (kW) | | 2 |
| Klystron voltage range (kV) | | 307 |
| Klystron current range (A) | | 340 |
| Pulse flat top length (μ s) | | 4.5 |
| Repetition rate (Hz) | | 10 |
| Pulse to pulse Phase Stability (p.t.p.) | | 1 |
| Pulse to pulse Amplitude Stability (p.t.p.) | | 10^{-3} |

As presented in section 4.5.2.2 the bunch compression is obtained in two steps. At first, a linear correlation between energy and bunch longitudinal position (energy chirp) is obtained in the linac by off crest acceleration (e.g. 25 degrees off crest operation). Then the energy chirped bunch will be compressed by travelling through a four dipole magnets chicanes (see Fig 4.5.2.3).

The dipole magnets parameters are summarized in Table 4.5.2.3 and figure 4.5.2.5. The four dipoles will be connected in series and powered by a bipolar DC power supply 200 A, 60 V with a current stability of 0.01 % peak to peak in the frequency range of 1 Hz to 100 Hz.

Table 3.5.1: Dipole magnets parameters

| | |
|--|--|
| Magnet effective length | 250 mm |
| Dipole Gap | 3 cm |
| Good field region width (dB/B < 5.e-4) | 80 mm |
| Maximum current | 200 A |
| Linear calibration (fit to measurements) | 2.32 mT / A |
| Magnet Resistivity | 48 m Ω |
| Power Consumption at 200A | 2 kW / magnet |
| Watercooling | 2 l/min. (no water manifold at magnet) |

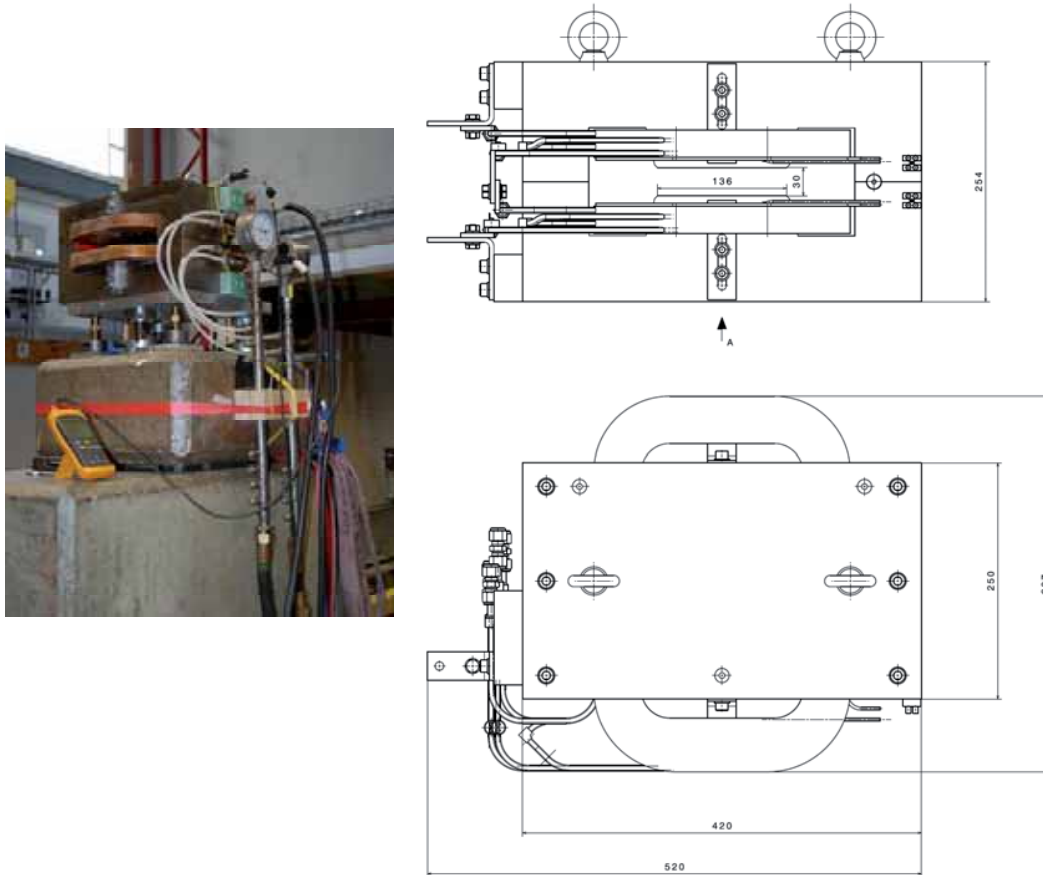


Figure 4.5.2.5: Dipole magnet on his measuring banc (left) and dimensions of the dipole.

Modification of the dipole (for example opening of the gap) is still possible to optimize the CSR THz extraction.

Detailed description of the THz transport line is still under design. Synchronisation of the THz pulses to the FEL pulses will be insured through the fiber laser reference signal which is distributed all along SwissFEL.

5 MACHINE ASSEMBLY AND COMMISSIONING

5.1 Machine installation

5.1.1 Assembly Plan

The detailed time plan for SwissFEL in the period 2012 – 2018 is still under discussion. Main steps are however shown in Fig. 5.1.1. The three main components, in terms of cost (hardware and manpower) are the building construction, the undulator modules and the RF acceleration modules.

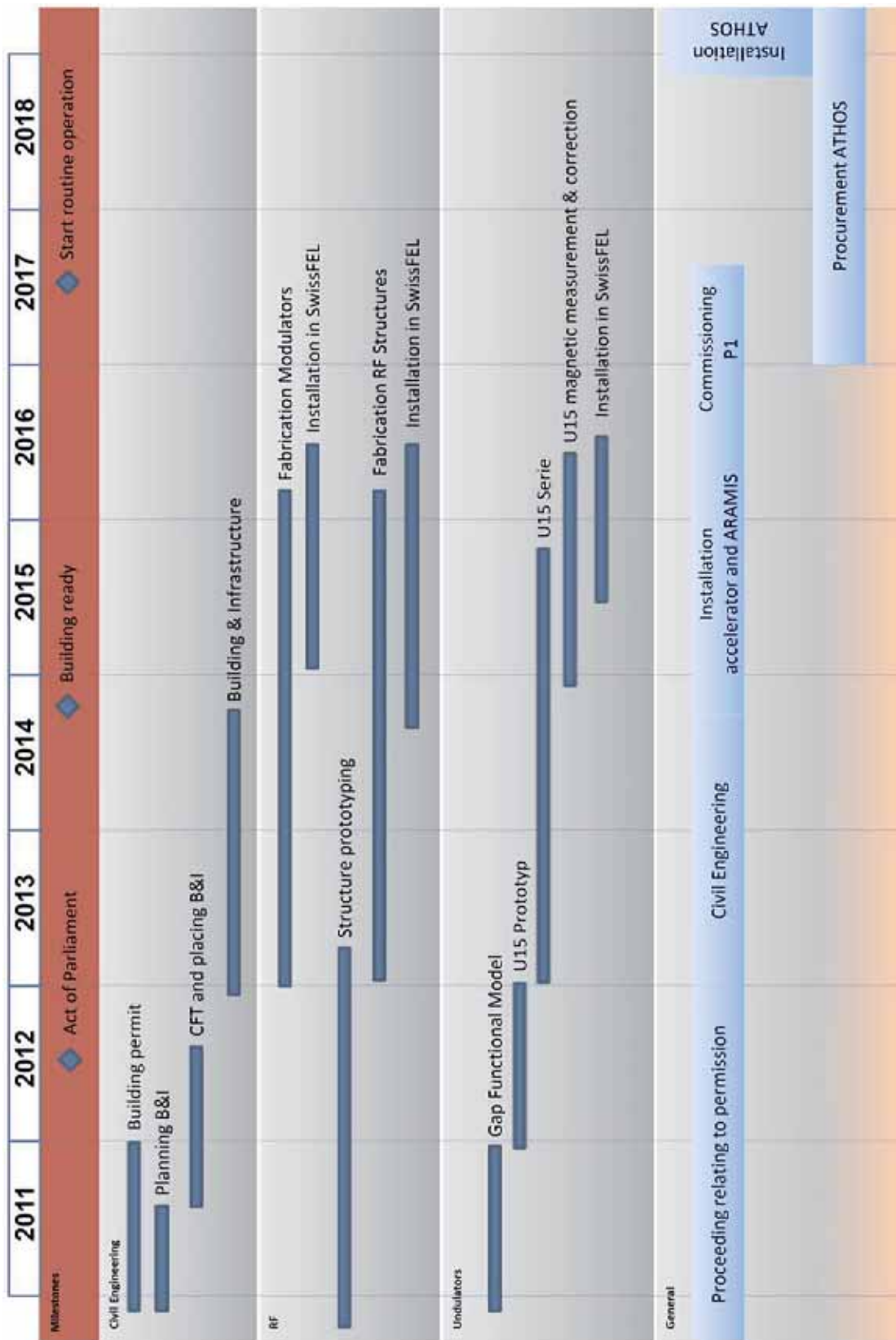


Fig. 5.1.1: SwissFEL main milestones and activity steps.

5.1.2 Components Assembly Concept

Installation of the SwissFEL is foreseen in a timeline of about three years, starting with the infrastructure and ending with the large machine components. For the large machine components, an installation time of about 18 months is foreseen. Pre-assembly and testing of linac and Undulator modules in advance is very important in order to stay on schedule, this will require dedicated areas at PSI or nearby. Moreover, successful machine installation requires dedicated manpower resources for planning, pre-assembly, installation, alignment and coordination, these resources have to be made available well in advanced.

Before handover of the tunnel, a first measurement campaign is required to define the alignment network. Therefore, all survey marks will be installed by the general contractor, and this network measurement campaign should start about 4 months before tunnel delivery for installation. The measurements needed are well-established, classical surveying methods, using high-accuracy theodolite Total Station, Laser Tracker, and leveling instruments. Since the environmental conditions at that time will not be suitable for high-accuracy measurements, the measurement campaign has to be repeated prior to the alignment of the machine components.

Based on this alignment network, some reference points for the theoretical beam axis and beam height will be marked at the tunnel wall and floor, to facilitate correct positioning of the infrastructure components, such as cabling and piping.

The position of component fixation points in the tunnel floor and beamline will be marked in the tunnel. Once the markings are available, drilling and other minor civil engineering adaption can take place. In the final stage, before component installation, the jacks and component supports will be installed and aligned at their definitive positions, where they will be cemented locally using a cast around the base.

Then will begin the installation of all large components into the tunnel, such as, for example, the linac girder modules, with a mass of up to 6 tons each, and the Undulator modules, with a mass of 25 tons each. Likewise, single quadrupoles with their supports and bunch compressor components, including the dipole magnets, will be installed in this phase. Also the beamdump as a single heavy components need to be installed in this phase. For this purpose a set of transport tools, air cushion based for the Undulators and wheel based for Linac and magnets will be available. An electric-powered tractor will also be required during the installation. Figure 5.1.2.1 shows an example of a transport convoy. Single magnets, such as BC dipoles, are brought in with a trailer and then installed with a local mobile crane in the tunnel. The heaviest single magnets have an estimated weight of 1.5 tons.

Once the main components are in the tunnel, HF, vacuum and other connections can be made. In the next phase, bakeouts of vacuum systems are carried out and several equipment checks are executed. It is quite clear that careful scheduling of the installation tasks is required and parallel working is essential for staying on the installation time schedule. Once more, pre-assembly and prior testing of components is indispensable, as well as having a ll components available on time during the installation.



Fig. 5.1.2.1: Example of transport convoy during DFB installation at LHC.

In the technical buildings, infrastructure work will progress at the same time as in the tunnel. Electrical racks will arrive before the foreseen double floor is built, and in the final stages the modulator and klystron modules will be installed.

5.1.3 Components Transport

The SwissFEL tunnel is foreseen to have two entrance points for large components, one main entrance in the end of the building which is on the same floor level than the main beam tunnel and one entrance at TBL2 downstream end (lift) (see Chapter 6). Figure 5.1.3.1 shows a preliminary proposal for the northern main entrance.

The main entrance in the north of the building is arrival hall, 10m deep and 5.5m wide. The hall has a crane with a capacity of at least 35 tons and a hook height at 6.5m. This entrance is foreseen to be used for the arrival of Undulators that are first brought to the Undulator measurement laboratory and then after some fine tuning, they are installed in the tunnel. The longest travelling distance is 200m. The Undulators are transported on an air-cushion vehicle and can only be installed via this entrance because of their size and mass. The specification document FEL-WO88-028-3 gives more details of the requirements of the Undulator installation tool. In figure 5.1.3.2 details of the final stage of the Undulator installation are shown. During the installation phase, this entrance shall also be used for both injector- and linac Girders.

The central entrance (TBL2) has an outdoor unloading area equipped with a 7.5 tons crane, from this area wheel based systems have to be used to enter the technical building. Next to the entrance inside the technical building, one level above the tunnel, a 6.3 tons elevator is located with cabin inner dimension 6m x 2m. The elevator offers a direct connection to the tunnel below, it has doors in both ends of the cabin to allow exit down- or upstream of the tunnel beamline. This secondary entrance point allows the installation of Girders, although a larger effort is required due to the many steps with crane / wheel / lift and the relatively limited area for maneuvering. Next to the lift, a staircase for personnel is foreseen as an access between the levels.

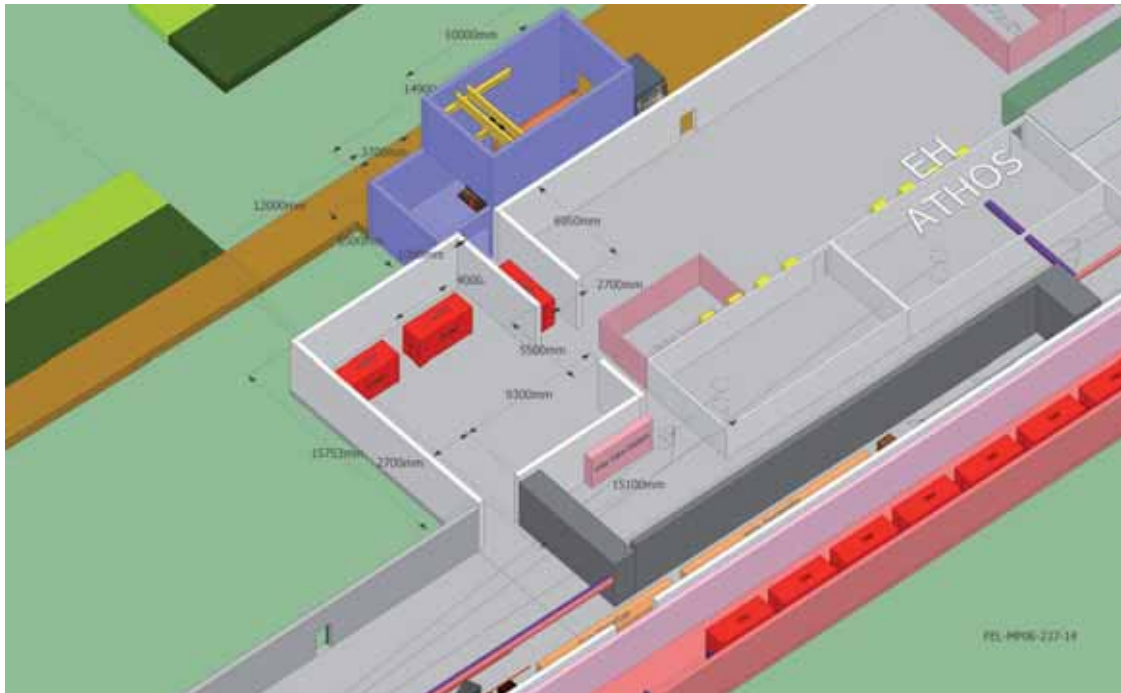


Fig. 5.1.3.1: The loading-zone building above the tunnel, with the arrival area and shaft.

The Linac girders are foreseen to be transported and installed on wheel based tooling, they will allow for longitudinal transport and the final transversal move into the beamline. In the first phase of the machine installation as the girders are brought in from the northern main entrance the distance to travel on wheel based transport will be up to 700m. In addition to the Girders and the Undulators that need to be installed in the tunnel, many other components also have to be installed among them a number of quadrupole and dipole magnets and the beamdump, see Table 5.1.3.1 below for a transport parameters summary.

The technical building (top floor) also has a number of large components that need to be installed, the largest being the Injector and Linac Modulators. They will enter the technical building mainly via the central entrance point and via a number of smaller access points available between the central entrance and the southern end of the building. The modulators have to enter the technical building on wheel based transport, once they are close to their final position they can be lifted with a local crane available next to the modulator final position, note that this crane has a limited travel, due to other infrastructure installation in the roof.

Table 5.1.3.1: List of large components in the first Phase of Construction

| Component | Dimension | Mass | Amount | Mass T |
|---------------------|-----------------------------|-----------|--------|----------|
| Injector Girder | L 4.7 m x W 1.1 m x H 2.4 m | 6500 kg | 12 | 70 tons |
| Linac Module | L 4 m x W ? m x H ? m | 4000 kg | ~50 | 500 tons |
| Undulator Module | L 4.1 m x W 1.7m x H 2.1m | 25000 kg | ~12 | 440 tons |
| BC 1 Dipole | L 1 m x W 0.5m x H 0.5m | 500 kg | ~4 | 2 tons |
| BC 2 Dipole | L 1 m x W 0.5m x H 0.5m | 1000 kg | ~4 | 4 tons |
| Quadrupoles | L 15-20 cm | 70 kg | ~120 | 8,5 tons |
| Beam dumps | ? | +10000 kg | 2 | |
| Injector Modulators | L 2.8m x W 1,7m x H 2.1m | 3 tons | 4 | ~12 tons |
| Linac Modulators | L 2.8m x W 1,5m x H 2.1m | 1 tons | ~25 | ~25 tons |

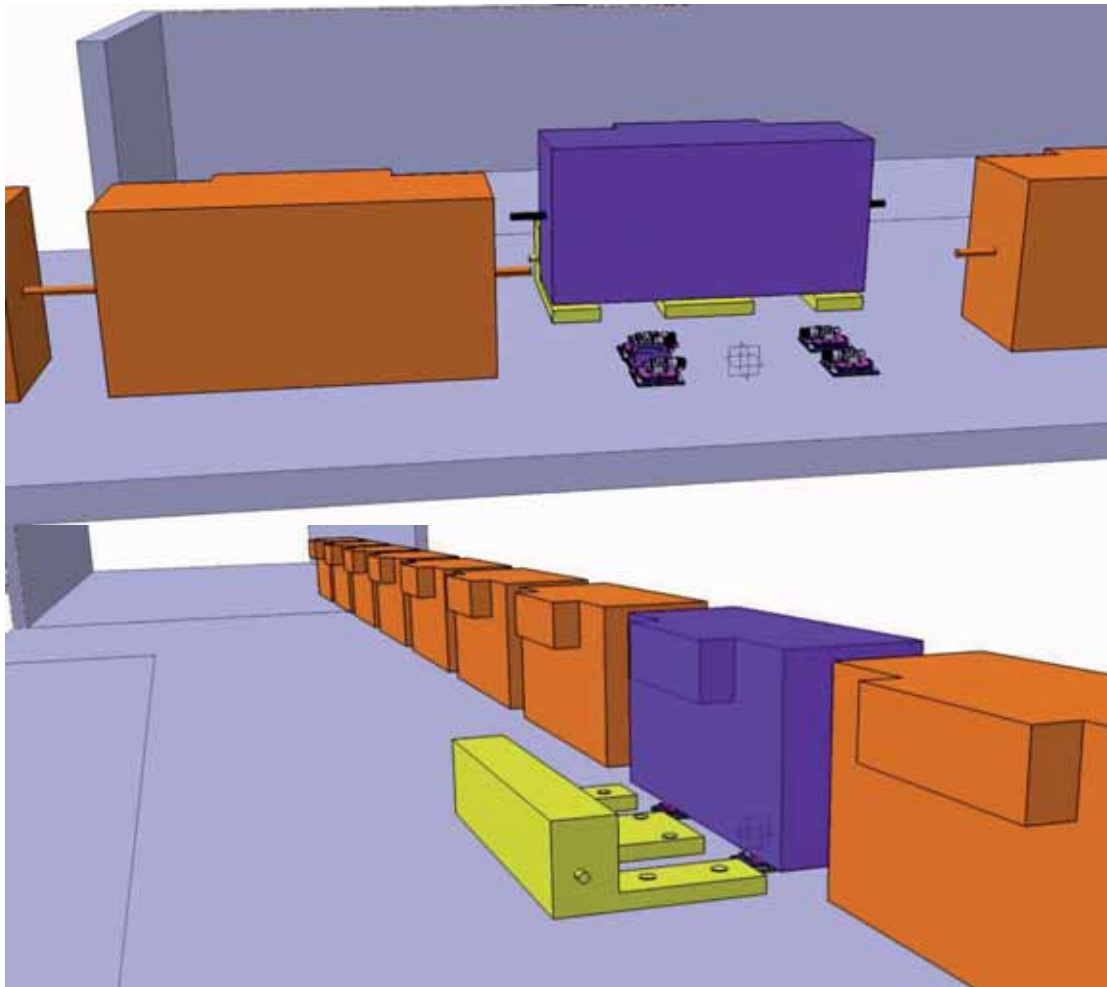


Fig. 5.1.3.2: Last stage of Undulator installation with Air cushion vehicle.

5.1.4 Assembly Alignment Concept

5.1.4.1 Reference Coordinate System

A local coordinate system has been defined to ensure the data administration and data exchange of the coordinate sets. This coordinate frame is a local metric 3-dimensional and right handed coordinate system which has been determined according to the machine axis (MCS i.e. machine coordinate system). This coordinate-system is the basic working coordinate frame for construction and alignment tasks. All necessary transformations between external global coordinate-systems (as LV03, LN02, WGS84, etc.) and the local coordinate-system will be done by the alignment group only!

The alignment group refers of the official computation service REFRAME provided by swisstopo (Bundesamt für Landestopografie).

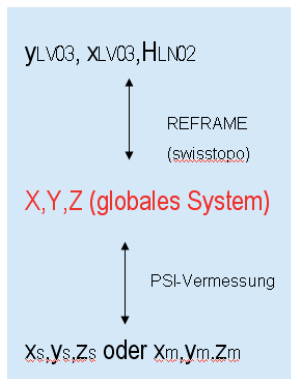


Fig. 5.1.4.1.1: Coordinate Transformations between global systems (LV03) and local coordinate system.

The fundamental point and the geodetic datum of the local coordinate-system has been defined according to the machine axis definitions of the preliminary planning (P.Ming). To minimize the geometric distortions, the fundamental point was set to the center of the facility.

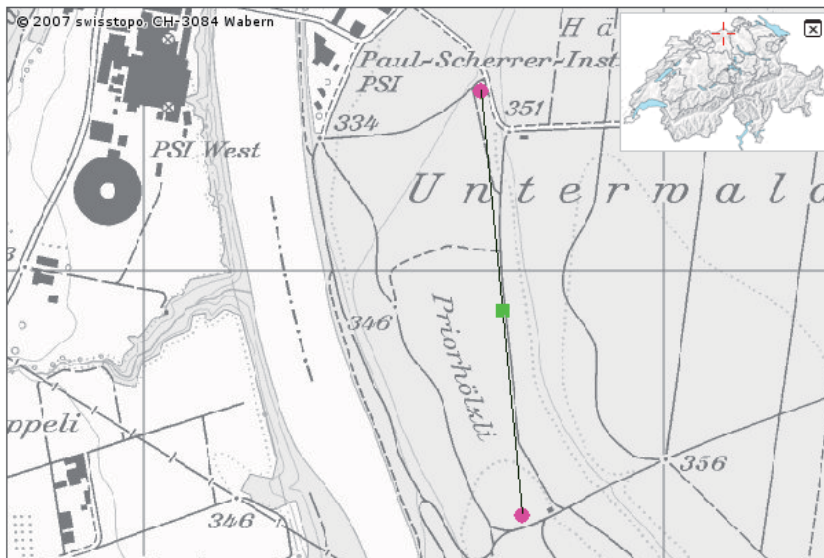


Fig. 5.1.4.1.2: Position of fundamental point (green square)

Kartenquelle: Swisstopo Dataviewer:

5.1.4.2 Alignment Steps

All beamline components will be pre-assembled and pre-aligned onto girders and support frames. The main instrument for the alignment procedure is a Laser Tracker. The expected accuracy for the internal geometrical alignment of components sitting on one girder assembly ($L \approx 5$ m) is better than 0.05 mm (σ_x, σ_y).

It is necessary that each component is equipped with at least 3 or better 4 visible and well distributed reference cones capable to hold the 0.5"CCR alignment reflector.

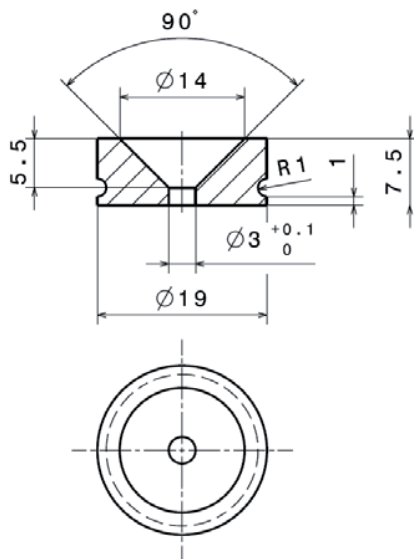


Fig. 5.1.4.2.1: Sample of conic reference mark, according to drawing 4-50021.031.

It is important, that the relation (distances) of the reference mark coordinates in respect to the physical center is completely known. The task of Fiducialisation has to be done well in advance before alignment. This should be generally done by the manufacturer or alternatively by the responsible PSI section.

The pre-assembled girder units will be positioned in the machine tunnel, based on the 3D survey and alignment network using the Laser Tracker. The local accuracy for component alignment in a typical measurement set-up in the machine tunnel (in a measurement range of +/-10m) is about $\sigma_x, \sigma_y, \sigma_z < 0.1$ mm. Curvature-of-earth compensation will be included in the reference point coordinates.

Using beam-based alignment methods (BBA) during commissioning, the position of each component could be optimized up to a relative accuracy of about 0.01 mm (rule of thumb - including limits of mechanical movements and measurement tolerances).

5.2 Components to Infrastructure Interface

5.3 Machine Commissioning Plan

5.3.1 Hardware commissioning without beam

5.3.1.1 RF Systems Commissioning Plan

Modulator commissioning plan, Water tests, LLRF Control; Structure Conditioning plan... .

5.3.1.2 Undulator Commissioning

Measurements, alignment, test plan, motor control

5.3.1.3 Vacuum Commissioning

Baking, Leak tests, environment requirement, interlock systems, control

5.3.1.4 Magnets Commissioning

Cooling test, polarity and amplitude test, Epics control tests, Degauss Procedure tests, control

The Magnet Power Supplies (PS) will be pre-tested outside the SwissFEL facility. After that the PSs are installed in the technical buildings and connected to the mains, the magnets and the EPICS control system. The on site commissioning of the PS will include the following steps:

- Check of external interlock signals
- Isolation measurements of DC cables and load magnets
- Load measurements (resistance and inductance)
- Check of correct cabling (current flow in the correct magnet with the correct polarity)
- Final adjustment and tuning of all controller parameters including the closed loop parameters
- Measurement of load current stability (short term)
- For corrector magnets in the BPM closed loop: Measuring and optimization of current step responses

Check of remote access from the EPICS control system

5.3.1.5 Laser Commissioning

Laser transport test, virtual cathode, synchronization, motor commissioning, camera, alignment

5.3.1.6 Diagnostic Commissioning:

Screen alignment calibration plan, motor control,

5.3.1.7 Control Commissioning

Control panels commissioning, control room commissioning, logbook,

5.3.2 Beam Commissioning Plan

No temporary shielding walls are foreseen to allow beam commissioning of local sections of the accelerator. However there will be a long conditioning period for the RF structures to allow parallel beam commissioning (for example in the injector part).

5.3.2.1 Radiation Monitoring Plan

5.3.2.2 First Injector Electron Beam Commissioning

5.3.2.3 First Linac Electron Beam Commissioning

5.3.2.4 First Photon Beam Commissioning

5.4 Feedback systems and electron beam-based alignment

5.4.1 Beam-based magnet and trajectory alignment

The goals for the alignment and correction of the beam trajectory in the SwissFEL are:

- 1) The establishment of a “golden orbit” through beam-based alignment and steering, where the orbit deviations and spurious dispersions are minimized, such that slice emittance stays less than $0.43 / 0.38 \mu\text{m}\cdot\text{rad}$ for the nominal mode (200 pC, compression factor 127 / 75) and $0.18 \mu\text{m}\cdot\text{rad}$ for the short-pulse mode (10 pC) (see Section 2). The growth of the projected emittance should also be kept reasonably small, in order to not deteriorate the beam envelope matching into the undulator.
- 2) The establishment of an orbit in the undulators that provides sufficient transverse overlap and relative microbunching phase error of electron and photon beams.
- 3) The minimization of transverse fluctuations around the golden orbit to a level that allows stable FEL operation, where the tolerances for a single perturbation are $14 \mu\text{m}$ and $1 \mu\text{rad}$ for beam position and angle at the undulator entrance (see Section 2). It is desirable to achieve smaller fluctuations, in order to allow more error budgets for other sources.

Concerning the first point, a simulation study using ELEGANT (as shown in Figure 5.4.1.1) indicates that the maximum orbit perturbation should be less than a few $100 \mu\text{m}$ for 200 pC operation. This corresponds to a few millimeters dispersion.

The trajectory alignment for linac and undulators is discussed separately in the following, since the requirements are largely different. In the following, BPM resolution of $3 \mu\text{m}$ in the linac and $1 \mu\text{m}$ in the undulator is assumed.

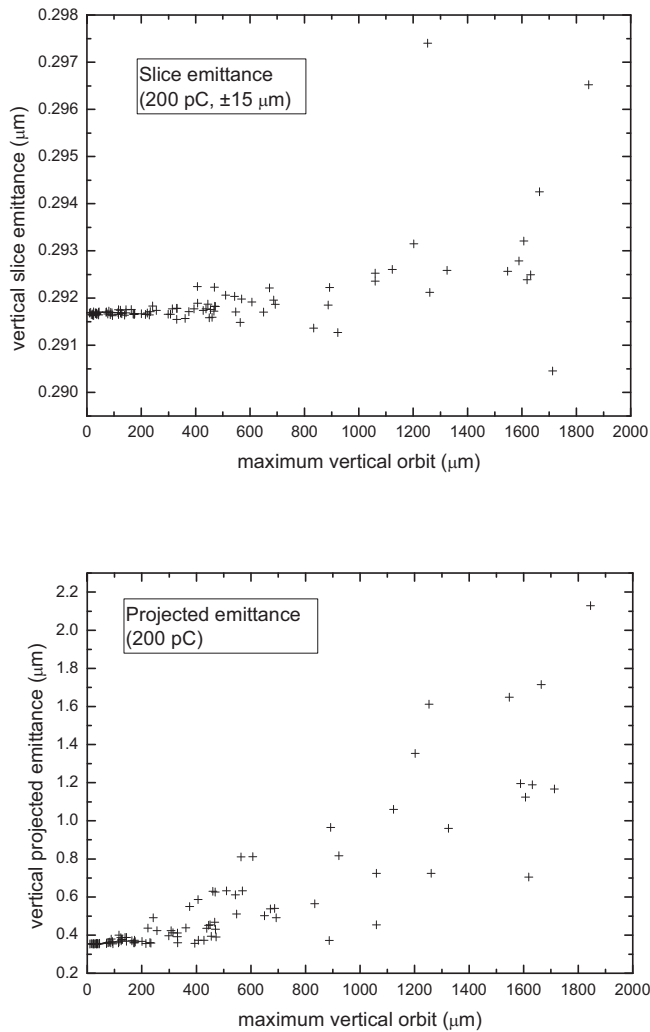


Fig. 5.4.1.1: Slice and projected emittance versus beam orbit. Best-case simulation for 200 pC operation.

As described in Section 5.1.4 (Assembly alignment concept and expected precision), the accelerator components will be aligned with about 50 μm rms short-range precision. Based on beam measurements, relatively large short-range alignment errors, of the order of 50~100 μm or more, will be detected and realigned in the early stage of commissioning.

Afterwards, the beam will be steered to minimize the orbit and dispersion. Dispersion-Free Steering (DFS) [98] is generally used, and also Ballistic Alignment (BA) [99] is applicable to the relatively short SwissFEL linac. It will be helpful to compare the results from different algorithms for a better understanding of the machine. For the early stage of commissioning, “quick-steering”, in which the beam is steered to go through BPMs’ centres, will be useful for establishing a beam orbit quickly. Typical results of beam steering are shown in Figure 5.4.1.2 (b), (c) and (d), together with the initial orbit and dispersion in (a).

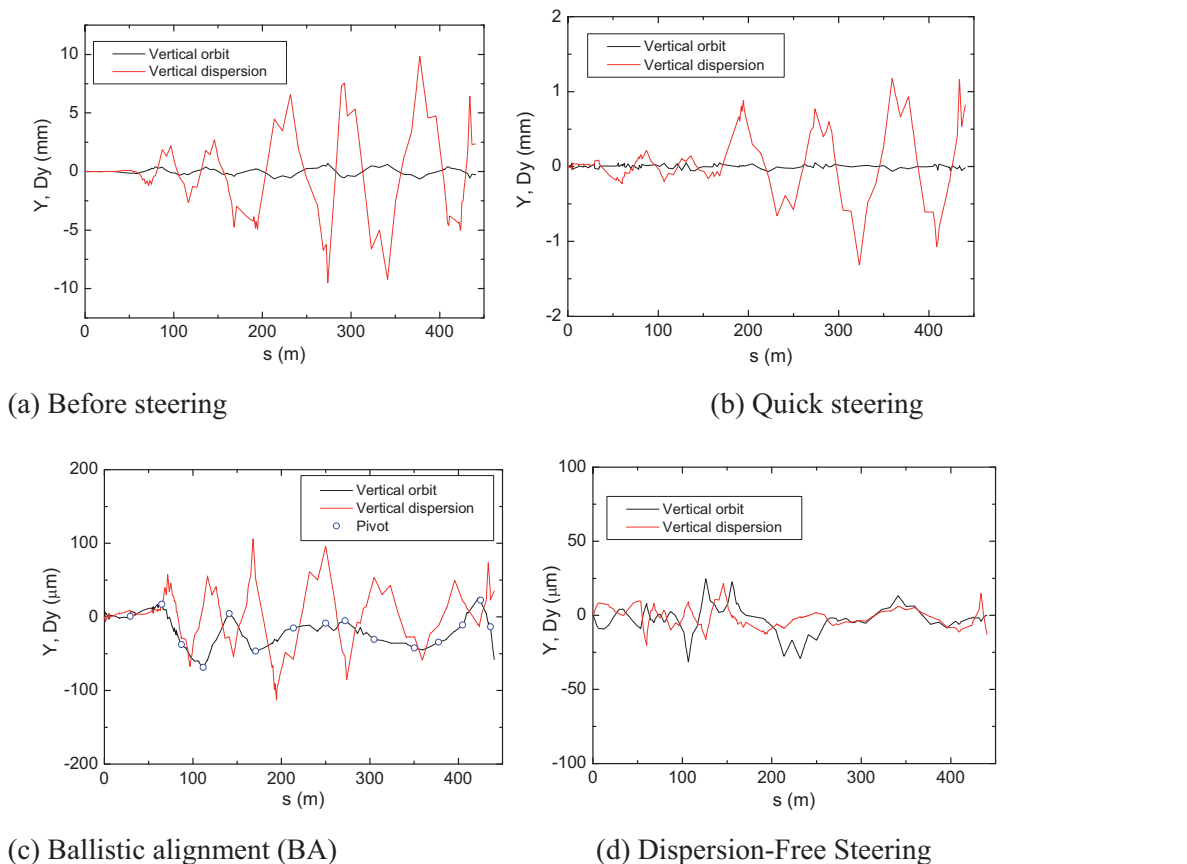


Fig. 5.4.1.2: Typical results for beam steering. Alignment error is introduced by random displacement of quadrupole magnets by $25 \mu\text{m}$ rms.

The beam steering results in Figure 5.4.1.2 were obtained from simulations using a MADX optics model, where the linac RF cavity is modelled with an arbitrary transfer matrix, with the determinant not equal to unity in order to simulate the orbit damping due to acceleration. The Earth's magnetic field, as well as external stray fields and misalignment of accelerating structures, were assumed to be negligible. An initial quadrupole alignment error of $25 \mu\text{m}$ rms and an orbit measurement error of $3 \mu\text{m}$ rms were assumed. In BA, the trajectory is confined to the ballistic orbit with $3 \mu\text{m}$ rms precision. The pivot BPMs are placed every ~ 30 m. In DFS, a dispersion measurement error of $15 \mu\text{m}$ rms is assumed for 20% momentum shift. The corrector strengths are found by SVD-based fit with an eigenvalue cut-off at 0.001 (rejecting 22 small Eigen values out of 111), where the full weighting factor for the dispersion is assumed. The residual orbit and dispersion can be exchanged by tuning the weighting factor.

In addition to these beam steering algorithms, residual dispersion up to $\sim 100 \mu\text{m}$ can be corrected without disturbing the orbit. When a local orbit bump is closed, the dispersion function is also closed, while this is not true if there is a quadrupole magnet inside. Thus it is possible to control dispersion using an orbit bump at the location of quadrupole (a similar technique using an orbit bump over a linac cell is described in [100]). In conclusion, the orbit and dispersion in the linac will stay much larger than the BPMs' resolution of $\sim 3 \mu\text{m}$.

The entire linac is not necessarily aligned to a straight line; that is, a distortion of a few mm in ~ 500 m machine length is acceptable. The orbit is then steered to be a straight line over a short range, but slightly bent over a long range. Additional bending components to follow the distortion result in dispersion of $\sim 100 \mu\text{m}$, which is an acceptable level and even correctable by the orbit bump.

It is worth mentioning that the Earth's magnetic field has a large impact on the beam orbit, especially for the low energy part, and that BA is disturbed because the straightness of the ballistic

orbit is then violated. Also, the beam-based alignment for the elements with relatively large initial alignment position errors becomes difficult, because of the trajectory curvatures with unknown local field intensity. Spurious dispersion due to the Earth's magnetic field is estimated to be a few hundreds of micrometers in the horizontal plane, without shielding, which could be corrected either by the orbit bump or at the expense of a comparable orbit excitation. Unwanted transverse coupling will be introduced due to the horizontal component of the Earth's field, since the machine will be located approximately in a North-South direction. The impact of the coupling to the beam, however, may be not as significant for the case of a nearly cylindrical beam. The tunnel will be shielded by an iron mesh structure and the Earth's field would be attenuated by a factor of ~ 3 . Future studies in the SwissFEL Injector Test Facility will allow specification of the requirements for the shielding.

The undulators should be carefully aligned, based on beam measurements, to achieve a sufficiently short X-ray saturation length. The undulator module is mounted onto a girder, together with alignment quadrupoles at the upstream and downstream ends, as described in Section 3.5.3, and a lattice quadrupole magnet and BPM mounted onto a separated small girder. Beam-based alignment will be carried out as follows:

- 1) Align the lattice quadrupole magnets by moving the girders transversally, to minimize the dispersion.
- 2) Correct the girder pitch and yaw angles such that the electron beam goes through the centre of alignment of the quadrupoles. Iterate 1) and 2).
- 3) Correct the girder rotation, if needed, based on beam coupling measurement.
- 4) Steer the beam to maximize the lasing performance.

Alternatively, a beam finder wire could be used instead of the alignment quadrupole, resulting in comparable beam position resolution. However, an advantage of the alignment quadrupole is avoiding the risk of the wire being damaged or even burned by the electron beam during beam-based alignment.

5.4.2 Transverse trajectory feedback

5.4.2.1 System layout

SwissFEL will have a beam-based transverse trajectory feedback system that allows the implementation of real-time feedback algorithms which calculate the set values for each dipole corrector magnet in the machine, using the position data of all BPMs. Feedback will be based mainly on the BPM and digital signal processing hardware, firmware and embedded software that is being developed by PSI as Swiss in-kind contribution to the European XFEL (E-XFEL) BPM and transverse feedback systems [101]. In contrast to the very long E-XFEL bunch trains of up to ~ 3000 bunches with 200 ns bunch spacing, that allow ultra-fast intra-train corrections with MHz correction rates and sub-microsecond latency, the transverse feedback of the SwissFEL, with its extremely short bunch spacing and train length, will only perform corrections at the bunch train repetition rate of up to 100 Hz, with a corresponding feedback loop latency below 2.5 ms. The data of all BPMs will be distributed via fast multi-gigabit links to a smaller number of interconnected digital signal processing (DSP) boards that calculate the corrector magnet set values and write them to digitally regulated corrector magnet power supplies. These power supplies will be the successor to the PSI in-house design used at the SLS [102], with digital current regulation, negligible noise, and several kHz small-signal bandwidth. Laminated iron magnets with a sufficiently thin (~ 2 mm) stainless steel beam pipe will ensure sufficient corrector bandwidth with negligible eddy current effects. Interfaces of the transverse feedback system to other machine subsystems, such as LLRF or photon BPMs, allow the integration of non-BPM sensors and actuators, where necessary, e.g. in order to determine the beam energy, or to adjust LLRF actuator settings that affect the beam trajectory.

5.4.2.2 Bandwidth considerations

In contrast to storage rings such as the SLS, where fast trajectory feedback allows the correction of random perturbations up to typical cut-off frequencies f_C up to 200 Hz or more, by measuring and correcting the trajectory at rates of many kHz, the SwissFEL BPMs can sample trajectory perturbations only at the bunch train repetition frequency f_{BT} of up to 100 Hz. Therefore the feedback can only damp random perturbations effectively if their frequency is significantly below the cut-off frequency $f_C \sim 0.1 \cdot f_{BT}$. Perturbations above f_C may even be amplified by the feedback loop, which can be prevented by low-pass filters or feedback loop gain reduction. In general, all relevant SwissFEL subsystems, such as girders, magnet power supplies, pumps, beam distribution kickers, etc, should be designed in a way that reduces all such high-frequency perturbations to a level where they do not affect the stability of the lasing process. It should be noted that high-frequency perturbations are downsampled, and therefore the feedback will also be able to damp perturbations that are sufficiently close to an integer multiple N of f_{BT} , e.g. a girder vibration, where the girder eigenmode is $N \cdot f_{BT} + \Delta f$, with $|\Delta f| \ll f_C$.

The stability of the RF system is also vital for transverse beam stability, since, for example, bunch length jitter due to RF phase jitter causes transverse trajectory jitter due to kicks of the last bunch compressor dipole, where the energy loss due to CSR, and thus the bending angle, depends on the bunch length. These kicks tend to dominate the transverse perturbation spectrum in the respective plane for low-charge, short-bunch operation modes [103,104]. Furthermore, a stable higher-harmonic RF system that creates a symmetric transverse charge distribution within each bunch is also vital for trajectory feedback, in order to guarantee that the part of the bunches with the highest density that lases has no significant offset to the centre of charge of the bunch that is measured by the BPMs, and thus used for transverse trajectory feedback in the undulators.

The signal processing system for the transverse trajectory correction will not only allow the implementation of feedback, but (if necessary) also the additional implementation of harmonic suppressor algorithms that can damp a narrow-band trajectory perturbation with reproducible frequency above f_C , if the perturbation amplitude is constant or varying sufficiently slow (e.g. 50 Hz mains noise), for example by using a narrowband filter that cuts out the relevant frequency component from the BPM data and feeds it back to the corrector power supplies with a suitably adjusted phase delay.

5.4.2.3 Algorithm

The feedback will calculate the corrector magnet settings from the BPM data using the singular value decomposition (SVD) method, with the required corrector current change being fed into a controller (e.g. PID) with adjustable gains. The required beam response matrix will be obtained from an optics model that will be optimized by fitting to measured response matrices and optics data. The matrix and its SVD-inverse will be re-calculated and the feedback system reconfigured when required, e.g. when a new optics is loaded or the energy is changed significantly without changing the quadrupole magnet currents in the undulator intersections.

The number of BPMs and correctors to be used by the algorithm can be selected using a high-level application. For initial trajectory correction when the machine is commissioned with 1st beam or switched on after a shutdown, the feedback can include all BPMs and correctors, in order to get the beam through the machine. For standard user operation, the number of BPMs and correctors, as well as the feedback bandwidth, can be adapted to the observed perturbation sources and frequencies, as required for maximal stability of the lasing process. The feedback will also support the multiplication of small SVD eigenvalues with weighting factors, before performing the SVD pseudo-inversion (Tikhonov regularization [104,105]), which allows running a global feedback with different bandwidths for different perturbation patterns (i.e. eigenvectors). By reducing the

bandwidth for perturbation patterns where small BPM readings cause large corrector magnet changes while using a larger bandwidth for other patterns, the impact of BPM noise and optics model imperfections on the trajectory, and thus on the lasing process and photon beam pointing stability, is minimized. The positions of BPMs, correctors and quadrupole magnets will be chosen in a way that minimizes the SVD conditioning number (i.e. the quotient between largest and smallest eigenvalues), maximizes the number of large SVD eigenvalues of the beam response matrix, and results in a mainly tri-diagonal structure of the SVD-inverted response matrix, with minimal off-diagonal values and a resulting maximal robustness of the algorithm with respect to beam optics and energy variations.

6 BUILDING AND INFRASTRUCTURE

6.1 Building layout

The building design and locations presented below correspond to the status as of January 2011, and is subject to modifications until it fulfils all necessary authorizations and machine requirements. With a total length of 713 m and a width ranging from 6 m to 36 m, the SwissFEL facility will be located a few hundred meters south-east of PSI-East (see Figure 6.1.1). This location presents the advantage of having a continuous area (with possibility of future extensions) and homogeneous ground to contain the SwissFEL installation, in contrast to the PSI-West area, which would be cut by a small river and limited in size. The east side of PSI has also shown the lowest level of ground vibration [106].

The foreseen location is situated in the forest, near the east entrance of the PSI. The building will follow an existing valley in order to have an optimal integration into the environment. Figure 6.1.1 (top) shows, in blue/green, the buildings half-covered by earth, and in gray the buildings under the natural ground level, as planned for 2016. The area coloured yellow / orange corresponds to the new access road and loading zone which need to be built.

Access to the facility is ensured via a road alongside the building. The Beam Tunnel and the Undulator area situated on the ground floor are accessible through escape stairs and via a loading zone equipped with a crane for large equipment installation (Figure 6.1.1). The electron beam is flowing from south to north.

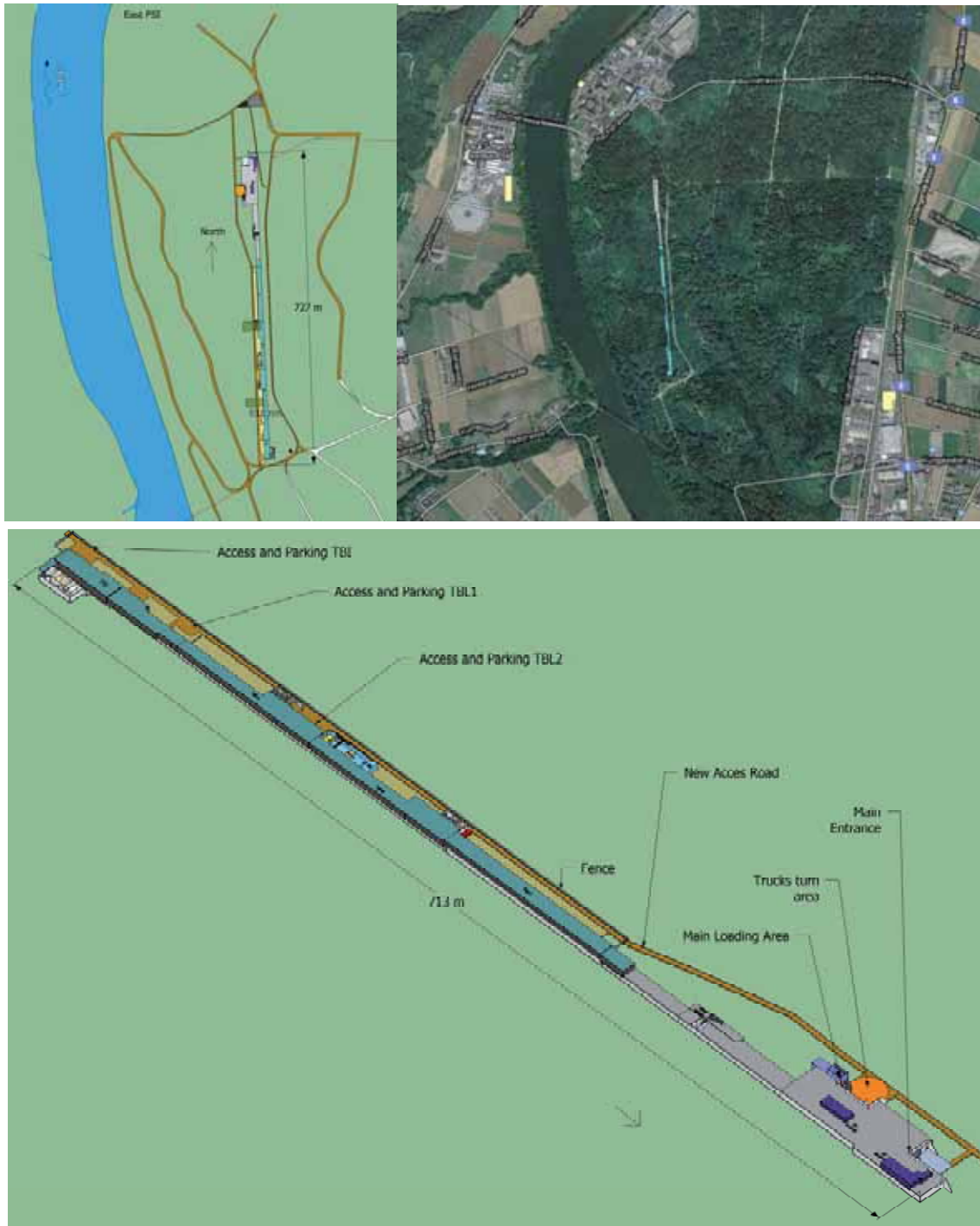


Fig. 6.1.1: Foreseen location for SwissFEL (Top: map; Bottom: aerial view with main access points).

Figure 6.1.2 (bottom) shows a 3D view of the building in its natural surroundings, with the lower floor completely under the natural level of the soil. The upper floor is completely covered with soil on one side, to minimize its visual impact on the environment. Two sections of the building are entirely covered with soil, to allow animals to cross the building. The SwissFEL building is cut longitudinally in sections or sub-buildings having almost independent infrastructures. The names of the different building sections is depicted in Figure 6.1.2 (top).

The different building names correspond to specific parts of the electron beam line:

- TBI (Technical Building Injector): details in Fig. 6.1.3
- TBL1 (Technical Building Linac 1): details in Fig. 6.1.4
- TBL2 (Technical Building Linac 2): details in Fig. 6.1.5
- TBL3 (Technical Building Linac 3): details in Fig. 6.1.6
- TBU1 (Technical Building Undulator 1): details in Fig. 6.1.7
- TBU2 (Technical Building Undulator 2): details in Fig. 6.1.8
- EH (Experimental Hall): details in Fig. 6.1.9

The electron beam accelerator sections (TBI to TBL3) have double-deck architecture (Figure 6.1.2 - top) with the RF accelerating structures being in the lower floor with an as short as possible connection to the RF power plant situated just above in the top floor. For convenience, the lower floor, which contains the electron beam line, is called the Beam Tunnel. The upper level, where all the necessary accelerator supplies (RF klystrons, control systems, etc) are installed is called the Infrastructure Gallery. Downstream of Linac 3, only the lower floor remains and contains the Aramis undulator section and the two experimental areas (Athos and Aramis experimental halls). The electrical infrastructure, cooling stations and air conditioning units are distributed in the Infrastructure Gallery (upper level of TBI to TBL3) and within TBU1, TBU2 and EH.

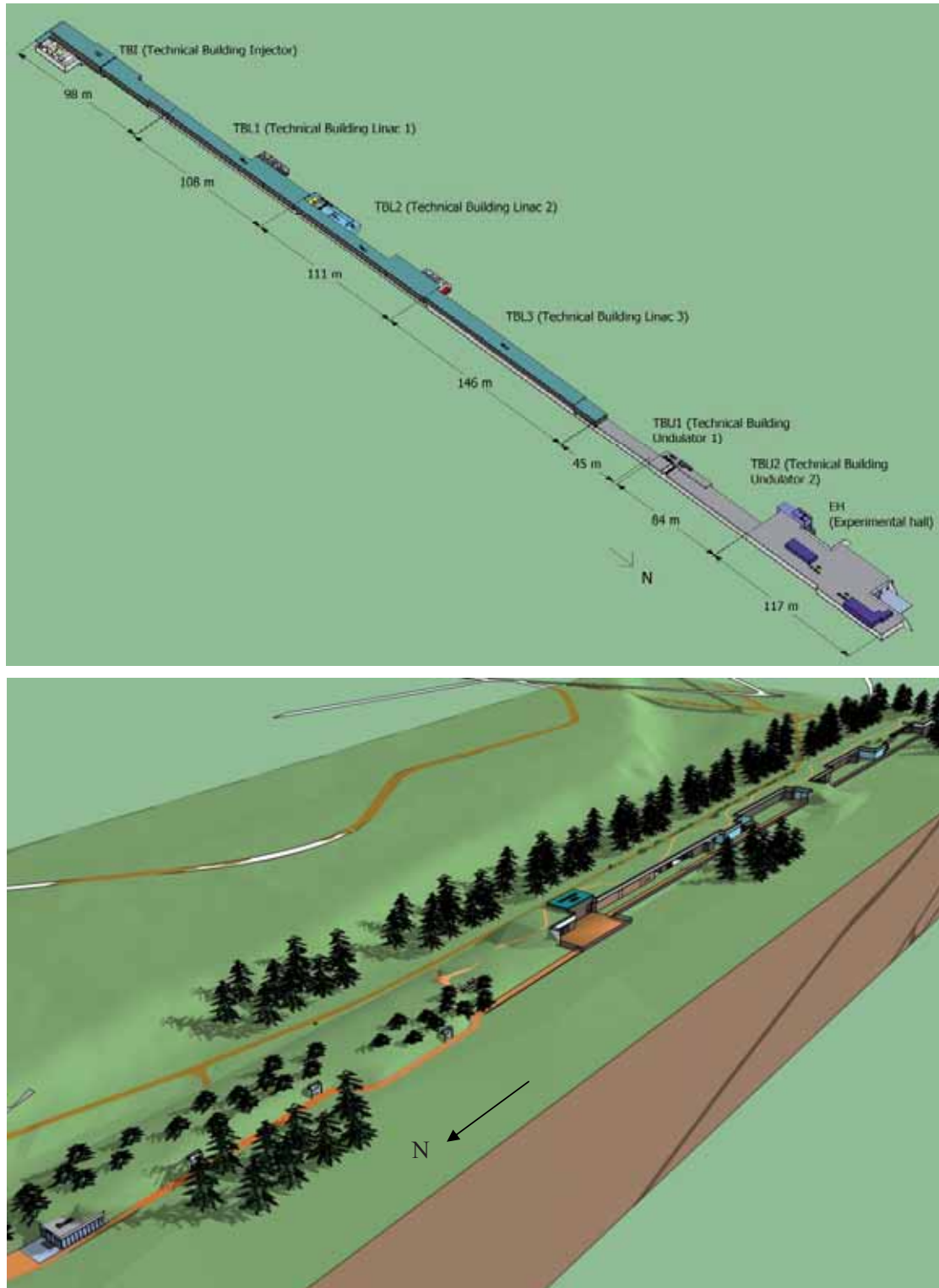


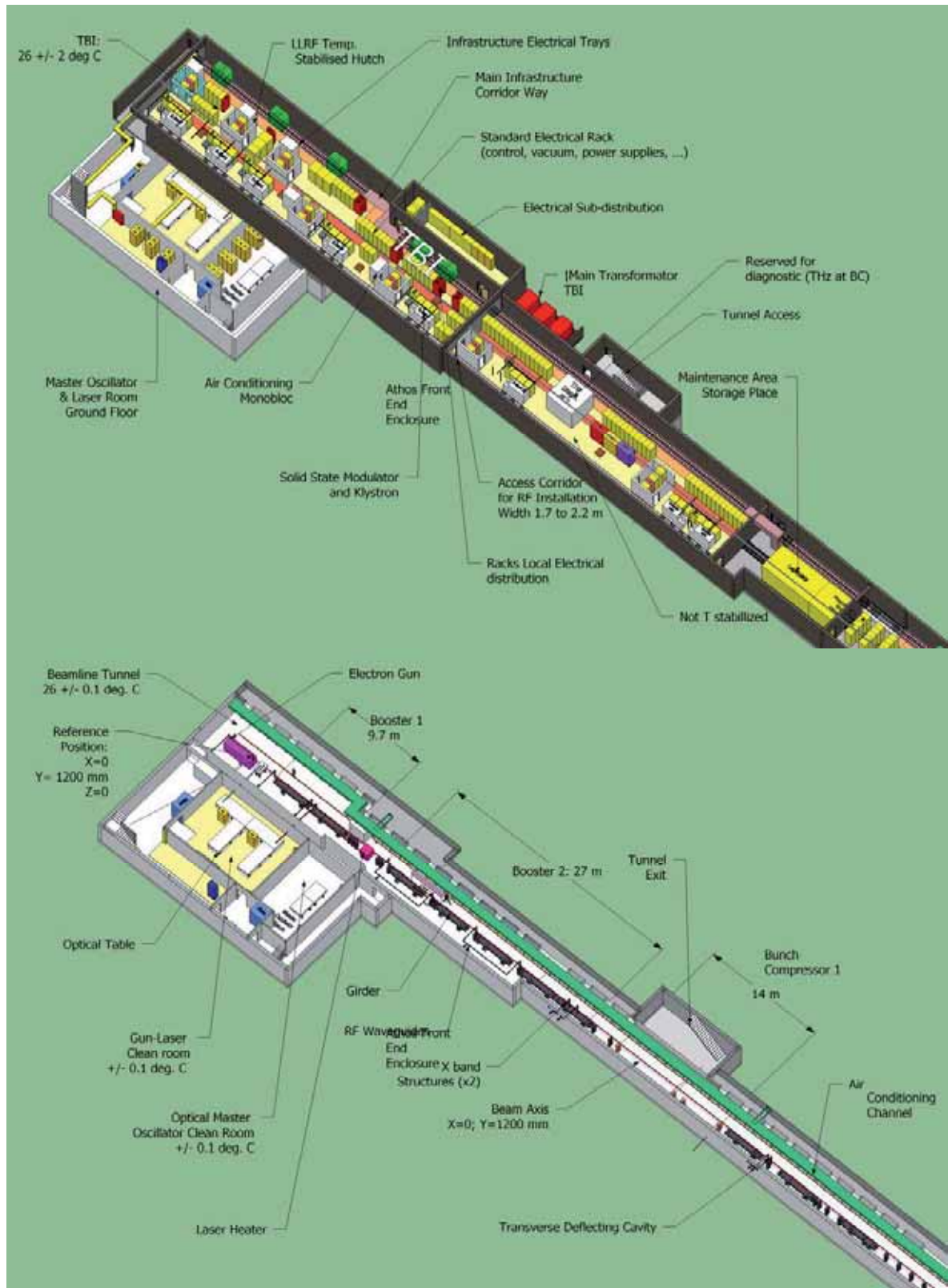
Fig. 6.1.2: SwissFEL building seen from the experimental area entrance, without (top) and with the natural surrounding land (bottom, status July 2010).

Table 6.1.1: Inside dimensions of the main sections in the SwissFEL building. A represents the inner surface and V_i the inside volume. The height corresponds to the outside height of the different building sections (status at December 2009).

| Level | Location Name | Location Description | A [m ²] | Height [m] | V_i [m ³] |
|-------|---------------|-----------------------|---------------------|------------|-------------------------|
| Upper | TBI | Injector upper level | 863 | 3.50 | 3'020. |
| | | Cooling Station 1 | 158 | 4.00 | 632. |
| | TBL1 | Linac 1 - upper level | 777 | 3.50 | 2'719 |
| | | Cooling Station 2 | 158 | 4.00 | 632 |
| | TBL2 | Linac 2 - upper level | 615 | 3.50 | 2'152 |
| | | Cooling Station 3 | 195 | 4.00 | 780 |
| | TBL3 | Linac 3 - upper level | 1'262 | 3.50 | 4'417 |
| Lower | TBI_SK | Injector underground | 454 | 3.20 | 1'452 |
| | TBL1_SK | Beam Tunnel Linac 1 | 464 | 3.20 | 1'484 |
| | TBL2_SK | Beam Tunnel Linac 2 | 499 | 3.20 | 1'596 |
| | TBL3_SK | Beam Tunnel Linac 3 | 999 | 3.20 | 3'196 |
| | UH1&UH2 | Undulator hall | 1'386 | 3.20 | 4'435 |
| | EH_AT_AR | Experimental hall | 1'619 | 4.60 | 7'447 |
| | | Total | 9'449 | | 33'967 |

More details on the dimensions of the different SwissFEL sections are depicted in Figure 6.1.2 (Top). The injector starts at the electron gun and finishes downstream of Bunch Compressor BC1. Linacs 1, 2 and 3 represent the total length of the C-band accelerator sections. The spaces between the linacs are filled with diagnostics, BC2 and matching optics. The space between Linac 3 and the Aramis undulator is also foreseen for the collimator and electron beam matching optics. Details of the length of the different accelerator components can be found in chapters 2 and 3.

Table 6.1.1 summarized the surface, inner volume and height of the different building areas. The facility has been optimized for minimum volume and has a total inner surface of 10,000 m² on two levels, with a total inner volume of 34,000 m³.



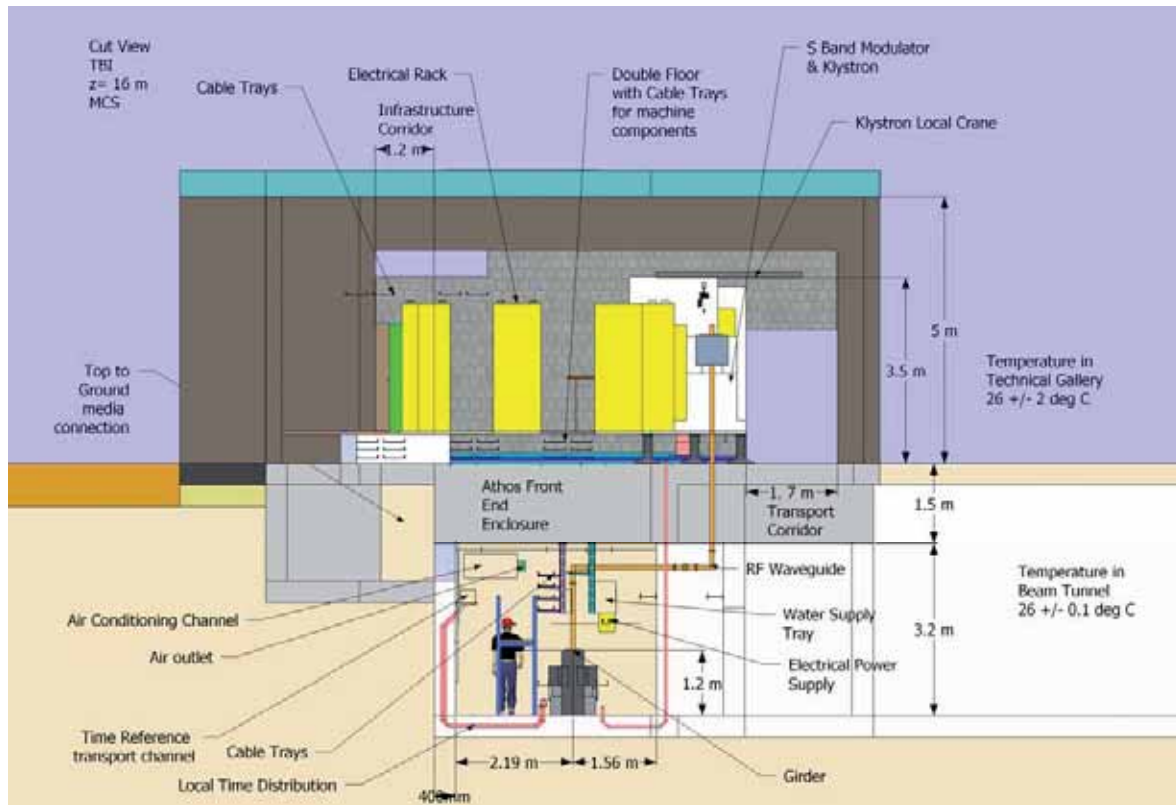


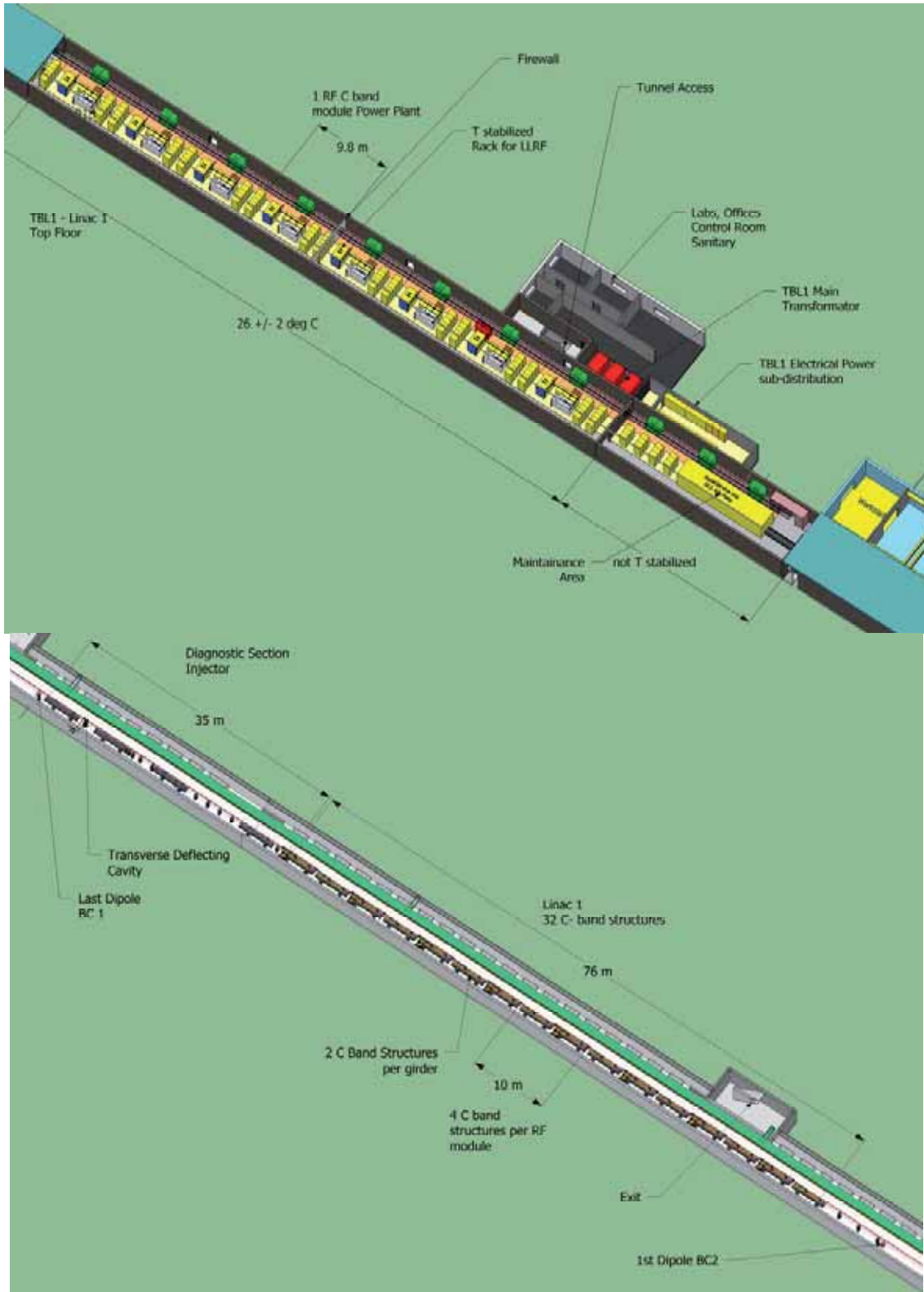
Fig. 6.1.3: Three views of TBI (Technical Building Injector); the infrastructure gallery in the upper floor (Top image), the beam tunnel with the electron gun (middle image) and a cut view showing the double floor building (bottom picture).

The injector components (gun, booster 1, 2 and bunch compressor 1) are installed in the ground floor tunnel at 2.19 m from the west wall side (Fig. 6.1.3). The beam tunnel in TBI, TBL1 and TBL2 has an inside width of 3.75 m and an inside height of 3.2 m. The electron beam axis height is 1.2 m.

Most of the necessary connections (power, control, water) to beamline component are coming from cable / water trays attached to the roof. The time reference signal, because of his sensitivity, is however on a separate support attached to the wall. The RF power plants are sitting upstairs in the upper floor above the accelerating structures to minimize waveguide length.

In the top floor of TBI, a 1.7 to 2.2 m wide way is reserved along the east wall for transport of large RF components. On the opposite wall (west wall), a 1.2 m wide corridor is reserved for building infrastructure components.

The electrical racks (about 400 in total) are all sitting on a 55 cm high double floor filled with cable trays to connect racks to machine components (magnets, diagnostics, ...). The connection from top floor to tunnel is insured via large access channel (Top to ground media connection – 0.8 m wide) along the west wall.



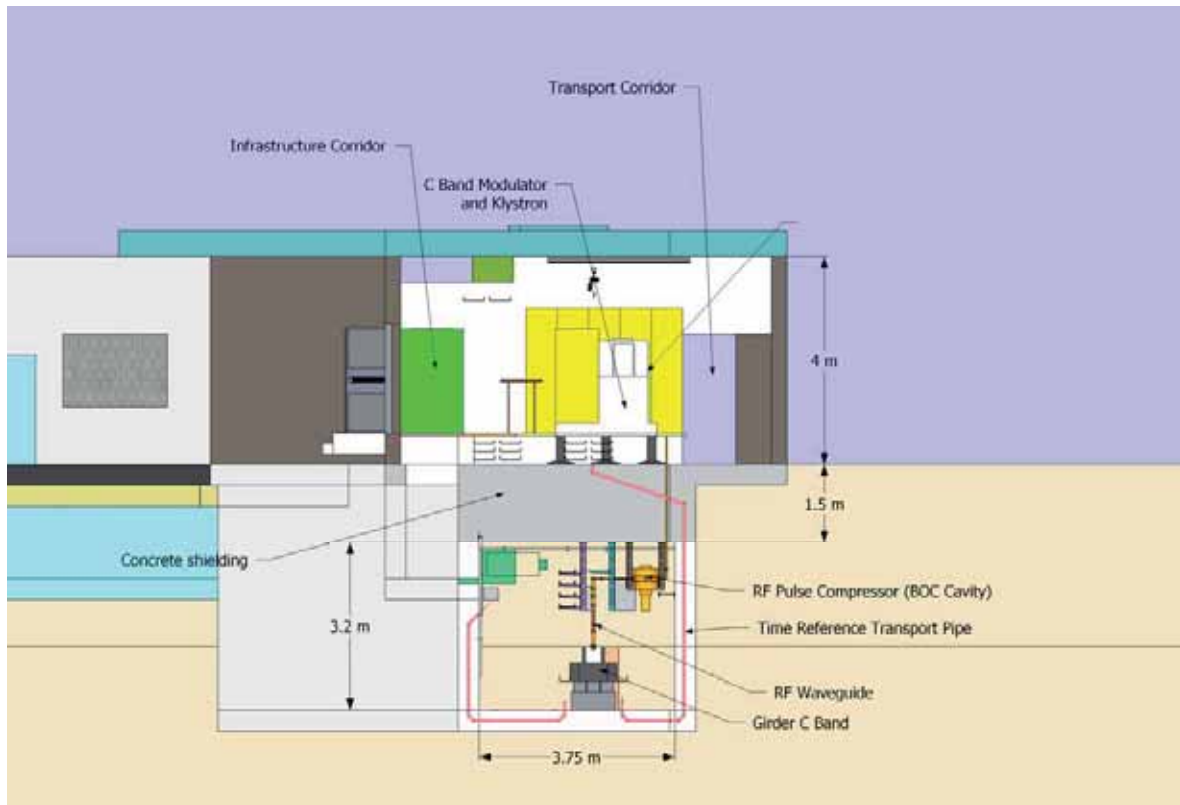
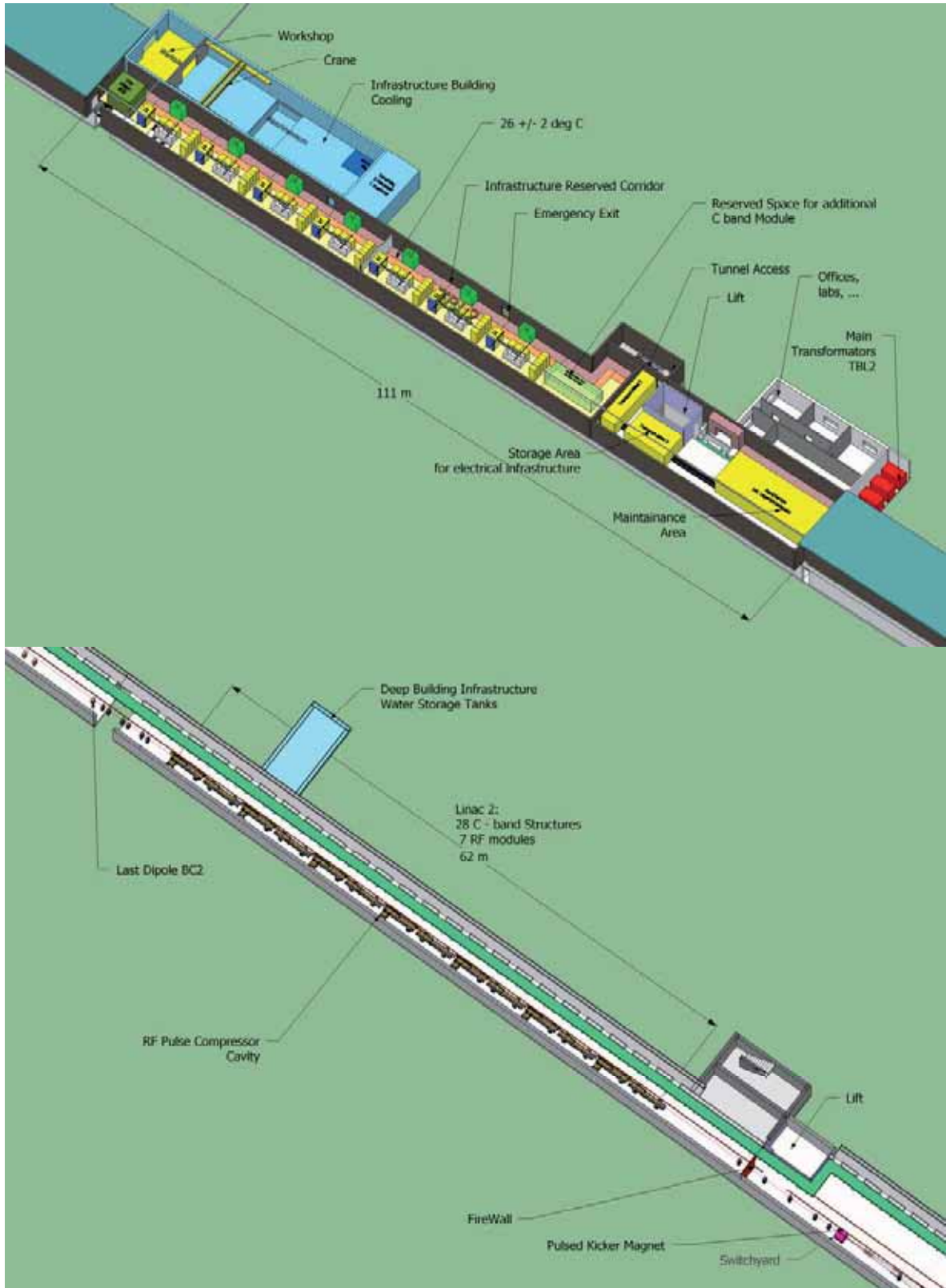


Fig 6.1.4: TBL1 (Technical Building – Linac 1) first floor with the infrastructure gallery (Top) and ground floor with electron beamline components (middle) and cut view (bottom)

The linac 1 and the bunch compressor 2 are installed in the beam tunnel of TBL1 (Fig 6.1.4). SwissFEL linacs consist in a succession of RF modules of 10 m length (4 C band structures sitting on 2 girders) and connected to one Klystron / modulator unit. One stairs access to the beam tunnel is located on the side of TBL1.

The Beam Tunnel (Figures 6.1.4) is shielded from above by a 1.5 m-thick concrete roof. The thickness of the Beam Tunnel walls and ground plate is planned to be 40 cm. This thick roof shielding allows full access to the Infrastructure Gallery during operation time.



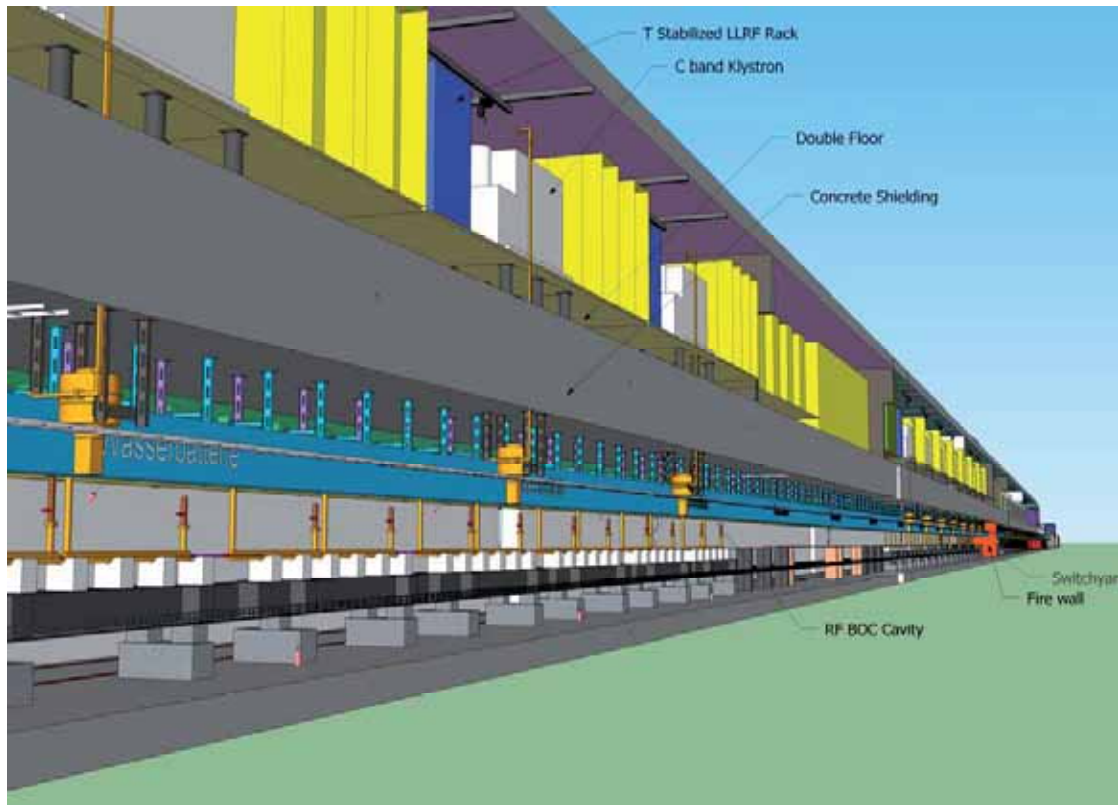


Fig. 6.1.5: TBL2 (Technical Building Linac 2) which includes a lift and stairs access to the tunnel. Top: Upper level TBL2; Middle: Lower level TBL2; Bottom: Vertical cut along the building.

Besides the RF Infrastructure Gallery of TBL2 top floor (similar to TBL1 RF gallery), an annex building (blue coloured in Fig. 6.1.5) will contain the main water pump station which will provide water to the entire building. The water is pumped in the ground and rejected in the Aare river after having cooled the electron beam components.

Downstream TBL2 the beam tunnel becomes wider (from 3.75 m to 6.9 m inside width) since the beamline is splitted into two lines 3.73 m apart.

Emergency exit doors are present every 100 m in the upper floors of TBI to TBL3.

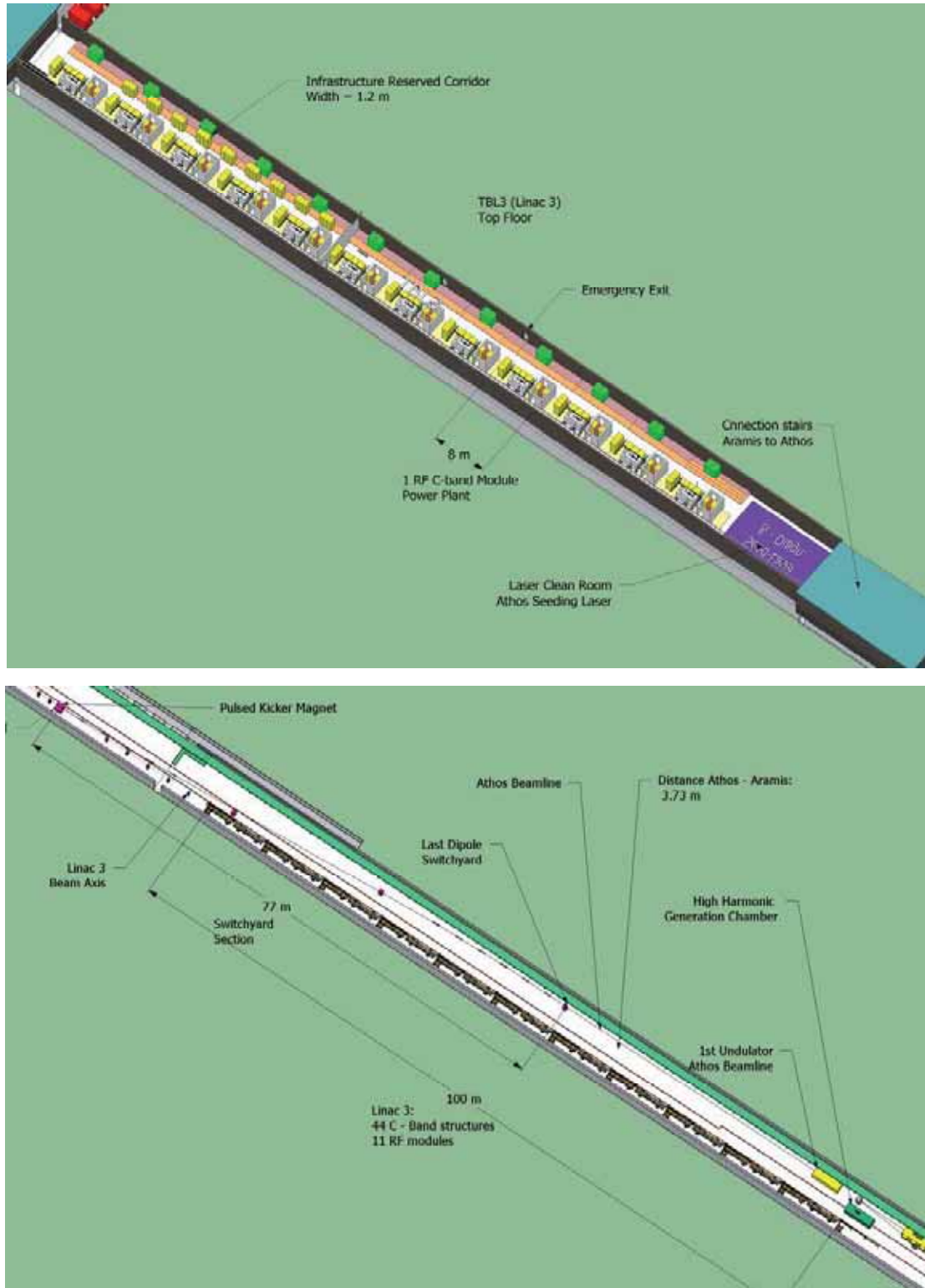


Fig. 6.1.6: TBL3 (Technical Building Linac 3): Linac 3 towards Aramis and Switchyard towards Athos beamline. Top: Upper level TBL3; Bottom: Lower level TBL3

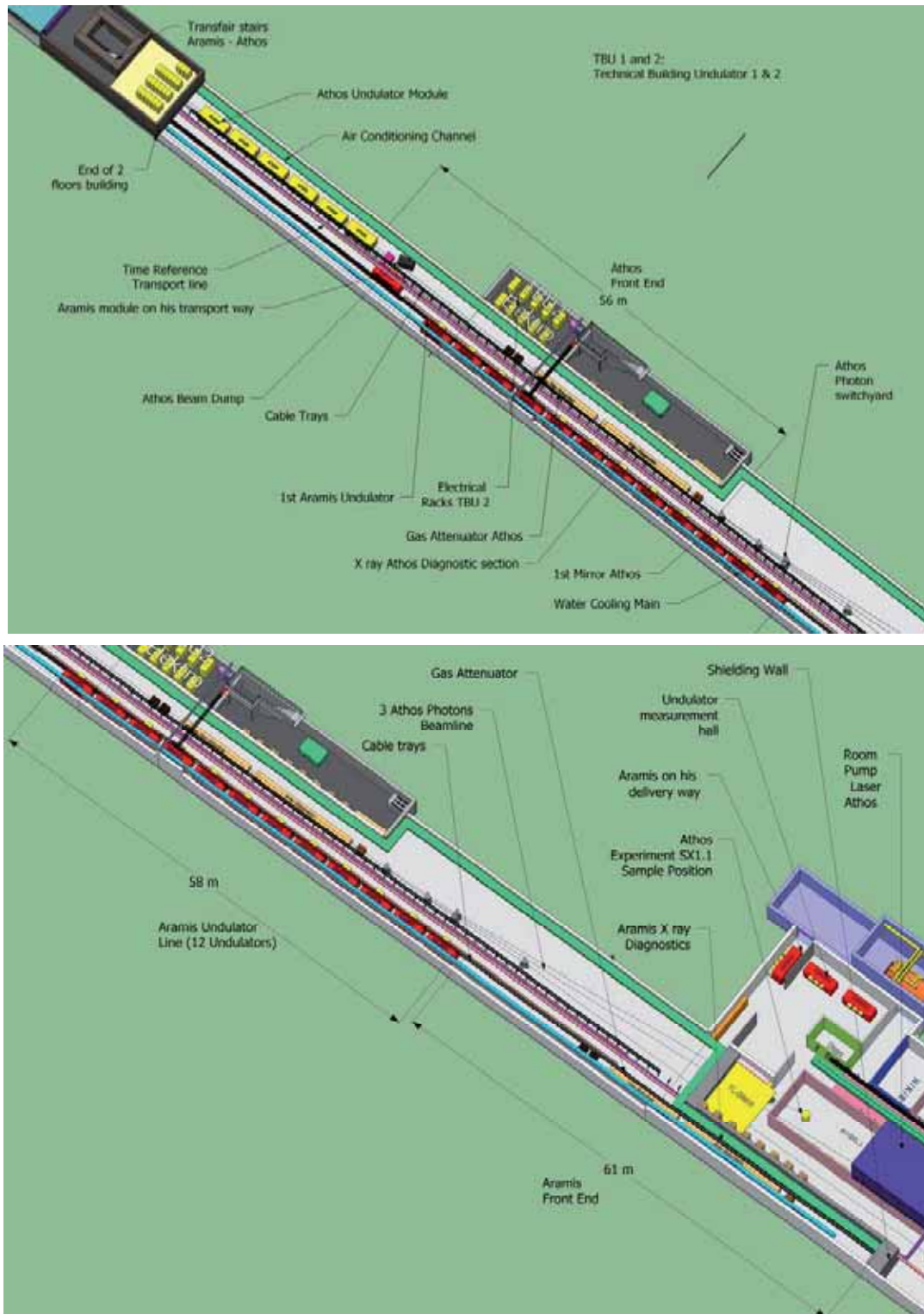


Fig. 6.1.7: TBU1 & 2 (Technical Building Undulator 1 and 2): Athos undulators are in yellow, Aramis undulators are in red. Top: TBU1 and part of TBU2; Bottom: TBU2 and part of EH.

Downstream TBL3, there is no more electron acceleration structures so that TBU1, TBU2 and EH are single floor buildings (at the same level than the Beam Tunnel).

TBU1 and 2 are single floor buildings, except for the transfer stairs: Athos to Aramis. EH do also have two rooms on a second floor (Pump Laser rooms, see Chapter 4 for details).

The Athos beam dump is installed a few meters before the first Aramis undulator. The Athos Front End (between Athos last undulator and the shielding wall of the Experimental Hall (EH)) is about 100 m long. In the front end, switching mirrors are installed which distribute photons to the 3 possible Athos experimental hutches (SX1 to SX3).

The 12 undulators of Aramis (red coloured in Fig. 6.1.7) cover a total length of 58 m, parallel to the Athos front end. The Aramis Front End Enclosure (see Chapter 4) is then about 60 m long. The EH (Experimental Hall) building is separated from the TBU buildings by a 2 m thick shielding wall to protect users from electron induced radiations.

Delivery and transport of the Aramis undulators (25 Tonnes) will be done from the Experimental Hall loading zone on air cushion (Fig. 6.1.7).

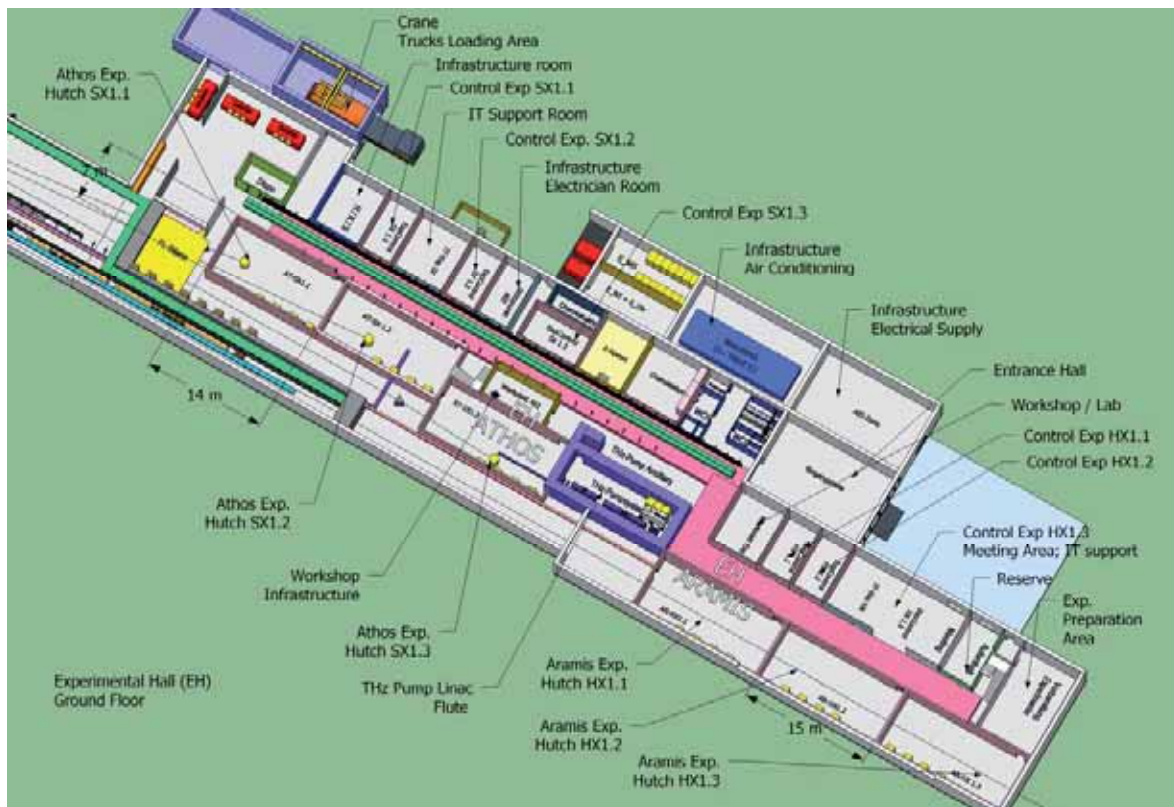


Fig. 6.1.8: Experimental Hall (EH) building layout.

The building has a simple architecture, with priority given to the functionality and respect to the environment (Figures 6.1.2). The maximum electrical consumption of the accelerator, undulator and experimental areas is estimated to be about 5.3 MW (4.7 MW for SwissFEL components and 0.6 MW for infrastructure components). The electrical energy will be transported at high voltage from PSI West to local transformers (see red boxes in Fig. 6.1.4), which will distribute electricity to sub-dividers and then to the different devices (RF modules, magnets power supplies, etc). About 440 standard electrical cabinets (racks) are foreseen, to contain all the necessary devices for low-level rf, magnets power supplies, vacuum, diagnostics and control devices. These racks will cover a large part of the infrastructure gallery surface, the rest of the space being used for rf-modulator/klystron assembly and for transport. The required cooling capacity will be of the same magnitude as the electrical consumption and will to 80 - 90 % be covered by water cooling. Ground water will be used for cooling through local heat exchangers. The rest of the heat will be dissipated to the atmosphere through an air conditioning system, which should maintain the temperature in the Beam

Tunnel to within $26 \pm 0.1^\circ\text{C}$, and within $26 \pm 2^\circ\text{C}$ in the other buildings. During shutdown, temperature stability will be ensured via connection to the distributed heating system REFUNA. Usage of the heat produced is not efficient, because of the low working temperature. Heat-up with excess heat from the PSI site will be tested. A detailed functional layout schematic of the SwissFEL infrastructure can be found in Appendix 4.1.

The foreseen safety rules for personnel and the environment will fulfil the strict Swiss regulations and are described in the following section.

6.2 Safety issues

6.2.1 Radiation protection

6.2.1.1 Radiation protection

The operation of the SwissFEL facility is subject to Swiss legislation, in particular to the radiation protection law (Strahlenschutzgesetz, SR 814.50) and related paragraphs. Also relevant are legal guidelines (among others, the "Richtlinie für den überwachten Bereich der Kernanlagen und des Paul Scherrer Institutes", HSK-R-07/d), as well as PSI internal directives. In this section will be summarized the preliminary radiological studies performed according to the present design phase of the SwissFEL facility and the beam tunnel, as well as the preliminary classification of the building and other supervised regions. For references and detailed descriptions, refer to PSI note FEL-FU96-008.

Direct radiation outside the supervised SwissFEL above ground building complex

According to the present design phase, the SwissFEL above ground building is half covered with at least 1 m of earth. This building and the forecourts have to be fenced against unauthorized access, independent of an Aare sinister or dexter realization. The limitations for the controlled emission of radioactivity (by the air- and water path) as well as the surveillance of radioactivity and direct radiation in the PSI-environment are defined in the "REGLEMENT" BAG 5.07.01-4, HSK 2/370 Rev.1 (2007).

The direct radiation outside the fenced area, may not lead to an individual dose above 0.1 mSv/year. Thereby the duration of stay has to be accounted for and furthermore Art. 102 StSV has to be considered. That is to say, the direct radiation outside the fenced area may not lead to an annual ambient equivalent dose overstepping 1 mSv in living- resting- or working rooms and 5 mSv in other regions. It can reasonably be assumed, that during a year no one may rest near the fence for more than 10 % of the time. Thus the tolerated annual ambient dose equivalent is 1 mSv. The monitoring will be done with at PSI commonly used "Arealdosimeters", adequately positioned.

Prevention, contingency

If an overstepping of the limits is happening due to some unexpected reasons several actions can be considered:

- Reduction of operation time (occupancy factor)
- Installation of additional local shielding
- Reduction of beam intensity

in such a way to reduce the ambient dose equivalent below the legal limits.

6.2.1.2 Incidents

The SwissFEL beamline will be equipped with a machine protection system (MPS). Besides machine-relevant parameters, the radiation background at the critical points will also be monitored by the MPS. In this way, a possible technical problem will lead to immediate shutdown of the electron beam (switch off of electron source or RF components for example) by the MPS. It cannot be excluded that the beam may be deflected towards the shielding for a certain MPS delay time;

nevertheless, the resulting temporary ambient equivalent dose rate outside the beamline bunker has to remain within legal limits (see Table 6.2.1.1).

6.2.1.3 SwissFEL Shielding

The operation of the SwissFEL accelerator complex inevitably gives rise of unwanted radiation fields. Unwanted beam misalignment, as well as necessary actions like beam cleaning by collimators, beam monitoring (screens) or finally the dumping of the electron beam result in beam loss and the generation of potentially harmful secondary radiation. The accelerator bunker will not be accessibly during operation unlike the technical galleries or laboratories for example. The installation of well designed shielding is a necessity to ensure safe operation, according to the Switzerland radiation protection legislation.

The radiation field resulting from beam losses at a high energy electron accelerator is fairly complex. The cascade like process, initiated by the interaction of an incoming electron with matter, results into a various physical processes. The five major electron radiation loss components are described briefly:

- Giant-Resonance-Neutrons (GRN): Those neutrons with energy range between 0.1 MeV and 20 MeV are photo-produced in the core of the shower. The emitted spectrum shows a peak at about 1 MeV with an average of about 2 MeV. The production threshold energy is about 4 MeV for heavy nuclide and about 12 MeV for the light one.
- High-Energy-Neutrons (HEN): Neutrons with energy above 100 MeV are initiated by high energy photons in the hadronic cascade. The production angle is in the forward direction. This radiation component dominates shielding calculations.
- Mid-Energy-Neutrons (MID): Neutrons having energies between GRN and HEN, being produced by quasi-deuteron reactions at energies above 25 MeV. The neutron energy lies between 20 MeV and 100 MeV, peaked in forward direction.
- Direct Bremsstrahlung (GAMD): Photons leaving the core with energies between 0.1 MeV and 20 MeV. In the presence of a nuclear field, these photons may go on to produce electron – positron pairs driving on an electromagnetic shower. The distribution is a slow decreasing function from 0° to 180°, superimposed to a more intense forward core between 0° and 5°.
- Indirect Gamma (GAMI): Photons and directly ionizing particles created during slowing down of the HEN. The dose rate contribution is about 25 % of the one from neutrons.

The application of Monte Carlo methods is a commonly used method for calculation of radiation fields caused by particle interaction in various materials and geometries. The interaction of electrons with matter results in an electromagnetic cascade generating a large number of secondaries. Therefore Monte Carlo based evaluations are very time consuming, even with the use of highly sophisticated computers.

Keeping in mind that the design phase of such a complex machine like SwissFEL appears to be iterative, the use of analytical methods to get a first estimate is a quite good and reasonable first step approach. The shielding analyses described here have been performed with the SHIELD 11 code [1]. It has been developed at Stanford Linear Accelerator Centre (SLAC) to perform shielding analyses in the vicinity of a high energy electron accelerator. It uses analytical expressions for the production and attenuation of neutrons and photons from electron beam loss at “thick targets” such as beam dumps or collimators.

Having calculated the overall shielding dimensions and identified the critical points, detailed studies can be started. For this purpose, general purpose Monte Carlo codes like FLUKA [2] are proved to be well suited and commonly used. More detailed predictions on the activation of components, secondary particle fluxes and hot spots based on a detailed geometric description can be made. The gained information can then be translated into optimized shielding design and entry maze, as well as decommissioning plans, with improved efficiency and possible financial gain.

Table 6.2.1.1: Limits for ambient dose rate for different type of zone classification

| Type | Value | Area Type / Location Description |
|-------------------------|---|--|
| Inside controlled zone | | |
| | < 1 $\mu\text{Sv/h}$ | Local control room, permanent workplace |
| | < 10 $\mu\text{Sv/h}$ | Area Type V, experimental area (such as SLS beamlines) |
| | < 25 $\mu\text{Sv/h}$ | Gallery, areaway, temporary workplace (within Type W, without beam) |
| | < 100 $\mu\text{Sv/h}$ | Temporary workplace at beam conditioning (within Type W, without beam) |
| | <ul style="list-style-type: none"> • > 1 mSv/h < 10 mSv/h • > 10 mSv/h | Area Type Y Area Types X and Y both prohibited during operation, secured by personal safety system (PSYS) |
| Outside controlled zone | | |
| | < 0.12 $\mu\text{Sv/h}$, (20 $\mu\text{Sv/w}$) | Permanent workplace, office, laser laboratory |
| | < 0.6 $\mu\text{Sv/h}$, (100 $\mu\text{Sv/w}$) | Outside building, non-permanent stay |

Table 6.2.1.2: Zone definitions for the different areas of SwissFEL

| Building name | Zone Type | Area Type | Dose Limit | Remark |
|---|-----------|---|---|---|
| TBI to TBL3 Upper level | 0 | W | 10 $\mu\text{Sv/h}$ < Dose < 100 $\mu\text{Sv/h}$ | Restricted presence according to operation regulation. Duration of stay has to be controlled. |
| | | V | < 10 $\mu\text{Sv/h}$ | (1) Workplace inside controlled area |
| Gun Laser Room | 0 | V | < 10 $\mu\text{Sv/h}$ | Experimental Area – Compliance to Class IV Laser Area (Badge, Signs, Glasses), see (1) |
| TBI to TBL2 – Lower Level | 0 | Prohibited Area during Operation secured by PSA (Remote Personal Safety System) | | |
| TBL3 to TBU2 – Lower level | 1 | Prohibited Area during Operation secured by PSA (Remote Personal Safety System) | | |
| EH (not in hutches) | 0 | V | < 10 $\mu\text{Sv/h}$ | See (1) |
| EH – Hutches without radioactive probes | 0 | V | < 10 $\mu\text{Sv/h}$ | Limited Access by LAC (Local Access Control), see (1) |
| EH – Hutches with radioactive probes | 1 | V | < 10 $\mu\text{Sv/h}$ | Limited Access by LAC (Local Access Control), see (1) |
| Outside on the West side within fence | No | - | < 0.1 mSv/week | PSI domain outside controlled area, non permanent stay |
| Roof and east side of building | No | - | < 1 mSv/year | Outside PSI domain, public access possible. Maximum of 10 % abidance assumed. |

PSI basic rule: according to the bid of optimization (StSG, art. 6) and justification (StSG, art. 5) optimized radiation shielding design should result in a 10 % exhaustion of the limits valid for the controlled areas.

The losses due to missteering effects are assumed to be in the 0.1% level of the full beam charge, whereas the total losses are strongly dominated by the dark current. The measurements for the evaluation of the dark current generated in the S-, respectively C-band accelerator structures of the SwissFEL Teststand are still in progress.

The preliminary shielding calculations are based on the design data “on crest” or, more precisely, on an acceleration voltage of 30 MV/m for the electron bunches. A security factor of 1 was applied

for the first estimate. In Table 6.2.1.3, a summary of the main sources of electrons and loss points is given in terms of: lost charge (pC), electron beam energy (GeV) at a given loss point, and resulting lost power (W).

Table 6.2.1.3: Summary of the SwissFEL electron charge losses:

| source: | Electron sources: [pC] | Position of loss: | Energy [GeV] | Cumulated lost electrons power [W] | Type of electrons losses : |
|----------------------|------------------------|-----------------------------|---------------------|------------------------------------|--|
| Electron Gun | 100 | | | | Photoemission |
| Booster (S-Band 1-2) | 3.33 | | | | Dark current (DC) |
| | 12 | Laser heater | 0.15 | 0.23 | |
| Booster (S-Band 3-6) | 6.67 | | | | |
| | | BC1 | 0.45 | 0.45 | Dark current (DC) from PEG is transferred, DC from Booster (3-6) |
| LINAC1 | 10 | | | | |
| | | BC2 | 2.1 – 0.45 | 1.65 | DC from PEG is transferred, DC from LINAC1 |
| LINAC2 | 10 | | | | |
| | | Switchyard | 3.4 – 2.1 | 1.3 | DC from PEG is transferred, 50 % DC from LINAC2 |
| | | KI-Transfer ATHOS | 4.0 | 20.0 | 50 % DC from PEG |
| LINAC3 | 10 | | | | |
| | | KI-LINAC3 | 6.88 / (6.88 – 2.1) | 34.5 + 2.4 = 36.9 | 50 % DC from PEG and LINAC2 each. KI-LINAC3 is segmented, 12 elements over a length of 100 m => 0.4 W/m line source |
| | | KI-Transfer ARAMIS (Dogleg) | (6.88 – 3.4) | 3.5 | 100 % DC from LINAC3 |
| | | KI-LINAC3 | 6.88 / (6.88 – 2.1) | 68.8 + 4.8 = 73.6 | 100 % DC from PEG and LINAC2 each KI-LINAC3 is segmented, 12 elements over a length of 100 m => 0.74 W/m line source(*) |
| | | KI-Transfer ARAMIS (Dogleg) | (6.88 – 3.4) | 3.5 | 100 % DC from LINAC3 |

(*) Only valid if the whole electron beam is guided into the ARAMIS beamline, that is to say the switchyard is not in operation.

6.2.1.4 Dose rate estimates at main beam losses positions

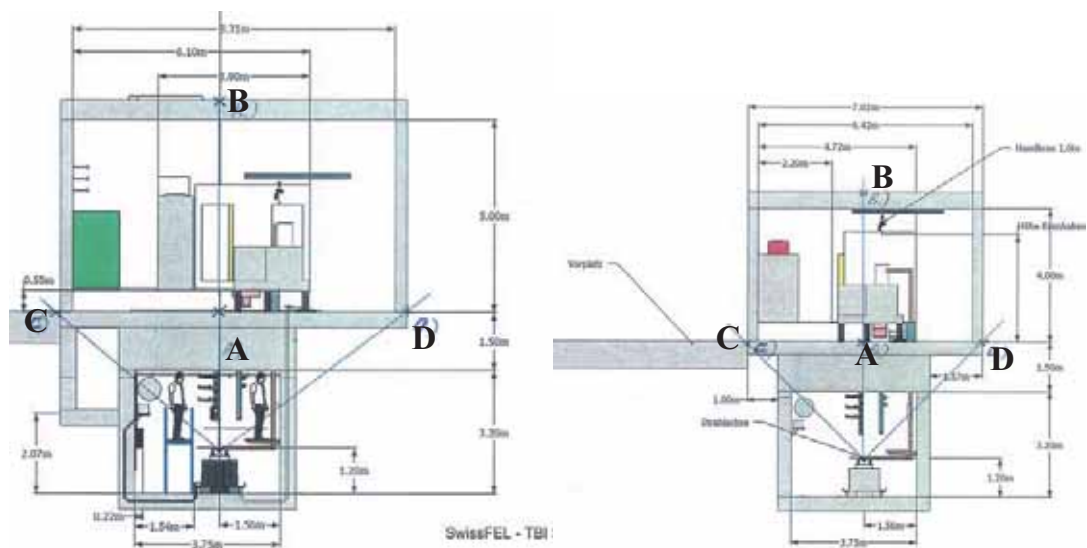
The calculations presented here (Table 6.2.1.4) are based on a shielding thickness of 0.4 m for the ground plate and side walls of the Beam Tunnel, and 1.5 m for the Beam Tunnel seal. In addition, 1 m of soil covers the top of the Infrastructure Building, so that the area above the SwissFEL building becomes a non-controlled zone.

The ambient dose equivalent has been calculated for 3 transverse positions (Figure 6.2.1.1), in seven different regions along the Beam Tunnel, namely at BC1 (Ee=0.45 GeV, beam loss: 0.45 W),

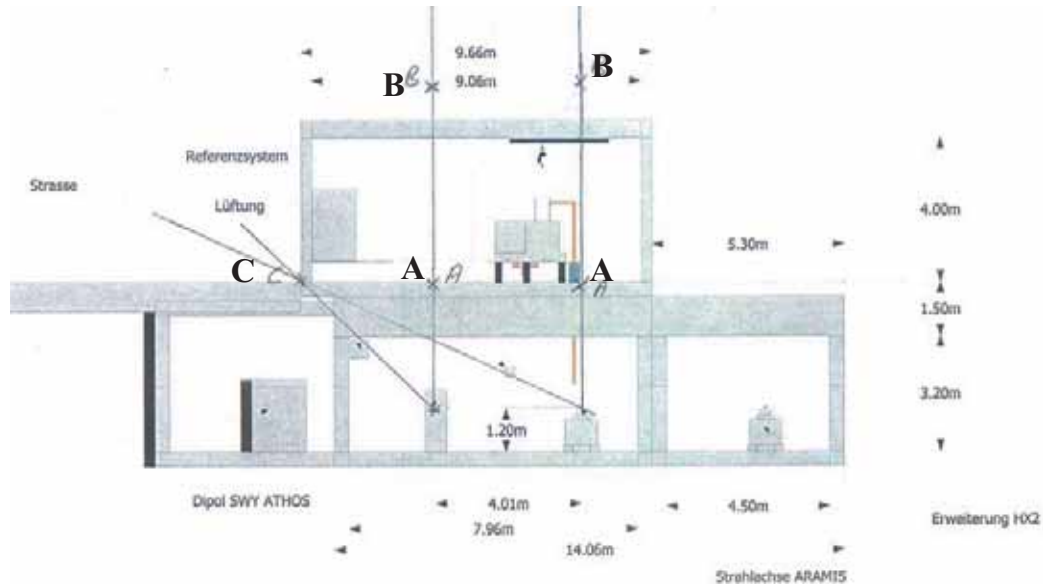
BC2 (Ee=0.45 - 2.1 GeV, beam loss: 1.65 W), switchyard (ejection ATHOS, Ee=4.0 GeV, beam loss: 1.3 W), Collimator Athos (Ee=4 GeV; beam loss: 20 W), Collimator Linac 3 (Ee=6.88 GeV; beam loss: 36.9 W); Collimator Aramis (Ee=6.88 GeV; beam loss: 3.5 W) and a hypothetic beam loss at Collimator Linac 3 (Ee=6.88 GeV, the 2 electron bunches are transferred to beamline ARAMIS; beam loss: 73.6 W).

Table 6.2.1.4: Ambient dose equivalent (ade) rate at specified loss points, based on Dark current assumptions given in table 6.2.1.3 and figures 6.2.1.1. In red, are the positions requiring local shielding.

| position: | dH*10/dt: [μSv/h] | remarks: |
|---------------|-------------------|---|
| BC1_A | 0.3 | POSITION A: technical gallery, zone type 0: area type V, ade _{max} : 10 μSv/h within area type W, gallery, temporary workplace, ade _{max} : 25 μSv/h generally W: abidance is restricted, by direction of authorized body according to operation regulation |
| BC2_A | 3.4 | |
| Switch yard_A | 2.7 | |
| KI-ATHOS_A | 41 | |
| KI-ARAMIS_A | 7.2 | |
| KL-LINAC3_A | 3.7 | |
| KL-LINAC3_A | 7.3 | |
| BC1_B | < 1E-2 | POSITION B outside works premises, public access, non permanent stay, ade _{max} : 0.125 μSv/h Local shielding is required |
| BC2_B | 3E-2 | |
| Switch yard_B | 2.6E-2 | |
| KI-ATHOS_B | 0.4 | |
| KI-ARAMIS_B | 7E-2 | |
| KL-LINAC3_B | 7E-2 | |
| KL-LINAC3_B | 0.14 | |
| BC1_C | 1.4 | POSITION C outside building inside works premises, non permanent stay, ade _{max} : 0.6 μSv/h Local Shielding is required |
| BC2_C | 8.1 | |
| Switch yard_C | 6.4 | |
| KI-ATHOS_C | 6.3 | |
| KI-ARAMIS_C | < 1E-2 | |
| KL-LINAC3_C | < 1E-2 | |
| KL-LINAC3_C | < 1E-2 | |



(left) Cutaway view of the TBI building showing dimensions at BC1 loss points: A, B and C; (right) Cutaway view of the TBL1 building showing dimensions at BC2 and Switchyard lost points: A, B, and C



Cutaway view of the TBL3 building showing dimensions at Linac 3, Athos, Aramis lost points: A, B, and C
 Fig. 6.2.1.1: Positions where the equivalent dose rate has been estimated assuming beam losses of table 6.2.1.2. Those positions are marked A, B and C. Position D is actually covered by soil.

Since the outside of the buildings is, in the current design phase, not declared as a radioactive controlled area, the legal limits for non-permanent stay is $0.6 \mu\text{Sv/h}$ (even $0.125 \mu\text{Sv/h}$ for the roof which is public access). Positions B and C (Figure 6.2.1.1, top) show dose rate estimates above the legal limit so that local shielding around loss position has to be considered (if dark current assumption is confirmed). For position B, the dose rate is 3 times higher than the legal limit at Athos collimator, so that local shielding has to be added. For position C, the legal limit is exceeded by a factor of 10 (at BC2 for example), leading to the same conclusion as for position B. Positions A, which are in the infrastructure gallery can fulfill legislation if the area is declared as a radioactive controlled area. In all cases, the legal limit of $0.125 \mu\text{Sv/h}$ has to be kept outside the fence of the security area.

The estimation of dark current levels is crucial to obtain realistic dose rate. The dose rate estimates of Table 6.2.1.4 are done with assumption on dark current level. Measurements of those level in SwissFEL Injector Test Facility will help to refine those estimations.

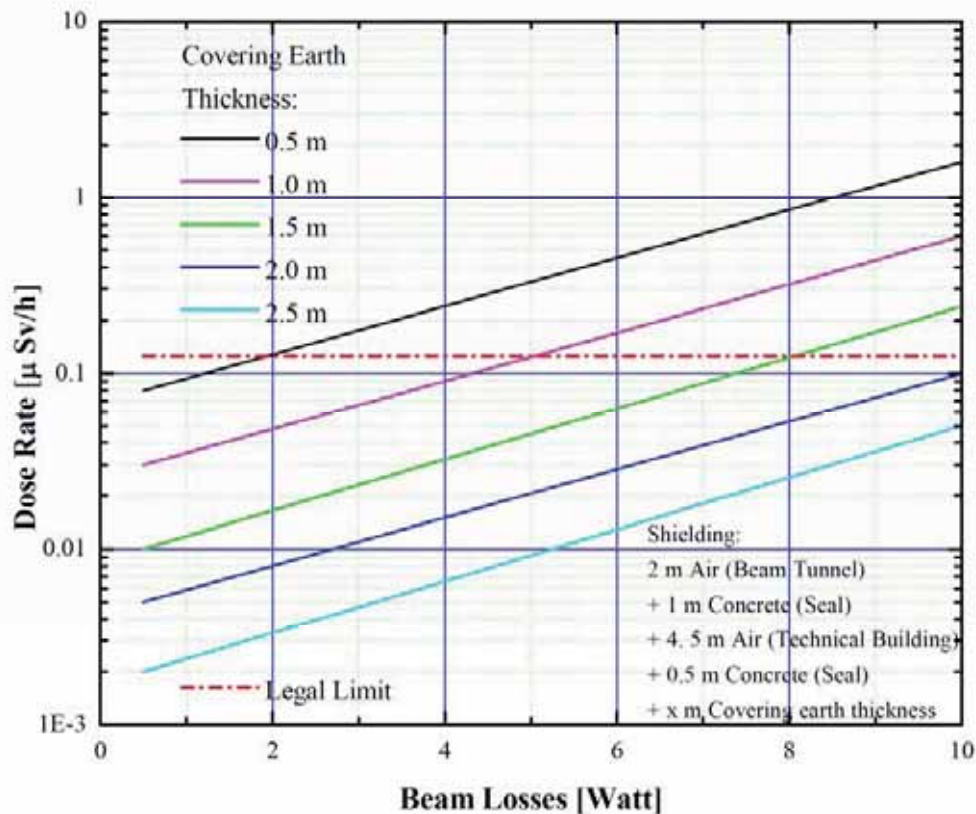


Fig. 6.2.1.2: Dose rate on the top (outside) of the SwissFEL Utility Tunnel as a function of beam losses and thickness of the earth covering the building.

Figure 6.2.1.2 shows that, with 1 m of earth covering the utility building, up to 5 W of local beam loss could be tolerated.

6.2.1.5 Gas Bremsstrahlung

High energy electron accelerator facilities like SwissFEL generate energetic gas bremsstrahlung (GB) photons by the interaction of the beam with residual gas molecules inside the beam tube. The GB is strongly forward peaked so that it accumulates along straight sections of the beam pipe. On the other hand, any curves or chicane in the vacuum chamber is an efficient attenuation of the “0-angle” GB cone. Such chicanes in the vacuum chamber are present for example at bunch compressors BC1 and BC2, collimators where a transversal displacement of about 1 m is realized. Actually the GB will first be scattered on the beam pipe wall at the first pipe curvature, thereby generating an electromagnetic cascade and further multiple scattering effects in the magnet yoke.

The undulator sections of ATHOS and ARAMIS are the most important GB source for the subsequent experimental areas. Indeed the vacuum chamber follows a long straight line until the beam dump (end of the electron beam). This means an accumulation of GB over more than 60 m for Aramis with a divergence of 0.07 mrad at $E = 6.88$ GeV. In order to get an estimate of the GB generated dose rate, semi empirical equations are useful. Assuming 60 m of GB accumulation in Aramis (10^{-7} mbar) and 60 m drift in the Front End section, it should result in a dose rate of 30 $\mu\text{Sv/h}$ in front of the Experimental Hall (EH) shielding wall. Because of the GB divergence (15 mm diameter after 120m), a good part of the GB should be scattered by the beam pipe (beam pipe diameter 8mm) before the EH. Nevertheless to attenuate 30 $\mu\text{Sv/h}$ to a legal value of 1 $\mu\text{Sv/h}$ in the EH, a shielding of 65 cm of normal concrete (or 7 cm of lead) would be sufficient. This shielding element should be placed after each experimental vacuum chamber of Aramis beamlines, if the

vacuum chamber is a straight section (no chicane) from first Aramis undulator to experimental chamber.

In fact, the GB cone will be scattered on the walls of beam tube at shorter distances as assumed for the GB calculations, generating also high energy, forward directed neutrons and muons. The attenuation length λ for high energy neutrons (HEN) is about 51.1 cm in concrete and 17.6 cm in lead respectively.

In order to get in-depth information of the local situation and better accuracy, Monte Carlo codes such as FLUKA or EGS5 have to be utilized – this also in view of optimizations of the problem and cost savings.

6.2.1.6 Dose rate estimates at special locations

Emergency exits:

The beam tunnel is equipped with emergency exits approximatively every 100 m. Each exit consists in a staircase on the side of the tunnel. Those staircase do not have a roof shielding of 1.5 m thickness and thus can present a potential hole in the overall shielding.

Calculation of the potential dose rate leaking in the top floor of the stair case (FEL-FU96-009-2) showed a maximum dose rate of 1.9 $\mu\text{Sv}/(\text{h}\cdot\text{watt})$. Considering the beam losses presented in Table 6.2.1.2, only the Athos Collimator loss point (20 W) might exceed the legal limit of 25 $\mu\text{Sv}/\text{h}$. However the longitudinal distance from Athos Collimator to the escape stairs has not been taken into account and should further reduce the dose rate.

Lift:

The lift well also represents a hole in the roof shielding of the beam tunnel. An ambient equivalent dose rate of 2.6 $\mu\text{Sv}/\text{h}$ at the ground floor of the lift entrance has been calculated (FEL-FU96-011) for a lost power of 1.3 W at the switchyard. This is below the legal limit of 25 $\mu\text{Sv}/\text{h}$ for controlled area.

Dose Rate Limit for Electronics before damage:

Devices with sensitive electronics, like for example electronics profile monitors (CCD cameras), will be positioned all along the SwissFEL beamline. At the location where one can expect electron beam losses (BC1, BC2, Athos collimator) those electronic devices will be irradiated by energetic photons or neutrons. This would cause damages which with time might destroy completely the electronic device. The easiest solution is to shield locally the sensitive electronics close to beam loss points.

Maximum acceptable doses depend on the type of electronic device and it is thus difficult to have an absolute tolerance limit. Tests on a cell phone, showed that it can still work properly after an accumulated dose of 3 Sv of energetic photons and 66 Sv of neutrons (FEL-FU96-014).

For comparison at SwissFEL, radiation dose rate estimated near BC2 (where profile monitor electronics will be installed) is about 126 Sv/year for photons and 5 Sv/year for neutrons. A shielding of 5 cm lead followed by 5 cm polyethylene would reduce this dose to 9 Sv / year and 3 Sv / year for photons and neutrons respectively.

More tests are required to estimate the exact tolerance limit of specific electronic devices, however one can see that local shielding together with longer distance would reduce significantly the risk of damages.

6.2.2 Activation

6.2.2.1 Introduction on material activation with electron beam

Radioactivity is induced in components that are directly hit by an electron beam and in materials surrounding such beam loss points in the close vicinity. It is dependent on the electron energy, the beam power and the material composition. Components such as beam dumps, magnets and collimators absorb most of the bremsstrahlung and will therefore be the most activated. However, high-energy secondary particles can also activate surrounding materials and shielding. A prediction of the expected activation is important for the planning of radiation protection measures, for the estimation of radioactive waste production and for waste disposal. In addition, activation plays a role in the radiation damage of undulator magnets (de-magnetization).

When an electron strikes material, many bremsstrahlung photons are created in the electric field of the nuclei. Most of the highly energetic photons undergo pair production, i.e. a positron and an electron are created, which can in turn produce more bremsstrahlung photons. The spatial extent of this electromagnetic shower is much smaller than that of a hadronic shower produced, for example, by protons. The maximum number of particles is developed at a distance from the first impact of the electron which can be expressed as:

$$t_{\max} = X_0 \left(\ln \frac{E}{E_c} - 0.5 \right)$$

In iron, for example, with a radiation length X_0 of 1.7 cm and a critical energy E_c of 22 MeV (above E_c , the emission of bremsstrahlung outweighs the ionization process), the shower maximum for a 6 GeV electron appears at about 9 cm depth. The shower dies out at about three times the shower maximum. The diameter of the shower is even smaller, for iron it is of the order of the radiation length. In this small volume most of the energy of the primary electron is deposited and radioactive isotopes are created by photonuclear reactions. Secondary particles produced in these interactions (mostly neutrons) also contribute to the activation. A small proportion of them has high energies and can thus initiate a hadronic cascade, thereby extending the activation region. The relevant photonuclear reactions are:

- a) The Giant Dipole Resonance (GDR) interactions ((γ, n) -reactions) between threshold (5-10 MeV) and about 30 MeV : GDR interactions produce neutrons with a Maxwellian energy spectrum ($0.5 \text{ MeV} < \text{kinetic energy} < 1.5 \text{ MeV}$) and an isotropic distribution. These neutrons can in turn interact with nuclei and contribute to induced radioactivity. Their mean attenuation path is of the order of 10 cm in concrete, so that the activity induced by them is roughly contained in the same region as that due to the primary photons. While the neutron fluence is much lower than for photons, their cross-sections are larger, so that they also contribute substantially to the activation.
- b) The quasi-deuteron effect takes place at energies between 30 and a few hundred MeV. In this process a photon is absorbed by a proton-neutron pair in the nucleus, with the possible subsequent emission of a neutron. The cross-section is small compared to the GDR interaction and thus contributes less to the direct activation. However, the neutrons produced have higher energies (depending on the photon energy) and their activating effect can extend over a wider region of space.
- c) Photoproduction of pions: at energies between 200 MeV and a few GeV (nucleon resonances), pion production sets in. Most of the pions are produced in the first resonance (Δ -resonance), whose maximum lies at 300 MeV. The cross-section is of the order of one half of the GDR. But, since photons in the high-energy range are much fewer, the contribution to total activation is comparably small – it may dominate, however, in thin targets, where the electromagnetic shower is not fully developed. Some of the secondary pions and neutrons can have sufficient energy to initiate a hadronic cascade which extends well beyond the GDR activation region.

Direct GDR activation can only lead to a small number of different radioactive nuclides, since only a few nucleons are removed in the interaction. Activation induced by higher-energy photons or secondary particles can yield practically all radioactive nuclides with lower mass number, through spallation or evaporation reactions. While the flux of thermal neutrons is generally small, they can produce large activities in nuclides with very high capture cross-sections, which may be present only as impurities. Because neutrons extend far beyond the region of the electromagnetic shower, the activation is spread over a larger region. With increasing energy of the electron beam, more high-energy neutrons are produced, which are strongly forward peaked. Since the cross-section for inelastic processes of neutrons is almost constant above 200 MeV, their interaction length no longer increases above that energy; for example, the attenuation length for neutrons above 200 MeV in concrete is about 50 cm.

In general, the total induced radioactivity at electron accelerators is less than at proton accelerators of comparable beam power, by typically two orders of magnitude. The number of neutrons and pions produced is, to a good approximation, proportional to the energy of the primary electrons. This can be used as a rough estimate if one compares with the calculations performed for the SwissFEL Injector Test Facility of SwissFEL. For a detailed prediction of the induced radioactivity, it is necessary to use Monte Carlo transport codes with photonuclear capabilities and the possibility to score residual nuclei. At PSI, three codes are available for this purpose, each with specific advantages and disadvantages: FLUKA, MCNPX (coupled to a buildup/decay code) and MARS. They will all be evaluated for their suitability and benchmarked against each other. In the following three paragraphs, a preliminary study of the ground, air and beam dump activation is presented.

6.2.2.2 Estimations of materials activation at SwissFEL facility

a. Activation of soil

Bremsstrahlung, the major part of the electromagnetic emission, is mainly emitted in the forward direction and will thus preferably be absorbed by beam guiding elements such as magnets, slits or similar. The characteristic of emission is isotropic in the lateral direction, where, in general, massive concrete shielding walls are positioned. Nevertheless, high-energy neutrons may be able to survive this barrier and activate the neighboring soil layer. The produced isotopes may diffuse to the ground water due to washout.

The base plate of the SwissFEL building complex has to be well dimensioned, to ensure that there are no operation-correlated soil activations measurable above the StSV exemption levels, expressed in units of LE after decommissioning. One LE is the legal limit for one type of isotope. In the framework of the SINQ approval procedure, extensive bores have been performed in the region of the former SIN, down to the Jura rock (a depth of 25 m). The subsoil of the western side of the Aare river is known to consist of a homogeneous distributed layer of brash down to the ground water level, at a depth of about 20 m, and conditions on the eastern side of the river are assumed to be the same. The mixture of flint and coarse gravel that is embedded in alternating sparse to fatly sand layers can be compared to normal concrete, with respect to its chemical composition.

In order to estimate the degree of soil activation around the SwissFEL beam tunnel, the following assumptions have been made:

- tunnel ground plate and wall thicknesses of 30 cm
- the soil composition described above
- 20 years of operation of SwissFEL (see beam loss assumptions in Tables 6.2.1.3 and 6.2.1.4)

The summation of the radioactivity of all soil components is then made in Table 6.2.2.1, in units of LE. For a typical beam loss of 1% (1.6 W), total activation will not exceed 0.02 LE. To reach the legal limit of 1 LE of activation would require the loss of 64 % (90 W) of the electron beam at 6.88

GeV and during 20 years of operation. Fortunately, such large beam loss can only happen as isolated events, which would immediately trigger the MPS (machine protection system).

Table 6.2.2.1: Total LE and fluence of the mid and high energy neutrons (MID and HEN) in the soil, after the shielding.

| Loss [W] | Total LE | Fluence of MID/HEN [$\text{cm}^{-2}\text{s}^{-1}$] |
|----------|----------|--|
| 1.6 | 0.02 | $3.7 \cdot 10^2 / 3.5 \cdot 10^1$ |
| 90 | 1.0 | $7.2 \cdot 10^4 / 3.5 \cdot 10^3$ |

b. Beam-dump activation

According to the principle of SwissFEL operation, the full electron beam will be dumped in two beam dumps. This corresponds to about 140 W (1 bunch; 100 Hz) in the case of the 6.88 GeV line. The activation has been calculated for different possible target materials. Aluminum shows the highest saturation activity but also presents the fastest decay. The emitted dose rate due to the activation during 20 years is shown in Table 6.2.2.2, after different cooling times. The activation and resulting dose rates are moderate, as far as safety requirements during deconstruction are concerned.

Table 6.2.2.2: Cooling-time-dependent dose rate in Sv/h due to activation for different materials irradiated by an electron beam of 140 W

| Cooling time | 0 sec | 1 hr | 1 year |
|--------------|---------------------|---------------------|---------------------|
| Concrete | $2.7 \cdot 10^{-3}$ | $1.7 \cdot 10^{-4}$ | $1.3 \cdot 10^{-4}$ |
| Alu | $1.9 \cdot 10^{-2}$ | $1.9 \cdot 10^{-3}$ | $5.3 \cdot 10^{-4}$ |
| Iron | $2.5 \cdot 10^{-3}$ | $2.4 \cdot 10^{-3}$ | $3.7 \cdot 10^{-4}$ |
| Copper | $3.6 \cdot 10^{-3}$ | $2.5 \cdot 10^{-3}$ | $1.1 \cdot 10^{-3}$ |
| Lead | $6.1 \cdot 10^{-4}$ | $3.7 \cdot 10^{-4}$ | $2.7 \cdot 10^{-4}$ |

c. Activation of air

The activation of the air around electron accelerators is mainly caused by (γ, n) reactions from bremsstrahlung gammas, induced by the interactions of the electron beam with the target. Secondary neutrons also contribute to activation of the air, mainly through the $40\text{Ar} + n_{\text{therm}} \Rightarrow 41\text{Ar}$ reaction, or from spallation due to high-energy neutrons. Among the isotopes produced, 3H , 7Be , 11C , 13N , 15O and 41Ar are in particular relevant for environmental safety. The half-lives of these isotopes are relatively short compared to the operation time, except for 3H and 41Ar . The expected activities at saturation level of the air activation are shown in Table 6.2.2.3, for different sections of the SwissFEL facility. The ambient air activity is given in units of CA (relative to the Swiss regulation [107]). The legal limit for a Type I zone (such as Linacs 1 to 3 and the undulator) is 0.1 CA, and for a Type 0 zone (such as the injector building and the experimental hall) it is 0.05 CA. Table 6.2.1.5 shows that calculated air activity is below those legal limits.

Table 6.2.2.3: Total air activity at saturation level, expressed in terms of CA, caused by fast neutrons (FN), thermal neutrons (TN) and bremsstrahlung (BS), for different sections of the SwissFEL facility.

| Section: | BS [CA] | FN [CA] | TN [CA] |
|-------------------|---------------------|---------------------|---------------------|
| Main building | $1.5 \cdot 10^{-2}$ | $2.0 \cdot 10^{-8}$ | $5.0 \cdot 10^{-9}$ |
| Linac 1 | $7.3 \cdot 10^{-2}$ | $1.0 \cdot 10^{-4}$ | $1.8 \cdot 10^{-5}$ |
| Linac 2 | $3.8 \cdot 10^{-2}$ | $5.9 \cdot 10^{-5}$ | $1.2 \cdot 10^{-5}$ |
| Linac 3 | - | - | - |
| Undulator section | $1.2 \cdot 10^{-2}$ | $5.1 \cdot 10^{-5}$ | $8.7 \cdot 10^{-6}$ |
| Experimental hall | - | - | - |

6.2.3 Personal Security System (PSYS: PSA; LAC)

The aim of a Personal Security System (PSYS) is to ensure that no access to a specific area is possible when beam operation might occur, while disabling beam operation in the area when access is allowed. Differentiation is made between systems controlled remotely ("Personensicherheits-anlagen", PSA) or locally (Local Access Control, LAC) on the basis of the risk associated with the maximum ambient dose rate caused by beam operation, i.e., the zone type as defined in the ENSI directive HSK-R-07 (June 1995). For SwissFEL, a similar concept to that implemented at the Swiss Light Source (SLS) is foreseen: PSA-controlled access to the accelerator parts (zone types Y or Z) and LAC systems for accessing the beamline areas (zone Type W).

As a fundamental rule, the PSYS has priority over all other control or monitoring systems. Any mistake or alarm signal withdraws the beam-enabling signal to the beam components, resulting in an ALARM status. This status can only be changed when the cause has been identified and resolved.

6.2.3.1 Remote access control systems (PSA)

The access to the beam tunnel is controlled by the PSA systems. The accelerator side (without experimental halls) can be subdivided into three separate areas: from the accelerator up to BC2, Linac 2 to Linac 3, and the area with the undulators. Access to each area is controlled through a fully autonomous PSA, with its own power supply, specific hardware and logics. A specific control panel is installed in the control room, through which the operators on shift duty remotely control access to the areas.

Access to an area is disabled for as long as the ionizing beam, RF or laser beam supply to the area is not securely disabled. Signal-enabling beam operation is distributed to the safety components only when the area is in the LOCKED status. Safety components can include machine components such as the laser shutter, the rf-supply to the gun and the rf-supply to the linac, as well as beamline devices such as dipole magnets and beam shutters.

An appropriate dose-rate instrument is connected to the PSA system, and should the measured radiation signal exceed an alarm threshold, this system will prevent access to the affected area.

6.2.3.2 Local Access Control systems (LAC)

Access to optical and experimental areas of the beamlines is controlled locally by an LAC. Every beamline has its own, independent LAC system, taking into account the specificities of the respective optic and experimental hutches. Access to each separate hutch is controlled through a fully autonomous LAC, with its own power supply, specific hardware and logics. A control panel is installed locally and operated by the user.

The LAC system prevents access to an area for as long as the beam transport to that area is not securely disabled. Signal-enabling beam operation is distributed to the safety components only when the optics or experimental hutches are in the LOCKED status.

Operation of any LAC is independent of the SwissFEL accelerator status. Alarm signals from an LAC are not forwarded, except with a failure signal from a beam shutter, resulting eventually in the withdrawal of the beam-enabling signal to the accelerator components.

6.2.4 General safety

Concerning industrial safety and health protection of staff, the Swiss Labour Law (Arbeitsgesetz) and all pertinent regulations will be followed. More details on the safety concepts for SwissFEL can be found in AN-80-11-01 [108].

Important remarks from [108]:

- There are no permanent workplaces at the SwissFEL Facility

- Construction material consist mainly of concrete
- All RF modulators together represent a stock of 900 liters of Oil.
- Electrical main Transformers will produce noise of 60 dB outside building.
- In the beam tunnel there are emergency exits every 100 m (150 m at one specific location).
- In the experimental hall (EH) and TBs, the standard emergency escape distance is 35 m

At PSI, responsibility and training concerning industrial safety are regulated in the so-called “SGU instructions” (AW-01-07-02). These regulations also hold for the entire SwissFEL project.

6.2.5 Fire safety

Regarding fire safety, the buildings and installations of SwissFEL will be equipped with full monitoring. The fire alarm system will correspond to the VKF guidelines, with control units placed at those entrances which are most relevant for the fire-brigade. Portable extinguishers, filled with the suitable fire extinguishing agent, will be placed in the necessary locations.

Fire compartments and protection distances will be provided in accordance with the VKF guidelines. Escape routes will be provided in accordance with the VKF guidelines and the "Verordnung 4 zum Arbeitsgesetz" (ArGV 4). Emergency vehicles can access the facility from the west side road all along the building. Hydrants will be positioned every 80 m along this road.

6.3 Supply installations (status as of January 2011)

6.3.1 Electrical supply and consumption

Total electrical consumption is a key parameter for defining the required building infrastructure in terms of electrical supply as well as cooling capacity. Table 6.3.1 depicts the electrical consumption in the different SwissFEL buildings (see Figure 6.1.2 for building names location). The table is based on 100 Hz operation repetition rate and show the maximum electrical consumption for each device. In fact, most of the consumption is for the RF power plants and those power plants will be operated at about 80 - 90 % of their maximum.

Table 6.3.1: Estimation of the maximum Electrical power consumption of SwissFEL building for operation at 100 Hz.

| Building name | Device | Maximum Electrical Power Consumption item [kW] | Number of Devices | Maximum Electrical Power Consumption [kW] | Water cooled power [kW] | Air cooled Power [kW] | Reference |
|-------------------|---|--|-------------------|---|-------------------------|-----------------------|-----------------------|
| TBI | RF Power Plants | | | | | | |
| | RF Gun Modulator Unit | 88 | 1 | 88 | 75 | 2.6 | FEL-MP06-257 |
| | S Band Modulators Units | 105 | 6 | 630 | 570 | 15.6 | FEL-MP06-257 |
| | X Band Modulators Units | 104 | 2 | 208 | 190 | 5.2 | FEL-MP06-257 |
| | Air Conditioning for LLRF Racks | 10 | 6 | 60 | 60 | | FEL-GR06-034 |
| | Magnets Power Supplies | | | | | | |
| | Dipole Power Supply (BC1) | 10 | 1 | 10 | 10 | 0 | ref. WLHA - R. Kuenzi |
| | Gun Dipole (7 MeV) | 4 | 1 | 4 | 4 | | ref. WLHA - R. Kuenzi |
| | Injector BC Dipoles (335 MeV) | 6 | 1 | 6 | 6 | | ref. WLHA - R. Kuenzi |
| | Quadrupole QFA Power Supply | 2 | 24 | 48 | 48 | 0 | ref. WLHA - R. Kuenzi |
| | Quadrupole QFD Power Supply | 0.1 | 25 | 2.5 | | 2.5 | ref. WLHA - R. Kuenzi |
| | Solenoid Power Supply | 7 | 9 | 63 | 63 | 0 | ref. WLHA - R. Kuenzi |
| | Corrector Power Supply | 0.1 | 30 | 3 | 0 | 3 | ref. WLHA - R. Kuenzi |
| | Vacuum Ion Pump PS | 0.6 | 20 | 12 | | 12 | FEL-GR06-034 |
| | Control (VME, PC, ...) | 0.3 | 14 | 4.2 | | 4.2 | FEL-GR06-034 |
| | Stepper Motor Driver Rack | 0.6 | 10 | 6 | | 6 | FEL-GR06-034 |
| | Laser | | | | | | |
| | Laser Diode Pumps | 5 | 1 | 5 | 3 | 2 | FEL-GR06-034 |
| | VME, PCs, Displays | 0.3 | 40 | 12 | | 12 | estimation from WLHA |
| | TBI Infrastructure Consumption | 85 | 1 | 85 | 65 | 20 | FEL-GR06-034 |
| TBL1 | RF Power Plants | | | | | | |
| | C Band Modulators Units | 111 | 8 | 888 | 776 | 32 | FEL-AJ84-008 |
| | Air Conditioning for LLRF Racks | 10 | 8 | 80 | 80 | | estimation from WLHA |
| | Magnets Power Supplies | | | | | | |
| | Dipole Power Supply (BC2) | 6 | 1 | 6 | 0 | 0 | estimation from WLHA |
| | Quadrupole QFD Power Supply | 0.1 | 28 | 2.8 | | 2.8 | SwissFEL_CDR_V19 |
| | Corrector Power Supply | 0.1 | 28 | 2.8 | | 2.8 | SwissFEL_CDR_V19 |
| | Vacuum Pump Power Supply | 0.6 | 64 | 38 | | 38 | SwissFEL_CDR_V19 |
| | Control (VME, PC, ...) | 0.3 | 40 | 12 | | 12 | estimation from WLHA |
| | Stepper Motor Driver Rack | 0.6 | 4 | 2.4 | | 2.4 | SwissFEL_CDR_V19 |
| | TBL1 Infrastructure Cons. | 85 | 1 | 85 | 65 | 20 | estimation from WLHA |
| TBL2 | RF Power Plants | | | | | | |
| | C Band Modulators Units | 111 | 7 | 777 | 679 | 28 | FEL-AJ84-008 |
| | Air Conditioning for LLRF Racks | 10 | 7 | 70 | 70 | | estimation from WLHA |
| | Magnets Power Supplies | | | | | | |
| | Quadrupole Power Supply | 0.1 | 18 | 1.8 | | 1.8 | SwissFEL_CDR_V19 |
| | Corrector Power Supply | 0.1 | 18 | 1.8 | | 1.8 | SwissFEL_CDR_V19 |
| | Vacuum Pump Power Supply | 0.6 | 56 | 34 | | 34 | SwissFEL_CDR_V19 |
| | Control (VME, PC, ...) | 0.3 | 40 | 12 | | 12 | estimation from WLHA |
| | Stepper Motor Driver Rack | 0.6 | 4 | 2.4 | | 2.4 | SwissFEL_CDR_V19 |
| | TBL2 Infrastructure Power | 85 | 1 | 85 | 65 | 20 | estimation from WLHA |
| TBL3 | RF Power Plants | | | | | | |
| | C Band Modulators Units | 111 | 11 | 1221 | 1067 | 44 | FEL-AJ84-008 |
| | Air Conditioning for LLRF Racks | 10 | 11 | 110 | 110 | | estimation from WLHA |
| | Magnets Power Supplies | | | | | | |
| | Quadrupole Power Supply | 0.1 | 44 | 4.4 | | 4.4 | FEL-RV84-002 |
| | Corrector Power Supply | 0.1 | 44 | 4.4 | | 4.4 | SwissFEL_CDR_V19 |
| | Dipole Power Supply (Switch Yard) | 6 | 2 | 12 | 12 | 0 | estimation from WLHA |
| | Seed Laser | 5 | 1 | 5 | 3 | 2 | |
| | Vacuum Pump Power Supply | 0.6 | 88 | 53 | | 53 | SwissFEL_CDR_V19 |
| | Control (VME, PC, ...) | 0.3 | 40 | 12 | | 12 | estimation from WLHA |
| | Stepper Motor Driver Rack | 0.6 | 6 | 3.6 | | 3.6 | estimation from WLHA |
| | TBL3 Infrastructure Power req. | 85 | 1 | 85 | 65 | 20 | estimation from WLHA |
| TBU1&2 | Undulator | | | | | | |
| | Undulator Positioning Motors | 0.4 | 24 | 9.6 | 0 | 9.6 | FEL-MP06-257 |
| | Magnets Power Supplies | | | | | | |
| | Quadrupole Power Supply | 0.1 | 95 | 9.5 | | 9.5 | FEL-RV84-002 |
| | Corrector Power Supply | 0.1 | 55 | 5.5 | | 5.5 | SwissFEL_CDR_V19 |
| | Dipole Power Supply (Echo, Collimators) | 6 | 9 | 54 | 0 | 54 | FEL-RV84-002 |
| | Vacuum Pump Power Supply | 0.6 | 72 | 44 | | 44 | SwissFEL_CDR_V19 |
| | Control (VME, PC, ...) | 0.3 | 8 | 2.4 | | 2.4 | estimation from WLHA |
| | Stepper Motor Driver Rack | 0.6 | 48 | 28.8 | | 28.8 | SwissFEL_CDR_V19 |
| | Front End Components | | | | | | |
| | TBU Infrastructure Power req. | 85 | 1 | 85 | 65 | 20 | estimation from WLHA |
| EH | THz Linac Modulator Unit | 105 | 1 | 105 | 95 | 10 | estimation from WLHA |
| | Pump Laser Labs | 5 | 2 | 10 | 6 | 4 | estimation from WLHA |
| | Experimental Hutches | 5 | 6 | 30 | | 30 | estimation from WLHA |
| Reserve | | 100 | 1 | 100 | 70 | 30 | |
| Total | | | | 5341.9 | 4322 | 686.3 | |

The maximum electrical power consumption is about 5.3 MW, of which 4.7 MW are used for beam accelerator components and 0.6 MW for infrastructure components (water pumps, air conditioning, etc). The power going to accelerator components (RF modulator; magnets; etc) is completely dissipated in heat losses (actually, the average FEL light power is only about 100 mW). The main consumption is for the RF power plants units (about 4.2 MW). The heat is dissipated by cooling – 4.3 MW are directly cooled by water (magnets or RF modulators) pumped from the ground and discharged into the Aare river (Figure 6.3.1). The rest of the heat (0.7 MW) is dissipated in the air, mainly in the supply tunnel and the cooling stations rooms.

As mentioned above, Table 6.3.1 shows the maximum possible consumption. In standard operation, the

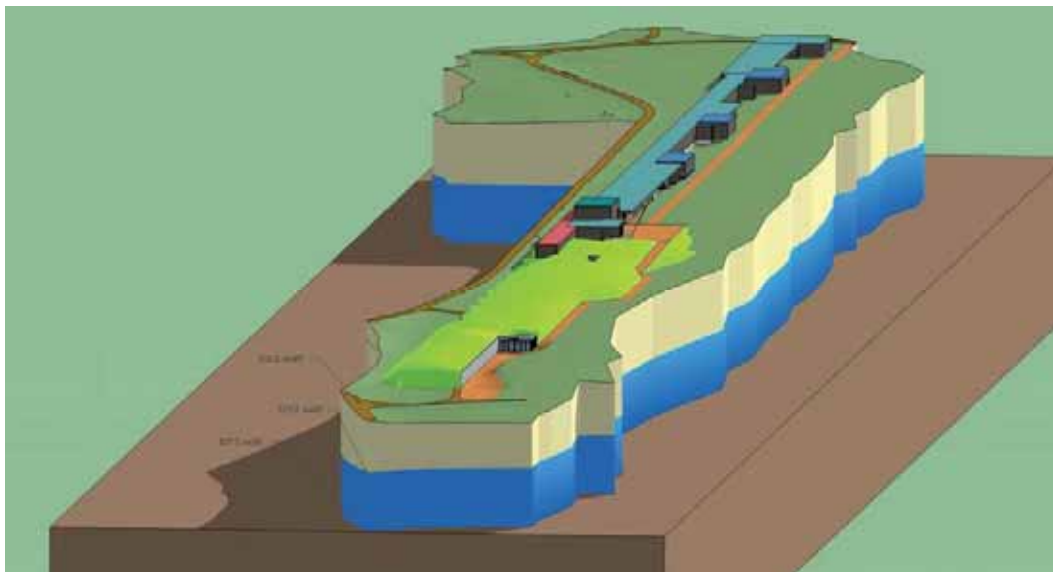


Fig. 6.3.1: SwissFEL building located near the eastern area of PSI. Ground water (25 m deep) is pumped and used for cooling the installation.

➤ **High-Voltage installation**

The 16 kV intermediate voltage feed comes from the existing PSI-East infrastructure, according to the concept: "PSI high-voltage feed connection SwissFEL (Option East)". The facilities to be provided include an intermediate-voltage cable, with intermediate voltage divider and related transformers. After the intermediate voltage divider, two separate networks will be installed. One network will supply the infrastructure (net infrastructure) while the other will feed the machine components (operation installations). Four 630 kVA transformers are planned for the infrastructure and four 1600 kVA transformers are planned for the machine section.

By using the most up-to-date techniques at the intermediate voltage divider (segmented separation) and transformers (fully isolated), the highest possible electrical availability will be provided. The intermediate voltage divider facility is fed from two sides independently by a circuit line connected to the PSI network.

➤ **Main distribution**

The main distribution is a modular design and is divided into infrastructure and machine. The concept is based on certificated MNS systems, Model 3b. Lines >100 A will have power switches, lines <100 A will have fuse techniques or power protection switches. The installation is based on a TN-S grid system. Overall, the electrical distribution systems will be provided with excess voltage protection switches. The MNS systems are foreseen with the so-called insertion technique and

devices can be changed under power. The large power switches will be controlled by a GLS system and an alarm system is foreseen in the case of a failure.

➤ **Overall emergency power supply**

It is not foreseen to install any grid back-up facilities, e.g. emergency diesel engines or connection to the PSI emergency power supply.

➤ **Emergency lighting**

The design follows the official regulations (VKF / GVA). All buildings, such as the experimental hall, injector building or utility buildings, will have stand-alone emergency lighting installations with individual batteries. All these lights are connected by a LAN system. In the case of an electrical network failure, this emergency system takes over the feeding of the emergency signs and safety lighting for a specified time frame (generally 60 minutes). All building units, technical stations and the beam channel will have separate circuit installations with function-conserving FE180 cables and separated luminous sources. To provide minimum maintenance effort and energy consumption, these light sources will be LED-based.

➤ **UPS facilities**

For each building, an Uninterrupted Power Supply (UPS) system of 30 kVA is foreseen. In case of a power failure, these systems will be used to supply the safety units (controls, data storage), such as: GLS, UKV components, ZUKO and door surveillance, and video for 15 minutes maximum. The centralized facilities are foreseen to be located in separated rooms with the transformer stations.

➤ **Sub-distributions**

It is foreseen to have type-proofed and partly type-proofed sub-distributions. The layout of the type-proofed sub-distributions will be modular and follows the definitions for the infrastructures and operating units. Basically the same principle will be used as for the main distributions. In infrastructure buildings, power and light are obtained from these sub-distributions. .

➤ **Development after the transformer units**

Due to voltage loss or break down currents with long cables, the supply grid will be constructed as encapsulated energy lines. Their layout and dimensioning will be made according to the consumption needs and installation regulations. The installation will be placed in the infrastructure tunnel, which leads to the main distribution centre in each technical building.

➤ **Earthing and lightning protection**

All earthing and potential equalising installations will follow the regulations of SN SEV 4113 and DIN 2005. Steel reinforcement within the concrete foundation is defined as part of the potential equalising. In the region of the beam tunnel, every 10 m the core wires will be welded to each other, thereby creating a Faraday cage. From the foundation earthing point onwards, every 10 m earthing points will be made for the connection set V65. All electrical facilities will be connected to the earthing network. All metallic building structures and building services will be connected to each other and to the potential equalising by a link to the earthing system. For the connection of building services and operation facilities, a copper band 20x3 mm will be installed in parallel to the cable trays.

The lightning protection system follows the regulations of SEV 4022 and consists mainly of tin-coated copper conductor, 8mm in diameter. The mesh size of the catching system will be 100m² at its maximum. All natural and artificial conductors will be connected at their deepest level with the earthing system.

➤ **Supplies to sub-distributions, cable trays and energy rails**

The supplies to sub-distributions for the infrastructure and machine components come, in general, with FE0 cables, starting from the main distribution units inside the building units. Large-consumption devices will be connected by encapsulated energy rails, to prevent voltage losses and to limit break-down currents. For the horizontal and vertical development, metallic and perforated cable trays will be used. These will be sorted according to voltage and high and low current. Within the beam tunnel and the utility tunnel, the multi-layer technique will be used for the cable trays. The same technique will also be used for the technical buildings, whenever possible.

➤ **Lighting, emergency lighting, outside Lighting**

Network distribution from the main distribution will supply the different buildings. A special conducting network for emergency lighting is foreseen. For illumination outside of a building, shielded outdoor cables will be installed in the ground. Lighting control will be ensured either by switches or by movement sensors.

➤ **Supply to heating, air, cooling, sanitation**

The electrical supply to the cooling station is carried via an earthed cable tray directly from the main transformer. In the cooling station, an electrical cabinet will distribute power to the different components, such as:

- Sensor and control devices (valves, levels, etc)
- Power devices (pumps, compressors, ...)
- Fire controllers

➤ **Installation electrical plugs, CCE 63A**

All electrical plugs will be compatible with UKV Plugs Type RJ45.

Such plugs are foreseen in every part of the building, as follow:

- every 15 m in the beam tunnel
- every 15 m in the beam tunnel ,CEE Plug 63 A
- every 30 m in the technical buildings
- every 15 m in gun building, experimental hall and cooling stations
- one plug in every air conditioning room.

➤ **Illumination, lighting delivery**

Illumination systems with reflectors and a large angle of diffusion will be hung in the cooling stations, air conditioning rooms, etc. In the beam tunnel and supply tunnel, lighting with high resistance will be installed. The surroundings outside the buildings (along the access path) will have, every 25 m, a lamp at a height of 1 metre. The illumination fluxes foreseen per building area are:

- 500 Lx in the experimental hall, gun building and cooling station
- 200 Lx in the beam tunnel
- 150 Lx in the supply tunnel

➤ **Phone and wireless hubs**

The wireless phone system will be connected to the PSI phone network, with 60 cover hubs distributed throughout the building. In the communication room (in the gun building), a main VS83 distributor for CU connection is foreseen.

➤ **Data transfer and communication**

Data transfer between SwissFEL and PSI will be ensured by monomode optic fibers. Between SwissFEL buildings, monomode and multimode optic fibers will be installed.

➤ **MSRL**

Connection to the MSRL distribution board is ensured by a bus structure, and can be transferred via the LAN to the intervention stations of PSI-East and PSI-West.

➤ **Interlock, video surveillance and door surveillance**

For each building, and at every entrance a video camera for facial recognition will be installed. In addition, a motorized dome camera for large-area surveillance will also be installed. Data are then transferred through the LAN network to the general surveillance centre at PSI-East. In the beam tunnel, a card reader at the entrance is foreseen. The beam tunnel doors are also connected to the general PSA system (see Section 4.2).

➤ **Fire detector system and emergency calling points**

A modular microprocessor-controlled fire-detector system is also foreseen. The installation of the fire detectors will follow the VKF and GVA rules. The main fire detector centre will be located in the experimental hall. This main fire detector will be connected by a communication interface to the GLS system. Connection to the PSI-East area is then ensured via a LAN. An emergency call and NFO system is integrated into the fire detection system.

➤ **Interim electrical supply during construction**

Interim low-power plugs will be available during the construction period. An interim lighting system for general illumination (not working illumination) is foreseen at special locations, such as the staircases, the tunnels, etc. Escape paths will be illuminated with emergency lights, as requested by the VKF regulations.

6.3.2 Heating, cooling, air conditioning and water supplies

6.3.2.1 Summary

The concept of the heating, cooling and air conditioning infrastructure is characterized by a combination of common, cost-effective techniques with low electrical consumption. The challenging requirements regarding temperature stability (± 0.1 K) inside the beam tunnel, as well as the large amount of heat dissipation, can be handled by a proven combination of direct cooling of the magnets, using ground water as sink and a simple forced-air cooling system over the whole tunnel length. The required air conditioning within the experimental hall is ensured by laminal air flow, generated by so-called displacement air outlets. The supply tunnel above the beam tunnel will be similar to server rooms, conditioned by local forced-air cooling systems.

The chosen concept will be applied throughout the whole year, without additional cooling. The cooling comes from existing ground water right at the facility location. The variation of the ground water temperature is extremely small, which helps greatly in meeting the high requirements on temperature stability. In addition, it allows the use of simple cooling techniques, and it is at the same time very ecological and economical. Further temperature stabilizing measures typically needed in chiller systems are not necessary.

6.3.2.2 Main distribution concept

Three infrastructure cooling stations will be built along the SwissFEL facility (see Figure 4.3.2.1). This arrangement has been chosen in order to have similar dimensioning of the cooling stations units. These cooling stations will be interconnected by cable trays. This will allow easy connection to the machine sub-systems, as they are distributed in the supply tunnel along the cable trays. It is foreseen to have all necessary supplies on these trays, such as heating, cooling, special gas lines, electrical power and communication. This main process media distribution system will be connected at its northern end to the PSI infrastructure.

Inside the beam tunnel, the process media trays will run along the ceiling, just above the beam components. The trays will contain the following supplies:

- Cooling water in/out
- Pressurized air
- Nitrogen
- Exhaust gas from vacuum pumps.

At the switchyard, they will be divided into two separate sections, which will follow the beam lines independently.

In general, for the water cooling the main water pipes will be connected to local distribution batteries (in the beam tunnel), to which the magnets can be connected. The incoming flow will be controlled by irises included in the magnet connection screws. The flow will also be controllable at the distribution batteries.

Pressurized air connection points will be installed every 25 m along the beam tunnel. Nitrogen (N₂) and exhaust gas circuits will be installed in the experimental hall. There will be connection points for all the above-mentioned supply lines on the outer wall of the experimental hall.

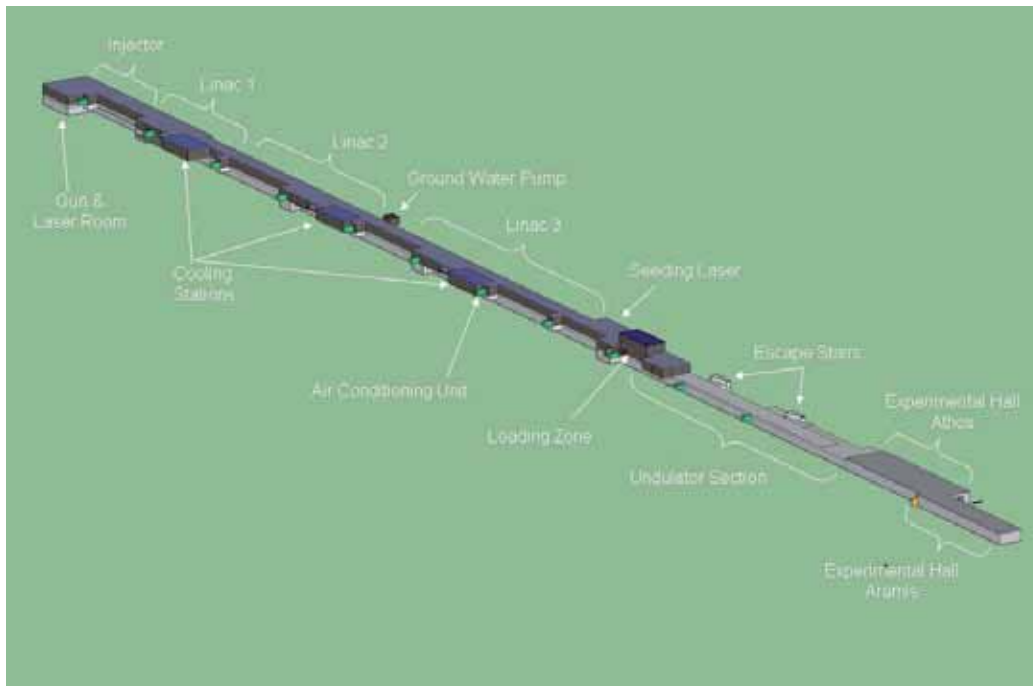


Figure 6.3.2.1: Overview of the SwissFEL facility showing the different infrastructure buildings.

6.3.2.3 Heating facilities

A connection to the Refuna district heating network at PSI-East will be led over the process media trays to the three cooling stations (Figure 4.3.2.1). The required heat will be produced through a heat exchanger and the temperature reduced to 50–30°C. This warm water will then be distributed to the local air conditioning units. Fine stabilization of the air temperature will be ensured by the local air conditioning units (monoblocks). The temperature of the undulator hall should never (also during shutdown) change by more than 2°C or it could irreversibly affect the position of the magnets in the undulator. The temperature of the beam tunnel still needs some optimization (between 26°C and 22°C, depending on the operating temperature of the RF accelerating structures, which is currently set to 40°C). A separate heating group is foreseen for heating the offices, restrooms and labs.

6.3.2.4 Cooling facilities

Cold production

The entire need for cooling will be provided by ground water. The SwissFEL facility will have its own ground water intake. The ground water will be delivered by pumps (Figure 4.3.2.1) to the three cooling stations. At these stations, the cooling power will be transferred through heat exchangers to an ambient conditioning and osmosis circuit. The warmed ground water (30°C maximum) will return under pressure through a pipe into the river Aare.

Cold circuit

In each cooling station there will be a cold circuit with a temperature of 16–22°C. The cold circuit will be stabilized to 16 +/- 0.5°C and the cold water will then be distributed to the users. Fine adjustment of the water temperature has to be made locally by the users (air conditioning unit, flow regulation in the magnets, etc).

4.3.2.5 Air conditioning units

The tunnel will be equipped with approximately 12 air circulation cooling units, to control the temperature within approximately $\Delta t = \pm 0.1\text{K}$ at a specific point in the tunnel. The temperature difference between different locations in the tunnel, however, will be higher. Each unit has a cooling capacity of about 12 kW and air exchange capacity of 6000 m³/h. They will all sit on vibration dumpers and are distributed inside the supply tunnel. Fresh air will be introduced at the gun side of the tunnel and exhausted at the experimental end. In the beam tunnel, air will circulate towards the experiment hall with a speed of 0.13 m/s; the temperature of the tunnel can be measured (and recorded) every 10 m in the tunnel and locally adjusted if necessary. The functional concept is similar to that which has been installed at the SLS.

The utility tunnel will be controlled within a temperature range of $\pm 2\text{K}$ via air circulation cooling units. Each supply building will be equipped with an air handling system, to supply filtered fresh air. The experimental halls will have two air conditioning units, each having a capacity of 20,000 m³/h and a cooling capacity of 40 kW.

6.3.2.5 Sanitation facilities

Wet units

Standard wet units are planned at the injector building and in the experimental hall. At the technical buildings it is foreseen to install a cold and a warm water supply to each sink.

Cold water

Cold water will be taken from PSI-East and distributed to all tap connections.

Hot water

Hot water will be produced at each technical cooling station, and at the experimental hall, using a hydro extractor boiler which also includes a reservoir.

Fire-hose cabinet

Fire-hose cabinets will be installed in all buildings, connected to the cold water supply.

Wastewater

All waste water will be collected by a waste-water pipe which runs underground along the SwissFEL facility. Due to the length of the tunnel and the low downhill gradient, pumping stations will be installed every 150 m.

Surface water

The whole drainage of the roof areas will take place through on-site seepage.

Compressed air

Compressed air will be taken from the connection point at the PSI-East site. From there, a pipe system will supply all technical buildings including the beam tunnel, with a connection point every 25 m. A ring main is foreseen within the experimental hall.

Nitrogen

A reservoir (21 m³) for liquid nitrogen will be placed outside the experimental hall. In addition to that, a vaporizer with a pipe system is foreseen for providing the SwissFEL experimental hall (quality 5.0 and at -70°C), with connection points every 25 m.

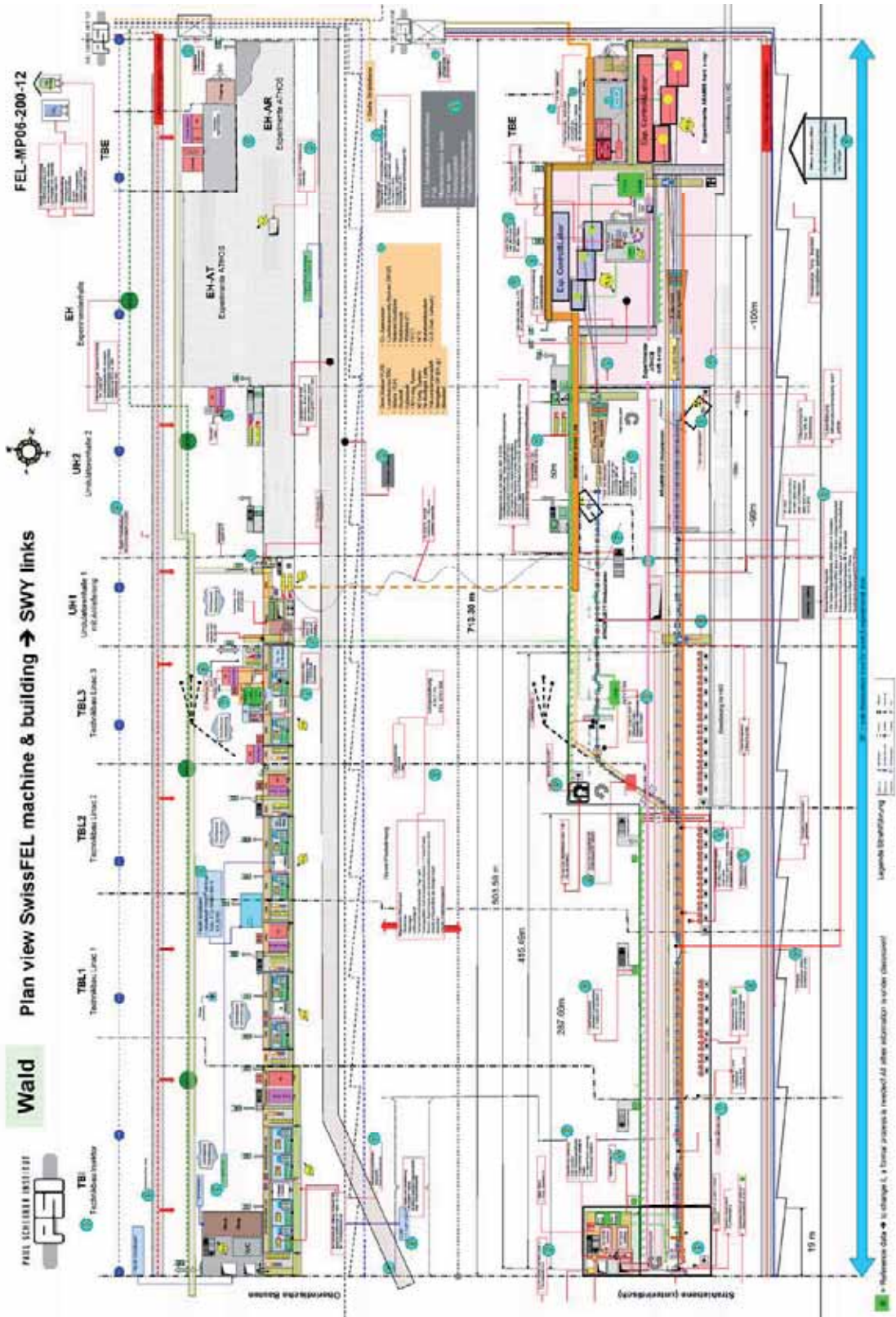
Helium recuperation system

Recuperation of helium gas in the experimental hall will take place through a collection pipe which will run along the complete beam tunnel. This collection pipe will be connected through the media tunnel with the PSI-East site, where a new helium conditioning plant will be installed.

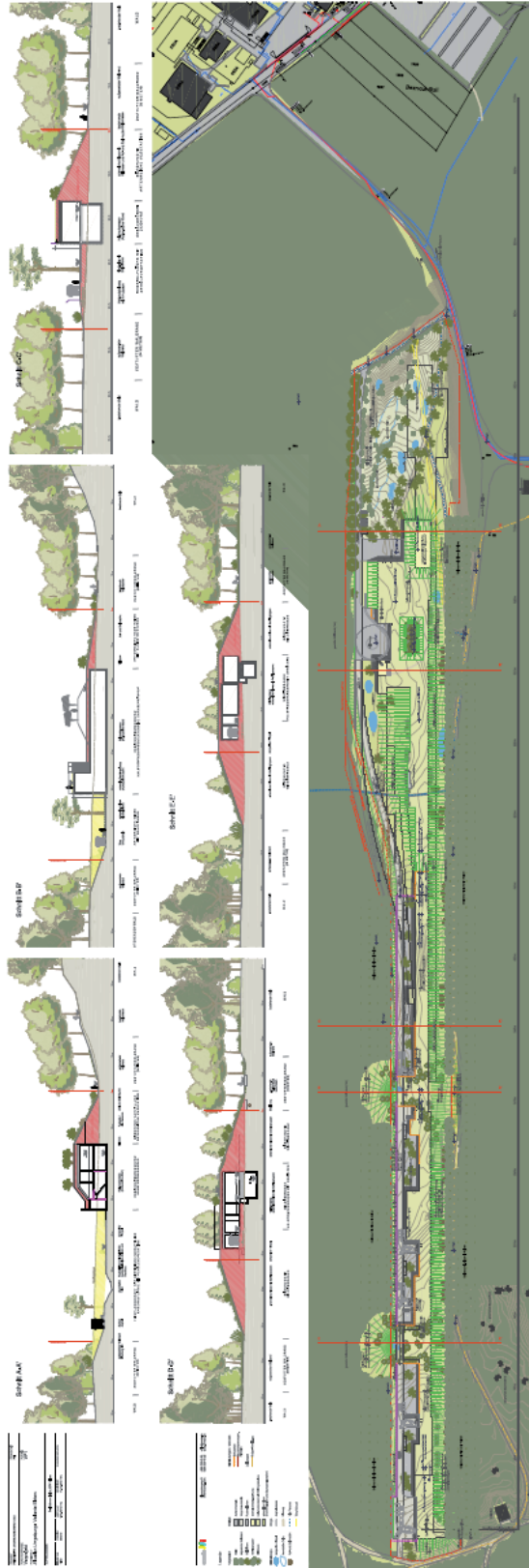
Building and energy management system (MSR)

The SwissFEL MSR facility will be connected to the PSI MSR installation.

6.4 Appendix 6.1: Functional layout of SwissFEL infrastructure



6.5 Appendix 6.2: Drawing SwissFEL Building (Jan 2011)



7 References

- [1] R. Bakker *et al.*, PSI, X-FEL concept based on a low emittance gun, Report No. Volume VI (2004).
- [2] R. J. Bakker *et al.*, Proceedings of the FEL06 Conference, Ultra High Brightness Accelerator Design, Berlin, Germany, 2006.
- [3] B. D. Patterson, Paul Scherrer Institut, (Editor), SwissFEL Science Case - Ultrafast Phenomena at the Nanoscale: Science opportunities at the SwissFEL X-ray Laser, Report No. 09-10 (2009).
- [4] P. Emma *et al.*, Proceedings of the PAC2009 Conference, First lasing of the LCLS X-ray FEL at 1.5 Angstrom, Vancouver, Canada, 2009.
- [5] P. Schmueser *et al.*, Ultraviolet and Soft X-Ray Free-Electron-Lasers: Introduction to Physical Principles, Experimental Results, Technological Challenges, Springer Tracts in Modern Physics (2008).
- [6] C. Hauri *et al.*, Intrinsic Emittance reduction of an Electron Beam from Metal Photocathodes, Phys. Rev. Lett. **104**, 234802 (2010).
- [7] A. Bolzmann, Thesis, Investigation of the longitudinal charge distribution of electron bunches at the VUV-FEL using the transverse deflecting cavity LOLA, Bayerische Julius-Maximilians Universitaet, 2005.
- [8] S. Reiche, Paul Scherrer Institute (PSI), Layout and Optics for SwissFEL Report No. FEL-RV84-002 (2010).
- [9] M. Ferrario *et al.*, *Particle Accelerators*, Vol. 52 (I) (1996).
- [10] M. Borland, APS, Elegant: A flexible SDDS-Compliant Code for Accelerator Simulation, Report No. APS LS-287 (2000).
- [11] W. Herr and F. Schmid, CERN, A Mad-X Primer, Report No. CERN-AB-2004-027-ABP.
- [12] K. L. F. Bane and P. Emma, LiTrack: A Fast, Longitudinal Phase Space Tracking Code with Graphical User Interface, Report No. SLAC-PUB-11035.
- [13] M. Dohlus and T. Limberg, CSRTRACK, <http://www.desy.de/xfel-beam/csrtrack/index.html>
- [14] S. Reiche, Nucl. Inst. and Meth. A **429**, 243 (1999).
- [15] A. Adelman *et al.*, Proceedings of the PAC2009 Conference, The Object Oriented Parallel Accelerator Library (OPAL), Vancouver (Canada), 2009.
- [16] A. Adelman *et al.*, A fast parallel Poisson solver on irregular domains applied to beam dynamics simulations J. Comp. Phys. **229**, 4554-4566 (2010).
- [17] Y. Kim, Future RF Gun for the SwissFEL Project, Presentation at the Project Meeting on July 1st, 2009, Private Communication
- [18] J. Arthur *et al.*, SLAC, LCLS Conceptual Design Report, Report No. SLAC-R-593 (UC-414) (2002).
- [19] R. Roux *et al.*, LAL-Orsay, PHIN - Design of RF Photo-Gun, Report No. CARE Note-2004-034-PHIN (2004).
- [20] C.-X. Wang *et al.*, Criteria for emittance compensation in high-brightness photoinjectors Phys. Rev. ST Accel. Beams **10**, 104201 (2007).
- [21] L. Serafini and J. B. Rosenzweig, Phys. Rev. E **55**, 7565 (1997).
- [22] K. Floettmann, ASTRA - A Space Charge Tracking Algorithm, DESY, <http://www.desy.de/~mpyflo/>
- [23] Y. Kim, Linac for the SwissFEL Facility, Presentation at the SwissFEL Meeting on September 14, 2009, Private Communication
- [24] Y. Ding *et al.*, Measurements and Simulations of Ultralow Emittance and Ultrashort Electron beams in the Linac Coherent Light Source, PRL **102**, 254801 (2009).
- [25] R. Ganter *et al.*, Proceedings of the FEL09 Conference, Commissioning of a diode / RF photogun combination, Liverpool, UK, 2009.

- [26] R. Ganter, B. Beutner *et al.*, Electron beam characterization of a combined diode - rf electron gun, *Phys. Rev. ST Accel. Beams* **13** (2010).
- [27] Y. Kim, Linac Beam Dynamics for the PSI XFEL, Presentation at the FLAC Meeting on April 21, 2009, Private Communication
- [28] K. L. F. Bane and G. Stupakov, Report No. SLAC-PUB-10707 (2004).
- [29] E. L. Saldin, *Opt. Comm.* **202**, 169 (2002).
- [30] L. Yu and I. Ben-Zvi, *Nucl. Inst. and Meth. A* **393**, 96 (1997).
- [31] M. Abo-Bakr *et al.*, BESSY GmbH, The BESSY Soft X-ray Free Electron Laser - Technical Design Report, (2004).
- [32] Z. Huang and K. Kim, *Phys. Rev. E* **62**, 7295 (2000).
- [33] K. Midorikawa, *Phys. Rev. Lett.* **88**, 1422 (1999).
- [34] L. Gianessi, Proceedings of the FEL04 Conference, Trieste, Italy, 2004.
- [35] S. Reiche, Proceedings of the FEL09 Conference, Liverpool, UK, 2009.
- [36] B. Beutner, PSI, Bunch Compression Scheme and Longitudinal Tolerance in SwissFEL Report No. FEL-BB84-001 (2010).
- [37] A. Andrejczuk *et al.*, Hasylab, Investigations of damage thresholds of optical components at the vuv tesla fel phase i, (2001).
- [38] S. Hau-Riege, Absorbed xfel dose in the components of the lcls x-ray optics, Report No. LLNL report UCRLTR-215833 (2005).
- [39] J. Chalupsky *et al.*, Characteristic of focused soft X-ray free-electron laser beam determined by ablation of organic molecular solids., *Optics Express* **15**, 6036-6043 (2007).
- [40] S. P. Hau-Riege *et al.*, Multiple pulse thermal damage thresholds of materials for x-ray free electron laser optics investigated with an ultraviolet laser, *Applied Physics Letters* **93**, 201105 (2008).
- [41] J. Arthur *et al.*, SLAC, Linac coherent light source (lcls) design study report, Report No. SLAC-R-0521 (1998).
- [42] T. Tanaka and T. Shintake, Spring 8, SCSS conceptual design report, Report No. Tech. Rep. SCSS (2005).
- [43] P. Kirkpatrick and A. V. Baez, Formation of optical images by x-rays, *J. Opt. Soc. Am.* **38**, 774-776 (1948).
- [44] U. Flechsig *et al.*, Extended SX-700 type monochromator combining normal and grazing incidence optics for a new undulator beamline at SLS, *Nucl. Instr. Meth. Phys. Res. A*, 467-468, 479-481 (2001).
- [45] R. Ganter, PSI - KIT Collaboration, CDR FLUTE a linac based THz source, Report No. FEL-GR06-120 (2010).
- [46] R. Bossart *et al.*, A 3 GHz photoelectron gun for high beam intensity, *Nucl. Instr. and Meth. in Phys. Res. A* **375** (1996).
- [47] R. Bossart and M. Dehler, Proceedings of the EPAC 1996 Conference, Design of a RF gun for heavy beam loading, Barcelona, Spain, 1996.
- [48] D. Dohan *et al.*, Proceedings of the EPAC Conference, The SLS Test Facility - First Results, Stockholm, Sweden, 1998.
- [49] B. Beutner, Thesis, Measurement and Analysis of Coherent Synchrotron Radiation effects at FLASH, University of Hamburg, 2007.
- [50] R. J. England *et al.*, Sextupole correction of the longitudinal transport of relativistic beams in dispersionless translating sections, *PRSTAB* **8**, 012801 (2005).
- [51] www.fastlite.com
- [52] B. J. Claessens *et al.*, Ultracold Electron Source, *Phys. Rev. Letters* **95**, 164801 (2005).
- [53] M. Dehler *et al.*, *Phys. Rev. ST Accel. Beams* **12** (2009).
- [54] T. Sakurai *et al.*, Proceedings of the IPAC Conference, High-Power RF test on the mass-produced C-band rf components for XFEL / Spring-8, Kyoto, Japan, 2010.
- [55] L. Doolittle *et al.*, Proceedings of the LINAC'06 Conference, Digital Low-Level RF Control Using Non-IQ Sampling, Knoxville, Tennessee, USA, 2006, p. 568.

- [56] S. Hunziker *et al.*, Proceedings of the DIPAC Conference, TOWARDS AN ULTRA-STABLE REFERENCE DISTRIBUTION FOR THE NEW PSI 250 MeV INJECTOR, Basel, Switzerland, 2009, p. 266.
- [57] J. Kim *et al.*, Proceedings of the FEL Conference, Large scale timing distribution and RF-synchronisation for FEL facilities, Trieste, Italy, 2004.
- [58] J. Kim *et al.*, Drift-free femtosecond timing synchronisation of remote optical and microwave sources, *Nature Photonics* **2**, 733-736 (2008).
- [59] S. Schulz *et al.*, Proceedings of the FEL Conference, Progress Towards a Permanent Optical Synchronisation Infrastructure at FLASH, Liverpool, UK, 2009.
- [60] S. Schulz, Proceedings of the 48th ICFA Advanced Beam Dynamics Workshop on Future Light Sources Conference, Progress of the laser - based Synchronization System at FLASH, Stanford, California USA, 2010.
- [61] O. Origami 15, www.onefive.com
- [62] T. Schibli *et al.*, *Opt. Lett.* **28**, 947 (2003).
- [63] J. Kim, *Opt. Lett.* **32**, 1044-1046 (2007).
- [64] S. Schulz *et al.*, Proceedings of the IPAC Conference, Precision Synchronisation of the FLASH Photoinjector Laser, Kyoto, Japan, 2010.
- [65] F. Loehl *et al.*, Proceedings of the PAC Conference, Albuquerque, USA, 2007, p. 3804-3806.
- [66] Corning, SMF-28 ULL Low PMD optical fiber, http://www.corning.com/opticalfiber/products/SMF-28_ULL_fiber.aspx
- [67] R. B. Wilcox *et al.*, Proceedings of the SPIE Conference, A 20 fs synchronization system for lasers and cavities in accelerators and FELs, 2010, p. 7581.
- [68] F. Mueller *et al.*, Proceedings of the DIPAC Conference, Ytterbium fiber laser for electro-optical pulse length measurements at the SwissFEL, Basel, Switzerland, 2009.
- [69] M. Felber *et al.*, Proceedings of the PAC Conference, Long-term femtosecond-stable rf signal generation from optical pulse trains, Vancouver, Canada, 2009.
- [70] J. Taylor *et al.*, Proceedings of the Precise Time and Time Interval PTTI Conference, Characterization of noise properties in photodetectors: a step toward ultra-low phase noise microwaves, Santa Ana pueblo, USA, 2009.
- [71] S. Hunziker *et al.*, Proceedings of the IRUVX Conference, Ultra-stable synchronization system development for FEL-sources:overview, status and perspectives Doellnsee-Schorfheide, Germany, 2010.
- [72] M. Pedrozzi *et al.*, PSI - Switzerland, 250 MeV SwissFEL Test Injector - Conceptual Design Report, Report No. FEL-PM06-089-18-Injector_conceptual_report.doc (2010).
- [73] N. Milas, Private Communication
- [74] H. Ego *et al.*, Proceedings of the EPAC'08 Conference, Design of the Transverse C-band RF Deflecting Structure for Measurement of Bunch Length in X-FEL, Genoa, Italy, 2008.
- [75] R. Ischebeck *et al.*, Proceedings of the DIPAC'09 Conference, Screen monitor Design for the SwissFEL, Basel, Switzerland, 2009.
- [76] P. Kung *et al.*, Generation and measurements of 50-fs (rms) Electron Pulses, *Phys. Rev. Lett.* **73**, 967 (1994).
- [77] J. Menzel, Thesis, THz Spektroskopie zur Bunch-Laengenmessung an der TESLA-Testanlage TTF, University Hamburg - DESY, 2005.
- [78] D. Suetterlin, Thesis, Single-Shot Electron Bunch Length Measurement with a Spatial Electro-Optical-Auto Correlation Interferometer using Coherent Transition Radiation at the 100 MeV SLS Pre-Injector LINAC Institute of Technology Zurich ETH-Z, 2006.
- [79] G. Andonian *et al.*, Proceedings of the PAC'09 Conference, A Single Shot Bunch Length Diagnostic Using Coherent Terahertz Radiation Interferometry, Vancouver, Canada, 2009.
- [80] B. Steffen *et al.*, Proceedings of the DIPAC'09 Conference, A Compact Single Shot Electro-Optical Bunch Length Monitor for the SwissFEL, Basel, Switzerland, 2009.

- [81] F. Mueller *et al.*, Proceedings of the DIPAC'09 Conference, Ytterbium Fiber Laser for Electro-Optical Pulse Length Measurements at the SwissFEL, Basel, Switzerland, 2009.
- [82] B. Steffen, Thesis, Electro-Optics Methods for Bunch Length Diagnostics at FLASH, University Hamburg DESY, 2007.
- [83] B. Schmidt *et al.*, Proceedings of the EPAC'08 Conference, Longitudinal Structure of Electron Bunches at the Micrometer Scale from Spectroscopy of Coherent Transition Radiation, Genoa, Italy, 2008.
- [84] F. Loehl, Thesis, Optical Synchronization of a Free Electron Laser with Femto-Second Precision, University of Hamburg - DESY, 2009.
- [85] M. Bock *et al.*, Proceedings of the FEL'09 Conference, Beam Arrival Time Monitors Used in a Time-Of-Flight Beam Energy Measurement, Liverpool, UK, 2009.
- [86] T. O. Raubenheimer, SLAC, A dispersion free trajectory correction technique for linear colliders, Report No. SLAC-PUB-5222 (1990).
- [87] H.-D. Nuhn, Proceedings of the FEL'06 Conference, Electron Beam Alignment Strategy in the LCLS Undulators, Berlin, Germany, 2006.
- [88] W. Decking, Private Communication
- [89] H. Maseaka *et al.*, Proceedings of the APAC'07 Conference, Beam Position Monitor at the SCSS Prototype Accelerator, Indore, India, 2007.
- [90] D. Lipka *et al.*, Proceedings of the DIPAC'09 Conference, Orthogonal Coupling in Cavity BPM With Slots, Basel, Switzerland, 2009.
- [91] L. Schulz, PSI, Heilige List Haupt Komponenten, Report No. FEL-SL88-027 (2010).
- [92] G. B. Bowden, Proceedings of the Linear Collider Collaboration Tech Notes LCC-0078 Conference, RF Accelerator Pressure Profile by Monte Carlo, 2002.
- [93] R. B. Neal *et al.*, SLAC, The Stanford Two Miles Accelerator.
- [94] M. Seidel, Private Communication
- [95] H. Kitamura, Spring-8/ Riken, In-Vacuum ID Technology, Spring-8/ Riken.
- [96] L. Yin and L. Schulz, Preliminary Design of the Undulator Chamber for PSI XFEL, (2009).
- [97] S. Johnson and U. Staub, Experiment at LCL - 07.2010, Private Communication
- [98] T. O. Raubenheimer and R. D. Ruth, NIM A **302**, 191-208 (1991).
- [99] D. Schulte and N. Walker, Proceedings of the PAC'93 Conference, 1993.
- [100] P. Tenenbaum, SLAC, Report No. SLAC-TN-03-058.
- [101] B. Keil *et al.*, Proceedings of the DIPAC'07 Conference, Design of an Intra-Bunch-Train Feedback System for the European X-FEL, Chicago, USA, 2007.
- [102] L. Tanner *et al.*, Proceedings of the PAC'01 Conference, Digital Control For Highest Precision Accelerator Power Supplies, Chicago, USA, 2001.
- [103] Y. Kim *et al.*, Proceedings of the FEL'09 Conference, FEL'09, Liverpool, UK, 2009.
- [104] M. T. Heron *et al.*, Proceedings of the EPAC'08 Conference, Performance and Future Developments of the Diamond Fast Orbit Feedback System, Genoa, Italy, 2008.
- [105] A. Neumaier, Solving Ill-Conditioned and Singular Linear Systems: A Tutorial on Regularization, SIAM Review **40**, 636-666 (1998).
- [106] A. Ziegler, Langzeitmessungen der Bodenerschuetterungen fur die Varianten "Wald" und "Aare", Report No. Ziegler Consultants #1666 (2010).
- [107] Strahlenschutzverordnung (StSV) vom 22. Juni 1994, Stand 1. Januar 2008.,
- [108] W. Roser and G. Janzi, PSI Switzerland, Planbschreibung SwissFEL, Report No. AN-80-11-01 (2011).